Enabling Capillary Self-Assembly for Microsystem Integration

Massimo Mastrangeli

May 28, 2010

PhD Thesis

Dissertation presented

in partial fulfillment of the requirements

for the degree of

Doctor of Engineering

Department of Metallurgy and Materials Engineering (MTM)

Katholieke Universiteit Leuven

In collaboration with

Abstract

Efficient and precise assembly of very-large quantities of sub-millimeter-sized devices onto pre-processed substrates is presently a key frontier for microelectronics, in its aspiration to large-scale mass production of devices with new functionalities and applications (*e.g.* thin dies embedded into flexible substrates, 3D microsystem integration). In this perspective, on the one hand established pick&place assembly techniques may be unsuitable, due to a trade-off between throughput and placement accuracy and to difficulties in predictably handling very-small devices. On the other hand, self-assembly processes are massively-parallel, may run unsupervised and allow contactless manipulation of objects. The *convergence* between robotic assembly and self-assembly, epitomized by capillarity-enhanced flip-chip assembly, can therefore enable an ideal technology meeting short-to-medium-term electronic packaging and assembly needs.

The objective of this thesis is *bridging the gap between academic proofs-of-concept of capillary self-assembly and its industrial application.* Our work solves several issues relevant to capillary self-assembly of thin dies onto pre-processed substrates. Very-different phaenomena and aspects of both scientific and technologic interest coexist in such a broad context. They were tackled both experimentally and theoretically.

After a critical review of the state-of-the-art in microsystem integration, a complete quasi-static study of lateral capillary meniscus forces is presented. Our experimental setup enables also a novel method to measure the contact angle of liquids. Recessed binding sites are introduced to obtain perfectly-conformal fluid dip-coating of patterned surfaces, which enables the effective and robust coding of geometrical information into binding sites to direct the assembly of parts. A general procedure to establish solder-mediated electro-mechanical interconnections between parts and substrate is validated. Smart surface chemistries are invoked to solve the issue of mutual adhesion between parts during the capillary self-assembly process. Two chemical kinetic-inspired analytic models of fluidic self-assembly are presented and criticized to introduce a novel agent-based model of the process. The latter approach allows realistic simulations by taking into account spatial factors and collision dynamics. Concluding speculations propose envisioned solutions to residual open issues and futher perspectives for this field of rapidly-growing importance.

List of contextual publications

Journal articles

1. **M. Mastrangeli**, W. Ruythooren, C. Van Hoof and J.-P. Celis, “Conformal dip-coating of patterned surfaces for capillary die-to-substrate self-assembly”, *J. Micromech. Microeng.* 19 (2009), 045012 (12pp) (***JMM Highlight 2009***)

2. **M. Mastrangeli**, S. Abbasi, C. Varel, C. Van Hoof, J.-P. Celis and K. F. Böhringer, “Self-assembly from milli- to nanoscale: methods and applications”, *J. Micromech. Microeng.* 19 (2009), 083001 (37pp)

3. P. Lambert, **M. Mastrangeli**, J.-B. Valsamis and G. Degrez, “Spectral analysis and experimental study of lateral capillary dynamics for flip-chip applications”, *Microfludics and Nanofluidics*, DOI 10.1007/s10404-010-0595-2, 2010

4. **M. Mastrangeli**, J.-B. Valsamis, C. Van Hoof, J.-P. Celis and P. Lambert, “Lateral capillary forces of cylindrical fluid menisci: a comprehensive quasi-static study”, *J. Micromech. Microeng.*, accepted for publication, 2010

5. **M. Mastrangeli**, W. Ruythooren, C. Van Hoof and J.-P. Celis, “Challenges for capillary self-assembly of microsystems”, *IEEE Trans. Adv. Pack.*, submitted for publication, 2009

Conference proceedings

6. **M. Mastrangeli**, W. Ruythooren, K. Baert, C. Van Hoof and J.-P. Celis, “Improving Conformality in Selective Dip-Coating of Patterned Planar Substrates”, *Foundations of Nanoscience*, Snowbird (UT, USA), 18-21 April, 2007

7. **M. Mastrangeli**, W. Ruythooren, C. Van Hoof and J.-P. Celis, “Establishing solder interconnects in capillary die-to-substrate

self-assembly", *3D System Integration Conference*, Tokyo (JP), May, 2008

8. **M. Mastrangeli**, W. Ruythooren, C. Van Hoof and J.-P. Celis, "Characterization of solder interconnects resulting from capillary die-to-substrate self-assembly", *IEEE Electronic Systemintegration and Technology Conference*, Greenwich (UK), 1-4 September, 2008

9. **M. Mastrangeli**, C. Van Hoof, R. Baskaran, J.-P. Celis and K. F. Böhringer, "Agent-based modeling of MEMS fluidic self-assembly", *IEEE 23rd International Conference on Micro Electro Mechanical Systems*, Hong Kong, 24-28 January, 2010

Patents

10. **M. Mastrangeli**, W. Ruythooren and C. Whelan, "Method for performing parallel stochastic assembly", PCT/EP2009/062469 *(patent pending)*

Technical Reports

11. **M. Mastrangeli**, K. Jans, T. Steylaerts, "Fast organic conditioning of patterned surfaces for capillary part-to-substrate self-assembly", *Internal report*, IMEC, November 2009.

Workshops

12. **M. Mastrangeli**, "Topological enhancement of binding sites for capillary self-assembly", *Hybrid and Self-Assembly Workshop*, Université Libre de Bruxelles (Bruxelles, BE), 12 March 2009

Seminars

13. **M. Mastrangeli**, "Assembly techniques for microsystems", Katholieke Universiteit Leuven (Leuven, BE), 9 March 2009

14. **M. Mastrangeli**, "Toward hybrid micro-assembly: the self-assembly side", Delft University of Technology (Delft, NL), 13 October 2009

15. **M. Mastrangeli**, "Enabling capillary self-assembly for microsystem integration", Ecole Polytechnique Fédérale de Lausanne (EPFL, Lausanne, CH), 18 March 2010

Lists of symbols and abbreviations

Symbols

α	roll $[deg]$
a	solute activity
β	pitch $[deg]$
b	beam width $[m]$
Bo	Bond number
γ	surface tension $[J/m^2]$
Ca	capillary number
δ	yaw $[deg]$
D	pad diameter $[m]$
ϵ	dielectric constant $[F/m]$
E	Young's modulus $[Pa]$
ζ	edge liquid slope $[deg]$
g	gravity acceleration $[m/s^2]$
h	fluid meniscus height $[m]$
H	mean surface curvature $[m^{-1}]$
I	2nd moment of area $[m^4]$
k	cantilever stiffness $[N/m]$
k_A	association rate constant $[s^{-1}]$
k_D	dissociation rate constant $[s^{-1}]$
K	spring stiffness $[N/m]$
l	auxiliary beam length $[m]$
L	spring beam length $[m]$
L_C	capillary length $[m]$
μ	dynamic viscosity $[Pa \cdot s]$
M	total spring mass $[Kg]$
M_b	mass of spring beams $[Kg]$
M_s	mass of shuttle $[Kg]$
M_{eff}	effective spring mass $[Kg]$
N_P	number of parts
N_S	number of sites
ϕ	edge pad angle $[deg]$
p	pressure $[Pa]$
ψ	liquid slope angle $[deg]$
Ψ	energy map
Q	capillary charge $[m]$
ρ	density $[kg^{-3}]$

r	radius of curvature [m]
R	pad radius [m]
R_A	assembly rate [s^{-1}]
R_D	disassembly rate [s^{-1}]
θ	static contact angle [deg]
θ^a	advancing contact angle [deg]
θ_b	θ on bottom pad [deg]
θ^r	receding contact angle [deg]
θ_t	θ on top pad [deg]
t	time [s]
T_A	time-to-assembly [s]
T_D	time-to-disassembly [s]
u	relative pad displacement [m]
U	withdrawal velocity [m/s]
V	volume [m^3]
v	velocity [m/s]
$x(t)$	number of assembled parts

Abbreviations

ABM	agent-based modeling
BEOL	back-end-of-line
CA	(static) contact angle
CCS	capture cross-section
DDT	dodecanethiol
DIC	differential interference contrast
EDX	energy-dispersive X-ray spectroscopy
FIB	focused ion beam
FSA	fluidic self-assembly
HD	hexadecane
HP	hot plate
IC	integrated circuit
IMC	inter-metallic compound
LED	light-emitting diode
MCCS	matching capture cross-section
MEMS	microelectromechanical system
NL	NetLogo
P&P	pick-and-place
pNIPAAM	poly-N-isopropylacrylamide
SA	self-assembly
SAM	self-assembled monolayer
SE	Surface Evolver
SEM	scanning electron microscope
TC	thermo-compression
TEGDMA	Triethylene-glycol dimethacrylate
UBM	under-bump metallurgy
VO	vacuum oven
W2W	wafer-to-wafer transfer

Acknowledgments

This is an evanescent trace of a transcendental journey.

Though it is hard to document within the narrow margins of this page the wide spectrum of emotions and reflections that riddled this evolutionary path, it is a pleasure to pay tribute here to special people who could witness this enteprise and somehow played a significant role in its accomplishment.

I shall start with Jean-Pierre Celis and Chris Van Hoof, who wisely helped me keeping focus to the ground and critically bore with me in spite of the abnormal fluctuations of my mood. Wouter and Ann took turn in the daily supervision of my wanderings for some time: I thank the former for his criticism, the latter for breaking my long sentences, and both for their patience in dealing with my freaky twists. I duly thank Karl Böhringer (EE Dept., UW, Seattle) and Pierre Lambert (BEAMS Dept., ULB, Bruxelles) for the kicks they gave to my research, the hospitality at their laboratories and their sustained interaction, suggestions and dialectics from afar. I mention Eric and Paresh for the informal technical chats, Rahul for his enduring technical help, Philippe to allow me freedom even in the late stringent IMEC conjuncture, and Marion, Katrien and Veronique for their constant availability and kindness.

Mention of honour to FWO for financial support, and to the wonderful crowd of the Santa Fe Institute and CSSS09 for inspiration.

Nonetheless, it goes without saying, the bulk of personal support during the last 4 years came from my friend network. Its diameter is now world-sized, so to avoid embarassment the following order is essentially topological - all evoked people know the strength of their own link to my node. Massimo F., Stefano P., Vincenzo P. (Sr) and Daniele N. were precious and implacable references and mirrors that helped me against vertigo. Silvia L. used her constant good temper to smooth my bad one, Pierluigi N. used to, as well, before returning to his nerdy roots. Marco S. and Salvatore P. were indisputably the locally-closest to me in a long period of darkness, and along with Vito G., Emanuele C., Marco F., Andrea F., Gerardo B., Elisabeth C., Ole L., Marie GB., Antonio LM., Marco T. and Marcello P. were amazing dudes to wisely appreciate my vicious insights and tolerate my excentricities. I am proud to share with Apo, Lucas, Martin, Jean-Baptiste, Gregory and Ji the same great funky nerdness.

Finally, the deepest gratitude goes to my family - that perpetually watched over me all this long time.

Contents

1 Microsystem Integration **13**
1.1 Monolithic integration of microsystems 13
1.2 Assembly of microsystems 18
1.2.1 Serial deterministic assembly 19
1.2.2 Parallel deterministic assembly 22
1.2.3 Parallel stochastic assembly 24
1.3 Integration by self-assembly: state-of-the-art 32
1.4 Thesis objectives and outline 40

2 Capillary Self-Assembly **45**
2.1 Capillary self-assembly of microsystems 45
2.2 Surface tension-related phenomena 47
2.3 Earlier works on lateral capillary forces 57
2.4 Lateral capillary forces of fluid menisci 58
2.4.1 Experimental study 59
2.4.2 Finite-element model 69
2.4.3 Results and discussion 70
2.5 Symmetry versus directionality 75
2.5.1 Performance of square parts 75
2.5.2 Unique in-plane part placement 82
2.6 Conclusions 85

3 Dip-coating of Patterned Surfaces **87**
3.1 Conformality matters 87
3.2 Fluid deposition techniques 88
3.3 Dip-coating of planar substrates: background 89
3.4 Conformal dip-coating of binding sites 90
3.4.1 Superficial versus recessed binding sites 90
3.4.2 Substrate conditioning 91
3.4.3 Experimental results 94
3.4.4 Numerical simulations 98
3.5 Control over dip-coated lens volumes 103
3.6 Conclusions 107

4 Interconnects in Part-to-Substrate SA **109**
4.1 Functional interconnections 109
4.2 The experimental procedure 110
4.2.1 Materials and methods 110
4.2.2 Solder oxide removal 112
4.2.3 The capillary assembly step 114
4.2.4 Post-assembly solder bonding 115
4.3 Results and characterizations 117
4.3.1 Phenomena associated with reflow 117
4.3.2 Characteristics of interconnects 122
4.3.3 Further insights 132
4.4 Conclusions 134

5 Avoiding Mutual Part Adhesion **135**
5.1 The interfering 3D self-assembly process 135
5.2 The unnecessary assumption 136
5.2.1 Molecular switches 137
5.2.2 Switching polymers 139

6 Modeling of Self-Assembly Dynamics **141**
6.1 Dynamics of self-assembling systems 141
6.2 Analytic models for static passive SA 142
6.2.1 The steady-state model 143
6.2.2 Nonlinear time-continuous model 145
6.3 Critics to analytical modeling 148
6.4 ABM of 3D fluidic self-assembly 149
6.4.1 ABM Investigations 152
6.4.2 Analogy with molecular dynamics 158
6.5 Conclusions 158

7 Conclusions and Further Challenges **159**

Bibliography **173**

Chapter 1

State-of-the-Art in Microsystem Integration

This Chapter presents a critical review of the state-of-the-art in the fabrication of microsystems (a synoptic map is presented in Fig. 1.1). After discussing monolithic integration, the focus concentrates on assembly techniques, exposing both deterministic (pick-and-place and wafer-level transfer) and stochastic (self-assembly) methodologies. It is concluded that self-assembly holds the best potentialities to efficiently address the assembly of microsystems at large scales (*i.e.* the assembly of tens of thousands of sub-millimetric parts). Specifically, capillarity-driven self-assembly is considered, among many alternatives, as most-promising to introduce the self-assembly paradigm in industrial microsystem manufacturing and, in the short-term, to complement and enhance established packaging methodologies. The reminder of this thesis will investigate several aspects of capillary self-assembly.

1.1 Monolithic integration of microsystems

The technological success of microelectronics is rooted in - besides economical and sociological factors - the development of a vast set of microfabrication techniques. This toolkit - including thin film growth and deposition, patterning, etching, cleaning, planarization processes and inspection techniques [1] - enabled the *monolithic* approach to the fabrication of integrated circuits (ICs). Monolithic electronic ICs first combined enhanced performances and reliability with a drastic production-cost reduction thanks to the large-scale batch-mode fabrication of devices of ever-shrinking dimensions [2].[1]

[1]The approach striving to keep up with the early scaling rate observed by G. Moore is dubbed 'More Moore'. It is confronted by the 'More than Moore' trend which collects all alternative approaches for further development of electronics (Fig. 1.2). Assembled heteroge-

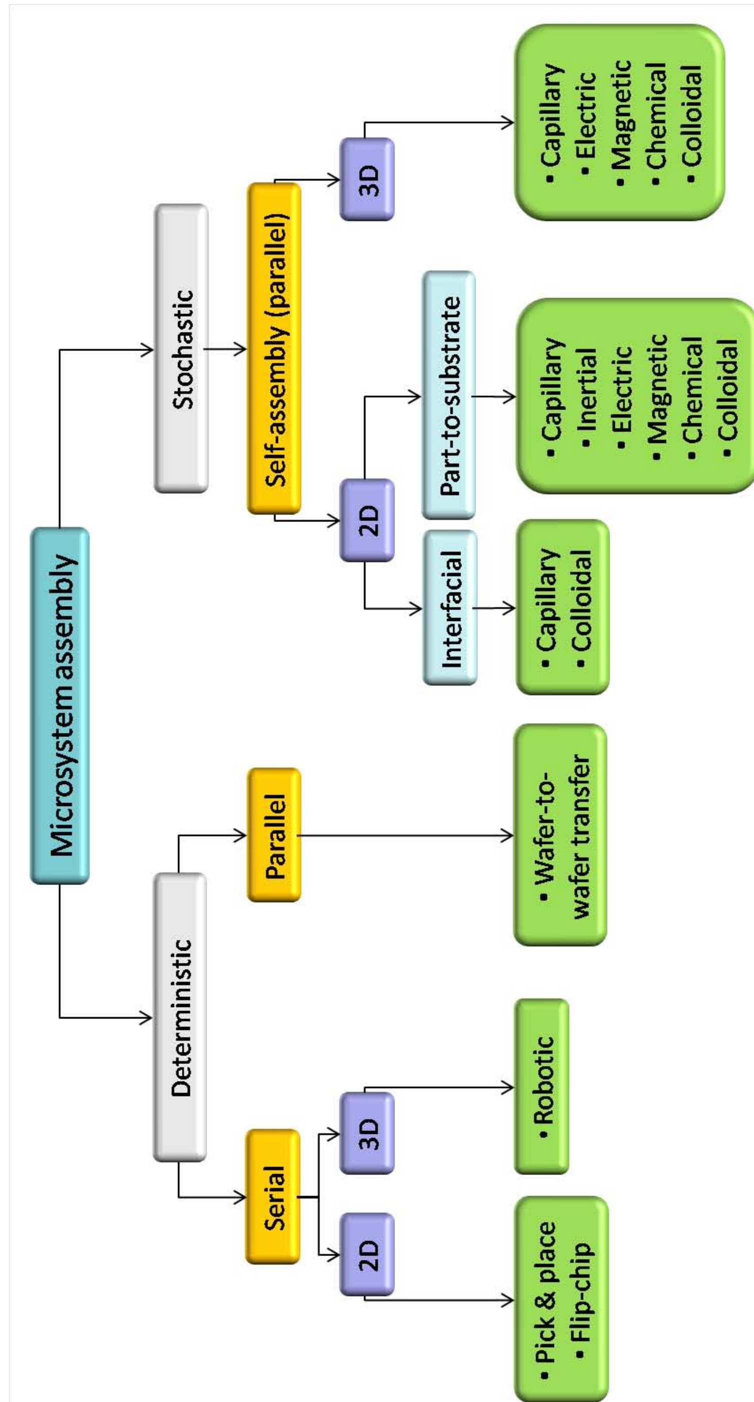

Figure 1.1: Assembly of microsystems (adapted from [3]).

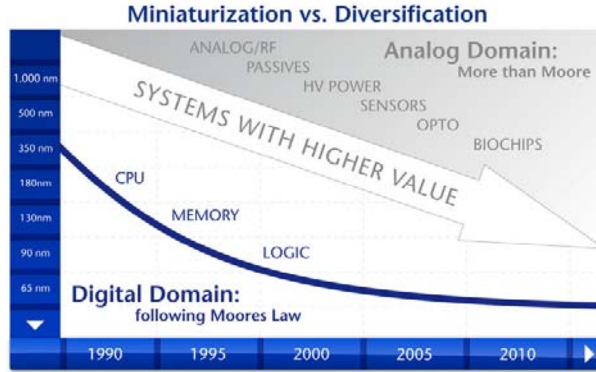

Figure 1.2: *More Moore* and *More-than-Moore* (source: X-FAB).

Sharing microelectronics' technological origins, micro/nano electro mechanical systems (M/NEMS) promise to extend ICs' revolutionary approach to mechanics, optics, chemistry, fluidics and possibly other appealing fields. MEMS ignited when it was realized that:

1. microfabrication techniques (including bulk [4] and surface micromachining [5], and high aspect-ratio structures [6]) could be used to build complex mechanical devices, as well;
2. many electronic materials could work as mechanically-remarkable structural materials, as well [1, 7]; and that
3. physical scaling laws allowed actuation mechanisms, poorly efficient at macroscale, to be advantageous at microscale [8].

The microsystem perspective can bring heterogeneous functionalities directly at the chip level. The closer interface between system's core and peripherals can reduce the gap between information retrieval and information processing, allowing a tighter interaction with the environment. Over the last three decades a large amount of microsystems appeared, addressing a wide range of functionalities and applications: from sensing to actuation and to microoptics, from RF devices to microfluidics and to energy management [9]. Ongoing miniaturization of devices may also enable the organization of distributed non-intrusive wireless sensor networks [10, 11] for *e.g.* environmental monitoring [12] and ambient intelligence [13, 14].

Ultimately, a successful technological convergence between electronics and M/NEMS could unleash truly complex and smart microsystems.

In *monolithic microsystem integration*, each component is fabricated directly at its desired location in the pre-planned system architecture. Some microsensors can be completely produced by means of standard IC process sequences (*e.g.*

---

neous microsystems belong to the latter trend.

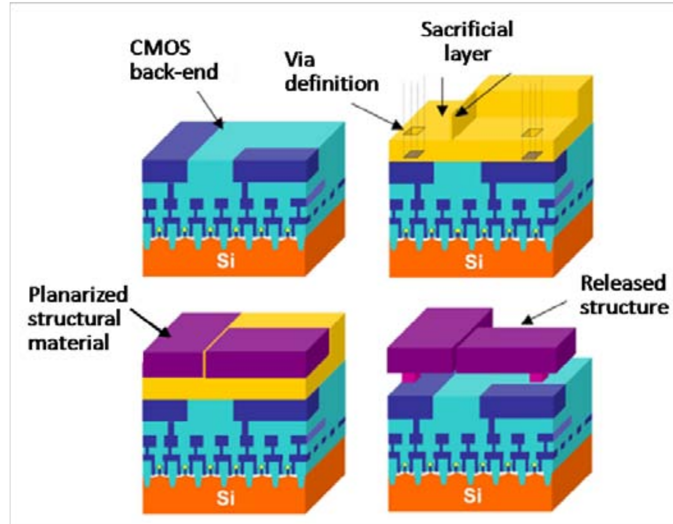

Figure 1.3: A MEMS resonator integrated over a CMOS substrate (after [15]).

temperature and magnetic field sensors, CMOS imagers). Others require only the modification of a CMOS layer and/or the deposition and patterning of additional films (*e.g.* ion-sensitive field-effect transistors, chemoresistors/capacitors, force sensors, biosensor arrays for DNA analysis) [16]. More generally, the fabrication steps of different devices can be interleaved ("intra-CMOS"), or performed sequentially in a modular fashion ("MEMS-first" or "pre-CMOS", and "MEMS-last" or "post-CMOS" processes, as in Fig. 1.3) [16, 15]. Such co-fabrication makes efficient use of source materials, and it aims at compactifying the design and maximizing the functional density of systems while minimizing die size, length of electrical interconnects (with associated parasitics and losses), noise sources and electromagnetic interferences, system-power requirements and packaging load on production costs [5]. Vivid examples of this approach are the integration of III-V optoelectronic devices over silicon substrates [17]; the Al-based digital micromirror display [18]; accelerometers and gyroscopes with on-chip electronics [19]; the poly-SiGe devices micromachined on top of CMOS ICs [20, 21, 22]; the AlN-based bulk acoustic wave resonators integrated on top of SiGe BiCMOS electronics [23].

Nevertheless, some intrinsic constraints could hinder the suitability of monolithic microsystem integration for mass production, as compared to alternatives:

1. ***Fabrication sequences and material requirements are often incompatible***. For instances: the deposition of GaAs over Si produces high densities of interfacial defects, densities, due to mismatches in lattice constants and thermal-expansion coefficients, and high-temperature passivation and doping steps can seriously damage GaAs wafers while contaminating circuitry and tools dedicated to Si; the high temperatures

needed for the deposition of (poly) crystalline silicon MEMS structural layers and for the post–deposition stress-reduction anneals of structural thin films are not tolerated by fully-processed CMOS substrates (as they induce *e.g.* resistance change in metallic interconnects, distortion of doping profiles, stresses by thermal-expansion mismatches, degradation of low-k dielectrics); plastic substrates cannot easily host electronic components, also due to thermal constraints; the need of selective, aggressive chemistries and ionic bombardments for etching may pose further problems to materials coexistence. While extensive material research is being pursued in these areas, inconsistencies of these kinds presently impose mutual constraints and compromises even among modularized process flows, resulting in suboptimal properties and/or limited range of functionalities for the overall systems.

2. ***Potential reduction of production yield***. Monolithic integration is fully-sequential. Each processing step has a non-null failure probability, and the cumulative fabrication yield results approximately [2]from the product of single steps' yield. Moreover, while the total number of steps required in monolithic process flows may be larger[3] than the sum of those needed for the mere production of single devices, each step's yield may be reduced by the aforementioned compatibility requirements. The number of sources of yield loss in monolithic productions is also apparently increasing due to increased complexity of process flows and downscaling of geometries [24].

   As a consequence, monolithic integration has poor portability: the compatibility issue has to be faced for every new combination of materials and techniques. This may significantly slow down the development cycle.

3. ***Spatial constraints***. Thin film-based microfabrication technologies fundamentally operate in a two-dimensional (2D) physical space. Three-dimensionality is normally obtained only as an extrusion of 2D features to the third dimension (*e.g.* through layer stacking and sacrificial layer removal [1, 5], isotropic and anisotropic etching [1, 4], post-fabrication actuation of microstructures [25, 26]). Therefore, monolithic integration, by itself, would probably not allow the full exploitation of spatiality. Conversely, 3D integration - besides being a promising frontier in ICs design [27] - appears pivotal to realizing complex architectures, thanks to much higher volumetric densities of components, larger surface-to-volume ratio (which would ease interfacing and thermal management) and superior design freedom.

The alternative to monolithic microsystem integration is microsystem *assembly.*

[2]Besides being sequentially performed, these steps are highly-correlated: the success of each step depends also on that of previous and subsequent steps. Eventual errors in each step can thus propagate both forward and backward.

[3]Additional steps, possibly introduced for safer device co-fabrication, may be *e.g.* coating and passivations/encapsulations, alignments, patterning and etching.

1.2 Assembly of microsystems

We define *microassembly* as *the discipline of positioning, orienting, and assembling sub-millimetric components into complex systems* with the goal of achieving *hybrid microscale devices of high complexity, while maintaining high yield and low cost* (adapted from [28]). In microsystem assembly, microdevices of heterogeneous nature are fabricated out of their most convenient process flow(s), then removed from their native substrates and put together to co-ordinately compose the overall system. Microassembly's application range is formally comprised between that of macroscale assembly (dealing with linear dimensions larger than 10^{-3} m) and that of molecular (or nanoscopic) assembly (*i.e.* linear dimensions smaller than 10^{-7} m).

Technological compatibility and modularity are critical here. Assembly should ideally preserve the integrity of devices and not preclude further processing on the final system, which could include coating, metallization, sealing and packaging[4].

Assembly has already been largely used in microelectronics: from the circuital level (*e.g.* quartz resonators in RF circuits) to the chip level (*e.g.* 0/1-level packaging) to System-on-Chip (SoC) level (*e.g.* Multi Chip Modules (MCMs)).

Microassembly brings forth some advantages compared to fully-monolithic fabrication:

1. ***Decoupling of fabrication processes***. Each constituent device can be produced by its optimized process flow: given its individual functionality, only its size, shape and its interfacial features should be beforehand considered in the design of the complete system. By eliminating most material and process constraints and retaining only geometrical ones, it can recover an optimal yield at device level[5].

   On the other hand, a substantial part of production yield, reliability and cost would then be dependent on the characteristics of the assembly technique itself.

2. ***Known Good Dies (KGD)***. The functionality of each microdevice could in principle be tested before assembly[6].

3. ***Fully three-dimensional architectures***. Assembly is an intrinsically three-dimensional technique, as it involves spatial roto-translations of parts. New coordination possibilities among modules could be feasible, allowing more freedom of ingenuity in microsystems architecture and design solutions. As an example, in Systems-in-Package (SiP) multiple modules are stacked vertically into a single package.

[4] Packaging may be integral in the assembly process as well (see *e.g.* [29])

[5] With reference to note 2: decoupling of production processes reduces the correlation among production steps, and puts an upper bound on the extent of errors propagation.

[6] The testing procedure may be time consuming, and it may have a non-negligible influence on production costs.

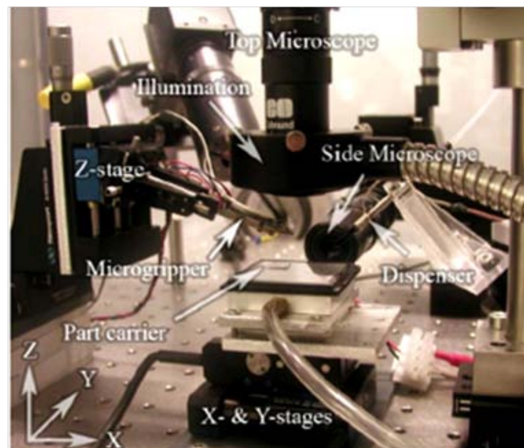

Figure 1.4: Serial assembly combining pick&place with capillarity, after [31].

While microsystems' fully-monolithic integration must be considered in most cases a long-term target, in the middle-term their assembly is of utter importance. Microassembly techniques should rank together with monolithic integration as fundamental instruments within the *microengineering toolbox*.

The rest of this Chapter reviews microassembly. Following the nomenclature sketched in [28, 30, 3], the deterministic approach is first exposed, both in its serial (Sec. 1.2.1) and parallel (Sec. 1.2.2) modalities, followed then by the stochastic approach (Sec. 1.2.3) - where the contributions of this work lie.

1.2.1 Serial deterministic assembly

Today's IC and MEMS assembly is mostly performed by robotic apparatuses. This approach can be described as *deterministic,* by which we define assembly methodologies in which the physical trajectory to be described by the parts - each having a predefined position in the aggregate - during the assembly is completely specified *before* the actual assembly takes place.

The reference paradign of serial assembly is *pick-and-place* (P&P) assembly. It consists in picking up a component (from its original support, or from dedicated part feeders[7]), transporting it to the targeted substrate and finally sticking it in its specific system location. High-precision automated facilities, such as multi-axes robotized manipulators (Fig. 1.4) are normally used.

Flip-chip bonding [32] is a common P&P assembly method for electronic chips with millimetric dimensions. The process requires three steps. First, chips and substrate are prepared for bonding by depositing thin metallic films (Under Bump Metallurgy, UBM) and solder bumps. Then, the chips are 'flipped' upside-down (*i.e.* turned to face the substrate with their to-be-bonded side),

[7]During a typical part feeding process, randomly-agitated components move through a series of mechanical filters until they assume a proper orientation toward the picking tool.

picked up and brought onto their *binding sites* on the substrate. Finally, the chips are metallurgically bonded[8]. Placement accuracy of the chips can be enhanced by solder/metal wetting [34] and proper design and spatial distribution of the solder bumps [35], eventually combined with mechanical stoppers [36]. Solder-mediated flip-chip technology provides relatively-short interconnections, small device footprints and good noise control[9]. While the characteristics of the bump are critical for interconnect parasitics and bond reliability, P&P is the most labour-intensive step and actually governs the cost of the process. Parameters optimization can lead to good yield at reasonable manufacturing costs [37, 38, 39, 36]. Interesting applications include optoelectronics (see [35, 36] and references therein) and RF-MEMS [40].

Adapting P&P to microassembly reveals not trivial, though. As a rule, the smaller the part to be handled, the larger (and more expensive) the machine required to manage it. Moreover, *seriality*, *contact handling* and *feedback control* are problematic issues of the P&P method:

1. ***Seriality***. Intrinsic to P&P, seriality is critically at odd with batch-mode ICs fabrication. Robotic assembly facilities can only compensate non-parallelism with speed: they can handle up to tens of thousands of surface-mount devices per hour, with part sizes ranging from hundreds of microns to millimetres. Whereas similar figures can be adequate for some consumer electronics applications, as for microsystems the evident advantages of batch ICs fabrication would be essentially lost unless massive parallelism would be extended to assembly.

2. ***Contact-handling***. To be grabbed, single parts need to be directly contacted by the manipulator[10]. Besides introducing the chance of damaging the parts, the physics of the interfacial interactions between the parts and the handler assume critical importance for the success and repeatability of the operation. Here downscaling plays a key role.

   The hierarchy of forces acting on microscopic objects is different from that holding for macroscopic ones. While body forces scale with the third power of the linear dimension, surface forces scale with its second power. The surface-to-volume ratio is also larger for smaller bodies. As a consequence, gravity and inertial forces become progressively negligible compared to surface tension and adhesion forces: smaller systems are much more influenced by interfacial effects [42]. While this behavior supports actuation mechanisms and functionalities peculiar to MEMS [8], it is also the cause of some of their problems, due *e.g.* to stiction and friction [43].

   Sticking effects are acknowledgedly the origin of difficulties in contact handling of microscopic parts [44]. Adhesion forces are caused mainly

[8]Relatively large chips can also undergo an underfilling step (*e.g.* by epoxy), to reduce the stress on the bump caused by mismatches in thermal expansions and to enhance reliability. Both sequential and concurrent reflow/underfill processes are possible [33].

[9]Because of this, the flipped configuration is the preferred final chip pose of most assembly techniques described in later Sections.

[10]What is considered here is the most common situation, though not the most general [41].

by [44, 45]: electrostatic attraction, arising from triboelectrification (due to friction), charge transfer (due to difference in contact potential) or charge trapped inside dielectrics (*e.g.* native oxide); Van der Waals interactions [42]; and surface-tension effects by the interaction of surface layers of adsorbed moisture. The relative importance of these components is influenced by surface conditions (chemistry, geometry, roughness) and environmental parameters (temperature and humidity); all effects can be larger than gravity at microscale.

The use of a fluid medium helps overcoming electrostatic and surface-tension effects[11]. Several design solutions for microgrippers and microtweezers are described in literature [46, 47, 48, 49, 50]; some ingeniously try to take advantage of the forces described above, as well.

It can be concluded that the ability to efficiently manipulate individual parts rapidly decreases with the reduction of their dimensions: P&P, by itself, is not suited for sub-millimetric dimensions. On the other hand, at nanoscale direct-contact manipulation through nanotweezers and AFM tips seems to constitute a viable solution for precisely-controllable addressing and placement of nanoscopic objects (see [51] and references thereby).

3. ***Supervision***. In P&P, the exact knowledge of the position of the part and its manipulator normally requires real-time tracking. Automated control is also required to develop a robust manipulation strategy. These tasks, routinely pursued at larger scale, face serious issues at microscale [52, 41].

   While the same kinematic models are applied in both circumstances, the main difference between macro- and microassembly is the required positional accuracy. The typical macroscale target of a few hundreds microns cannot be tolerated at microscale, where (sub-)micron precision is required. This degree of accuracy is outside the calibration range of open-loop, precision assembly devices, so that sensor-based, closed-loop control techniques are needed[12] to compensate for model approximations and errors deriving from thermal expansion[13] and computation.

   Real-time visual feedback and/or force sensing are normally suited for this purpose, but retrieving accurate sensor information at microscale can be hard. Tweezers with integrated actuators and sensors of high sensitivity to minimal forces and displacements are required [54]. For visually-guided assembly [53, 55] image processing can be slow and susceptible to environmental conditions (light, reflections, colour change). Moreover, multiple optical axes are required for three-dimensional manipulation, but the line-of-sight may be obstructed by much larger tools that, together with cameras, may also impede the proper manipulation of objects.

[11] This is one rationale behind fluidic self-assembly approaches (Sec. 1.3).

[12] Feedback control is also needed because of poor micromanipulation predictability [53].

[13] For large, precision machines, compensating for thermal growth errors may require dedicated cooling systems, or waiting hours to achieve thermal equilibrium.

Finally, in the case of handling accomplished with microscopes and tweezers, manipulation tools have fewer degrees of freedom than hands, and they may have no force feedback. Microscopes can restrict the operator's view, as well, consequently loosening hand-eye coordination [41],

Thus, although feasible and in fact the first to be industrially accomplished, the P&P approach is not optimal for assembling very-large amounts of very-small devices. Its advantages are mainly: the compatibility with existing microfabrication techniques, and the large flexibility and dexterity in handling parts of arbitrary shapes and in aggregating them into two- or three-dimensional systems[14]. While all these must be fundamental features of an ideal microassembly technique, the considerations presented above at points 1) to 3) suggest that, at the same time, P&P lacks other, no less important attributes of that supposed technique, such as: 1) massive, large-scale *parallelism*, 2) *contactless manipulation* of components, and 3) *sensorless, open-loop control*. These features are addressed in the next Sections.

1.2.2 Parallel deterministic assembly

Arraying operationally-serial tools (*e.g.* for parallel transfer of palletized parts, as in [48, 56]) does not fundamentally solve the issues of P&P. A more interesting step toward parallel microassembly can be achieved by extending to wafer-level the flip-chip technique.

The *wafer-to-wafer* (W2W) transfer approach aims at collectively transferring, in a single operation, microstructures fabricated over a whole donor substrate to a host one, which normally is endowed with electronics and interconnections. This requires the layout of the donor wafer to be strictly-correlated to that of the target wafer: the placement of the structures is predetermined by their layout, so that a wafer-level alignment does imply the alignment of the features of both supports, needed for the correct build-up of the systems.

In [58] arrays of electrostatic motors were assembled with this method (Fig. 1.5). A UV-transparent donor wafer holding LIGA microstructures was precoated with a sacrificial polymeric layer. After face-to-face wafer-level alignment, the sacrificial layer was vaporized by an excimer laser pulse, causing the released structures to land on the final substrate. With a similar procedure, parallel placement of bumps for flip-chip applications can be obtained, with the advantage of testing the bumps before transfer and no need of under bump metallurgy [59].

Solder bonding can also be used as temporary mechanical link to break micromachined tethers for structure transfer, as in [60] and [61]. Further mechanisms for wafer-level transfer and bonding of structures are described in [62].

W2W transfer possesses two remarkable features [30]: compatibility with existing CMOS and MEMS processes; and good throughput: the parallel-structure

[14]While in principle ideal, such manipulation freedom is practically bounded, as high-precision industrial robotic devices are normally constrained to handle standardized mechanical parts and to perform standard operations.

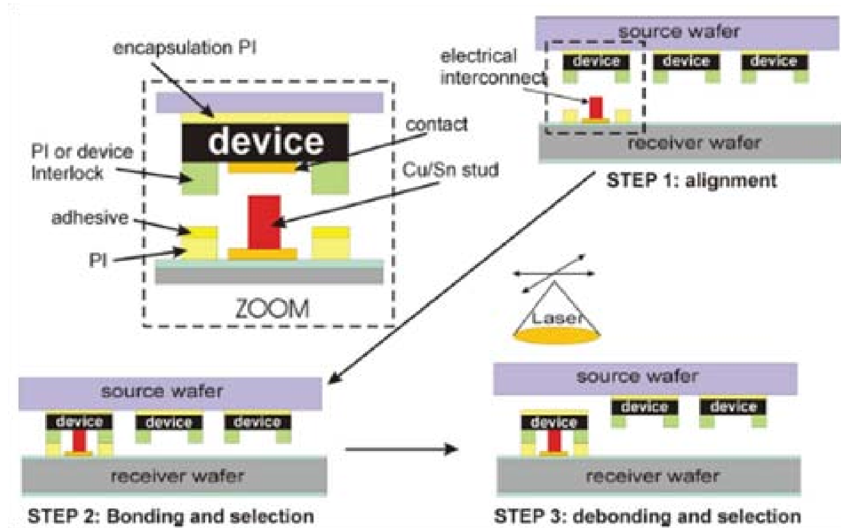

Figure 1.5: Selective wafer-to-wafer transfer process, after [57].

transfer may be fast enough to allow for step-and-repeat operations. Anyway, the method suffers from some drawbacks:

1. ***Inefficient use of the donor substrate***. By design, the chip footprint is the same on both donor and target substrate, and the position of the structures to be transferred replicates the layout of the system to be assembled: this often implies a sparse distribution of the structures over the wafer. Besides, the structures may be much smaller than the footpring. This could prove too expensive when using precious substrates (*e.g.* GaAs).

   Recently, Guerre *et al.* addressed this issue proposing a selective transfer technology for microdevice distribution: devices (*e.g.* AFM cantilevers) selected from a single donor can be transferred to several target wafers by laser polymer ablation and 3D device selection [57].

2. ***Stringent alignment constraints***: wafer-level misalignment implies that of *all* features.

3. ***High bump uniformity and wafer planarity mandatory***. As a corollary, W2W is hard to apply to non-planar substrates.

4. ***Only for "projection" assembly***. W2W is to be used only for devices that could be assembled by adding components along only one direction (normally, their local vertical axis).

Compared to micro P&P, W2W has the potentiality of higher throughput and it avoids direct contact with microdevices; but it lacks P&P's part-shape independence and three-dimensional versatility.

1.2.3 Parallel stochastic assembly

Deterministic methods belong to the *top-down* approach to microassembly. They only-marginally exploit – when not try to get rid of – many of the phaenomena peculiar to the microscale. A substantial part of the efficacy of the *bottom-up* approach described in the next Sections comes from harnessing driving mechanisms latent in such domain.

Thermodynamics and optimization

An assembly procedure can be thought of as a mapping between an initial set of elements[15] and a final set, whose elements are normally a subset of the elements of the initial set, and whose arrangement, different from the original, satisfies pre-assigned constraints - mainly concerning the mutual spatial coordination of its elements. The final arrangement of the elements is generally more ordered than the initial one. When not imposed by an external agent, the ordering derives from precise coordination rules encoded within the system.

In the deterministic approach the mapping is externally-driven and explicit, as demonstrated by the existence of a fixed assignment between each part and its final placement and, when using real-time feedback, by the possibility of describing, in details and even a priori, the part's physical trajectory extending from its initial to its final position (refer to Sec. 1.2.1). Moreover, both in the serial and in the parallel modality the initial configuration of parts must be pre-ordered to a certain extent. In the former modality, this is preferable to ease and speed up the pick-up of components by the manipulating tool; in the latter, structure pre-ordering needs to be designed at layout level and preserved during processing.

All the constraints mentioned above are *not necessary* to the purpose of assembly, as demonstrated by the self-assembly approach to microassembly. We first introduce it from an information-theoretic point of view.

The elements to be assembled are considered in relation to the ensemble they constitute and to the final structure they are required to compose. The ensemble is embedded into a bounded spatial region (the *assembly space*) where it can assume a variety of configurations or *states*, starting from an initial, specifically- or randomly-chosen configuration. Each state is determined by the spatial distribution and pose of all elements as related to or induced by the features of the assembly space. Being both the assembly space and the elements of finite dimensions, the number of allowed states will be infinite or finite numerable depending on whether a continuous range or a discrete set of element placements is thereby allowed. Accessibility of states will depend on specific characteristics of the assembly space and of the elements. Some states may be degenerate; state degeneracy may arise from symmetries (*e.g.* of the topology of the assembly space, of an organizing template, or of the geometry of

[15]For our purpose, these elements are (parts of) devices. Here we abstract from the details of their fabrication.

the parts) and from the allowed permutations of positions assumed by identical elements on identical locations.

Assuming to know the total number of system's accessible states[16], in principle a scalar-valued *fitness* (or cost) function can be uniquely-assigned to each of these states[17] to indicate the degree up to which each arrangement of the ensemble elements satisfies the set of prefixed global constraints. Once univocally defined, such metrics can be visualized in an abstract multi-dimensional *configuration space*. In this space the scalar function describes a (hyper)surface[18] which will be referred to as the *landscape*.

A prototypical issue in *constraint satisfaction problems* [63, 64] is the search for the system's state for which the minimum – in general, a specified extremum – of the cost function is achieved, implying the optimal satisfaction of the constraints imposed to the system. Efficient and flexible algorithms are described in information science literature to address such problem [65, 66].

Most notable for our perspective are the *annealing algorithms* [67, 68](Fig. 1.6). They arose in attempts to simulate the properties of condensed matter systems from the principles of statistical mechanics. The original algorithm by Metropolis [69] aimed at simulating a collection of interacting atoms at equilibrium at a given temperature. The algorithm combines a deterministic schedule for control parameters and a probabilistic treatment of system's modifications. At each simulation step, each element of the finite ensemble is given a small random displacement, and the resulting cost-function change is computed. This displacement is accepted with probability one, and thus becomes the starting point for the next step of the simulation, if the change is profitable. Otherwise, the probability of acceptance of the displacement is small yet non-negligible, and higher for higher temperatures: this is of critical importance to avoid the system being blocked in local minima while exploring its cost function. The temperature controls the system noisiness. The temperature is first brought to high values, then it is lowered slowly enough so that at each stage the system reaches a steady state. The procedure ends at the temperature for which no further change in the system happens.

Hajek's theorem [70] proves that annealing algorithms converge in probability, *i.e.* they lead the system toward its minimum-cost configuration in the limit of infinitely- many system displacements. This result can be extended to any distributed system or collection of parts for which a coherent cost function can be defined, if a consistent interpretation of the temperature parameter is provided.

The annealing algorithms represent the abstract counterpart of the homony-

[16]Using templates to define binding sites in the assembly space, the number of significant configurations can be roughly thought of as a combinatorial function of the number of parts and binding sites.

[17]In analogy with statistical mechanics, a hierarchy should be defined where each ensemble *macrostate* is defined by the states of all individual elements with respect to the assembly space, *i.e.* the ensemble *microstates*. This would consequently define a hierarchy of landscapes (see further). This concept needs further thoughts, and is not developed in this thesis.

[18]This is strictly true only in the limit of continuous variation allowed for the system's configurations. In the discrete case, it is a function defined over a lattice.

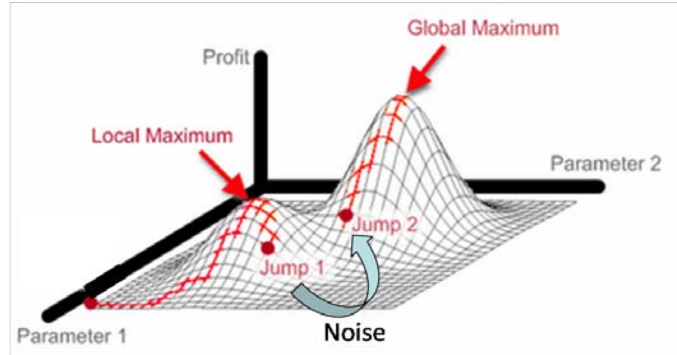

Figure 1.6: Simulated annealing to maximize a profit function.

mous physical method extensively used to make matter approach its energetic ground state [71]. First melting a material substance and then slowly[19] cooling it down toward its solidification point may result in the production of a highly-ordered, defects-free crystalline structure. This process is subtended by the third thermodynamic principle, assessing that, after starting at high temperature, the reduction of the system's atomic kinetic energy under equilibrium conditions will minimize the potential energy of the system[20] [72]. Furthermore, the growth of crystal-like structures can be enhanced by the preliminary introduction of templates (such as *e.g.* the seed layers used in epitaxy): with their geometrical symmetries and/or physical anisotropies, these patterns constrain the growth process by promoting nucleation and structuring the system to achieve its optimally-ordered configuration.

These concepts underlie *stochastic* assembly.

The core idea is to view the free energy of the physical ensemble of assembling parts as the natural cost function of the system, whose features can be influenced by the properties of the environment and of the parts. A necessary (but not sufficient) condition for the assembly to work is that the system energy landscape must have a well-defined global minimum: this must coincide with the desired assembled state of the system. If so, the final assembly would be the most stable and configurationally-ordered. Finally, as detailed in a later Section, two means are functional to help getting the desired configuration: an external source of kinetic energy (*i.e.* noise), promoting the evolution of the system; and the introduction of a template (in the form of a patterned support, or of peculiar parts' features) to better define the correct minimum-energy state.

As compared to the deterministic approaches, in stochastic assembly there is no strict need of an ordering of the system's components prior to the assembly – though it may ease the process in some cases. More fundamentally, in the stochastic case the physical mapping between the initial and the final set

[19] In principle, the material should reach thermal equilibrium at each temperature.

[20] This principle applies to biological processes, as well (*e.g.* self-assembly of ribosomes, antibodies-antigens recognition, hybridization of complementary DNA strands).

of parts is aleatory and not explicit[21]; it can be nonetheless described in its general properties and dynamics. This subtends the potential for accomplishing assembly using new tools and radically different strategies.

Stochastic assembly has intrinsically a massively-parallel nature. Its consistency and usefullness dramatically increase with the dimension of the ensembles. The collective properties of the system are as important as those of the single elements, while at the same time emerging from them – particularly, from the interactions of the parts among themselves and with the environment. The statistical process of approaching the final desired arrangement proceeds by progressively selecting among the accessible arrangements according to their increasing satisfaction of imposed constraints. It constitutes a *biased statistical sampling* within the assembly space: many possible solutions are explored before settling into the final, ideally optimal one [73].

Self-assembly

A common way to look at stochastic assembly is to think of the parts of the ensemble to be able of optimally assembling by themselves (*i.e.* without external supervision or control), accomplishing *self-assembly* (SA) and more generally achieving self-organization [74].

The concept of SA emerged in the study of supramolecular chemistry, where the formation of regular molecular aggregates, mediated by non-covalent anisotropic interactions, out of random collisions and proper thermodynamic conditions was first studied [75]. Chemistry, both organic and inorganic, is still the main source of inspiration and of working examples [76].

Self-assembly can be broadly classified according to the role played by energy and information (Fig. 1.7). As opposed to *active* SA, *passive* SA involves components which do *not* expend energy to accept or reject interactions with other components: the components only interact according to their geometry, interfacial features and physical forces[22] [77]. *Static* SA involves systems in which the organized state coincides with a (stable) thermodynamic equilibrium condition, global or local, so that energy is dissipated *only* while the system is approaching this state. This is the type of SA to which energy minimization arguments can be effectively applied[23]; it is typically exemplified by molecular crystals. On the contrary, in *dynamic* SA energy dissipation *itself* is the mechanism originating and preserving the interactions, structures and patterns among the components [78]. Such assemblies (such as *e.g.* cells) exist only away from thermodynamic equilibrium. In *directed* (or *templated*) SA, the structural information regarding the desired aggregation is implicated in the interactions between the components and regular features of the environment [79]. The kind of SA embodied *e.g.* by protein formation or programmable robots can be de-

[21] This is the only acception in which the attribute “stochastic” is hereby used - fluctuations and quantum uncertainties are nowhere invoked.

[22] The possibility of making choices, enabled in active agents, can be considered as an enlargement and generalization of the sets of available interactions.

[23] The theoretical arguments exposed in Sec. 1.2.3 technically refer to this SA class.

Figure 1.7: Classification of self-assembly processes.

fined as *hard-wired* (or *coded*), since that structural information is physically stored into their components (by *e.g.* DNA and software, respectively). SA processes where the sequence of assembly steps can be pre-defined are called *programmable*[24]. Finally, a system can be assembled out of parts which in turn are the result of a previous (eventually iterated, or different) assembly process: this is called *hierarchical* SA [80, 81].

SA seems to be ubiquitous and universal [82]: components of basically any size (from molecules to galaxies) may self-assemble, if given permissive conditions [83]. In this huge range of dimensions, a few domains are conventionally distinguished as nanoscopic, microscopic and macroscopic SA. The rules for SA in each of these realms are similar but not identical. According to [76], *supramolecular* SA spans from 0.1 to 10^7 nanometres: it can thus directly addresses microassembly tasks, besides being of formidable interest for many other technological applications (*e.g.* self-assembled monolayers [84], nanotubes [85], photonic crystals [86, 87], functional materials [88], DNA computation [89]).

SA may prove very useful for microsystems, because of:

1. ***Unicity***. SA can accomplish operations, build objects or enable functionalities that could otherwise be made or accessed in no other way. For instance, it could realize and deal with structures which are too large to be prepared by chemical synthesis but too small to be assembled by macroscopic methods [90, 91]. This feature's relevance rises as the parts' dimensions scale down.

2. ***Variety***. Using components larger than molecules allows choosing among many different interactions (*e.g.* Van der Waals, gravitational, capil-

[24]This may represent a sub-class of coded processes.

lary, electrostatic, magnetic, hydrophobic, steric) and tuning their range, strength and selectivity. Similar freedom is excluded at other scales.

3. ***Three-dimensionality***. SA can constitute a viable route to the efficient fabrication of 3D functional microstructures - more suitable and flexible than stacking and extrusion of two-dimensional thin films [25, 92].

4. ***Leveraging***. SA may leverage the manufacturing load of many standard microassembly tasks by enhancing and complementing them, and with the possibility of accomplishing them in a parallel way, quicker and with equal or higher precision - thus more cost-effectively.

In the perspective of engineering SA for the realization of microsystems, an interesting issue concerns the compromise between the size and the degree of complexity and functionality demanded to the single components and those of the overall system. Larger parts are easier to fabricate and can be more complex, but the resulting functional density of the system may result lower than for an assembly of smaller and simpler parts, whose production is in turn less efficient and, so far, more cumbersome - especially when their shape and functionality are to be properly tailored for SA.

Before reviewing the state-of-the-art in parallel stochastic assembly (PSA), we expose the general principles of self-assembly.

Ingredients and recipe for self-assembly

Self-assembly can be defined as a *spontaneous self-organizing*[25] *process involving preexisting components, which is adjustable and controllable by proper design of components, environment and driving forces* [95].

As already mentioned, for the assembly to be effective the desired assembled state must represent a point of energy minimum in the landscape. Ideally, such landscape should present only one (*i.e.* global) attractor, whose attraction basin should extend over all configuration space: this would make the assembly procedure insensitive to any initial configuration of the components. Also, the landscape minimum should be very-deep compared to its local neighborood, to be sufficiently stable against kinetic activations and assembly disruptions[26].

Such situation may be disturbed by the presence of energy barriers and consequent local minima of energy. The latters represent configurations that, while locally-optimal, are globally-suboptimal - including defects of some sorts. Together, they may considerably prolong the assembly time and even hinder its accomplishment. It is thus required that the local energy barriers be small compared to the driving local energy difference. By drastically reducing adhesion

[25]This holds only *for all practical purposes* (Bell). In fact, semantic arguments may rightly point out an underlying contradiction in evoking spontaneity and autonomy, since *all* physical processes are sustained by gradients of some sort and thus a director can always be found, if only at cosmological scale [93, 94].

[26]In the terminology of graph grammars introduced by Klavins [96], the target structure should ideally be the *only stable element* in the set of structures reachable by the system.

and friction - two of the main causes of energy barriers - *e.g.* by lievitation, vibration or fluidic means, *non-prehensile* and *non-contact manipulation* of microparts greatly benefits a self-assembly technique. Also, an external source of kinetic energy is necessary to overcome local minima. The amplitude and/or frequency of this energy source could be tuned according to an annealing procedure, as earlier mentioned.

The energy difference between the global energy minimum and the local energy minimum with energy closest to the global is called *energy gap*: it can be considered a measure of the stability of the assembled system against noise, disruptions or modifications. Furthermore, there can exist more than one, equivalent, globally-optimal configuration for the components of an assembling system which satisfies all the constraints, *i.e.* the energy minimum of the system may be multi-degenerate. *Degeneracy*[27], which is typical of ensembles containing elements geometrically- and/or functionally-equivalent to each other, and/or elements geometrically- and functionally-symmetric by themselves, is highly-beneficial with respect to error tolerance and assembly time reduction. On the other hand, unique in-plane alignment is mandatory for parts whose functionality depends on electrical polarity - the majority of electronic devices. The issue may be addressed introducing anisotropic features in binding sites design [28].

A general self-organizing process may be described by three phases [76]:

a) selective recognition between the parts;

b) growth - by nonlinear, sequential and/or hierarchical coordination and binding of the components;

c) occurrence of a stop signal - sometimes built-in.

Within this frame of reference, the ingredients required for SA are: [83, 92]:

1. ***Components***. Size, shape, geometry, surface chemistry and interaction forces can be used to code information into the single parts about their cooperative and selective interaction, recognition and coordination - with respect both to the others and to the environment. These *local* instructions define the *global* emergent system structure: moving from a disordered to an ordered (final) state, the system reduces its configurational entropy[29].

2. ***Interactions***. As already mentioned, in the supramolecular domain the range, selectivity and strength of forces can be fairly tuned. The forces

[27] Not to be confused with the *designability* of a structure, which is defined by the number of sets of its components that assemble into the same (class of functionally-equivalent) global structure(s) [73]. Mathematically, a highly-designable structure involves a non-injective mapping from the original to the final element sets, while degeneracy a multivalued one.

[28] Further details are provided in Sec. 2.5.

[29] Following the analogy with the statistical mechanics' description of phase transitions, the evolution from an original, disordered (gas-like) state to a final, ordered (crystal-like) one normally involves symmetry-breaking, the final state being less symmetric.

must enable selective binding of components in the correct relative placement. Selectivity of interactions is also required to avoid unintended interferences during the assembly process[30], [31].

3. ***Adjustability***. The components should be able to move after mutual encounters and change their relative positions within the aggregate until the correct[32] one is reached. This requires the binding forces to be equipollent to the detaching ones, and it is related to the gradient of the energy landscape around the assembled state. Reversibility in the binding leads to self-repairing and the creation of ordered crystal-like structures, as compared to dendritic or amorphous ones consequent to irreversible aggregations [74].

4. ***Stirring and mass transport***. To enhance the chance of mutual mating and provide adjustability, the parts must be able to explore the bounded assembly space. This may require the use of a fluid carrier medium and the control of the roughness of surfaces. External kinetic energy is required to promote part mobility and to release parts from local energy minima: it must replace thermal fluctuations, which dominate at molecular scale but are overcome in magnitude by the effects of gravity and friction at larger scales. A surrogate of Brownian part motion can be induced by employing mechanical agitation [98], hydrodynamic [99] and surface-tension-induced flow [100], and ultrasonic vibration[33]. On the other hand, adhesion and friction might eventually prevent the system from reaching its designed asymptotical configuration - which could be problematic for high-precision, small-scale applications. Thus, a lower bound on the amplitude/frequency of kinetic stimulation may be required to preserve part mobility. Finally, temporally- and spatially- (non-)uniform external force field (*e.g.* charged/magnetized parts in electrical/magnetic fields; mechanically-actuated substrates [101]) may introduce preferentiality among the spatial directions of motion[34], thus enhancing directionality and the rate and precision of mating.

[30] For example, in part-to-substrate SA the components should exclusively assemble on the binding sites located on the template. In this case mutual binding among parts, especially if irreversible, is to be avoided as it can sensibly reduce the overall assembly's yield (see Ch. 5).

[31] In graph grammars, selective interactions introduce unreachable system configurations.

[32] For static assembly, "correct" is synonymous of "energy-minimizing". This is not necessarily the case for dissipative structures, for which a general criterion identifying steady-states is not known yet [97].

[33] For the assembly processes involving the interaction of parts with a template (*e.g.* part-to-substrate SA), external agitation of the assembly space or of the substrate itself may be efficient in promoting the assembly, because it causes the motion of the template relative to the parts. On the other hand, for the assemblies requiring mutual interactions among the parts (*e.g.* 3D assemblies, 2D assemblies at a fluid/fluid interface), the injected kinetic energy should induce the motion of the parts *relative* to the others to be effective. This is the reason why Brownian motion is effective in promoting chemical reactions and assemblies of nanometric particles.

[34] In analogy with statistical mechanics, this acts as a spatially-anisotropic global drift imposed over a locally-diffusive motion. It may originate *e.g.* from attraction to or repulsion from force field sources, as in (di)electrophoresis-driven SA (see Sec. 1.3).

5. ***Environment***. The environment can influence the history[35] of the assembly, modify the interactions and provide seeds [103] (*e.g.* a template patterned with target sites for the parts) and constraints to direct the assembly process, to limit the reachable configurations and to oppose the formation of defects [104]. The template symmetries underlie the structural order of the final aggregates.

6. ***Freezing***. Once the desired configuration of the system is achieved, it must be preserved against disruption through a definitive bond[36], which in microsystem applications needs to supply both mechanical and electrical interconnections. This is in contrast to the prerequisites of *adaptive* systems, whose dynamic response to internal or external stimulations might require the permanent possibility of structural revisions.

All these key features can be found, in various forms, in most of the experimental results which are discussed in the next Section.

1.3 Integration by self-assembly: state-of-the-art[37]

Capillary and surface tension-driven self-assembly

Fluid-mediated approaches to SA extensively build upon the modulation of the chemical properties of the surface of the system's components. Self-placement and alignment refinement driven by the minimization of molten-solder/air interfaces is common in soldering and bonding (see Sec. 1.2.1). More recently, the surface tension of water was used to precisely self-align patterned wafers [106, 107] and to wrap up *capillary origami* [108, 109], while that of molten glass, resist and solder is used to deploy complex 3D MEMS structures [25].

The Whitesides Group at Harvard University pioneered the potentialities of capillary SA. Their 2D co-planar assembly acted at the interface of immiscible fluids (*e.g.* air or perfluorodecalin, and water). Thin polygonal parts functionalized to obtain on their sides complementary wetting characteristics - such as hydrophobic and hydrophilic - experienced lateral flotation forces (Sec. 2.2) [110, 111, 112, 113, 114], and aggregation was eventually aided by the introduction of templates [115]. Klavins developed a "waterbug" model to describe and control such tile-based 2D assemblies [116]. A similar fluidic system, involving lateral capillary forces acting between sets of planar microtiles, was exploited by Rothemund in a partially-successful attempt to practically demonstrate the universal computational potentialities of a physically-predictable, tiles-based self-assembling system [117].

[35] SA programmability is related to *conformational switching*: the mating properties and affinities of parts or binding sites are not hard-coded but can be - selectively, in the ideal case - turned on or off depending on global or local environmental conditions, interactions or decisions. [102].

[36] In the configuration space, this means making the landscape infinitely-steep and -deep around the current system state.

[37] Refer to [105] for an extended exposition of the content of this Section.

The Whitesides Group also introduced a general fluid-mediated methodology to achieve both 3D and 2D SA. In this approach, the parts and/or the target structures are endowed with matching geometric features and binder fluids[38] on superficial patterns. When put into a proper fluid environment, high surface-energy areas are thereby formed, which work as receptor sites. As the parts approach their targets, their dynamics is constrained by strong capillary forces that lead the parts into mutual registration. Using oxide-free solders as binders (so-called *molten-solder-driven* SA [118]), the bonding can at the same time work as an electrical interconnection.

The Whitesides Group applied such comprehensive technique in many settings, with part dimensions ranging from tens of microns to millimetres [119, 120, 121, 122, 123, 124, 125]. Arrays of light emitting diodes (LEDs) on flexible substrates [126], working three-dimensional electrical networks [127] and the assembly of asymmetric protein-inspired structures for electronic devices [128, 129] were among the main achievements.

Other research groups further developed these methodology.

Srinivasan adapted the Whitesides Group's capillary approach to part-to-substrate SA [130]. Lenses of hydrophobic adhesives were deposited over arrays of hydrophobic sites patterned over hydrophilic substrates submerged in water. The lenses made the sites receptive toward the parts to be assembled. The parts were pipetted toward the substrate, and upon mating capillarity led the parts to a highly-accurate placement and orientation. Permanent bonding was achieved by solidifying the adhesives [131]. The technique was successfully applied to the assembly of micromirrors on top of micromachined actuators for adaptive optics [132] with claimed errors as low as 0.2 μm for placement and of 0.3^o for angular displacement. Scott resorted to a variation of the above technique to assemble RF inductor chiplets over CMOS integrated circuits [133].

Böhringer's team further extended Srinivasan's methodology to allow for programmable multi-batch assembly of microparts. The selective deactivation of binding sites was in this case achieved through electrochemical desorption of the thiol-ended SAMs from the binding sites where an assembled part was not desired [134]. The mechanical bond was still provided by adhesives, and electroplating was used, after the assembly step, to electrically-link the parts to the substrate [135].

As for programmability: Liu used solders of different melting points, thermally-activated (*i.e.* molten) consecutively, to assemble parts in a multibatch-wise manner [136]; Sharma utilized the local, thermally-induced gelling behavior of a hosting fluid to prevent the assembly of parts on selected sites of a target template [137]; in Jacobs's team approach, copper binding sites coated with low-melting-point solder were defined over the surface of a polyimide sheet and individually activated (*i.e.* molten) by integrated resistive heaters (Fig. 1.8), so that multi-batch assembly of heterogeneous parts (*e.g.* multicolor LEDs for flexible displays) on the same substrate could be achieved [138, 139, 140].

[38] In many experiments hereby reviewed lead-based low-melting-temperature solders (with melting temperatures ranging from 47° C to 135° C) were used. Recent legal prescriptions

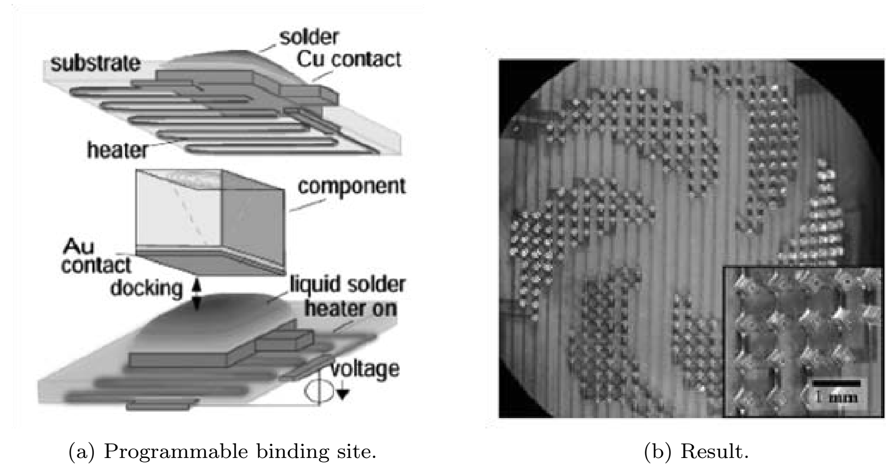

(a) Programmable binding site.

(b) Result.

Figure 1.8: Programmable molten-solder driven SA process, after [140].

Jacobs' team combined 3D shape recognition and solder-driven assembly in a sequential SA process [29, 99]. In one demonstration, semiconductor devices were first assembled into glass carriers, then these aggregates were in turn assembled onto encapsulation units to form the final disposable systems. Part agitation was provided by turbulent flow induced in the hosting fluid. Cumulative claimed yield was 97%. Recently, they demonstrated an energy cascade-based, Langmuir-Blodgett-like method to assemble segmented silicon solar cells with very-high throughput [141].

Stauth and Parviz combined sites/parts shape recognition with the capillary forces of molten solders to achieve SA of microdevices onto flexible, planar substrates (Fig. 1.9) [143]. This way, the group assembled *e.g.* single-crystal silicon devices [142], optoelectronic devices [144] and fluorescence detection systems [145] on plastic and glass substrates. Similarly, Jacobs' group achieved unique in-plane orientation of few hundred micron-sized symmetrical devices onto preprocessed substrates by molten solder-driven SA: they exploited pedestals, chaperons and asymmetric placement of solder bumps and bonding pads [146].

A general method for self-assembling modular 3D systems was presented by Cannon and colleagues [147]. Individual components were encapsulated into polymethylmethacrylate (PMMA) cubes, which were then cross-wrapped with strips of solder-coated copper tape. The cubes underwent capillary-driven self-assembly in a heated solution, and if required the PMMA could be selectively removed by chloroform after assembly.

Koyanagi's group introduced a capillary self-aligning step into a 3D electronic integration process flow [148]. Square dies collectively picked up by a dedicated tool were dropped onto a temporary carrier wafer, where they quickly

---

prohibit the use of lead-based solders in electronics for commercial applications.

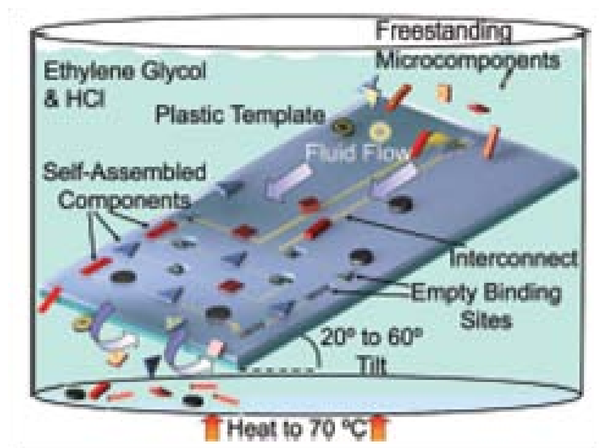

Figure 1.9: Gravity- and molten solder-driven SA process, after [142].

self-aligned to receptor sites coated with a water-based solution. An average accuracy of less than $0.5\mu m$ was claimed for this alignment step [149].

Fluidic self-assembly

Fluidic Self-Assembly (FSA) was introduced in 1994 by J. Smith at University of California at Berkeley [150]. It exploited 3D geometric shape matching and complementarity for selective binding of microdevices onto pre-processed substrates [151, 152].

In the original proposal, the parts had dimensions ranging from few microns to millimetres and trapezoidal shapes. The host substrates featured arrays of engraved receptors of almost-complementary geometry, to enforce a unique vertical orientation of the parts.

The parts, suspended into an inert carrier fluid or mixed in slurries, were directed by gravity toward the host substrate submerged in the same medium. Upon reaching contact with the substrate, the parts were thereby confined [39] by gravity and adhesion forces. Parts' mobility was enhanced by external vibration of the substrate [153]. When reaching the binding sites, the parts plugged in by gravity, and subsequently adhered in place by van der Waals interactions. Unfavourable downscaling of gravitational force was considered the cause of this step's decreasing yield for shrinking parts dimensions. Unbound parts were recirculated by a bubble pump and used for successive trials until the desired substrate coverage was reached [151]. After the assembly, the substrate was flat (or it could be easily planarized), so that standard BEOL processes or screen

[39] Viewing SA as an optimization algorithm, this marks the transition from 3D to 2D spatial search, *i.e.* the reduction by one of the dimensions of the search space, which largely reduces the complexity of the search task. Chung *et al.* further developed the idea into 1D railed fluidic assembly [104].

printing techniques could be applied for the electrical interconnection to the surrounding electronics.

FSA was used for the assembly of *e.g.* GaAs devices onto Si [150, 154, 155, 156, 157] and ceramic [158] substrates, flat-panel displays, high-speed or high-power circuits into VLSI ICs, long-wavelength detector arrays into silicon, electronic components on plastic flexible supports [153].

The main advantages of FSA are: high yield and very-high throughput; efficient use of source materials, thanks to parts' densely-packed production and recycling; and self-alignment of the blocks - its relative precision depending on geometrical details. Nevertheless, yield and precision of part registration decline for smaller block dimensions; the required 3D geometries constitute a tough constraint for the design and processing of devices; and assembly of multiple non-identical parts on the same substrate may be inefficient (*e.g.* small parts may register into sites destined to larger parts).

Magnetic self-assembly

After a pioneering work from Yando [159], Fonstad proposed the magnetically-assisted statistical assembly (MASA) [160]. MASA can be thought of as a variation on the FSA theme: as the devices stochastically settled from a carrier fluid into shallow substrate cavities, a strong short-ranged magnetic retentive force produced by CoPt magnets embedded in the cavities kept them from being removed by gravity and fluidic drag [161]. Further processing on the planarized substrate finalized the assembly.

Shet [162] enhanced the MASA process by introducing an external long-ranged magnetic field source at the backside of the target substrate, to enhance its part capture power. Ramadan [163] proposed a dry MASA process where the cavity-patterned host substrate was superposed to a matching array of NdFeB magnets. After stochastic assembly, the master array could be removed and reutilized, while the chips could be further processed by wire bonding or flip-chip techniques. Assembly of 2500 chips in 5 minutes with 97% yield was claimed.

Shetye proposed a dry magnetic SA process where permanent SmCo micro-magnets were embedded both in the parts and in the binding sites of the target substrate, which featured no other templating structure (Fig. 1.10) [164]. The substrate, set upside-down 10 mm above a shaker, was shot by the parts agitated by the shaker. The magnets were polarized to avoid mutual adhesion between parts. Assembly took place when the overlap between parts and binding sites ensued an attractive magnetic force superior to gravity. Misalignment could be alleviated by vibrating the substrate after assembly. Assembly yield close to 100% was claimed. The same group similarly demonstrated part-to-part (in a liquid environment) and part-to-substrate self-assembly with unique in-plane orientation [165].

Grzybowski used competition between magnetic and hydrodynamic interactions to build dynamically self-assembling systems [166]. A set of magnetite-doped PDMS disks were placed at liquid-air or liquid-liquid interfaces in a beaker, subject to a central rotating magnetic field. The disks spun in syn-

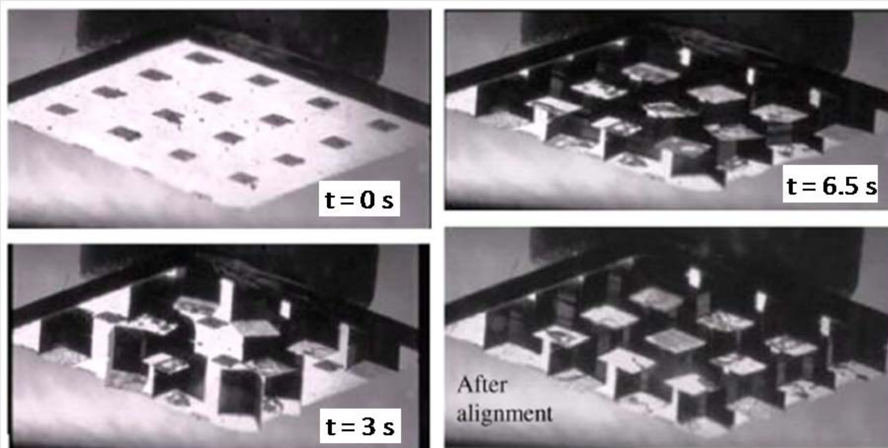

Figure 1.10: Dry magnetic SA, after [164].

chrony with the rotating field: they repelled each other hydrodynamically, but at the same time they were attracted to the axis of magnetic rotation. Such interplay led to the formation of a wide variety of tunable spatial patterns, which behaved as dissipative structures [167, 168, 169, 170, 171].

The group of Tanase demonstrated the magnetic trapping of composite Pt-Ni-Pt nanowires between a pair of permanently-magnetized Ni electrodes [172]. The assembly was enhanced by the application of an external magnetic field which aligned the nanowires along the long axis of the electrodes. The inclusion of Pt caps at the edges of the nanowires helped the formation of low-resistance metal contacts with the gold-coated electrodes. With a similar technique, Ye aligned and assembled ferromagnetic Au-Ni-Au nanowires between pairs of solder-coated, magnetic contact pads [173].

Electric-field assisted self-assembly

Early works (*e.g.* [174, 175]) regarding levitation, holding and orientation of particles and cells showed that fluid phaenomena associated with both static (*i.e.* electrophoresis, EP) and dynamic (*i.e.* dielectrophoresis, DEP) electric fields could be successfully applied to drive microassembly, and could afford non-contact handling of parts [41].

Heller and colleagues [176] used EP to assemble 20 μm-diameter InGaAs LEDs onto tin/lead electrodes designed over silicon substrates. The bias applied to the electrodes established an electrophoretic current in a buffer fluid and aided the placement of the LEDs, which were then extracted from the solution and reflowed for the bonding. A programmable electrostatic field was used by O'Riordan to drive both deterministic and stochastic assembly of GaAs-based LEDs between receptor electrodes [177].

Esener DNA-functionalized the assembling parts to provide them a strong

coulombic attraction toward mating binding sites, and to exploit the hybridization of complementary DNA strands for highly-selective transient bonding of the parts [178]. Lee and colleagues used a similar concept to direct the assembly of generic silicon parts [179].

DEP and electrothermal effects were employed by Bashir's group to direct the assembly of silicon resistors between Au/Cr electrodes [180]. After assembly, the electric field was maintained so to preserve the resistor assembly while the liquid solution evaporated. In another work involving micron-sized three-terminal MOSFETs, the electrodes were functionalized with thiol-ended SAMs, which created a bridging bond to the devices once they assembled over the electrodes; a post-assembly thermal anneal helped reducing the contact resistance between the MOSFETs and the electrodes [181].

In several works DEP was used for the manipulation and assembly of nanowires [182, 183, 184, 185, 186] and nanotubes [187, 188] from suspensions placed between pairs or arrays of AC-polarized electrodes. Rao et al. used charged patterns to assemble ordered arrays of even single CNTs on substrates [85].

Other approaches to wafer-level 2D self-assembly

Fang and Böhringer proposed a process for high-density mounting of microcomponents onto planar substrates (Fig. 1.11) [189]. In the process, thin square parts, having one hydrophobic side, were distributed over a plate patterned with an array of apertures and thereby randomly agitated till they fell into the apertures. The yield of this feeding and mechanical filtering step [98] can be enhanced by introducing proper "catalysts", in analogy with chemical reactions [190]. Then, the parts vertically-standing over a temporary carrier were projected onto the water-coated binding sites of a palletizing plate. When the aperture plate was removed, capillary torques (aided by mechanical agitation) drove the parts to lie flat over the sites with their hydrophobic side facing upwards. After water evaporation, a bonding plate was aligned and brought into contact with the parts before performing a reflow step.

Fang and Böhringer also demonstrated two feature-directed methods to achieve unique in-plane orientation of parts: they exploited micromachined pegs which extrude from the bottom side of the parts and fit into complementary-shaped holes of the hosting substrates [191].

In the semi-dry method, one of the major sides of the square parts was made hydrophobic; the opposite side features a circular peg offset from the centre. The hosting substrate is prepared with square sites featuring holes complementary to the pegs. Once palletized, the parts were released to the hosting substrate, which was shaked to accomplish the parts registration. The alignment accuracy could be enhanced by capillarity [192].

The fully-dry method involved square parts with two pegs on one major side: a circular one, offset from the centre, and a thinner cross-shaped one; both were complementarily reproduced on the binding sites of the hosting substrate. First the parts were randomly agitated till their circular pegs fit into the circular holes: in this way each part roughly located an assembly site over the substrate.

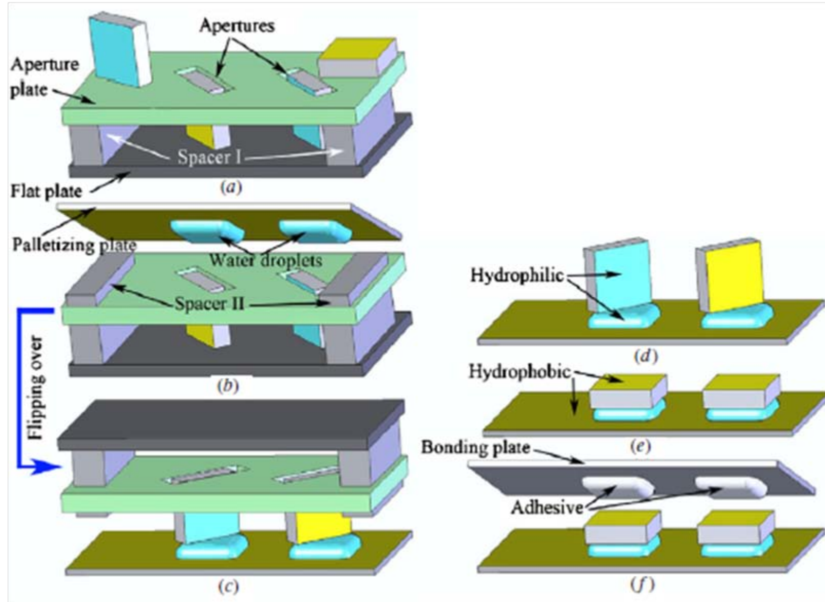

Figure 1.11: Combined dry and capillary SA process, after [189].

Then, the external vibration induced fixed-axis rotation of the parts around their circular peg till the cross-shaped peg fits into its complementary trench, which signals the achievement of the desired in-plane orientation [193].

Ong topped a very-similar dry assembly method with the establishment of metal interconnects between the parts and 8" target substrates. In their first process, after palletization the carrier substrate was aligned with a corresponding bumped substrate, and gang bonding was performed. An average assembly yield of $95.8 \pm 2.1\%$ over 9 trials with $\sim$2000 parts was reported [194]. In a second process, the protrusions themselves were used for the bonding, as well: the electroplated copper protrusions fit into the complementary cavities in the target substrate, which were filled with solder. After palletization, the substrate wafer was reflowed to form the metallic interconnections. This process had increased throughput, though not all the electrical interconnections worked properly; the claimed yield was 90% over $\sim$1700 parts [195].

Concluding the literature survey, we thought Scott's capillary part-to-substrate SA represented the most-promising attempt to combine serial robotic and parallel stochastic assembly, and to introduce the SA paradigm in industrial electronic packaging practices. This was also consistent with IMEC's 3D system integration perspective. We consequently set out to investigate the technique in details, elucidating several aspects and open issues - see Sec. 1.4.

During the progress of our work, the capillary enhancement of robotic P&P assembly (*i.e.* a side application of the full capillary SA methodology) came to be called *hybrid microhandling* [196, 31].

1.4 Thesis objectives and outline

Efficiently assembling very-large quantities of sub-millimeter-sized devices onto functional substrates is presently a key frontier in electronic manufacturing. Not only is this coherent with microelectronics' aspiration to large-scale mass production and commercialization of devices - driven by continuous device downscaling and expansion of markets for mobile and computing media; it is also of growing importance for many new applications (*e.g.* embedding of thin dies onto flexible substrates, fully three-dimensional assembly of heterogeneous microsystem, integration of thermoelectric cooling elements onto CPUs) - which possibly will in turn further fuel the former trend. As discussed in Sec. 1.2.1, in this manufacturing perspective established, flip-chip-like assembly techniques may presently perform not optimally, due to a long-lasting trade-off between throughput and placement accuracy and to physical and algorithmic difficulties in handling very-small devices. On the other hand, self-assembly processes are intrinsically massively-parallel, may run unsupervised and may allow contactless device manipulation. Thus, and as it is presently being recognized in wider manufacturing contexts, we thought the *convergence* between robotic assembly and self-assembly (summarized in Fig. 1.12) - as epitomized by capillarity-enhanced flip-chip assembly of small dies - could lead to an ideal assembly technique, able to embody the benefits of both its sources and consequently meet at least short-to-medium-term electronic packaging needs. Equivalently said, capillary self-assembly may complement, enhance and eventually replace established assembly techniques in coming years.

The objective of this thesis is *bridging the gap existing between the academic proofs-of-concept of capillary (self-)assembly and its industrial application to electronic packaging.* The bulk of the present work will contribute to address and eventually solve several issues relevant to capillary (self-)assembly of thin dies onto back-end-of-line pre-processed substrates. In such a broad playground very different phaenomena and aspects, of both scientific and technologic interest, coexist and need to be tackled in parallel. Moreover, compliance with industrial needs, constraints and boundary conditions - rather different and much tougher than those of academic settings - will involve re-thinking of earlier ideas, demanding alterations of seemingly-established techniques and new breakthroughs. We will operate experimentally, theoretically and numerically.

Our research started with a critical literature review of the field [105]. Systematic study and reflection was anyway only a part of our activity. Experimental errors and serendipity duly complemented it and led to additional insights and creative thoughts, altogether. Here is a preview of what is next (Fig. 1.13).

1 Physics of capillary self-alignment (Ch. 2). The system composed by a thin part floating on top of a fluid drop confined by a geometrical pattern on a flat surface was already studied, but mainly by numerical simulations: few works had reported reliable experimental data to compare with. We will try to fill this vacancy. We will expose the quasi-static measurements of the lateral capillary forces arising from small perturbations of cylindrical

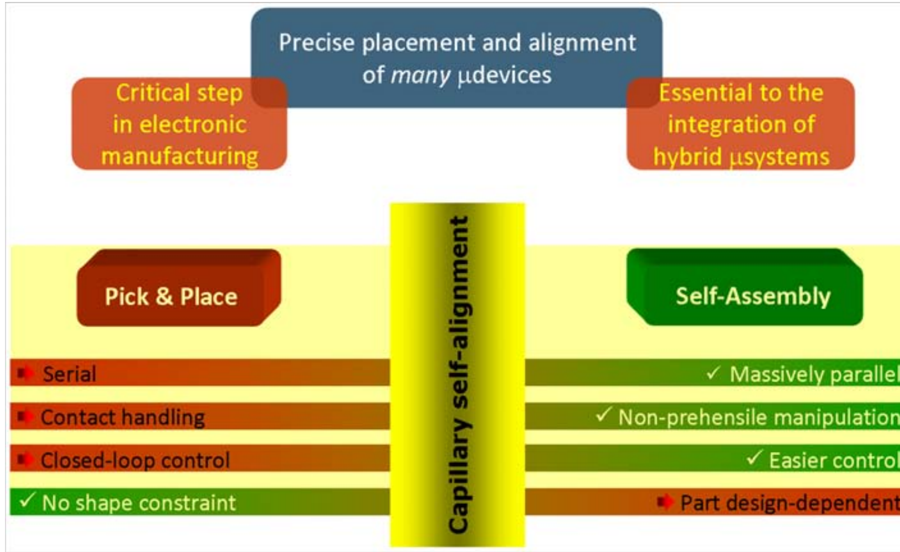

Figure 1.12: The convergence of P&P and capillary assembly.

fluid menisci. The same experimental apparatus used for the purpose will also enable an alternative method (the *overflow* method) to estimate the contact angle of liquids. We will then match our experimental data with numerical simulations. Our results will be extended with numerical simulations of less-symmetric parts. Altogether, this will bring a deeper understanding of the system.

2 ***Conformal binding sites dip-coating*** (Ch. 3). The geometric patterning and selective pre-conditioning of target substrates is critical to enable capillary part-to-substrate SA. But the geometrical information embedded in the binding sites is effective *only if* faithfully reproduced by the lubricant coating. We will describe a simple topological enhancement to binding sites to allow their perfectly-conformal coating by means of dip-coating. This modification will also make the coating process more reproducible and robust against surface contaminations. We will moreover present experimental evidence on the difficulty of precisely controlling the volumes of lenses deposited by dip-coating on patterned surfaces.

3 ***Interconnections*** (Ch. 4). Once mechanically assembled on their binding sites, the parts need to be electrically connected to the substrates. We will propose a procedure to seamlessly-establish solder-based electrical interconnections in capillary part-to-substrate SA, with the aim of generalizing earlier attempts for the more common case involving solders with melting point comparable or higher than the boiling point of the surrounding fluids. The established interconnections will be contextually characterized, both mechanically and electrically, so to assess eventual differences be-

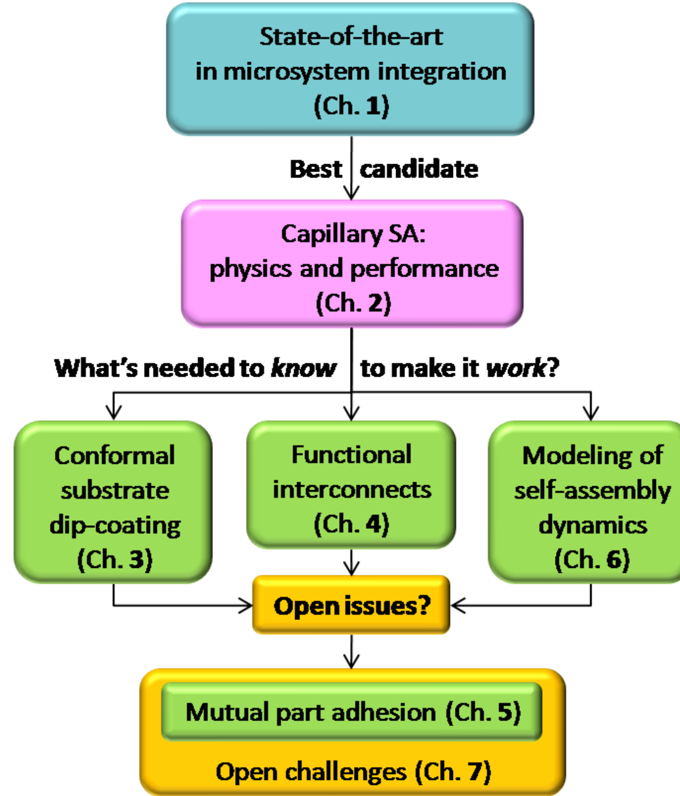

Figure 1.13: Logical map of the thesis.

tween interconnections obtained with and without application of external pressure during thermal treatment.

4 ***Smart chemistries against interferences*** (Ch. 5). In the embodiment hereby developed, capillary part-to-substrate SA exploits the hydrophobic interaction in water. However, while wandering in the assembly space the parts are susceptible to get into intimate contact and consequently aggregate by the same form of interaction. This evenience makes them useless for the assembly purpose and sensibly affects the assembly yield. We will face this neglected issue disclosing a patent pending method based on the exploitation of switching surface chemistries, *i.e.* surface coatings able to sense their local chemical environment and accordingly change their wetting character from hydrophilic to hydrophobic.

5 ***Modeling SA dynamics*** (Ch. 6). Modeling of fluidic 2D and 3D SA processes will be addressed next. We will first propose the generalization of two chemical kinetics-inspired analytical models presented in earlier

literature. This closed-form mean-field background will then be used to expose the limits of analytical modeling, and to appreciate the potentiality of a numerical framework (*agent-based modeling*, ABM) that will allow us to simulate with realism and accuracy realizations of geometric SA processes. ABM will be used to numerically-reproduce experimental data published back in 2005 and to investigate for the first time the effects of some previously-unaccesible assembly parameters .

6 Conclusions, critics and speculations (Ch. 7). After drawing the conclusions of our work, we will top off our activity on capillary part-to-substrate SA with a personal outline of its challenges - untackled, disclosed or envisioned by our investigations. Issues concerning binding sites conditioning and coating, part transport and mixing, thermal post-assembly treatment and more will thereby be discussed and, for each evoked issue, solutions or perspectives will be contextually proposed - mainly based on our direct experiments, but also indirectly suggested from our literature noodlings.

Some of the results hereby reported can be interpreted as generalizations of earlier findings - obtained by removing unnecessary constraints, developing alternative points of view to their full consequences and/or focusing on specific issues apparently neglected in literature.

We hope to have solved some issues and got some new insights with our work. We confess, nonetheless, that we may have disclosed new challenges.

Chapter 2

Physics and Performance of Capillary Self-Assembly

The physics underlying the assembly of microsystems by means of capillary forces is investigated.

A comprehensive quasi-static study of lateral capillary meniscus forces is presented, which compares experimental, numerical and analytical analyses of the same system. We describe the highly-sensitive experimental setup that we designed to quasi-statically measure lateral restoring forces arising from fluid menisci of known physical and geometrical properties. The experimental results obtained for circular pads (*i.e.* for cylindrical fluid menisci) are supported by both a simple analytical model and by a finite-element numerical model of the same system. Our setup enables a novel method to measure contact angles of liquids on flat surfaces based on the Gibbs' inequality, and may constitute a reference testbench for further investigations on confined fluid menisci.

Finite-element simulations concerning the capillary self-alignment performance of a thin part floating on a fluid drop confined a by binding site - *i.e.* the system that will be the main player in later Chapters - are then summarized in the context of the symmetry-versus-anisotropy trade-off.

The present Chapter focuses on statics only. The dynamics of lateral capillary forces was investigated in a complementary study (see [197]).

2.1 Capillary self-assembly of microsystems

Capillary SA was adapted to the assembly of parts to planar substrates by Srinivasan and Scott at UC Berkeley (Sec. 1.3). Fig. 2.1 defines what in the following will be referred to as its *standard embodiment*.

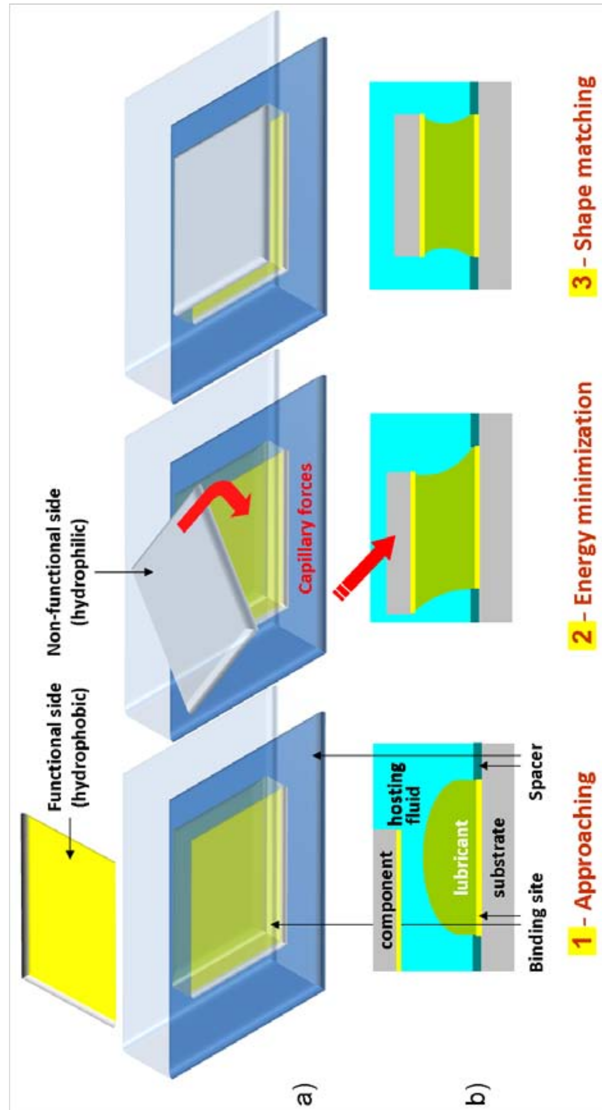

Figure 2.1: Capillary part-to-substrate SA in its standard embodiment: top **(a)** and side view **(b)**. **Step 1**: a part, suspended in the *hosting fluid*, approaches a binding site selectively-coated with a *lubricant* lens. **Step 2**: as the hydrophobic part side touches the lubricant surface, the former hosting fluid/lubricant interface is substituted with the less energetic part/lubricant one. **Step 3**: capillarity aligns the part with the underlying site.

The underlying thermodynamic idea - common to all *static* SA processes (Sec. 1.2.3) - is to derive the force driving the assembly of the *parts* (hereby representing *e.g.* IC dies, microdevices, MEMS components) from the minimization of the energy of the system. Specifically, the *binding sites* defined on the target template (standing for *e.g.* IC wafer, PCB board, flexible substrate) are conditioned to be *selectively*-capped with a thin fluid layer (*i.e.* the *lubricant,* represented by *e.g.* hydrophobic polymers [131], water-based solutions [148] or molten solders [118]) forming a high-energy interface with the *hosting fluid* (*e.g.* water-based solutions or air). The parts, in turn, are conditioned to be selectively-attracted toward the sites once mating with the lubricant. Upon contact between the pre-conditioned (*e.g.* made hydrophobic if hosted in water) side[1] of the parts and the lubricant lenses, the original high-energy fluid/fluid interface gives place to a less energetic fluid/solid one. Such surface energy minimization induces capillary torques [198] and forces - both perpendicular (*i.e.* axial) and parallel (*i.e.* lateral) to the substrate - on the parts, which consequently move to maximize their overlap with their underlying binding sites [134]. In this position (*i.e.* floating on the fluid meniscus) the part achieves its rest (*i.e.* minimal energy) configuration. The aforementioned capillary forces intervene also to oppose any sufficiently-small displacement of the part from its rest position, and are therefore also referred to as *restoring* forces. Additionally, the target sites and the parts may feature geometrical patterns which direct the self-alignment process by exploiting geometrical shape recognition and matching. Unique in-plane orientation can be achieved in principle [199], together with very-high alignment accuracy (of the order of 1 μm) [131, 200] – both being very attractive qualities for electronic device packaging. Finally, many applications require the establishment of reliable electrical interconnections between parts and sites - besides the permanent mechanical binding (See Ch. 4).

2.2 Surface tension-related phenomena

Capillarity concerns interfaces mobile enough to eventually assume the equilibrium shape dictated by thermodynamics [201]. Menisci, drops, bubbles and waves are fluidic examples [202]. Here we summarize basic phaenomena related to surface tension that will later play a role in our work.

Surface tension

Surface tension is responsible for that sort of elastic membrane that shapes fluid drops and acts against their deformation. It is rooted in an unbalance of intermolecular forces at the interface of a homogeneous liquid in equilibrium with its vapour[2] (Fig. 2.2). When in the bulk, the molecules experience on

[1]If the pre-conditioned side does (not) coincide with the functional (*i.e.* predisposed to enable further processing steps, *e.g.* metal bonding) side of the parts, we define the assembly process as *face-down* (*face-up*).

[2]Here we assume, for simplicity of exposition, that the liquid/vapour interface is sharp. In reality, no neat interface exists and many thermodynamic calculations are affected by the

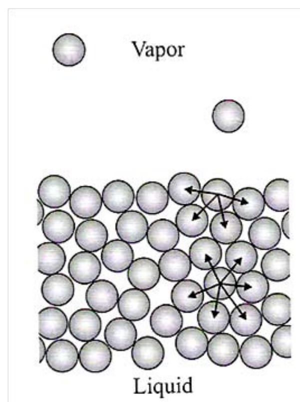

Figure 2.2: Molecular origin of surface tension.

average no net force, being symmetrically surrounded by other molecules of their same type; however, at the interface the molecular neighbourhood symmetry is broken, and a net force pulls the molecules toward the bulk. Work is therefore required to bring a molecule from the bulk to the surface of the liquid. This work defines the *free surface energy* of the liquid (measured in J/m^2). The *surface tension* γ (N/m) is equivalent to the previous, quantifying the compressive force that acts to remove every linear cut applied to the ideal liquid surface.

The state of a molecule at the liquid surface is thermodynamically unfavorable: hence the tendency of the liquid to assume a global shape that minimizes its energy. This is called *capillarity*. Intermolecular forces are weakened when the temperature (*i.e.* kinetic energy) of the molecules is increased: therefore, surface tension decreases with temperature, and it cannot be defined at the boiling point[3]. By the same token, the boiling point of a liquid is proportional to its surface tension. Corollaries: 1) the stronger the intermolecular forces, the higher the value of surface tension; and 2) the forces generated by surface tension scale linearly with the dimensions of the liquid sample.

There are many types of intermolecular forces [42]. For liquids, van der Waals and dispersion forces provide rather weak interactions between molecules and consequently low surface tension values, typical of *e.g.* hydro- and fluorocarbons (for which γ proportional to the length of the carbon chains*; e.g.* $\gamma = 27.47\, mJ/m^2$ for hexadecane (HD)). At the other extreme, polar and particularly hydrogen bonds induce significantly stronger interactions between molecules, as exemplified by water ($\gamma \simeq 72\, mJ/m^2$). Typical values for conventional liquids lie within these limits (*e.g.* ethanol ($23\, mJ/m^2$), acetone ($24\, mJ/m^2$), glycerol ($63\, mJ/m^2$)). Nonetheless, the surface energies of (oxide-free) molten solders are about an order of magnitude higher (*e.g.* for mercury, $\gamma = 485.5\, mJ/m^2$).

(mathematical) positioning of the interface [201].

[3]Except where noted, all values of γ will refer to room temperature (RT, *i.e.* 25° C).

The miscibility of a *fluid couple* is related to interfacial tension. Two liquids at equilibrium[4] are *immiscible*, and consequently create an interface, if the interactions between non-identical molecules are much weaker than the interactions between identical molecules. The work required to extend the interface between two liquids A and B may be assumed to be the sum of the works γ_A and γ_B minus the free energy of interaction across the interface w_{AB}, *i.e.*:

$$\gamma_{AB} = \gamma_A + \gamma_B - w_{AB} \tag{2.1}$$

Many models were proposed to relate the energy w_{AB} to the surface tensions γ_A and γ_B of the single fluids. As an example, Girifalco and Good proposed the geometric mean rule:

$$w_{AB} = 2\phi \cdot \sqrt{\gamma_A \gamma_B} \tag{2.2}$$

where ϕ is a fitting parameter, function of the molar volumes of the two liquids, with empirical values ranging from 0.5 to 1.15 [203]. However, the $A-A$ and $B-B$ intermolecular interactions may not equally contribute to $A-B$ interactions; hence, more detailed characterizations were proposed [201]. From such models, it is desumed that the highest interfacial energies belongs to liquid couples composed by a polar and an apolar liquid[5], like *e.g.* the water/hydrocarbon couples.

In our studies on capillary self-assembly, we therefore chose water as hosting fluid and hexadecane as lubricant ($\gamma_{H_2O/HD} \cong 53\, mJ/m^2$ [130]).

Addition of a solute to a liquid can significantly change the liquid's surface tension. The *Gibbs' adsorption isotherm* relates the excess solute concentration at the liquid interface Γ to the solute activity a and to the liquid γ:

$$\Gamma = -\frac{a}{RT} \cdot \left.\frac{\partial \gamma}{\partial a}\right|_T \tag{2.3}$$

so that when a solute is enriched at the liquid interface ($\Gamma > 0$), the surface tension decreases when the solute concentration is increased. Such solutes are said to be surface-active (*i.e.* surfactants), and are typically represented by amphiphilic molecules composed by two distinct parts, one lyophilic and one lyophobic. Note that Eq. 2.3 also predicts an *increase* of surface tension when a solute is added that avoids the interface ($\Gamma < 0$).

Similarly, mixing two miscible liquids affects the surface tension of the resulting solution. For instance, if the surface tensions of the pure liquids differs appreciably (as in the case of *e.g.* water and ethanol), the addition of small

[4] External perturbations alter the equilibrium. For instance, ultrasonic acoustic waves is used to solubilize emulsions.

[5] A rough measure of a liquid's polarity is its dielectric constant ϵ. Liquids with $\epsilon < 15$ are generally considered apolar. Other polarity measures are: the Grunwald-Winstein mY scale, which measures the influence of a solvent in building up the solute's positive charge during a chemical reaction; Kosower's Z scale, which measures the solvent influence on the UV-absorption maxima of a salt (*e.g.* pyridinium iodide or the pyridinium zwitterion) [204]; and the donor number and donor acceptor scale, which measures how a solvent interacts with specific substances, like a strong Lewis acid or a strong Lewis base [205].

amounts of solute (ethanol) generally induces a marked decrease in the surface tension of the solvent (water). This effect may be due to the selective adsorption of the solute at the solvent surface, and may be accounted for by the semi-empirical *Szyszkowsky equation*:

$$\frac{\gamma}{\gamma_0} = 1 - B \cdot \ln\left(1 + \frac{C}{b}\right) \tag{2.4}$$

where γ_0 is the surface tension of the pure solvent, B and b are constants characteristic of the solute and C is the solute concentration [201]. For our purposes, this implies *e.g.* that the surface tension of water is reduced when water is diluted with ethanol.

Furthermore, local gradients in surface tension along liquid interfaces, caused by *e.g.* concentration and/or temperature gradients, induce mass transport of the liquids along the same interfaces. This constitutes the *(Gibbs-)Marangoni effect*. Since a higher surface tension liquid pulls more strongly on the surrounding liquid than one with lower surface tension, the presence of a surface tension gradient will naturally cause the liquid to flow away from regions of low surface tension. The ensuing flui flow can be exploited *e.g.* for propulsion purposes.

Finally, due to their linear scaling property, surface tension effects dominate at small (*i.e.* sub-millimeter) scale, particularly over gravitational/inertial effects. In this respect, the *capillary length* L_c, defined as:

$$L_c \equiv \sqrt{\frac{\gamma_{AB}}{g \triangle\rho}} \tag{2.5}$$

or the related Bond number:

$$Bo \equiv \frac{g \triangle\rho L^2}{\gamma_{AB}} = \left(\frac{L}{L_c}\right)^2 \tag{2.6}$$

with $\triangle\rho \equiv |\rho_A - \rho_B|$, set a rough demarcation scale: for parts of characteristic size L that satisfy $L < L_c$ or equivalently $Bo \ll 1$, gravitational effects can be reasonably neglected compared to surface tension effects. In those conditions, the minimization of the system's energy can be reduced to the minimization of its surface free energy.

Contact angles

When a liquid droplet lies unconstrained on a flat, chemically- and geometrically-homogeneous solid surface, three phases (solid S, liquid L and vapour V) coexist separated by three pair-wise interfaces, all joining together at the *(triple) contact line* (Fig. 2.3). At this singularity, the liquid/vapour interface makes an angle θ with the solid substrate. Under equilibrium conditions, θ is called the *static contact angle* (CA). From the balance of the lateral components of

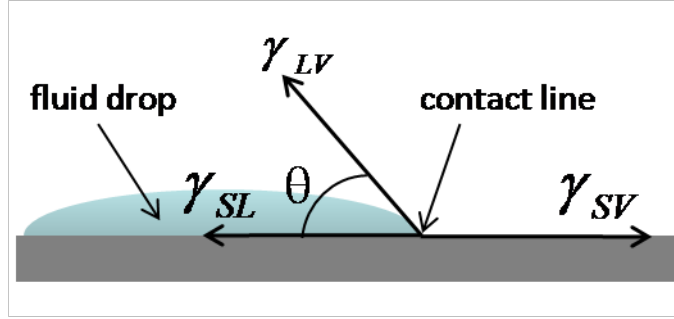

Figure 2.3: Interfacial energies γ_{LV}, γ_{SL}, γ_{SV}, and the static contact angle θ.

the interfacial tensions[6] the *Young-Dupre' equation* is derived:

$$\gamma_{SV} = \gamma_{LV} \cos\theta + \gamma_{SL} \tag{2.7}$$

A liquid is *fully wetting* when $\theta \rightarrow 0$. The spreading of a liquid on a solid surface is also measured by the *spreading coefficient*:

$$S \equiv \gamma_{SV} - \gamma_{LV} - \gamma_{SL} \tag{2.8}$$

which is positive when the spreading is accompanied by a decrease in free energy.

θ is not to be confused with neither the *advancing* (θ^a) nor *receding* (θ^r, with $\theta^r \leq \theta^a$) contact angles of the liquid on the substrate, which appear when the liquid drop is dynamically stressed [201]. The difference $\triangle\theta = \theta^a - \theta^r$, called *contact angle hysteresis*, plays an important role in microfluidics [206].

θ is essentially a microscopic parameter. It is known that the *apparent* contact angle, *i.e.* the value obtained by macroscopic measurement, may differ from θ because of local chemical [207] and geometrical heterogeneities of the solid surface, such as its roughness (see *e.g.* [208]). In spite of the vast literature on the topic, some famous models (*e.g.* the ones of Wenzel [209] and Cassie-Bexter [210]) were recently questioned (as in [211]).

If the triple contact line is posed at the very boundary between two chemically-different co-planar surfaces a and b, or at the very edge of a substrate (*e.g.* at the solid/air boundary), the angle ζ between the liquid/vapour interface and the solid substrate is *not* the liquid's CA (as θ cannot thereby be defined) [212]. In the first case (Fig. 2.4a), ζ can assume any value (depending on *e.g.* geometrical and volume constraints) given by:

$$\theta_a^r \leq \zeta \leq \theta_b^a \tag{2.9}$$

where θ_a^r and θ_b^a are the receding and advancing CAs, respectively, of the liquid on the joining surfaces (assuming $\theta_b > \theta_a$). In the latter case (Fig. 2.4b),

[6]The balance of the vertical components entails the vincular reaction of the substrate. This may eventually cause the local deformation of the substrate.

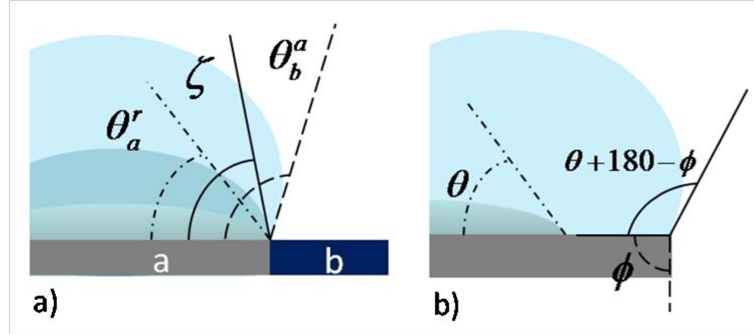

Figure 2.4: The contact angle is *not* defined at the borders surfaces, as *e.g.* on a heterogeneous surface **(a)** and at the edge of a substrate **(b)**.

the upper bound on the value of ζ is set by the *Gibbs' inequality* [213]:

$$\zeta_{max} = \theta^a + 180^o - \phi \tag{2.10}$$

ϕ being the angle between the top and the side surface of the solid substrate. For $\zeta > \zeta_{max}$ the drop is no longer constrained within the original surface.

The Young-Laplace and the Kelvin equations

Because of surface tension, there exists a pressure difference $\triangle p$ across a liquid/vapour interface. Such pressure difference is related to the curvature of the interface by the *Young-Laplace equation*:

$$\triangle p \equiv p_{in} - p_{out} = 2\gamma H \tag{2.11}$$

where H is the mean surface curvature. Note that $\triangle p$ has the same sign of H. As an example, for a soap bubble of radius r the internal pressure is higher to compensate for the external pressure and for the effect of the surface tension; in this case $H = 1/r$, thus according to Eq. 2.11 $\triangle p = 2\gamma/r$.

Kelvin first proposed a relationship between the equilibrium vapor pressure p of a liquid and the mean curvature H of its liquid–vapor interface, which can be expressed as [214]:

$$\ln \frac{p}{p_0} = 2H \frac{V_m \gamma \cos\theta}{RT} \tag{2.12}$$

where p_0 is the saturated vapour pressure, R the universal gas constant, T the temperature, V_m the molar liquid volume. If $p > p_0$ ($p < p_0$), the liquid evaporates from (condenses onto) the interface. A large interface curvature enhances evaporation.

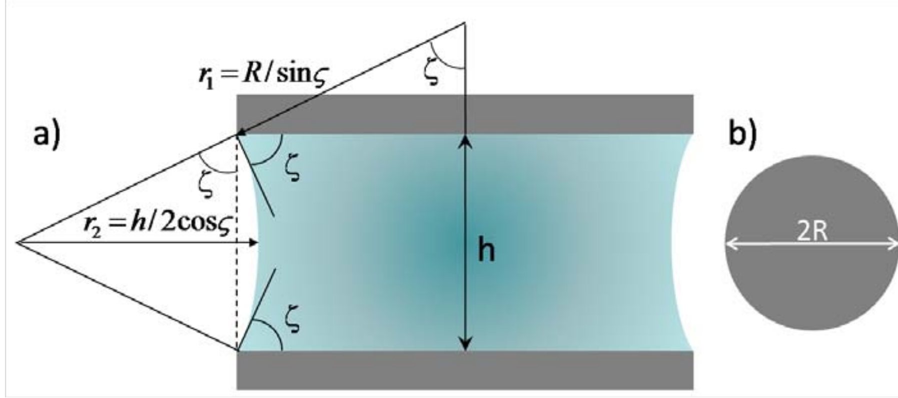

Figure 2.5: A cylindrical fluid meniscus. **a)** Side view, **b)** top view.

Fluid meniscus forces

Fig. 2.5 shows the physical system that will be investigated in later Sections: a cylindrical liquid bridge of height h connects two equal, flat circular plates (also called *pads* in the following) of radius R and area $A = \pi R^2$. The static forces acting vertically on this system for the case of concentric aligned pads are:

1. the *Young-Laplace force* due to the pressure drop across the liquid/vapour interface, which according to Eq. 2.11 is given by:

$$F_{YL} = 2\gamma H \cdot A = \gamma \pi R^2 \left(\frac{\sin\zeta}{R} - \frac{2\cos\zeta}{h} \right) \tag{2.13}$$

   where ζ is the angle between the liquid/vapour interface and each pad surface (being posed at the pads edge, it obeys $\theta^r \leq \zeta \leq \theta_{max}$, where ζ_{max} is given by Eq. 2.10). Note that this force component can be either attractive or repulsive according to the curvature of the liquid interface.

2. the *tension force* applied by the liquid on the solid surface. This force component is always attracting, and derives from the vertical projection of the surface tension acting on the rim of the pads:

$$F_T = -2\pi R\gamma \sin\zeta \tag{2.14}$$

Hence, the total capillary force is given by:

$$F_C = F_{YL} + F_T = -\pi R\gamma \sin\zeta - 2\pi\gamma \frac{R^2}{h} \cos\zeta \tag{2.15}$$

For the particular case of a perfectly-cylindrical fluid meniscus (*i.e.* for $\zeta = \pi/2$), the total capillary force becomes:

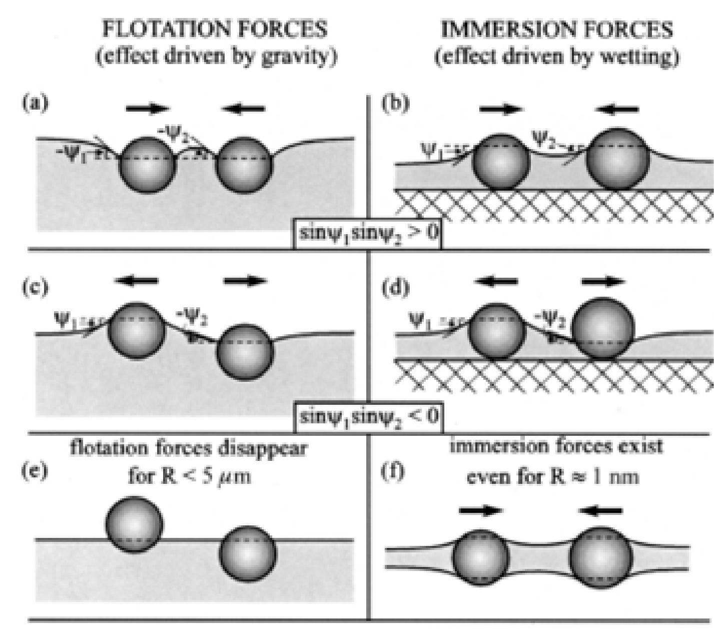

Figure 2.6: Lateral flotation and immersion forces, after [216].

$$F_C^{cyl} = -\pi\gamma R \tag{2.16}$$

For completeness, when the bridge-connected plates undergo vertical motion with relative speed v, an additional *dynamic* force acts on them, given by the *Stefan equation* [215]:

$$F = -\frac{3\pi R^3 \mu v}{h^3} \tag{2.17}$$

where μ is the fluid dynamic viscosity.

A simple analytic model for *lateral* capillary forces of cylindrical fluid menisci was recently proposed by Lambert [197]. According to the model, small perturbations $u < h$ of the relative alignment of the pads give rise to a lateral restoring force linear in u given by:

$$F_L \cong -\pi R\gamma \frac{u}{h} \tag{2.18}$$

Flotation and immersion forces

Particles protruding from or floating on a liquid surface experience lateral capillary interactions (Fig. 2.6). The origin of these forces is the deformation of the liquid surface, flat in absence of particles. The larger the interfacial deformation created by the particles, the stronger the capillary interaction [216].

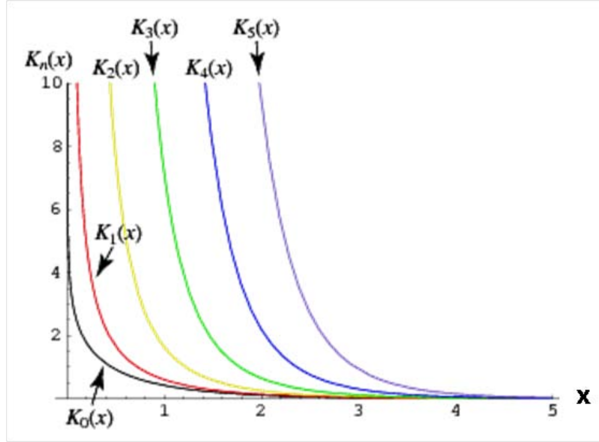

Figure 2.7: Modified Bessel function of the second kind $K_n(x)$.

Lateral flotation forces act between particles *floating* on the liquid surface. This interaction appears because of the particle's weight and buoyancy: the liquid meniscus deforms in such a way that the gravitational potential energy of the two particles decreases when they move relative each other. Lateral immersion forces act instead on particles that are partially *immersed* into a liquid layer. The deformation of the liquid surface in this case is related to the wetting properties of the particle surface, *i.e.* to the position of the contact line and the value of the contact angle, rather than to gravity.

The forces can be both attractive or repulsive depending on the signs of the meniscus slope angles at the two contact lines (ψ_1 and ψ_2 in Fig. 2.6): they are attractive (repulsive) when $\sin\psi_1 \cdot \sin\psi_2 > 0$ (< 0). For flotation forces, $\psi > 0$ for light particles including bubbles and $\psi < 0$ for heavy particles. For immersion forces, $\psi > 0$ for wettable particles and $\psi < 0$ otherwise. When $\psi = 0$ there is no meniscus deformation, and hence no capillary interaction between the particles.

The forces exhibit similar dependence on the interparticle separation, but very-different dependencies on particle radius R and liquid surface tension γ. When the particle center-to-center distance L is $r_i \ll L \ll L_c$, r_i being the radius of the contact line at particle i, the lateral forces are approximated by:

$$F \simeq -2\pi\gamma Q_1 Q_2 / L \tag{2.19}$$

The difference lies in the capillary charges $Q_i = r_i \sin\psi_i$, such that ($K_1(x)$ is the modified first-order Bessel function of the second kind, Fig. 2.7):

- $F_{flotation} \propto (R^6/\gamma) \cdot K_1(L/L_c)$
- $F_{immersion} \propto \gamma R^2 \cdot K_1(L/L_c)$

Consequently, the flotation force decreases, while the immersion force increases, when the surface tension γ increases. Besides, the flotation force decreases much

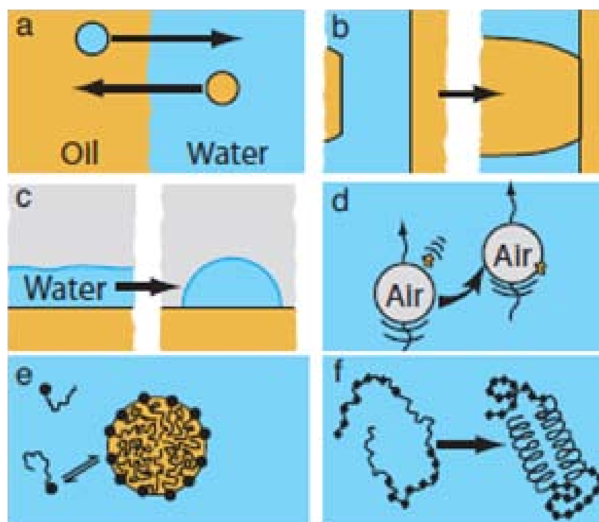

Figure 2.8: Manifestations of the hydrophobic interaction, after [218].

stronger with the decrease of R than the immersion force. The flotation force is negligible for $R < 5 - 10\ \mu m$, whereas the immersion force can be significant even for $R < 2\ nm$. These facts are significant for colloidal assemblies [105].

The hydrophobic interaction

The hydrophobic interaction (or effect) is qualitatively due to the tendency of nonpolar moieties immersed in polar liquids to cluster to minimize their contact with molecules of the liquids [217]. It is a property of the *solvent*, not of the affected solutes (particles or molecules). Traditionally, this behaviour was thought to be of entropic origin, due to its dependence on temperature; recent studies are showing a more complex picture [218].

The interaction manifests itself in many commonly-observed ways (refer to Fig. 2.8): low solubility or immiscibility of nonpolar solutes in water (a); the significant work of adhesion between solid hydrophobic surfaces and the rapid coalescence or flocculation in colloidal systems of hydrophobic liquid droplets or solid particulates (b); large liquid contact angles of water on hydrophobic surfaces (c); absorption of surfactants, proteins and polymers at the water/air interface (d); self-assembly processes such as micelle formation (e); and vesicles, bilayers and protein folding (f).

The hydrophobic interaction acts over intermolecular distances of several tens of nanometers [42]. The role of polar molecules in the average attraction between nonpolar groups might be larger than that of the direct van der Waals interaction between these groups. Anyway, the force-versus-distance or energy-versus-distance law of the hydrophobic interaction is not precisely known yet.

2.3 Earlier works on lateral capillary forces

Fundamental in bio-chemistry [42], capillary phaenomena are presently at the core of many technological applications, as well, such as *e.g.* microfluidics [9], switchable lenses [219], tightness systems [220] and precision manufacturing [221]. Packaging techniques involving metallic bonding and soldering [222] also share the underlying mechanism illustrated in Sec. 2.1.

Theoretical and numerical studies

Early studies aimed at predicting - both analytically and numerically - the shapes and corresponding self-aligning performance of fluid drops (representing *e.g.* molten-solder bumps) vertically-constrained by parallel plates and laterally-confined by the patterns defined on the same plates (*i.e.* the binding sites) [223, 224, 225].

Finite-elements quasi-static simulations of physical systems similar to that depicted in Fig. 2.5, with the top plate normally represented by a part of finite dimensions free in all translational and rotational degrees of freedom (DOFs), further illustrated the dependency of lateral capillary forces on the physical properties of the fluid meniscus and on the geometry of the confining geometrical patterns [226, 227]: briefly, the forces are proportional to the surface tension of the fluid, and inversely proportional to the height of the meniscus (also referred to as the *gap* in the following). Moreover, the magnitude of the lateral forces follow the (a)symmetry of the patterns of the confining sites; namely, they depend on the direction of the perturbation of the meniscus (*i.e.* on the displacement of the top part) from its rest configuration as compared to the sides of the confining planar patterns: forces arising from displacements along shorter sides are stronger.

Böhringer proposed a geometrical model that, while capturing many known properties of confined capillary menisci, greatly simplified energy and force calculations [228]. Built around the two-dimensional convolution of the patterns of the confining surfaces, the model easied the theoretical investigations on geometry-dependent self-alignment performance of binding sites [229, 199] - as illustrated in Sec. 2.5. Nonetheless, being essentially two-dimensional, the model accurately matches earlier results only for relative displacements from the rest position larger than the meniscus height; it also neglects the gravitational potential energy of the system, implicitly assuming to work under low Bond number conditions (see Sec. 2.2). Therefore, it cannot be used to accurately model the self-alignment performance in close proximity to the rest position - which is conversely of utmost importance in capillary self-assembly of parts with very-small interconnection pitches (*i.e.* few tens of microns). Particularly, the model neglects the curvature of the surface of the fluid meniscus, which significantly affects the capillary restoring forces for small meniscus perturbations [226, 230]. Given fixed geometrical boundary conditions, the meniscus curvature is directly influenced by the volume of the fluid: hence the need for accurate fluid volume control to achieve high process reproducibility (Sec. 3.5).

Experimental studies

Experimental quasi-static characterization of lateral capillary forces were up to now unsatisfactory. A few works reported on the determination of the alignment accuracy achievable between part and binding site by means of capillary self-alignment: this was done either optically [131, 231, 200] or analyzing assembly cross-sections by scanning electron microscopy [149]. Best claimed figures were of the order of $1\,\mu m$ or lower, which are amenable to advanced packaging applications. Other researchers [232, 233] were able to estimate the maximum adhesion force binding flat parts onto fluid drops by tracking the velocity of the fluid flow that caused the detachment of the parts in blowing tests [234]. Though these may be assumed as reasonable estimates of the maximal lateral capillary restoring forces of the menisci, we remark that in such conditions, where the direction of displacement of the floating part is not constrained to be parallel to the substrate, the measured values may hardly be entirely attributed to lateral force components.

To our knowledge, only Zhang reported experimental measurements and numerical simulations of lateral capillary forces for the same physical system [235]. The system was composed by a 450 μm x 250 μm flat silicon piece floating on a matching rectangular site confining a thin fluid drop - all immersed in water. The measurements of lateral capillary forces were performed in situ by means of a micromachined optical encoder, featuring laser-illuminated calibrated optical gratings and a horizontal probe that displaced the part from its rest position along a direction parallel to the substrate. Anyway, though the proposed numerical model showed reasonable match with experimental data, there was no mention of *e.g.* surface tension and volume of the fluid nor of meniscus height, which are pivotal parameters to reproduce and appreciate the numerical results. Moreover, the way the physical system was set up is difficult to control and reproduce; and only one experimental measurement was presented.

2.4 Lateral capillary forces of fluid menisci[7]

This Section presents our comprehensive quasi-static investigations on lateral capillary forces arising from small perturbations of cylindrical fluid menisci. In pursuing this work, we aimed at getting first-hand understanding on self-alignment driven by capillarity, and at providing a sound foundation for it. Contextually, we developed a novel sensing apparatus, since existing tools like *e.g.* mechanical shear testers (used *e.g.* in Sec. 4.3.2) or lateral-mode AFM were either not suitable or not compliant with our requirements[8].

[7]Work done at the BEAMS Dept., Université Libre de Bruxelles (Bruxelles, BE) in collaboration with Pierre Lambert and Jean-Baptiste Valsamis.

[8]We nonetheless do not exclude that such tools may still serve the purpose. Particularly, lateral-mode AFM may be useful to investigate capillary forces at (sub)micrometric scale, eventually in an aqueous environment to reduce parasitic interferences (*e.g.* tip-sample adhesion by capillary condensation or stray electrical charges).

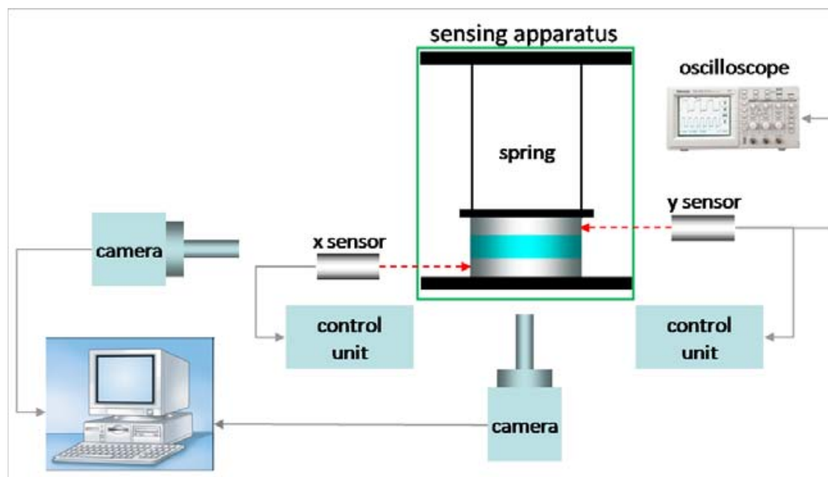

Figure 2.9: Schematic representation of the experimental setup used in this work. Relative dimensions are out of scale for representation purposes.

2.4.1 Experimental study

The experimental setup

In designing our measurement apparatus, we satisfied several requirements:

1. We wanted a simple apparatus for precise spatial manipulations;
2. the apparatus had to enable carefully-controlled and reproducible experiments: all relevant meniscus parameters of each experiment had to be reliably known (before or after the experiment itself);
3. we were interested in precisely measuring lateral forces of the same order of magnitude of those arising in the technological applications of our interest, *i.e.* forces reportedly of the order of tens of μN [227];
4. we wanted to measure *only* lateral capillary forces;
5. our main objective was sampling the capillary force-versus-lateral displacement curve close to its rest position, *i.e.* for displacements smaller that the meniscus height. Finally
6. the fluids to be used had to have low volatility, so to allow for up tens of minutes-long measurements.

A schematic diagram and the actual implementation of the experimental setup are shown in Fig. 2.9 and Fig. 2.10, respectively[9]. The actual system

[9]Our setup may be roughly likened to an upscaled version of the *flexure-based microgap rheometer* developed by Clasen *et al.* to study microgap-dependent flow behavior of complex fluids [236].

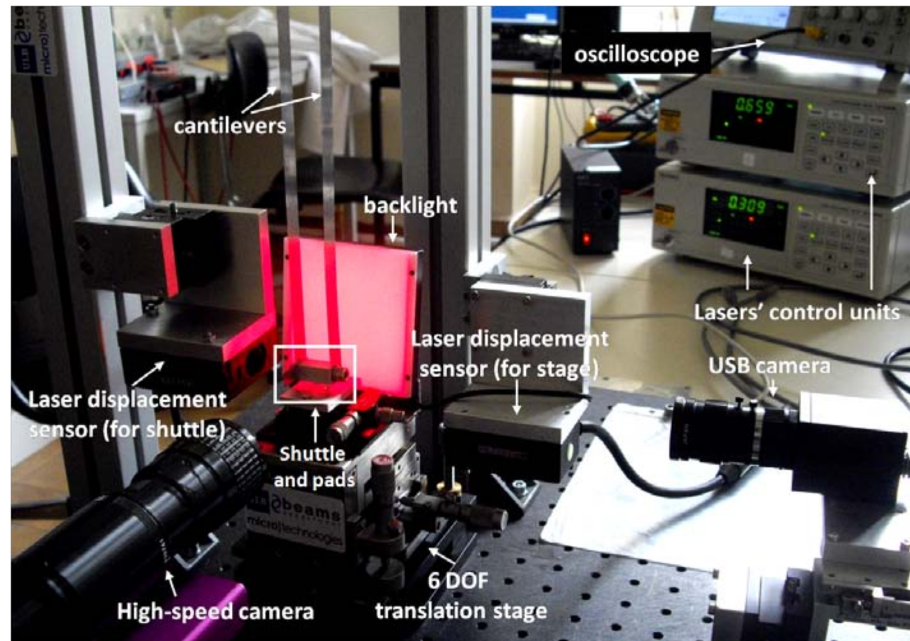

(a) Full view.

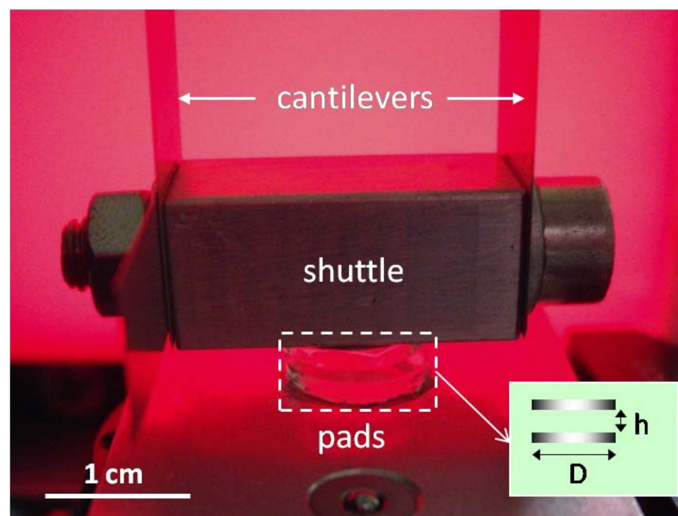

(b) Close-up view of the inset.

Figure 2.10: The experimental setup for lateral capillary force measurements.

under investigation was composed by two equal glass cylinders of known dimensions (diameter $D = 2 \cdot R = 9.4\,mm$, thickness $t = 1.6\,mm$) which vertically- and laterally-shaped the liquid menisci. The bottom cylinder was rigidly-attached to a stage that could be manually moved along all 6 roto-translational DOFs with micrometric precision (Newport M-562-XYZ). The lateral position of the translation stage was tracked by a laser displacement sensor (Keyence LC-2440) featuring a linear output characteristic for a displacement range of 3 mm within the sensor's optimal working distance (*i.e.* 3 cm from the laser source). The sensor's controller unit (Keyence LC-2400W) displayed either absolute or relative calculated displacements in real time, and allowed direct filtering and averaging operations on acquired signals. The top cylinder was rigidly-attached to the bottom surface of a finely-machined aluminum parallelepiped (hereby referred to as the *shuttle,* of mass $m_{sh} = 12.748\,g$ including the top pad), which in turn was held by two equal blades of certified dimensions (feeler gage in close grain high carbon spring steel, Precision Brand) and mass $m_b = 2 \cdot 2.85\,g$ hanging from an overarching solid bridge (not shown). Upon attachment of the coupled blades to the bridge, the sliding motion of the shuttle (*i.e.* the bending motion of the blades) was constrained to take place exclusively[10] along the single (lateral) direction where the measurements of displacement were performed. This double-cantilever-supported shuttle constituted the actual sensing device of the apparatus, and is hereby referred to as the *spring.* The lateral position of the shuttle was tracked by an independent laser displacement sensor (and control unit), identical to the aforementioned but pointing in the opposite direction. The vertical position of the (shuttle, and consequently of the) top pad was kept fixed throughout all the experiments in order to consistently dispose of exactly the same sensing device in all experiments. From this fixed boundary condition it followed that: 1) the vertical distance between the glass cylinders, *i.e.* the height h of the fluid menisci, could be precisely set at the beginning of each experiment using only the controlled vertical motion of the translation stage; and that 2) the axial components of the capillary force were excluded from measurements (point 4), being balanced by the vincular reactions of the rigid supports. To inspect the initial relative pad alignment, the plane parallelism of the surfaces of the pads and the initial profile of the fluid menisci, the positions of the top and bottom pads were visually-tracked by two cameras connected to PCs: an USB camera pointed along the direction of lateral motion of the shuttle, and a high-speed camera (Photron Fastcam SA3 120K) pointed along the direction perpendicular to the previous and intersecting it in correspondence with the initial position of the bottom pad. The pads were illuminated by a flat backlight (LDL-TP-83x75) with very-uniform red light emission profile. Pictures of the menisci were taken with the high-speed camera at the beginning and at the end of every experiment to check whether the volume of the meniscus eventually changed during the measurements. The 1024 pixels-wide pictures spanned a field of view of about $20\,mm$, providing a resolution (and accuracy of initial position) of about $20\,\mu m$.

[10]For an estimate of the vertical parasitic displacement of the top pad, see note 11.

Name	ρ $[Kg/m^3]$	γ $[mN/m]$	**Supplier**
Water	1000	72.2	Tap water
Oil 5	934	20.1	Dow Corning DC200FLUID10
Oil 6	960	20.9	Dow Corning DC200FLUID100
Oil 1	970	21.1	Rhodorsil R47V500
Oil 7	971	21.2	Dow Corning DC200FLUID1000
Oil 2	973	21.1	Rhodorsil R47V5000

Table 2.1: Fluids used in the experiments.

All the experiments were performed in a laboratory environment; room temperature varied between 25 ^{o}C and 28 ^{o}C, air humidity was about 38 %. Silicone oils were used as fluids, whose properties are summarized in Table 2.1.

The capillary lenght $L_c = \sqrt{\frac{\gamma}{\rho g}}$ of the oils was about $1.5\,mm$. In all experiments, the imposed heights of the cylindrical menisci were smaller than L_c, so that gravity could be neglected as compared to capillary forces. For each fluid, we performed a series of experiments with progressively smaller meniscus heights. In the first experiment of each series, the meniscus height was calibrated to exactly $1\,mm$ by means of a ceramic slip gage of known thickness (Mitutoyo). The CA of silicone oils on hydrophilic surfaces is rather small ($\leq 20^o$) [201]. This put a geometric constraint on the maximum meniscus perturbation to avoid fluid overflow beyond the edges of the bottom pad, and consequent change of the volume of the fluid meniscus (see Sec. 2.4.3). Nevertheless, the range of allowed top pad relative displacements was fully-coherent with our focus on small lateral meniscus perturbations. Oil evaporation was negligible throughout all our experiments, consistently with their low volatility. On the contrary, in some explorative experiments we also used water as meniscus fluid ($\gamma = 72\,mJ/m^2$, $L_c = 2.72\,mm$); as expected, its high volatility made our quasi-static measurements problematic, difficult to reproduce and model (see Sec. 2.4.3).

The fluids were dispensed between the pads by manual pipetting from calibrated pipettes. Because of the intrinsic dispensing imprecision due to hardly-controllable tip pinch-off effects, we calculated the actual volumes V and height h of the fluid menisci by digital post-processing (assuming axial symmetry of the menisci) of the pictures taken at the beginning of the experiments. Our semi-automatic, numerical algorithm computed V, h and D for each experiment. We calibrated the images using the $1\,mm$-thick ceramic gage, leading to a resolution of $14.2\,\mu m/pixel$. For each dispensed fluid drop, we enforced an initially-cylindrical profile for the meniscus (*i.e.* a strictly-vertical lateral meniscus surface), as judged by visual camera inspection (see *e.g.* Fig. 2.12a). We made 3 numerical estimates on each calibration picture; and we *a posteriori* discarded all experiments for which we could not get a ratio between the average values of V and h and their respective standard deviations larger than 10.

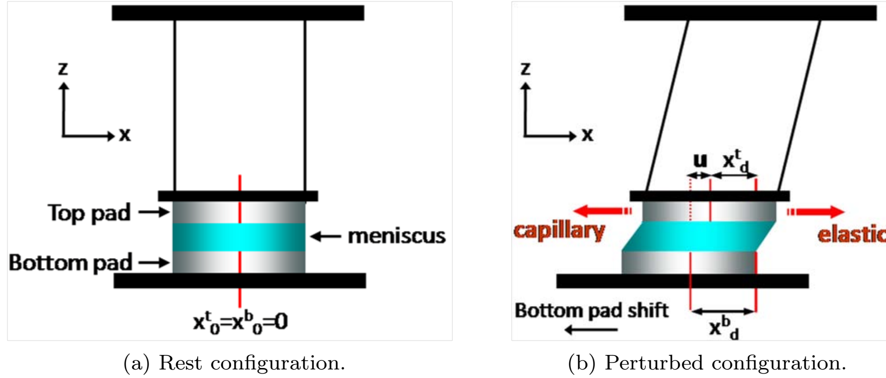

(a) Rest configuration. (b) Perturbed configuration.

Figure 2.11: The sensing principle, based on the balance between capillary and elastic lateral forces. Relative dimensions are out of scale for illustration purposes. (Actual rest and perturbed configurations are shown in Fig. 2.12)

The uncertainty on the heights was typically 2 pixels, *i.e.* about $28\,\mu m$. Thus we kept the heights of the menisci always higher than $280\,\mu m$. By comparing the reconstructed value of D to its caliber-measured value, we could assess the accuracy of the numerical estimates of D, V, and h (see Table 2.3).

Though our experiments focused on circular pads only, lateral capillary forces arising from fluid menisci shaped by pads of arbitrary geometries could in principle be measured with our setup - though the exact knowledge of the dispensed fluid volume may be harder to get for non-axisymmetric menisci.

The sensing principle

The working principle of the sensing apparatus is sketched in Fig. 2.11. During initial manual trimming, complete alignment (*i.e.* vertical superposition of the centers of both pads, with respective coordinate x^b and x^t) was reached when both perpendicular cameras showed alignment of the edges of both pads. Then the vertical position of the bottom pad was manually set so to get a cylindrical profile, as previously discussed (Fig. 2.12a). In this condition, both the fluid meniscus and the spring were in their rest configurations: consequently, both interferometers were reset to null relative displacement to define the reference starting position (*i.e.* $u = x_0^b = x_0^t = 0$; see Fig. 2.11a and 2.12a).

The measurements were then performed by imposing a known lateral displacement x_d^b to the bottom pad, as tracked by the dedicated sensor (Fig. 2.11b and 2.12b). This lateral shift perturbed both the fluid meniscus and the spring from their respective rest positions. As a consequence, two opposing lateral forces acted on the top pad: the capillary force tending to restore the meniscus rest position, and the elastic force tending to restore the shuttle rest position. The equilibrium of the lateral forces - achieved after some settling time, dependent on the viscosity of the fluid and the velocity of the movement imposed on

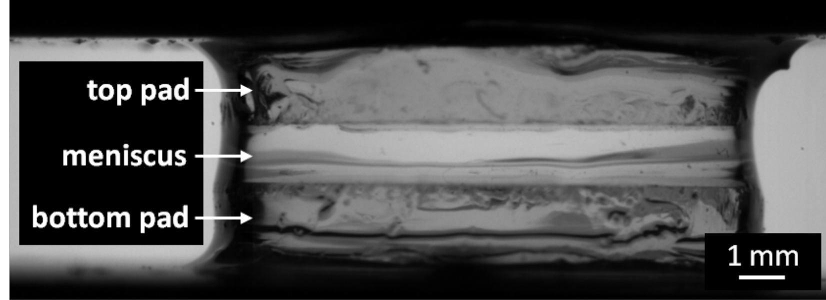

(a) Rest configuration. Top and bottom pads are visually aligned, the height of the meniscus ($1.205\,\mu m$) is trimmed to get a cylindrical profile.

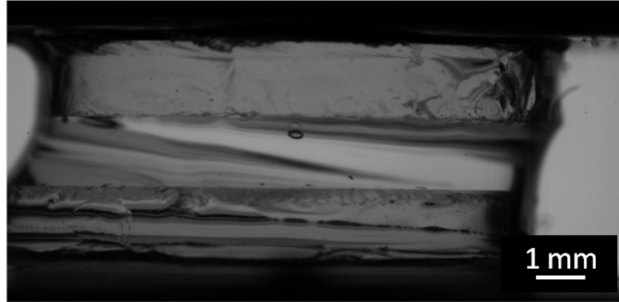

(b) Perturbed configuration. After imposing a displacement ($x_d^b = 812\,\mu m$) to the bottom pad, the lateral force balance between capillary and elastic spring forces determines the equilibrium displacement of the top pad ($u = 660\,\mu m$) relative to the bottom pad.

Figure 2.12: Measurement of lateral capillary forces of a cylindrical meniscus.

the shuttle - determined the actual displacement of the top pad: this was x_d^t (as tracked by the dedicated sensor) with respect to the rest position of the spring, and $u = x_d^b - x_d^t$ relative to the bottom pad. Hence, because of lateral force balance, the restoring lateral meniscus force corresponding to the net displacement u of the top pad relative to the bottom pad could be calculated by multiplying the absolute displacement x_d^t of the top pad times the bending stiffness of the spring K - whose estimation is described in the next Section.

By imposing subsequent displacements to the bottom pad, we could experimentally sample the restoring force-versus-lateral displacement characteristic curve of our physical system. From this curve, the lateral stiffness of the fluid meniscus K_m^L could be obtained by first-order polynomial fitting. In each experiment, the same set of bottom pad displacements $\{x_{d_i}^b\}$ were imposed in both directions around the initial aligned position to ascertain eventual asymmetries and/or hysteretic phenomena.

Estimation method	K $[N/m]$
Auxiliary cantilever - analytical	1.1506
Auxiliary cantilever - dynamic	0.9323
Auxiliary cantilever - weighting	1.0563
Dynamic	0.9375
Analytic	0.9036

Table 2.2: Summary of the estimates of the spring's bending stiffness.

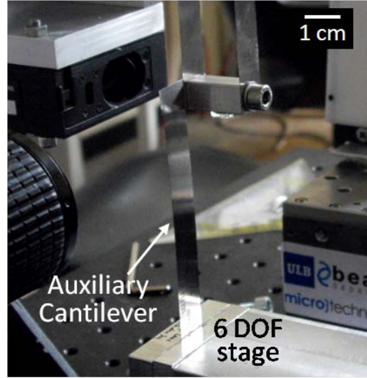

Figure 2.13: The auxiliary cantilever for estimating the spring stiffness.

Bending stiffness of the spring

We estimated the bending stiffness K of our double-cantilever spring holding the shuttle at its sliding extremity in 3 different ways, obtaining a total of 5 estimates. All geometrical parameters of the spring were accurately known: beam lenght $L = 282\,mm$, thickness $h = 0.102\,mm$, width $b = 12.7\,mm$, total spring mass (including both beams, shuttle and top pad) $M = 18.448\,g$. Multiple alternative estimates were motivated by the uncertainty on the effective Young Modulus E (assumed value: $210\,Gpa$) and density ρ (assumed value: $7800\,kg/m^3$) of our steel cantilevers. A good agreement between all estimates was obtained (see Table 2.2). Nonetheless, we attributed higher confidence to the two fully-experimental estimates of K (defined below as K_3 and K_4), which both avoided the use of E and ρ. Therefore, we assumed for the spring a bending stiffness equal to the average of K_3 and K_4, *i.e.* $K = 0.9969\,N/m$, with a relative uncertainty of $5.96\,\%$.

Such high sensitivity enabled both the spring's desired force resolution and its susceptibility to environmental perturbations (see Sec. 2.4.3).

The auxiliary cantilever method

The first estimates involved an auxiliary steel cantilever of known dimensions (length $l = 86.4\,mm$, thickness $h = 0.102\,mm$, width $b = 12.7\,mm$, Precision

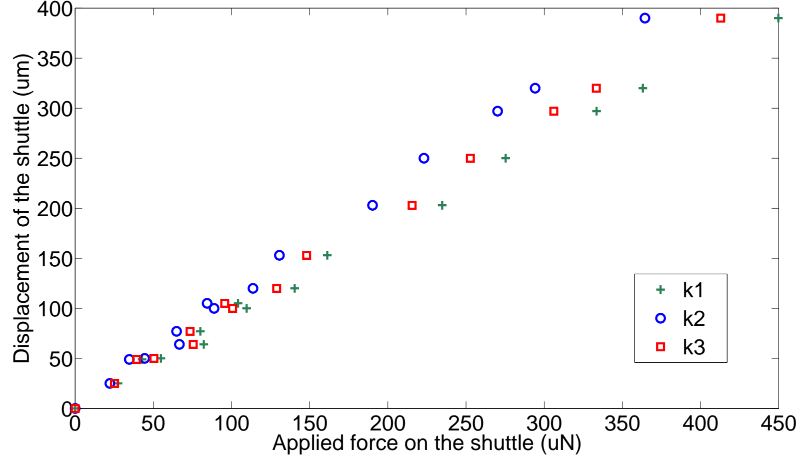

Figure 2.14: Shuttle displacements induced by the auxiliary cantilever. Three estimates for the force applied by the cantilever are given for each displacement value, according to the three estimated values of $k_{\#}$.

Brand). The measurement principle exploited the lateral force balance between the cantilever and the spring (Fig. 2.13). Starting from the initial rest position, common to both cantilever and spring, a laser-tracked lateral displacement imposed on the cantilever induced a laser-tracked lateral displacement on the spring. After determining the bending stiffness of the cantilever, the stiffness of the spring was obtained from its force-versus-displacement curve (shown in Fig. 2.14) by first-order polynomial fitting.

We estimated the bending stiffness for small deformations k of the auxiliary cantilever in three ways. Assuming the stainless steel's Young's Modulus E and density ρ, k is given by linear material strength theory (see [237]):

$$k = \frac{3EI}{L^3} \tag{2.20}$$

where I is the cantilever's second moment of the area. We estimated I:

1. Analytically, as $I = \frac{bh^3}{12}$. In Eq. 2.20 this leads to $k_1 = 1.097\, N/m$.

2. From the knowledge of the first resonance f_1 of the cantilever, as obtained by solving *Euler's beam equation* ([237], p. 273):

$$I = \frac{2\pi f_1 \rho}{E\beta_1^4} \tag{2.21}$$

where $\beta_1 = 1.875$. We measured the vibration period $t = 97\, ms$ of the cantilever analyzing its laser-tracked oscillations on a digital oscilloscope. Hence, from Eqs. 2.21 and 2.20 we got $k_2 = 0.8889\, N/m$.

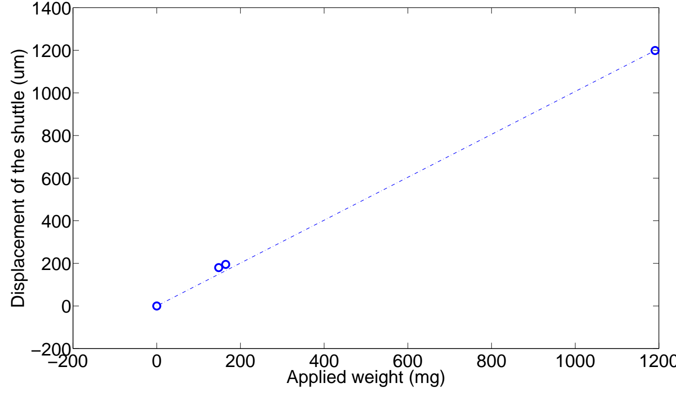

Figure 2.15: Experimental calibration of the auxiliary cantilever.

We also experimentally estimated the bending stiffness of the cantilever by measuring its tip load-versus-tip displacement characteristic (shown in Fig. 2.15) using several known loads. This gave us a value of $k_3 = 1.0071 N/m$. We consider this the most reliable of our estimates of k.

From the measured force/displacement curve we got one value of $K_{\#}$ for each $k_{\#}$: $K_1 = 1.1506\, N/m$, $K_2 = 0.9323\, N/m$ and $K_3 = 1.0563\, N/m$.

The dynamic method

Knowing the natural oscillation frequency f_1 of the double-beam spring, its stiffness K_4 can be directly estimated according to:

$$K_4 = 4\pi^2 f_1^2 M_{eff} \tag{2.22}$$

where M_{eff} is the effective spring mass, including the mass of the shuttle and the kinetic energy-averaged mass of the cantilevers. In fact, the mass of the spring's 2 cantilevers ($m_b = 5.7\, g$) was not negligible compared to that of the shuttle and top pad ($m_{sh} = 12.778\, g$). Therefore, according to the *Rayleigh method* ([237], p. 23), we introduced an equivalent mass for both beams m_{eq}, which would have the same kinetic energy as the actual cantilevers for the same shuttle velocity v according to:

$$\frac{1}{2} m_{eq} v^2 = 2 \cdot \frac{1}{2} \int_0^L v^2(z) dm' = 2 \cdot \frac{1}{2} \lambda \int_0^L v^2(\xi) d\xi \tag{2.23}$$

where $dm' = \lambda d\xi$, and λ has the dimension of mass per unit length. The velocity $v(z)$ of each cantilever element located at a distance z from the clamped extremity was assumed to be proportional to its displacement computed by material strength theory:

$$v(z) = \frac{q(z)}{u} v \tag{2.24}$$

where the element $q(z)$ is given by (F is the applied load):

$$q(z) = \frac{F}{EI}\left(\frac{Lz^2}{4} - \frac{z^3}{6}\right) \tag{2.25}$$

and $u = q(L)$. Using Eqs. 2.25, 2.24, and 2.29 we get:

$$v^2(z) = v^2\left(\frac{9z^4}{L^4} - \frac{12z^5}{L^5} + \frac{4z^6}{L^6}\right) \tag{2.26}$$

which, inserted in Eq. 2.23, leads to:

$$m_{eq} = \frac{13}{35}m_b \tag{2.27}$$

Finally, the effective spring mass M_{eff} is given by:

$$M_{eff} = m_{sh} + m_{eq} = 14.8171\,g \tag{2.28}$$

The oscilloscope-measured natural frequency of the spring was $f_1 = 1.266\,hz$ which through Eq. 2.22 leads to $K_4 = 0.9375\,N/m$.

The analytic method

A fifth estimate of K was calculated fully-analytically. We assumed that K_5 had 2 components: 1) the mechanical stiffness of 2 parallel, coupled cantilevers - with their unclamped extremities constrained by the shuttle to slide along a direction perpendicular to the cantilevers - given by linear material strength theory; and 2) a component due to the gravitational potential energy, which we converted into a so-called *gravitational stiffness.*

The mechanical component was obtained from:

$$K_{mech} = 2 \cdot \frac{12EI}{L^3} \tag{2.29}$$

The gravitational component of the spring's stiffness arises from the fact that an horizontal displacement u of the shuttle is concurrent to a *vertical parasitic displacement* q given by Henein ([238], formula 5.13)[11] as:

$$q \approx \frac{3u^2}{5L} \tag{2.30}$$

Considering that the shuttle undergoes a p upward displacement while each beam's mass center undergoes a $p/2$ vertical displacement, the gravitation stiffness K_{grav} is defined as follows:

$$\frac{1}{2}K_{grav}u^2 = m_{sh}gq + m_b g\frac{q}{2} \tag{2.31}$$

[11] Eq. 2.30 can estimate the q induced by our lateral force measurements. For *e.g.* Exp. 2 of Table 2.3, a $u_{max} = 273\,\mu m$ led to a negligible $q_{max} = 0.16\,\mu m$.

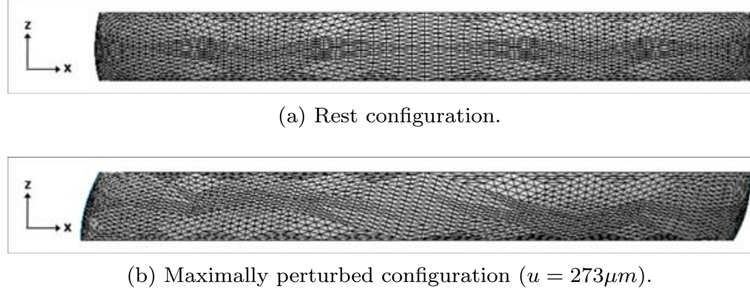

(a) Rest configuration.

(b) Maximally perturbed configuration ($u = 273\mu m$).

Figure 2.16: The finite-element fluid meniscus model for Exp. 2 of Table 2.3.

which together with Eq. 2.30 leads to:

$$K_{grav} = \frac{6g}{5L}(m_{sh} + \frac{m_b}{2}) \tag{2.32}$$

where g is the acceleration of gravity. All parameters being known, we got a value of $K_5 = 0.9036\,N/m$.

2.4.2 Finite-element model

We modeled our experiments on cylindrical fluid menisci with Surface Evolver [239] (Fig. 2.16). The code was adapted from the *column* example wrote by SE's developer K. Brakke[12]. All geometrical (radius of the pads R, meniscus height and volume as obtained by image post-processing for each experiment) and physical (fluid density and surface tension) parameters reproduced those of the chosen experiments. We imposed the pinning of the fluid triple contact-line along all the circular edge of both pads. This condition was enforced at the beginning of each experiment, and was satisfied for all measurements of small meniscus perturbations, as judged by visual inspection. The angle ζ between the lateral meniscus surface and the pad surfaces at the triple contact-line (Fig. 2.5) was therefore not imposed, as it was a consequence of the physical (*i.e.* fluid surface tension) and geometrical (fluid volume and pad areas) boundary conditions of the problem.

The capillary forces were calculated by the method of virtual works (see *e.g.* [237], p. 25) using central differences. Our script for mesh refinement and geometry evolution made repeated use of the hessian of the energy function, achieving energy convergence to its 5th significant digit and a satisfactory match against the benchmark given by the total capillary force acting on a perfectly cylindrical fluid meniscus, analytically given by $F = -\pi\gamma R$ (see Sec. 2.2). In simulating the force-versus-displacement curve of few of our experiments, we input the same set of displacements of the top relative to the bottom pad $\{u_i\}$

[12]The code is available at http://www.susqu.edu/brakke/evolver/html/column.htm

that were measured in the experiments. We extrapolated the simulated lateral stiffness K_m^L of the fluid menisci by polynomial first-order fitting of the curves.

2.4.3 Results and discussion

The magnitude of the displacements $\{x^b_{d_i}\}$ of the bottom pad was empirically determined as a compromise between two competing needs: 1) to accurately sample the curves, and 2) to avoid the effects of environmental noise. The spring was indeed as sensitive as to be clearly perturbed by the movement of the surrounding air. This was the main source of noise, together with the impulsive vibration of the movable stage (induced by floor vibrations, though partly-attenuated by an absorbing plastic multilayer set underneath the apparatus). As a consequence, the spring could eventually undergo stochastic swinging movements (as large as few tens of micrometers, at maximum) before settling to the equilibrium position imposed by the boundary conditions. To cope with this: 1) we spaced the successive positions $\{x^b_{d_i}\}$ of the bottom pad $50\,\mu m$ apart; 2) we moved the bottom pad slowly enough in between the prefixed positions to avoid inducing excessive air and fluid flows; 3) we waited up to several tens of seconds after each prefixed position was reached to let transient air and fluid flows, and fluid velocity gradients and shear stresses inside the meniscus, go extinct: at each step, the spring settled in its new equilibrium position after undergoing few decaying oscillations and within a time dependent on fluid viscosity and the imposed shuttle velocity; and 4) we averaged (131072 times) the interferometric laser signals to cancel out fluctuations and thus achieve the best force resolution possible. Note that such relatively-wide spacing between sampling point, as compared to the full range of imparted displacements, made no harm to faithfully reconstruct the desired curves: close to the origin, the behavior of the fluid menisci was indeed expected to be essentially linear [226, 227] - as we experimentally confirmed it to be *a posteriori* (see *e.g.* Fig. 2.17).

Table 2.3 shows a summary of results of our investigations. We performed a total of 34 experiments; however, we report for comparison only those experiments for which 1) no fluid overflow nor sensible evaporation was detected, and 2) the estimates of volumes and heights of the menisci were accurate (see Sec. 2.4.1). As an example, Fig. 2.17 shows the specific capillary force-versus-lateral displacement characteristic relative to the second experiment reported in Table 2.3, with both experimental and modeling data.

The experimental results confirm that lateral capillary forces arising from cylindrical menisci of lower height (which also means lower volumes in our case, because of the adopted procedures) are proportionally larger. Furthermore, the comparison of the results reveals that both numerical and analytical models tend to overestimate the meniscus stiffness, with the numerical estimate closer to the experimental values. This is evidenced in Fig. 2.18 by the deviation of model data's trend lines from the ideal trend. The relative errors of analytical estimates (up to 32 %, with an average of 18.6 %) are larger than those of the numerical model (up to 14 %, with an average of 7.2 %), as well. We attribute these facts to several factors and sources of errors, discussed in the next Section.

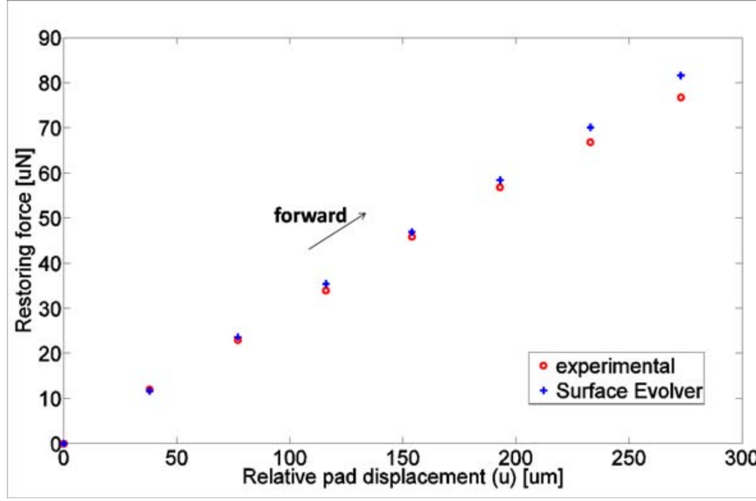

Figure 2.17: Experimental and finite-element data for Exp. 2 in Table 2.3.

Sources of error

The relative error on the reconstructed value of pad diameters D (shown as RE in the second column of Table 2.3) is an indication of the error on the estimates of volumes and heights of the menisci. These errors in turn directly affect the geometry of the reconstructed menisci, and thus both models' estimates of their lateral stiffnesses. Given the relative errors $\delta h/h$ and $\delta R/R$ on the estimates of h and R, respectively, the relative error on the volume of a cylinder is:

$$\frac{\delta V}{V} = \frac{\delta h}{h} + 2 \cdot \frac{\delta R}{R} \tag{2.33}$$

which equals $3 \cdot \delta R/R$ assuming equal relative errors for h and R. Considering *e.g.* the case of experiment 2 described in Table 2.3, the effects of a 2.45 % relative error on h, D and V give a relative error on the simulated versus experimental values of meniscus stiffness of 8.6 % (for the case of all errors in excess) and 7.62 % (in the opposite case), respectively. Thus, this and similar error propagation analyses make the relative error between SE data and real data more acceptable, and may partly explain it. By the same token, we also remark that the relative uncertainty on the experimental value of the stiffness of the spring (~ 6 %) is by itself very-close to the average relative error of the SE model compared to experiments (7.2 %).

Relative errors on estimates of D do also affect, though to a lesser extent, the analytical estimates for K_m^L. However, we could deduce *a posteriori* that the axysimmetric meniscus geometries we tried to enforce by visual inspection at the beginning of each experiment were eventually not perfectly-cilindrical; we think this may be the main reason of the systematic analytical overestimations.

Furthermore, in both models we used the values of fluids' surface tensions γ

Exp	**Geometry**	**Fluid**	K $[N/m]$	**Error**
1	height: 1.138 mm	Oil 2	Ex: 0.2466	
	volume: 85.6 nL		SE: 0.2415	2,07 %
	diameter: 9.186 mm (RE: 2.28 %)		An: 0.2797	13.42 %
2	height: 1 mm	Oil 6	Ex: 0.2827	
	volume: 74.2 nL		SE: 0.294	3.99 %
	diameter: 9.63 mm (RE: 2.45 %)		An: 0.3152	11.48 %
3	height: 0.852 mm	Oil 6	Ex: 0.3392	
	volume: 57.1 nL		SE: 0.3456	1.89 %
	diameter: 9.41 mm (RE: 0.11 %)		An: 0.3698	9.01 %
4	h: 1 mm	Oil 2	Ex: 0.2407	
	V: 65.5 nL		SE: 0.2648	10.01 %
	D: 9.29 mm (RE: 1.21 %)		An: 0.3182	32.19 %
5	h: 0.906 mm	Oil 2	Ex: 0.2962	
	V: 54.2 nL		SE: 0.3285	10.90 %
	D: 9.15 mm (RE: 2.64 %)		An: 0.3510	18.50%
6	h: 0.720 mm	Oil 2	Ex: 0.3485	
	V: 47.3 nL		SE: 0.3989	14.46 %
	D: 9.44 mm (RE: 0.42 %)		An: 0.4417	26.75 %

Table 2.3: Lateral stiffness of fluid menisci. Relative error (RE) in pad diameter reconstruction by image post-processing reported in the second column. Relative errors of the SE and of Lambert's analytical (An) models with respect to the experimental (Ex) estimates shown in the last column.

given by the providers. It cannot be excluded that adsorbtion of contaminants from air during the experiments might have made the actual values different from the nominal ones (see Sec. 2.2). A change in γ would proportionally affect the restoring forces, thus the stiffnesses of the menisci.

In view of all these plausible sources of errors, we consider the matching between our models and experiments to be satisfying.

Hysteresis

Fig. 2.19 shows the results of one early experiment, where relatively-large top pad displacements were induced. A change in slope for large displacement is seen in the forward curve, which may be attributed to *saturation,* as expected from numerical simulations (see Sec. 2.5.1). Moreover, comparing the forward and the backward curves, a clearly hysteretic behaviour was seen. This was due to the overflow of the fluid beyond the edge of the bottom pad (Fig. 2.20a). This happened when the angle ζ comprised between the lateral surface of the meniscus on its advancing side and the surface of the bottom pad was larger than the value ζ_{max} set by the Gibbs' inequality (Eq. 2.10), *i.e.* $\theta^a + 180^o - \phi$, ϕ being the angle between the top and the side surface of the bottom pad (approximately equal to 90° in this case). The overflow changed the residual amount of fluid

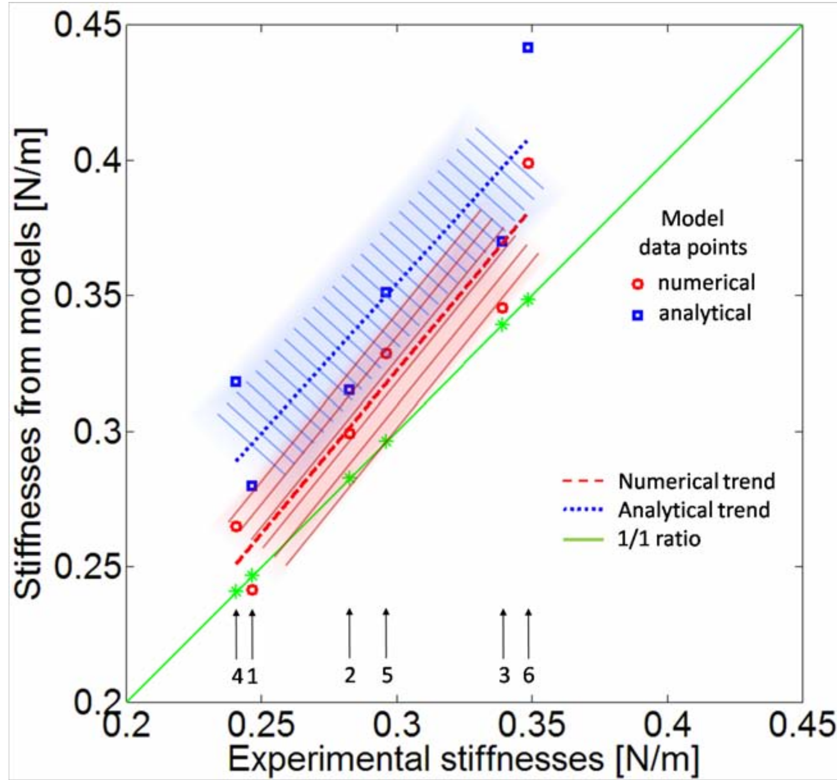

Figure 2.18: Comparison of lateral stiffness of 6 cylindrical menisci (labels refer to Table 2.3; K values ordered along x axis), as estimated from experimental measurements and from numerical and analytical models. The trend lines represent first-order least-mean-squares fits of model versus experimental data.

in the meniscus. The profile of the meniscus during the backward movement was thus different as compared to the forward movement; hence the difference in the resulting restoring force. Depending on θ^a and the actual height h of the meniscus, fluid overflow could be avoided by ensuring $u < u_{max} = h \cdot \tan(\theta^a)$ (Fig. 2.20b). For a typical case with $h = 1\,mm$ and $\theta^a = 20^o$, $u_{max} = 364\,\mu m$.

Incidentally, thanks to 1) the (inverted form of the) aforementioned geometrical relation (Eq. 2.10), and 2) the possibility to exactly track in real time the values of $\{u_i\}$, our setup *enables* the use of the Gibbs' inequality to experimentally determine the θ^a of liquids. The model (Fig. 2.20b) assumes a linear profile of the fluid meniscus, as obtained for small meniscus perturbations as shown earlier. Such method could be robust and reliable because based on the invervention of an isolated, sudden and dramatic event (the overflow), and avoiding the use of numerical image fitting; also, no thorough calibration of the sensing apparatus would be necessary for the application, apart from the synchronization of the laser and visual tracking system, and the measurement

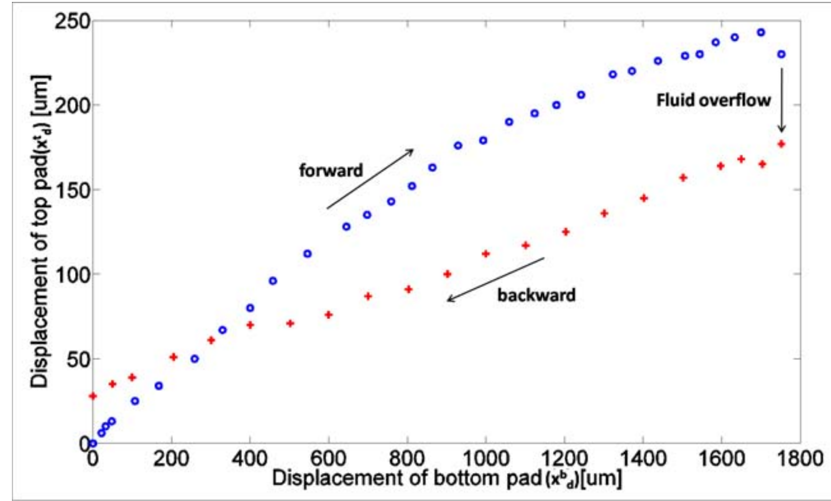

Figure 2.19: Experimental top pad-versus-bottom pad (*i.e.* x_d^s vs. x_d^b) displacement curve in presence of hysteresis induced by fluid overflow.

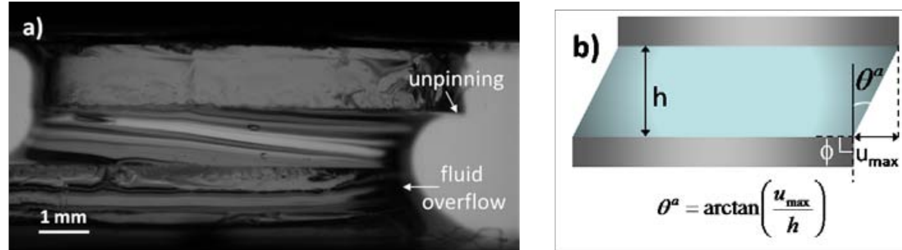

Figure 2.20: **a)** Liquid overflow and contact-line unpinning due to excessive relative pad displacement. **b)** Geometrical model to calculate θ^a.

could be automated. This novel method could be particularly useful for estimating and discriminating very-small θ^a's (because θ^a's are hereby "magnified" by the additional value of $180^o - \phi$), which, besides requiring as of now cumbersome interferometric techniques, is important to assess the state of high-energy surfaces and the wetting quality of detergents. An implementation would use non-circular pads with dimensions much larger than the fluid drops, to avoid stresses, and require ideal control of the solid edges of the confining surfaces.

Hysteretical results were also reported when applying small displacements when using water as fluid. The source of hysteresis was here the rapid evaporation of water - that evidently affected the meniscus - and/or the higher susceptibility of the water surface to adsoption of surfactants from air.

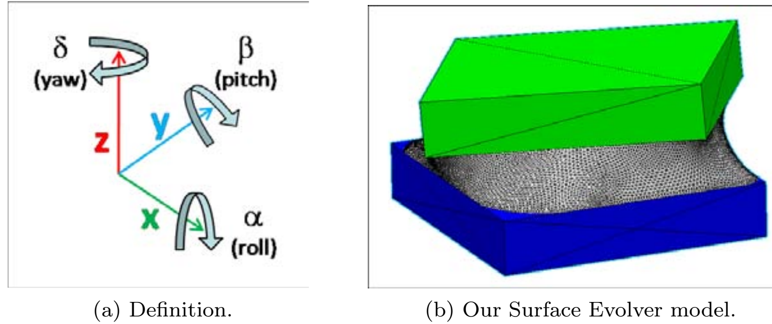

(a) Definition. (b) Our Surface Evolver model.

Figure 2.21: Degrees of freedom of the top pad.

2.5 Symmetry versus directionality

Less-symmetric shapes, as compared to the ∞-degenerate central symmetry of circles, introduce directionality in capillary self-alignment. Directionality, and more generally anisotropy, is needed to constrain the number of assembled positions of parts. This is necessary in packaging, because the electrical polarity of the vast majority of electr(on)ic devices prescribes a maximum number of equivalent poses limited to two (for symmetric two-ports devices, such as passive components) or one (for more general multi-port devices).

From a design perspectives, the actual part poses to be considered are only those coincident with the *global* energy minimum of the system[13]. Global minima are normally much more stable and robust against perturbations; they may still be degenerate. Poses corresponding to *local* energy minima may be multiple and difficult to control: besides being rather unstable, they introduce kinetic barriers which reduce the yield and throughput of the process.

The symmetry versus directionality trade-off has also important effects on assembly rates: the higher the symmetry (the lesser the directionality) of the sites/parts, the faster the assembly. This is probabilistically intuitive: higher symmetry means larger number of equivalent correct poses for parts, thus higher chances that the right part pose is sooner reached.

2.5.1 Performance of square parts

The thermodynamic point of view (see Sec. 1.2.3) is most suitable here.

The energy landscape associated with the fluid meniscus-mediated assembly of a single part on its binding site is calculated assigning to each relative part/site configuration (*i.e.* microstate) the corresponding value of total energy. This includes the gravitational potential energy of the fluid and of the top pad, and the free surface energy of all interfaces. Using the fluid's volume V, density ρ,

[13]Equivalently stated: the system needs to be designed so that the desired poses coincide with global energy minima.

interfacial tension γ and contact angle θ on the pad's surfaces as parameters, and using the position and orientation of the fixed bottom pad as spatial reference, the energy landscape Ψ is defined as a parametric map associating a scalar $E \subset \mathbb{R}$ to each vector $\overrightarrow{x} = (\text{x,y,z}, \alpha, \beta, \delta)$ defining the spatial configuration (*i.e.* the 6 roto-translational DOFs x_i ($i = 1...6$), defined in Fig. 2.21a) of the top relative to the bottom pad, *i.e.*:

$$\Psi(\overrightarrow{x})|_{V,\rho,\gamma,\theta} : \mathbb{R}^6 \to \mathbb{R} \tag{2.34}$$

The successive partial derivatives of this map physically describe (but for a multiplicative constant) the local forces/torques F_i (first derivatives) and elastic ("spring") constants K_i (second homogeneous derivatives)[14] acting on the system described by $\overrightarrow{\mathbf{x}}$ with all parameters fixed, *i.e.*:

$$F_i(\overrightarrow{x}) = -\left.\frac{\partial \Psi}{\partial x_i}\right|_{x_{j\neq i},V,\rho,\gamma,\theta} \tag{2.35}$$

$$K_i(\overrightarrow{\mathbf{x}}) = -\left.\frac{\partial F_i}{\partial x_i}\right|_{x_{j\neq i},V,\rho,\gamma,\theta} = \left.\frac{\partial^2 \Psi}{\partial x_i^2}\right|_{x_{j\neq i},V,\rho,\gamma,\theta} \tag{2.36}$$

Knowing the K_i and the total system mass M, the natural resonance frequencies f_i of the associated vibration modes could in principle be estimated as $f_i = \sqrt{K_i/M}/2\pi$.

Ψ can be calculated by Surface Evolver, as described here below. Only projections of the full map can be represented graphically[15]. Projections of Ψ can also be calculated by the Böhringer's model (see *e.g.* Fig. 2.22), bearing in mind its assumptions and domain of validity (Sec. 2.3).

We used SE to derive the energy landscape for the capillary self-alignment of a *square* thin silicon part (area of major sides: $1\times1\,mm^2$, thickness: $200\,\mu m$) on a superficial[16] binding site of identical shape, mediated by a hexadecane meniscus (density: $770\,kg/m^3$), all surrounded by water (HD/water interfacial energy: $53\,J/m^2$ [130]). As model geometry, the square is a good compromise between symmetry (as compared to circles; for the effect of square corners rounding-off, see Fig. 2.22), directionality (as compared to asymmetric polygons) and simplicity of implementation. This exercise was proposed by Greiner [240] and developed by Lieneman [227], Tay [241] and others.

Our SE model was adapted from Lieneman's [242]. It allows to encode all geometrical and physical parameters relevant to the system performance and mentioned in these Sections: masses, density, surface tension, contact angle, geometries, and full control over the 6 DOFs of the top pad. The lubricant wetting depended on the lubricant's surface tension and contact angle, and on boundary conditions.

[14] This estimate of K_i is implied in the method of virtual works [237]. Analytically, it holds only in the limit of small oscillations around a locally-stable equilibrium configuration of the system. Being quasi-static, this calculation may *understimate* the actual values of K_i.

[15] The force-versus-(relative) displacement curves presented earlier (Sec. 2.4.3) for the case of circular pads (cylindrical menisci) are in fact representations of F_i's.

[16] See Sec. 3.4.1 for the definition.

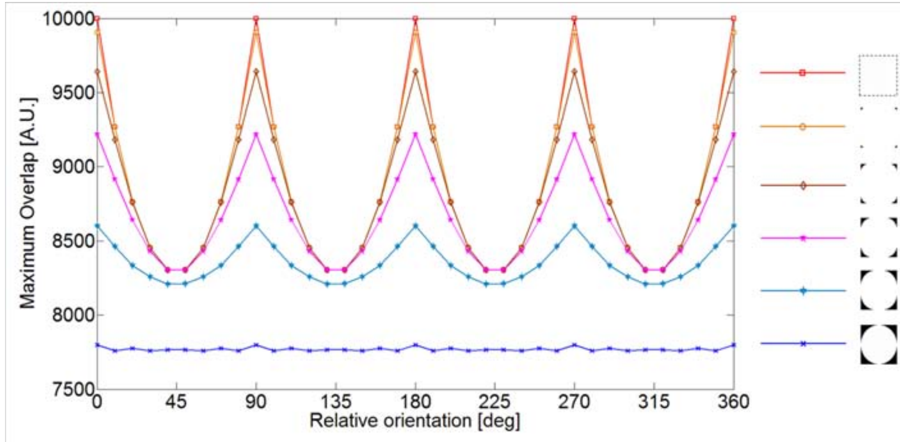

Figure 2.22: Symmetry versus directionality trade-off: the "circularization" of a square binding site. The plot (computed after the Böhringer's model [134]) represents the maximum value of the 2D auto-convolution of the polygons obtained by progressive round-off of the corners of the original square (shown in the legend) for each given relative orientation.

Our main results:

1. The part pose with global energy minimum is unique. It has the part floating parallel to the bottom pad, perfectly-concentric and edge-aligned with it, at an height that minimizes the total system energy. In this pose, both pads are fully-wet by the lubricant.

2. The behaviour of the system can be likened to that of an anisotropic fluid joint with tensorial spring constant.

3. The restoring forces acting on the part are proportional to the surface tension of the fluid meniscus and inversely proportional to the height/volume of the meniscus (being the meniscus confined, its height is proportional to its volume). Therefore, accurate choice of the interfacial energy and of the volume of the fluid is required to control the forces.

4. The restoring forces arising from displacements of the part along the vertical direction are about one order of magnitude larger than those consequent to in-plane displacements of comparable magnitude. This implies a separation of time scales: when a part is approaching its binding site, its vertical motion precedes its lateral motion[17].

5. The directionality of the lateral restoring forces is consistent with the design of the parts/sites: they are therefore anisotropic. In the case of

[17] According to this, in the simulations for every lateral displacement first the vertical equilibrium position was determined, then the restoring force was calculated.

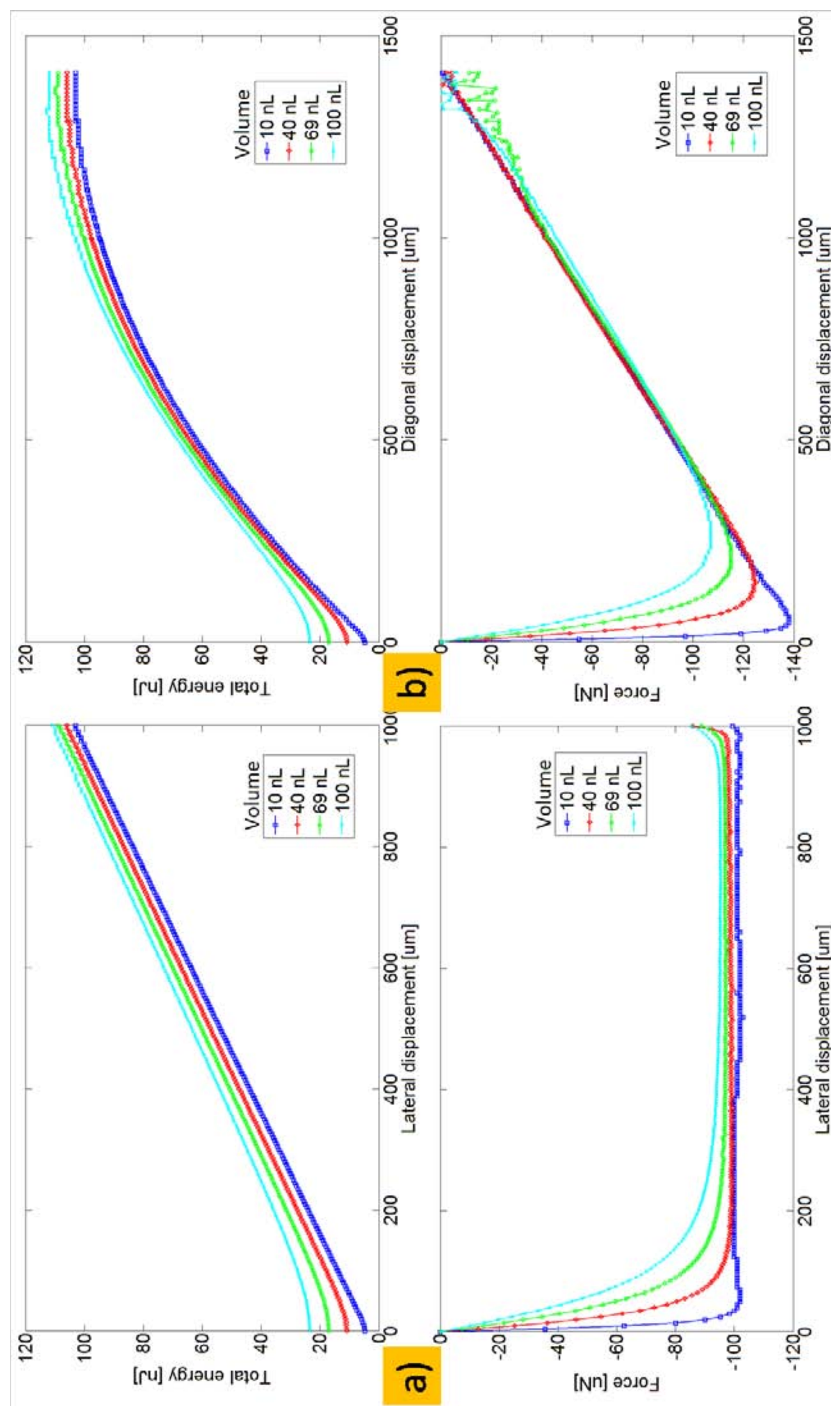

Figure 2.23: SE simulations for $1 \times 1\,mm^2$ part and binding site: total energy and restoring force vs. lateral (x or y) **(a)** and diagonal **(b)** displacements, and parameterized by the volume of the fluid meniscus. Positive displacements only are shown, for symmetry.

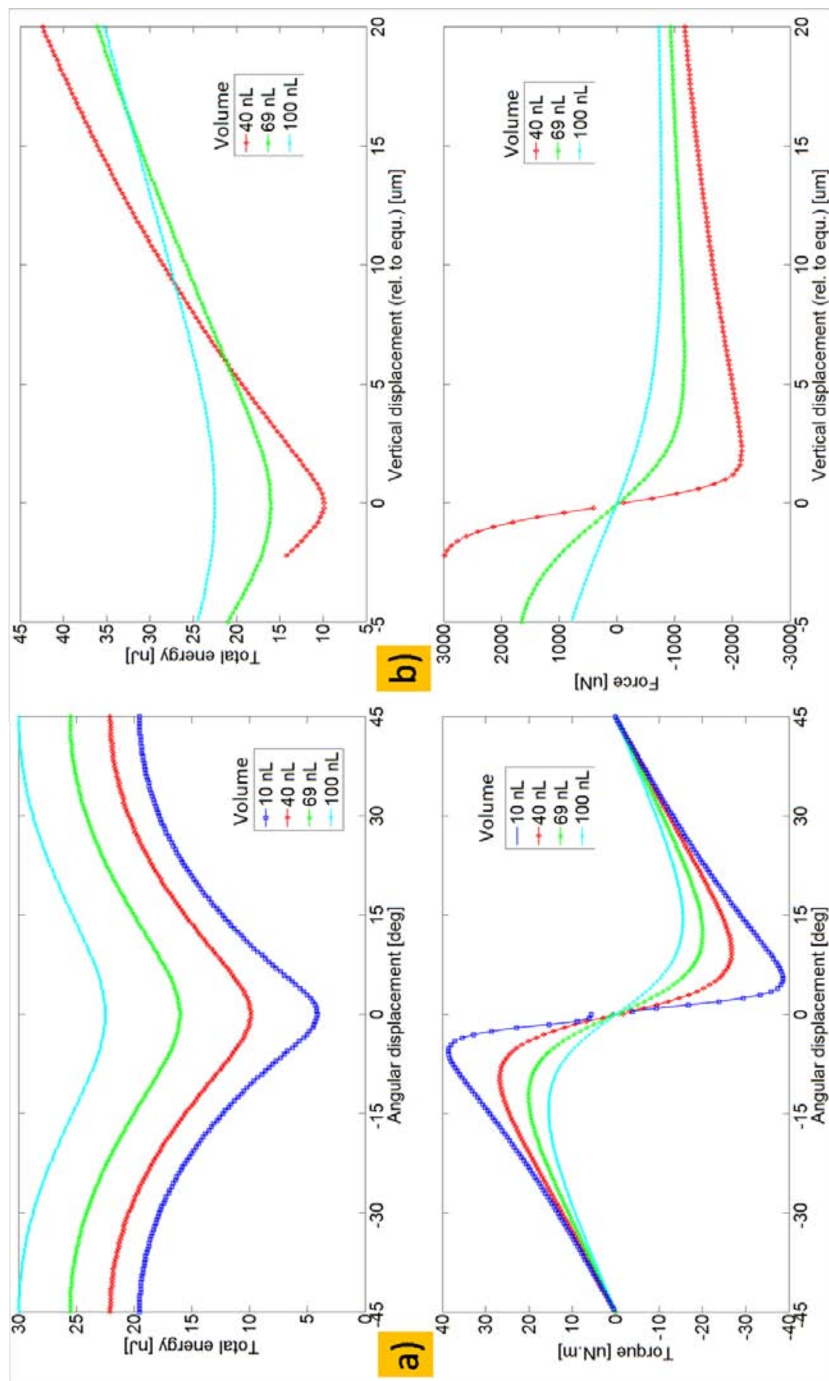

Figure 2.24: SE simulations for $1 \times 1\, mm^2$ part and binding site: total energy and restoring action vs. angular displacement α **(a)** and vs. vertical displacement around the equilibrium height of the meniscus **(b)**, and parameterized by the volume of the fluid meniscus.

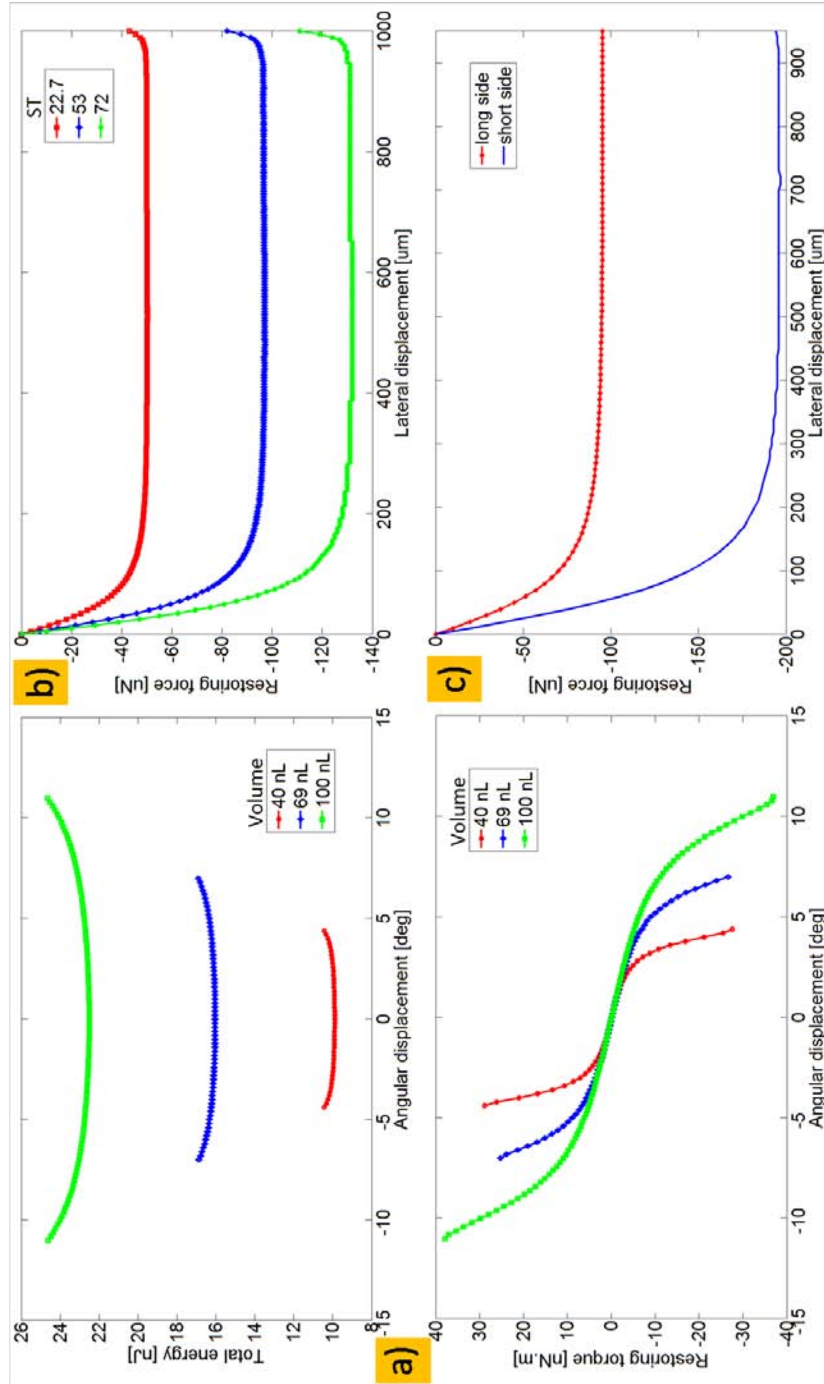

Figure 2.25: SE simulations. **a)** Total energy (top) and restoring torque (bottom) vs. angular displacement β or δ and parameterized by the volume of the fluid meniscus, and **b)** restoring force vs. lateral (x or y) displacement and parameterized by the interfacial energy for $1 \times 1\,mm^2$ part and binding site. **c)** Restoring force vs. lateral displacements of a $2 \times 1\,mm^2$ part and binding site.

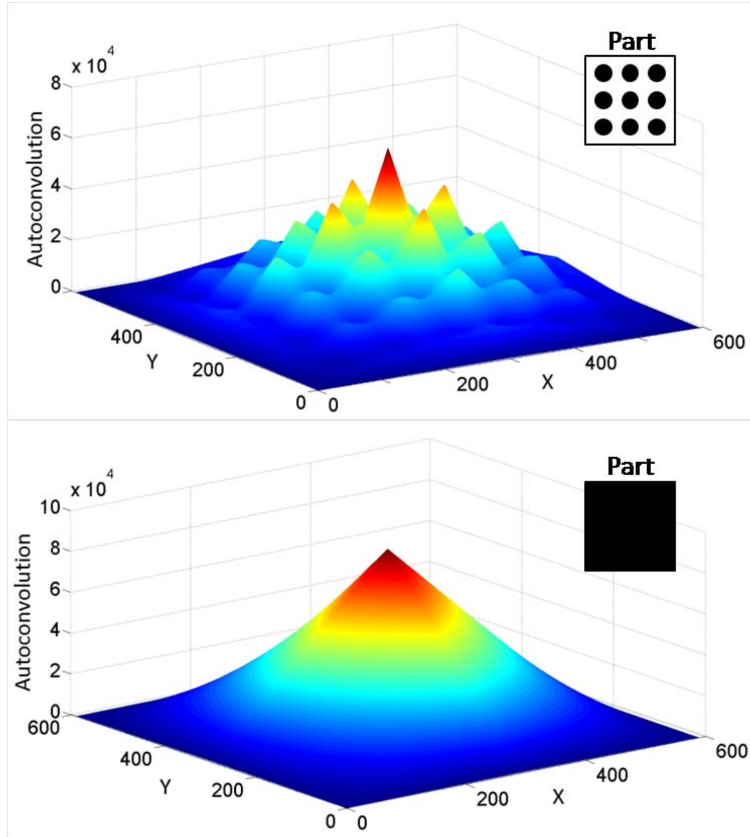

Figure 2.26: The energy landscapes associated with bumps- (top) and full site-based capillary self-alignment (bottom).

asymmetric part/binding site shapes, restoring forces are larger for lateral displacement along shorter sides.

Point 1) is interesting when comparing capillary part-to-substrate SA to standard flip-chip assembly in terms of placement accuracy and throughput. To see why, let's consider the same part as above, endowed with *e.g.* 9 equal bonding pads that match (in diameter and relative position within the site) the corresponding solder bumps on the binding site. When using the wetting of molten solder bumps on metal bonding pads as driving force for self-alignment, the part has to be brought in almost exact alignment with the site to start self-aligning: specifically, the part center has to lie within a circle centered on the site center and of radius equal to the diameter of the bumps. That is, the diameter of the *capture cross-section* (CCS) of the binding site is, in this case, equal to two times the diameter of the *bumps*. On the contrary, when using capillary SA with the full binding site coated with lubricant, capillary self-alignment may

start from any partial overlap of the part to the site: the CCS is, in this case, equal to two times the diameter of the *site*. Fig. 2.26 exemplifies this in the energy landscape perspective. Point 1) also enforces that, if local energy minima - due *e.g.* to friction [243, 31] or excess lubricant volume [244] - are avoided, the final placement of the part is correct, so that all bonding pads are also perfectly aligned with the corresponding bumps. Nevertheless, dedicating the entire site or part's functional side to capillary self-alignment may be expensive or not feaseble from the system floorplanning perspective; a compromise between the discussed extremes may be advantageous.

Thus, combining this *shielding effect* with fast and rough part placement provided by robotic pick&place, the accuracy-versus-throughput trade off typical of standard pick&place could be overcome to a significant extent.

2.5.2 Unique in-plane part placement

The issue of getting a unique in-plane pose for parts is a prerogative of the stochastic approach to SA, where (averaging over large ensembles) parts possibly impinge to substrate's binding sites from all possible directions and with all possible orientations and still need to reach the only admitted pose.

In capillary part-to-substrate SA[18], the Böhringer's group addressed this important problem mainly using the aforementioned model based on 2D convolutions (Sec. 2.3). They were able to define a general class of 2D patterns that theoretically possess a unique global energy minimum for all possible relative position of equal-shaped parts and sites [199]. There is no proof yet that this is the only possible class of patterns able to achieve this. We undertook extensive investigations on the issue, both theoretical and experimental, building from their results.

Theoretically[19], we investigated the orientering performance of many 2D shapes. We gathered empirical evidence regarding the following conjecture:

> *a) let $c \subset \mathbb{R}$;*
> *b) let $\Theta : \mathbb{R}^2 \to [c]$ have a convex, connected, compact support;*
> *c) let $\star$ be the two-dimensional convolution product of functions with support $\subset \mathbb{R}^2$;*
> *then:*
> *for every Θ, $\Theta \star \Theta : \mathbb{R}^2 \to \mathbb{R}$ has at least one local, isolated maximum apart from the global maximum.*

i.e., unless holes are properly inserted inside the two polygons acting as matching sites, every polygon lacking in-plane symmetry has at least two maxima in its 2D auto-convolution: one corresponds to the global, as-designed maximum, the other is an isolated local maximum, which appears typically for an almost-opposite relative orientation of the polygons (the relative position of their centroids may also differ in the two cases). See Fig. 2.27 for an example.

[18] Unique in-plane poses were also addressed in dry [191] and molten solder-driven [146] SA.
[19] We thank prof. Karl F. Böhringer for kindly providing his suite of Matlab functions.

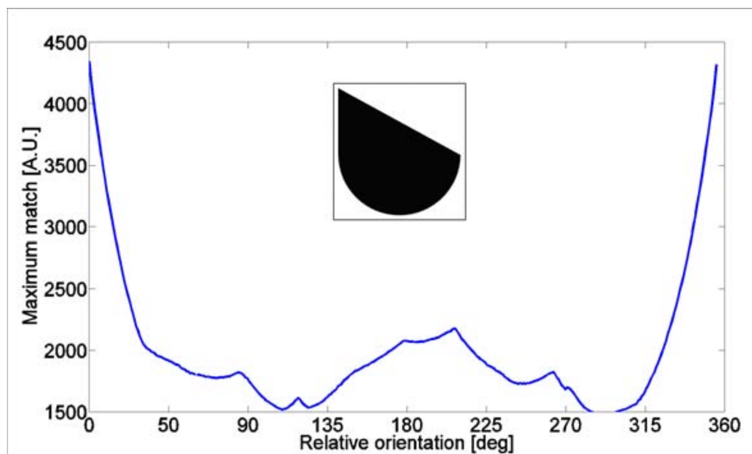

Figure 2.27: 2D auto-convolution performance of a convex, connected, "hole-less" and asymmetric pattern (shown in the inset). The best non-global match is obtained for a relative orientation of 209°.

Experimentally, we performed capillary self-assembly of thin parts using the concave ring-shaped pattern devised by the Böhringer's group - which can theoretically admit only a single global minimum in the entire energy landscape (Fig. 2.28) [229] - for both binding sites and functional side of the parts. The ring-shaped binding sites where lithographically patterned on glass substrates, to optically assess the alignment performance enabled by the pattern, and selectively dip-coated with HD to enable capillary SA[20] (Fig. 2.29). We were *not* able to achieve systematic unique in-plane part orientation. In spite of HD's high selectivity toward hydrophobic surfaces when in water, we observed that the devised pattern was not able to induce any torque on parts when these approached the desired pose from a very different and far spatial configuration - as in a fully-stochastic process. Instead, capillary part alignment happened as if driven by a featureless circular binding sites. We think this is due to bridging of HD menisci once in contact with the part's pattern, so that the features of the actual ring-shaped pattern are obscured and ineffective. As an indirect confirmation, we note that the original experimental demonstration of the pattern's performance [229] was performed using a part with a through-hole, and starting only from a slightly-misplaced pose with respect to the final pose. In our opinion, that's the only condition where the aligning property of the pattern can work - most unlikely the theoretical prediction[21].

We desume that, to our knowledge and experience, the quest for 2D patterns effectively inducing unique in-plane part pose is still without general solution.

[20] All mentioned experimental procedures are fully-detailed in later Chapters.

[21] Lin *et al.* confirmed our insight using an asymmetrically-holed tear-shaped pattern to drive capillary self-alignment of parts [245]. They showed that the restoring torques induced by the pattern act only in a limited angular range around the fully-aligned pose.

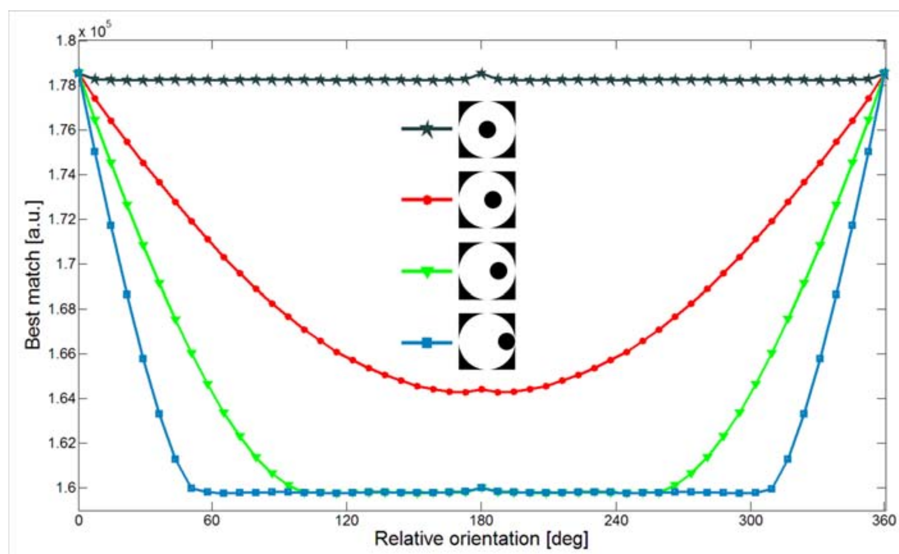

Figure 2.28: 2D auto-convolution performance of the asymmetrically-holed class of patterns devised by the Böhringer's group. The glitch around 180° is due to pattern discretization errors.

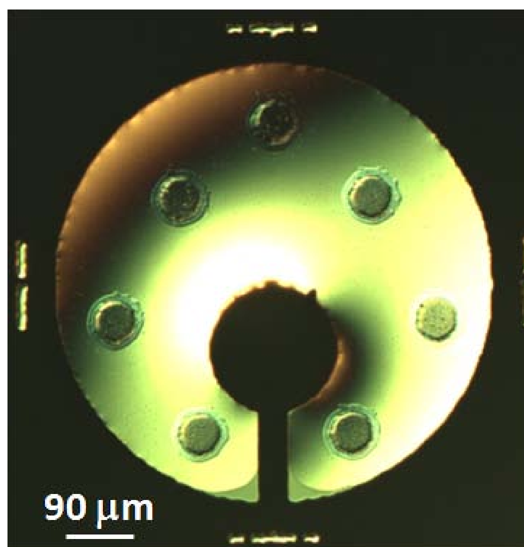

Figure 2.29: Asymetrically-holed DDT-functionalized Au binding site over glass (implementing the second, best-performing pattern in Fig. 2.28) selectively-coated with HD. The substrates are submerged in water. Colors and depth enhanced by differential interference contrast (DIC) optical microscopy.

2.6 Conclusions

This Chapter analyzed the concept, the physics and the performance of capillary part-to-substrate SA.

We presented a comprehensive *quasi-static* study on lateral capillary forces. We experimentally measured the restoring forces by means of a dedicated sensing apparatus. The predictions of a finite-element model and those of a recent analytical model [197] of cylindrical fluid menisci showed good agreement with the experimentally-measured values of meniscus stiffnesses - the more so when considering the sources of noise, error and hysteresis possibly affecting our sensing apparatus and/or intrinsic to such type of experiments.

Our experimental apparatus could constitute a *reference testbench* to further investigate lateral capillary forces, arising from fluid menisci of even arbitrary profiles and shapes. Scaling properties may be also investigated, using smaller menisci and connecting the pads to dedicated force sensors, as well as the self-alignment *dynamics* enabled by capillary forces - fundamental to many present-day technological applications and investigated in a complementary study [197].

The possibility of tracking in real time and with micrometric accuracy the relative displacements of top and bottom pads of our system let our apparatus enable the direct measurement of the *advancing contact angle* of liquids. This novel method exploits the sudden and dramatic liquid overflow over the edge of the confining bottom surface for lateral meniscus perturbations exceeding the limit set by the Gibbs' inequality. The validation of such *overflow* method, which may be particularly useful to assess the state of high-energy surfaces as an alternative to interferometric tools, is currently being pursued.

We then remarked the importance of *anisotropy* to SA. We numerically predicted the capillary self-alignment performance of a square thin part on an equal square binding site, and presented a negative general conjecture on the self-alignment performance of 2D patterns.

All these insights and numerical data will serve as reference for further experiments and theoretical developments, described in the next Chapters.

Chapter 3

Studies on Dip-Coating of Patterned Surfaces

Studies on selective fluid dip-coating of patterned planar surfaces - key to capillary part-to-substrate SA - are presented. An experimental study on the dip-coating of chemically- and topologically-patterned surfaces is first exposed. We demonstrate both experimentally and numerically that perfectly-conformal and robust fluid coverage of sites can be obtained using *recessed* sites of arbitrary shape. Then, the results of experimental studies on the control and repeatability of the volumes of lenses deposited by dip-coating on patterned surfaces are discussed. They support earlier, negative claims on the matter, but they may nonetheless be not definitive: we may have missed the proper region in parameter space where volume control of dip-coated lenses may be possible.

3.1 Conformality matters

The yield of capillary part-to-substrate SA depends on several geometrical and chemico-physical factors. Among these, the selective and conformal coating of the binding sites with the *lubricant* (defined Fig. 2.1) is preeminent.

The lubricant assolves multiple functions:

1. it enlarges the spatial range of the hydrophobic interaction (Sec. 2.2);

2. (as a consequence of 1) it improves the parts' ability to selectively recognize the binding sites available across the substrate, *i.e.* it signals the sites location and amplifies their reachability;

3. it provides, in combination with the hosting liquid, the interfacial energy that drives the self-alignment of the part;

4. it avoids the friction between the surfaces of the parts and the substrate, allowing the parts to efficiently reach their desired pose (Sec. 2.5);

5. it provides temporary mechanical binding to the parts during assembly;

6. it can enforce the permanent, mechanical (*e.g.* curable polymer) and/or electrical (*e.g.* solder) binding of the parts to the sites.

Given the geometrical congruence of the mating patterns, the precision of part-to-site registration depends, apart from the properties of the lubricant and accidental surface defects, on the conformality of the lubricant lenses to the geometrical pattern of the site. Therefore, the lubricant needs to replicate the exact profile of the site with high fidelity to convey the exact *information* required for the self-alignment. Sato confirmed experimentally that wetting defects and poor conformality of the lubricant coating to the site patterns translate into misalignment of parts [231]. The worst performance was achieved with shapes having sharp corners or convexities, like crosses, stars and, above all, triangles.

To address this issue, in the following Sections we demonstrate experimentally and numerically a new design enforcing *perfectly-conformal* selective dip-coating of binding sites. Though we applied our design only to fluids like water and alkanes, we assume it may work for molten solders as well, since clean metallic (oxidized) surfaces are selectively wet (not wet) by them.

3.2 Fluid deposition techniques

Jetting is one interesting option to deposit fluid drops on planar substrates [246]. The direct ejection of drops onto localized substrate spots, as done *e.g.* in inkjet printing [247], may provide better control of the volume of the drops, as compared to the alternatives presented below. We had no means to investigate these issues directly. Besides, jetting does not address by itself the coating conformality issue: the ideas presented below may benefit jetting, as well.

We focused on the simplest technique which can coat large arrays of patches on planar substrates at once: *dip-coating* (also knows as *withdrawal method*) [248]. Together with the *repelling* and the *dipping method*, dip-coating belongs to the family of *all-liquids* fluid coating techniques, which achieve selective fluid depositions on pre-conditioned substrates by involving no other means than the substrate and the fluids themselves [249]. Dip-coating consists in sliding the substrate at a controlled velocity across the interface between a wetting fluid and a non-wetting one. An extensive literature on the dip-coating of planar substrates is available (see next Section). Nonetheless, to our knowledge only limited work was dedicated so far to the investigation of conformal dip-coating of arrays of patches patterned on planar substrates.

3.3 Dip-coating of planar substrates: background

Landau and Levich [250] and Deryagin and Levi [251] first derived a closed-form expression for the maximum thickness h_∞ of a film of Newtonian liquid deposited on an infinite flat homogeneous surface vertically-withdrawn from a reservoir of the same liquid [248]:

$$h_\infty = c\frac{(\mu U)^{2/3}}{\gamma^{1/6}}(\rho g)^{1/2} = cL_c Ca^{2/3} \tag{3.1}$$

where g is the gravitational constant, the constant $c = 0.944$ for Newtonian liquids, μ, γ and ρ are the liquid viscosity, surface tension and density, respectively, U is the withdrawal speed of the surface, L_c the capillary length (Sec. 2.2) and the *capillary number* $Ca = \frac{\mu U}{\gamma}$. The result, valid only for $Ca \ll 1$, was later extended by other authors for larger capillary numbers and to include the effects of substrate inclination angle and mass loss during coating [248, 252].

Darhuber studied the dip-coating of vertically-oriented hydrophilic strips chemically-patterned onto planar surfaces [252]. In this case, beside the curvature of the vertical static meniscus, the pinning of the liquid at the edges of the strips induces a second curvature in the direction perpendicular to the first. The thickness of the entrained film followed the relation:

$$h_\infty = W \cdot Ca^{1/3} \tag{3.2}$$

where the control length scale is no longer the capillary length, as in Eq. 3.1, but the channel half-width W. This, together with the dependence on a lower exponent of Ca, allows for the deposition of thinner films, ceteribus paribus. The effects of withdrawal speed and angular orientation of the substrate and of additional geometrical features were also investigated [252].

Hartmann used the controlled withdrawal of hydrophobic flat transparent surfaces patterned with hexagonal arrays of circular hydrophilic patches to fabricate microlenses out of hydrophilic polymers on them [253]. Lenses with almost hemispherical profiles were obtained for patch dimensions smaller than the capillary length. Using the f-number ($f^\#$) of the lenses as a reference value for the deposited polymer volume - the lens volume being qualitatively inversely proportional to $f^\#$ - they experimentally found that, at low substrate withdrawal speed, the average $f^\#$ (volume) of formed lenses could be reduced (increased) by increasing the withdrawal speed or polymer viscosity or decreasing the polymer surface tension. They also reported large dispersions in the measured values of $f^\#$, *i.e.* large lens-to-lens variation in the value of the deposited lens volumes, even though the lenses were pinned to the edges of the circular patches. Such dispersion was explained with edge effects and dependency on withdrawal speed.

Jackman filled large arrays of microwells, fabricated into a chemically-uniform elastomeric substrate, with a variety of liquids by letting the liquids drain from the surface of the substrate that was pulled out of a liquid reservoir [254]. Such *discontinuous dewetting* exploits the difference in interfacial energy of the substrate and the liquid, and the liquid pinning at the edges of the wells. According

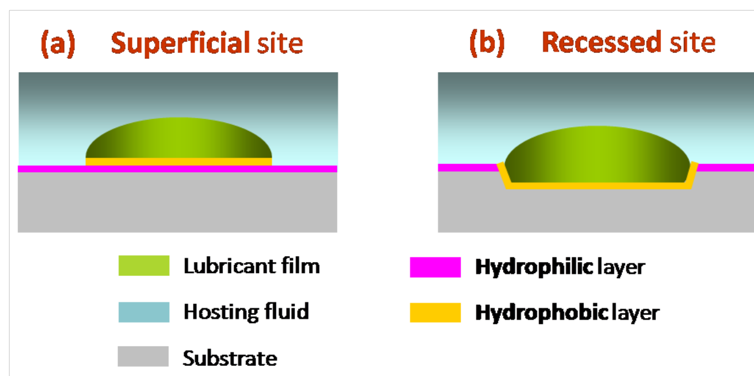

Figure 3.1: Schematic cross-section of superficial (a) and recessed (b) binding sites. Relative dimensions are out of scale.

to the authors, liquids with too small a contact angle would wet both wells and background, while liquids with too high a contact angle would not spread on the substrate at all.

Our approach, presented in the next Sections, in hindsight combines and generalizes Hartmann's and Jackman's.

3.4 Conformal dip-coating of binding sites

3.4.1 Superficial versus recessed binding sites

A chemical heterogeneity of the surface of a planar substrate can be exploited to direct the selective coating of the surface with two immiscible fluids. For this purpose, the surface needs to be conditioned with adjacent regions of contrasting wetting properties, such as hydrophobic and hydrophilic or metallic and non-metallic ones (for molten solders). When the fluids get in contact with the surface, they segregate forming structures that reflect the wettability and the geometrical patterns of the regions [255].

In dip-coating, the immiscible fluids are sequentially brought into contact with the pre-conditioned surface by sliding the entire substrate through their interface. In our set-up (Sec. 3.4.2), a hydrocarbon floated on top of water in a container. The substrate to be coated was slid vertically through the hydrocarbon/water interface, and allowed to rest in water. As a result, the hydrocarbon was repelled by water from the hydrophilic regions and formed lenses on the hydrophobic regions [255].

The equilibrium shape of a fluid lens[1] chemically- and geometrically-confined inside a planar *superficial* site (Fig. 3.1a) is affected by the lens volume, the fluid surface tension, its chemical affinity to the surface underneath, and by the

[1] Equilibrium, not to be confused with lens stability, is reached when all transient phaenomena are extinct.

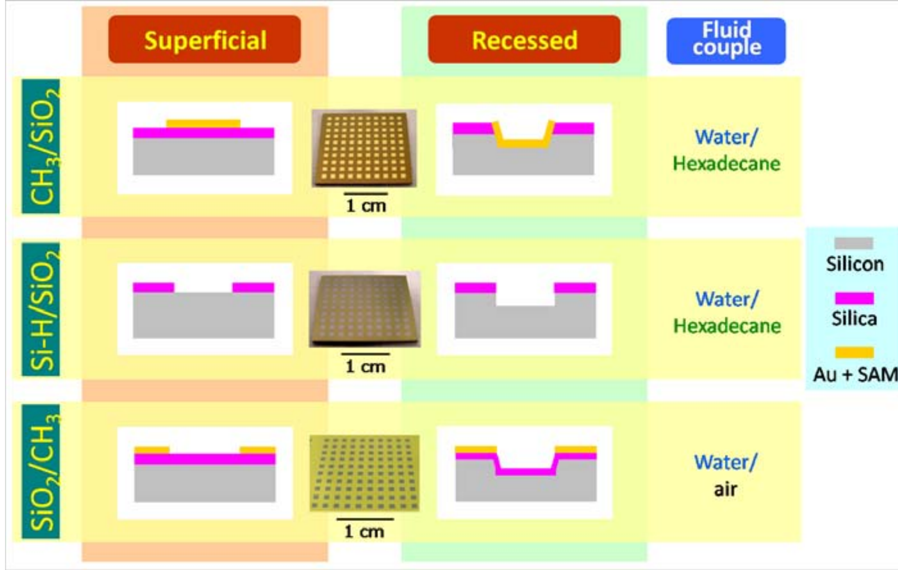

Figure 3.2: The six types of square sites used in the experiments. Relative dimensions of the layers in the sketches are out of scale for illustration purposes.

shape of the confining patch [256]. For polygonal shapes, incomplete wetting of sharp angles was reported [130]. Such partial coverage may be reduced by decreasing the interfacial tension γ_{LF} between the lubricant L and the hosting fluid F. This would increase the wetting capability of the lubricant, as measured by the spreading coefficient $S = \gamma_{SF} - \gamma_{SL} - \gamma_{LF}$ (Sec. 2.2). However, this would at the same time decrease the magnitude of the capillary forces, which are proportional to γ_{LF} (Sec. 2.5.1). This would make the part assembly more susceptible to perturbations and misalignments.

To achieve a perfectly-conformal lubricant coating of sites of arbitrary geometries while preserving the lubricant properties, we acted on the site geometry. We introduced a relatively-thin *wetting sidewall* around the entire perimeter of the binding site. The pattern of the site was otherwise not modified; *i.e.* the site was *recessed* into a shallow cavity (Fig. 3.1b). The additional contour was chemically-homogeneous to the rest of the recessed site. It pulled the lubricant toward the edges of the site, thereby enforcing the pinning of its triple-contact line and thus the complete, conformal coverage of the entire site.

3.4.2 Substrate conditioning

Sample preparation

To demonstrate the effect of the wetting sidewall on conformal site coverage, we first focused on square binding sites, with side length L of 1 mm.

We fabricated both superficial and recessed binding sites using three combinations of surface chemistries, for a total of six types of sites (Fig. 3.2). In all cases, we started with (100) silicon substrates with a 250 nm-thick thermal silica layer as top surface. We patterned 10 x 10 arrays of sites and we diced the substrates into 2.2 x 2.2 cm^2 chips for dip-coating experiments. The first class of patterns (referred to as CH_3/SiO_2) had hydrophobic binding sites made of methyl groups separated by hydrophilic silica spacer areas. The second class of patterns ($Si - H/SiO_2$) had hydrophobic binding sites made of hydrogen-terminated silicon separated by hydrophilic silica spacer areas. The third class of patterns (SiO_2/CH_3) had hydrophilic binding sites made of silica separated by hydrophobic, methyl-terminated spacer areas.

To realize superficial sites of the first class, a Ti/Au metal layer (50/100 nm-thick, respectively) was evaporated over the silica surface and lithographically-patterned into squares. For the recessed sites of the same class, 2.5 μm-deep cavities were etched into the silicon substrate by SF_6/Ar-based reactive ion etching (RIE). The Ti/Au metal layer was then evaporated and patterned by resist lift-off. The superficial site had the metal layer on top of the silica surface, devoid of any peripheral wetting layer; in the recessed type, the metal layer was located below the silica surface. After dicing, the chips were thoroughly rinsed with acetone, iso-propyl alcohol (IPA) and de-ionized (DI) water, soaked in 30% hydrogen peroxide for 15 minutes, dried under a nitrogen flow and finally stored overnight in a 1 mM solution of dodecanethiol (DDT, $CH_3(CH_2)_{11}SH$) in pure ethanol. As a result of this last step, self-assembled monolayers (SAMs) [257] selectively adsorbed to the Au-sites with their thiol headgroups, while exposing their methyl endgroups at the surface[2]. Just before dip-coating, the chips were extracted from the SAM solution, rinsed with ethanol to remove excess unbound organic molecules, and dried with nitrogen.

Superficial sites of the second class were realized by etching away the silica layer in diluted hydrofluoric acid (HF), exposing the underlying silicon substrate in square regions. Recessed sites of the same class were obtained simply by adding, after SiO_2 etch, the same 2.5 μm-deep RIE step as above to create shallow cavities inside silicon. In this class, both types of sites lied below the silica surface. They both had peripheral walls. However, in the superficial type the walls were not chemically-homogeneous with the rest of the site, being entirely made of silica, while in the recessed type their largest part was constituted of silicon. Immediately before dip-coating, the chips were immersed in ammonium fluoride for 5 seconds, then rinsed with DI water and dried with nitrogen. This was done to passivate the bare silicon surface of the sites with hydrogen, thus making it hydrophobic [259], while preserving the hydrophilic silica spacer.

To fabricate superficial sites of the third class, the Ti/Au metal layer was evaporated on the silica surface and patterned lithographically to expose the layer of silica in square areas. For the recessed sites, the patterned metal layer was used as hard mask during a subsequent SiO_2 etch in diluted HF and an

[2]Alternatively, plasma treatment of polymeric films can also be used for the chemical conditioning of substrates. Other conditioning procedures were investigated by Scott [258].

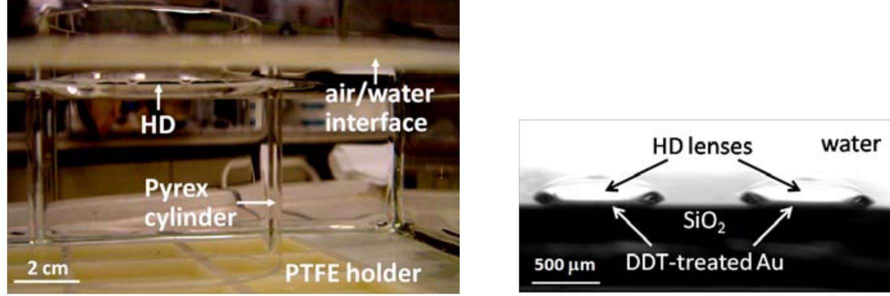

(a) A pyrex cylinder, standing on a PTFE holder, confines the HD lens which floats on water.

(b) Side-view of HD lenses selectively dip-coated onto hydrophobic binding sites.

Figure 3.3: Selective HD lens dip-coating in water.

anisotropic silicon etch in potassium hydroxide to create 5 μm-deep sloped cavities. The bare silicon surface was in this case not passivated to keep it rather hydrophilic. DDT SAMs were then assembled on the exposed Au surfaces, as described above, to make the spacer areas hydrophobic. Also in this class both types of sites lied below the top surface level, but only in the recessed type the sidewall and the bottom of the cavities were chemically-uniform.

Water contact angles (CAs) were measured on test substrates to assess the conditions of the surfaces after complete chemical treatment and before dip-coating. The CAs were measured with a OCA-20 contact angle meter (DataPhysics Instruments GmbH) with SCA20 software, using 1 μl water drops.

Dip-coating procedure

All dip-coating experiments were performed at room temperature. For the first and second classes of sites we chose water and hexadecane (HD) as lubricant and hosting liquid, respectively ($\gamma_{HD/H_2O} \cong 53\,mJ/m^2$)[3] [130]. Since $L_c^{HD/H_2O} = \sqrt{\frac{\gamma_{HD/H_2O}}{g\Delta\rho}} = 4.88\,mm > L$ and the Bond number $Bo^{HD/H_2O} = \frac{g\Delta\rho L^2}{\gamma_{HD/H_2O}} = 0.04 \ll 1$, with $\Delta\rho \equiv \rho_{H_2O} - \rho_{HD}$, gravitational effects were negligible compared to surface tension effects on the formation of fluid lenses (Sec. 2.2).

A dip-coating procedure analogous to that presented in [255] was adopted. The experimental set-up is shown in Fig. 3.3. A PTFE holder, featuring square, shallow compartments roughly of the size of the chips, was placed at the base of a DI water-filled beaker, and a Pyrex tube was inserted right above the

[3] We experimented dip-coating on these classes of sites using also other lubricants (*e.g.* iso-octane, hexane) and hosting liquids (*e.g.* ethylene glycol, glycerol). The dip-coating yield was always inferior to the HD/water case. Glycerol and ethylene glycol had to be diluted with water in order to enable the desired dip-coating performance. We think there may be limits in the lubricant-to-hosting fluid density and/or viscosity ratio within which selective dip-coating on patterned surfaces is reliable and has satisfying yield. The full investigation of this aspect is left for future work.

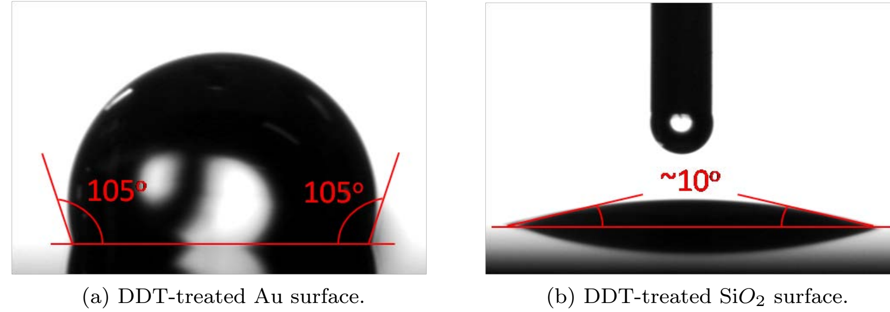

(a) DDT-treated Au surface. (b) DDT-treated SiO_2 surface.

Figure 3.4: Water CAs on DDT-treated surfaces.

holder to confine a 1 mm-thick HD film floating on the water surface. After complete preparation, the samples were individually vertically lowered inside the tube across the HD/water interface, with the rows of sites parallel to the liquid interfaces, and then left lying in the holder compartments in water. The lowering speed of the substrate was approximately 1 mm/s; the corresponding capillary number was $Ca = \frac{\mu U}{\gamma_{HD/H_2O}} = 5.7 \cdot 10^{-5}$, μ being the HD viscosity and U the dip-coating speed. After the experiments, optical photographs of the chips, resting in water on the holder, were taken to inspect the results.

For the third class of sites, water and air were chosen as the immiscible fluid couple to prove that the results were independent of the specific fluid couple used. In this case, $\gamma_{H_2O} = 72.8\, mJ/m^2$, $L_c^{H_2O} = 2.72$ mm, and $Bo^{H_2O} = 0.13$. The chips were immersed in a DI water-filled beaker and vertically withdrawn from it keeping the rows of binding sites parallel to the water/air interface, at a speed of about 1 mm/s ($Ca = 1.37 \cdot 10^{-5}$). Since the laboratory atmosphere was not saturated with water vapour, in less than a minute after extraction from the beaker evaporation severely perturbed the shape of the water lenses till their complete disappearance. Optical pictures of the lenses were captured well before this happened.

3.4.3 Experimental results

Wetting contrast

The average CAs of water (see Fig. 3.4) measured on clean thermal silica and silicon surfaces were inferior to 10°, which is the lowest CA value measurable by our instrument. On the contrary, CAs on DDT-functionalized Au surfaces and on hydrogen-terminated Si surfaces were close to 110° and above 70°, respectively.

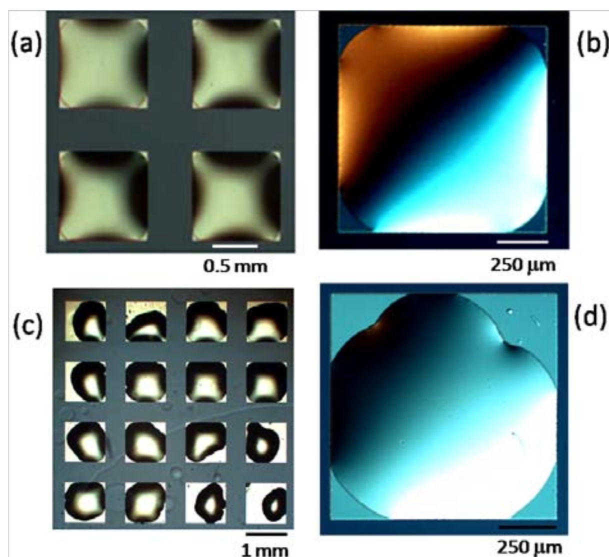

Figure 3.5: HD dip-coating of superficial square CH_3/SiO_2 sites. **(a)** and **(b)** Typical results. **(c)** and **(d)** Unpinned contact lines perturbed by local surface defects. The substrates are submerged in water. Colors and depth enhanced by differential interference contrast (DIC) optical microscopy.

CH_3/SiO_2 sites

Dip-coated HD lenses followed the in-plane rotational symmetry of the sites, but never conformally covered them. The HD lenses, though constrained by the side edges of the sites, never completely reached into the corners (Fig. 3.5a and b). The absence of triple contact-line pinning made the position of the line susceptible to local surface defects (*e.g.* scratches, local impurities residual from surface conditioning or fluid coating, resist residues, incomplete SAM formation on Au surfaces or SAM degradation due to prolonged exposure to corrosive agents) and to variations in the local dynamics of the coating process: it was therefore unpredictable (Fig. 3.5c and d). This implied a site-to-site difference in relative surface coverage and in the volume of the lubricant lenses, even for sites in close proximity. Hence the process repeatability was negatively affected. These results were consistent with previous reports [131].

Evident benefits came from adding a hydrophobic sidewall to the site sides. Dip-coated recessed CH_3/SiO_2 square sites routinely showed complete HD adhesion to the entire perimeter of the sites, including all corners (Fig. 3.6a and b). More than 98 % of the processed sites were correctly covered. We observed a superior robustness against aforementioned surface defects (Fig. 3.6c and d). Marginal dewetting was rarely seen in random locations, always close to the site edges, hinting at local pinning of the HD lenses due to imperfections in the lift-off process as possible cause.

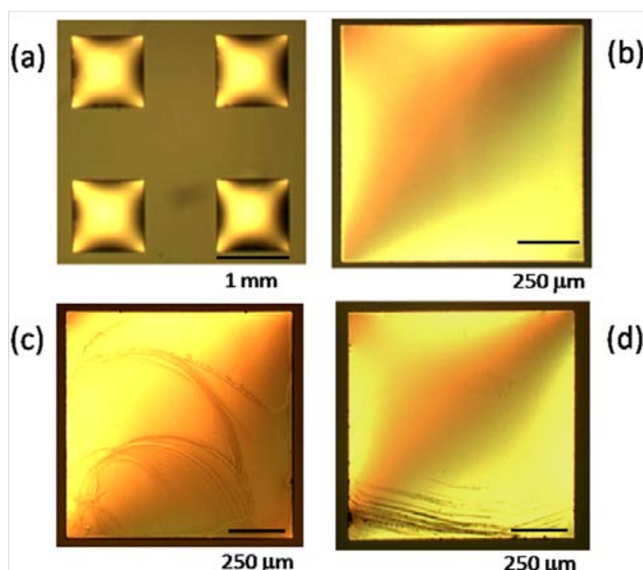

Figure 3.6: HD dip-coating of recessed square CH_3/SiO_2 sites. **(a)** and **(b)** Typical result. **(c)** and **(d)** Robustness against surface defects. The substrates are submerged in water. Colors and depth enhanced by DIC optical microscopy.

Si-H/SiO_2 sites

Almost all dip-coated sites had *no* lubricant coverage at all. The few coated lenses were always metastable and quickly experienced capillary lens break-up after HD deposition. A partial explanation for the lack of coating may involve the hydrophilicity of the entirety of the SiO_2 sidewalls which, being wet by water, repelled HD and thus prevented the pinning of the lenses.

Conversely, recessed Si-H/SiO_2 sites typically revealed perfect fluid film conformality (Fig. 3.7a and b). The coverage yield was however lower than for the first recessed class, due to a higher incidence of local surface imperfections - possibly incomplete Si passivation. Sites with only partial coverage resulted, as well, where significant de-wet site areas were seen, together with asymmetric HD drops (Fig. 3.7d). These drops were always clamped to a fraction of one or more edges of the cavities, probably resulting from capillary break-up of former full site-covering lenses.

SiO_2/CH_3 sites

The results for the third class of samples replicated the same trend of those for the first class. Non-conformal coverage was detected in most cases for superficial sites (Fig. 3.8a). This observation was interesting, because the topology of the sites was in this case similar to that of the wells conformally-filled by

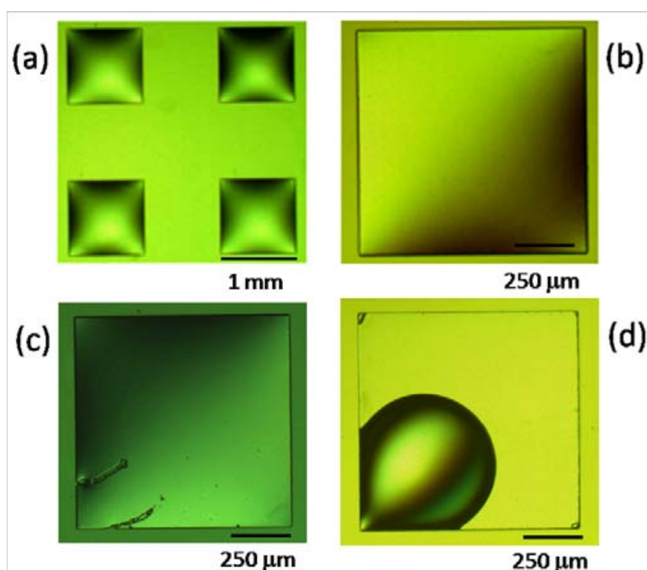

Figure 3.7: HD dip-coating of recessed Si-H/SiO_2 square sites. **(a)** and **(b)** Typical results. **(c)** Robustness against surface defects. **(d)** Residual lens pinned along site edges. The substrates are submerged in water. Colors and depth enhanced by DIC optical microscopy.

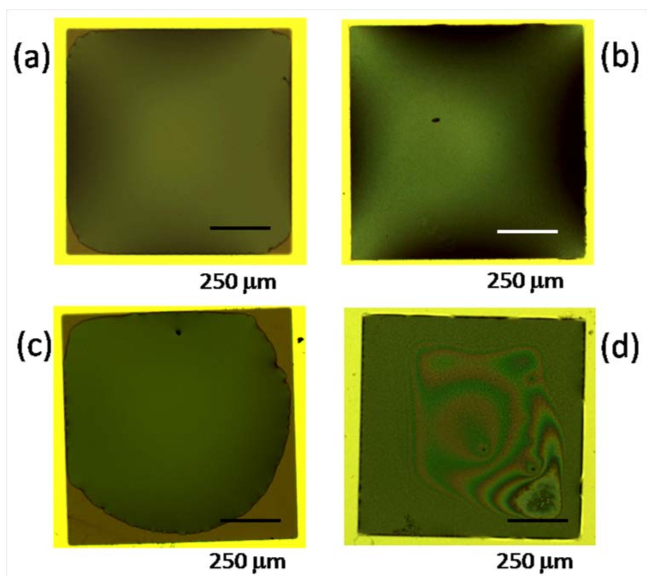

Figure 3.8: Water dip-coating of SiO_2/CH_3 square sites. Typical result and lens evaporation modality for superficial (**(a)** and **(c)**) and recessed sites (**(b)** and **(d)**), respectively. Colors and depth enhanced by DIC optical microscopy.

discontinuous dewetting in [254] except for the absence of a wetting sidewall around the site. As expected, dip-coating of recessed SiO_2/CH_3 sites produced perfectly-conformal fluid coverage (Fig. 3.8b).

Interestingly, the two site topologies resulted in different water evaporation patterns. For superficial sites, evaporation produced lens shrinking which started from the lens edges (Fig. 3.8c), resembling a constant contact angle drop evaporation modality [260]. On the contrary, in recessed sites lens break-up caused by evaporation started from the centre and moved toward the site edges (Fig. 3.8d), confirming the strong fluid pinning at the site sidewalls.

Triangular sites

We wanted to ascertain whether with our method even polygonal sites with extremely acute angles and very anisotropic shapes could be conformally covered with lubricant, and whether the performance was scale-independent.

For this purpose, we designed 6 sets of 24 isosceles triangular sites of the first class. The triangles were designed with angles ranging from 2.5^o to 175°, and all the triangles of the same set had the same area A of 1, 0.81, 0.64, 0.49, 0.36 and 0.25 mm^2, respectively. It was not possible to sample the whole space of possible site pattern, still we thought this set was significantly representative.

As expected, the coverage of superficial triangular sites was largely non-conformal (Fig. 3.9a) The site corners were de-wet by the lubricant. On the contrary, all sets of sites of the recessed types were perfectly coated (Fig. 3.9b). Sidewall pinning enforced conformal coverage inside every angle. This clearly confirmed that, in absence of a well-defined wetting boundary along the site perimeter, the full site-covering state of the lenses has higher energy than the energy-minimizing state, *i.e.* the natural tendency of the lenses to assume their energy-minimizing configuration (at fixed volume) is in general not compatible with full-site coverage.

Given the wide range of site shapes that we tested, we assume that our method can possibly work for sites of *arbitrary* shapes. The ensuing high-fidelity coating can *effectively* enable peculiar geometric features improve alignment or induce desired part poses (as discussed in Sec. 2.5).

3.4.4 Numerical simulations

Focusing on the equilibrium shape - which constitutes a surface of constant mean curvature, as deriving from the Young-Laplace equation (Sec. 2.2) [212] - of lubricant lenses deposited over binding sites, we opted for a quasi-static simulative approach using Surface Evolver (SE) to support our experimental results. This way we excluded any consideration of dynamical (*e.g.* viscosity, coating speed, pinch-off) and inertial effects in the coating process. We were aware that this made the simulations not entirely realistic, since said effects *do* play an important role in the dip-coating performance. However, our approach mainly aimed at expliciting the energetic underpinnings of the influence of the

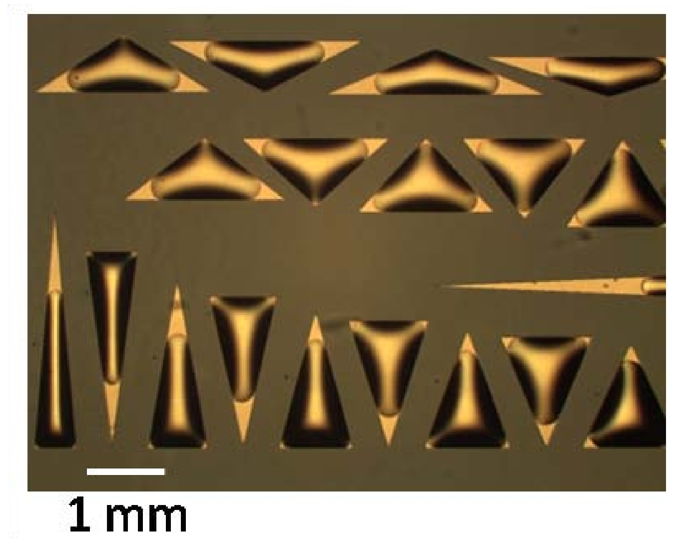

(a) Superficial sites ($A = 0.81\,mm^2$).

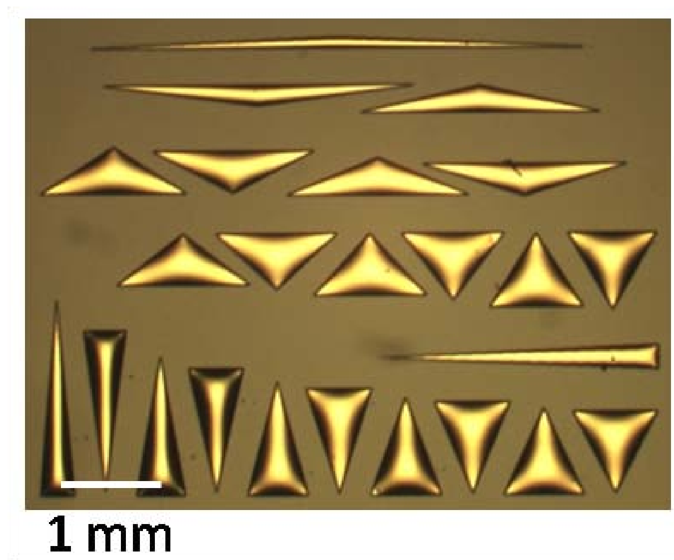

(b) Recessed sites ($A = 0.36\,mm^2$).

Figure 3.9: Dip-coated HD lenses on triangular CH_3/SiO_2 sites. Substrates submerged in water. Colors and depth enhanced by DIC optical microscopy.

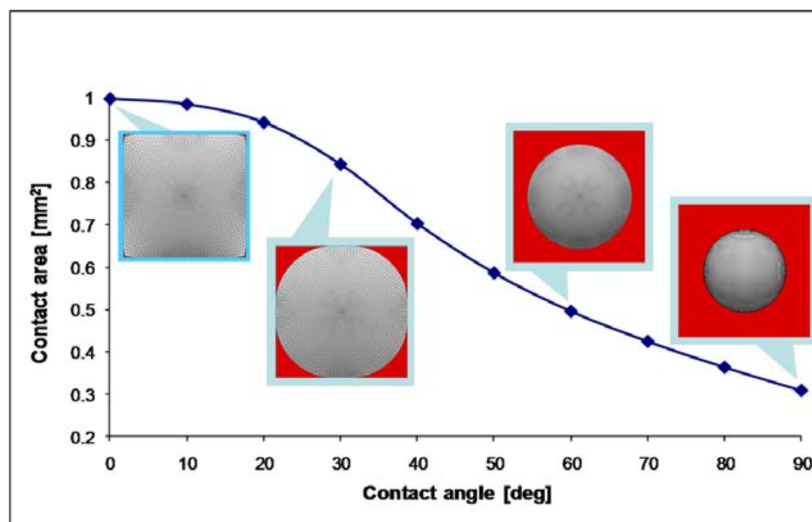

Figure 3.10: Finite-element simulations of the contact area of lubricant lenses as function of lubricant/site CA on a $1 \times 1\ mm^2$ superficial square CH_3/SiO_2 site for fixed lubricant volume (65 nL). Insets illustrate top views of some cases.

wetting sidewall and of other material parameters on the coverage results - an aim for which SE was specifically suited.

Quasi-static spreading of HD lenses on CH_3/SiO_2 types of square 1 x 1 mm^2 sites in water were simulated. Simulations took account of the total (gravitational and interfacial) energy of the system (*i.e.* lens and binding site). In the simulations of superficial sites, completely non-wetting boundary conditions at the edges of the binding site were introduced. This was consistent with experiments, as the CA of HD on silica in water is 180°. For recessed sites, triple-contact line pinning at the site sidewalls was included after contact between the lens and the sidewalls. Data for interfacial energies and fluid densities, earlier mentioned, were taken from literature [130].

Site surface coverage

First the impact of 1) lubricant wetting and 2) lubricant volume on the lens coverage over the superficial site type was studied.

For the first case, the simulations confirmed that, by decreasing (increasing) the CA (the wetting) of the lubricant, the lens contact area increased until the asymptotic coverage of the entire site was achieved, which happened in the limit case of null contact angle (complete wetting) (Fig. 3.10).

For the second case, full site coverage was asymptotically obtained in the limit of large lubricant volumes, at constant lubricant CA (Fig. 3.11).

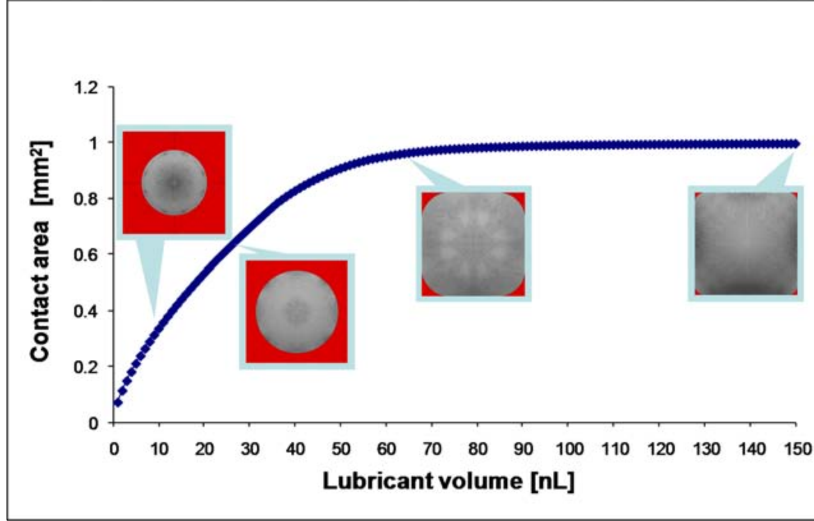

Figure 3.11: Finite-element simulations of the contact area of lubricant lenses as function of lubricant volume on a 1×1 mm^2 square superficial CH_3/SiO_2 site for fixed $\theta = 22^o$. Insets illustrate top views of some cases.

Energy-minimizing lubricant volumes

To investigate the quasi-static equilibrium shape of HD lenses, the total energy of the system (as defined in Sec. 2.5.1) in its minimal energy state was calculated as function of the volume of the lubricant lenses[4].

As a reference, the lubricant coverage behaviour on a 1 mm^2 circular superficial binding site was initially studied. The simulated energy function is depicted in Fig. 3.12. As the lubricant volume was increased, the system energy decreased because the highly-energetic SAM/water interface was progressively substituted by the less energetic SAM/lubricant one, while the increasing gravitational contribution from the lubricant was negligible and that of the lubricant/water interface was nearly constant. The curve had a definite minimum which coincides with the value of lubricant volume (53 nL) for which complete site coverage was first achieved. After that, the system energy increased indefinitely because of the expansion of the lubricant/water interface while the SAM/lubricant interface was fixed. The cusp around the energy minimum is the signature of complete lubricant pinning at the site edge.

In comparison, the function simulated for the square superficial site (Fig. 3.13), while having an analogous overall trend, showed a less definite and broader energy minimum. We suppose this is due to the absence of lubricant pinning in the corners of the sites: in absence of a wetting contour, lubricant spreading inside straight angle edges of planar sites is energetically not favourable.

[4]An idea first introduced, for superficial sites only, by Srinivasan [130].

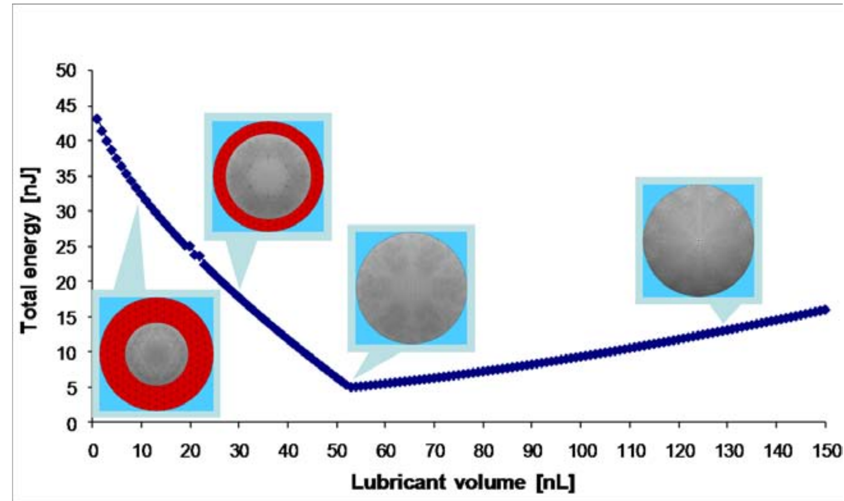

Figure 3.12: Finite-element simulations of total system energy as function of lubricant volume for a 1 mm^2 circular superficial CH_3/SiO_2 site for fixed $\theta = 22^o$. Insets illustrate top views of some cases.

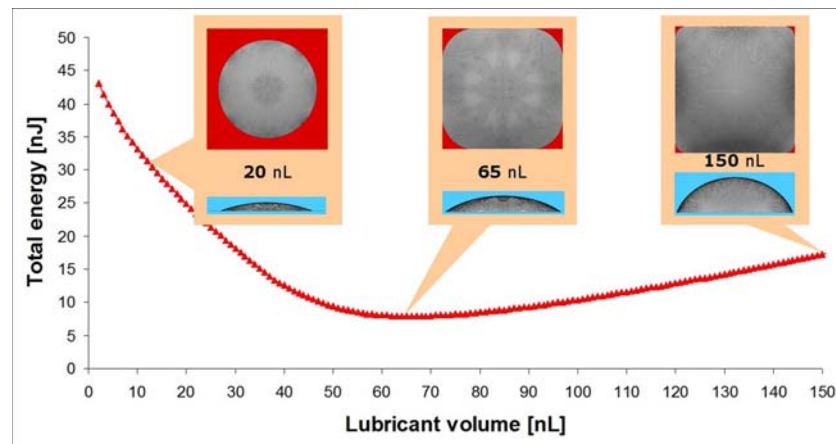

Figure 3.13: Finite-element simulations of total system energy as function of lubricant volume for a 1×1 mm^2 square superficial CH_3/SiO_2 site for fixed $\theta = 22^o$. Insets illustrate top views of some cases.

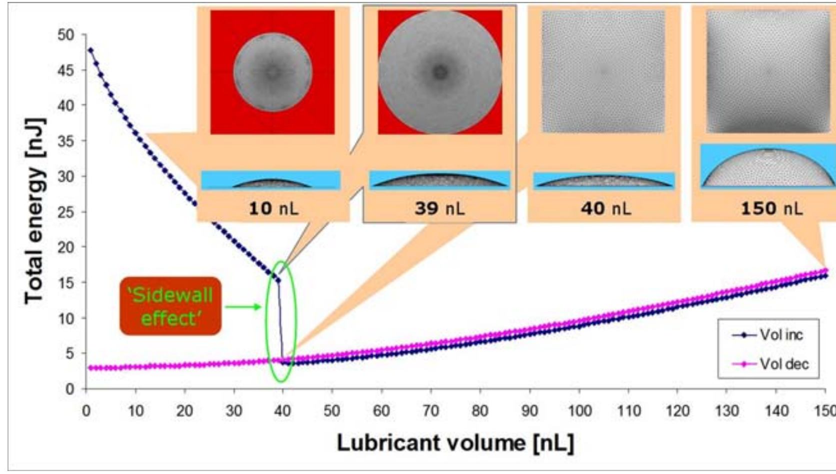

Figure 3.14: Finite-element simulations of total system energy as function of lubricant volume for a 1×1 mm^2 recessed CH_3/SiO_2 square site for fixed $\theta = 22^o$. Insets illustrate top views of some cases.

Simulations also showed that the ratio of lens contact area to superficial site area stayed constant as the side length of the site was scaled down: corner de-wetting appears to be scale-independent[5].

Using the same parameters as above for the simulation of a HD lens on a square site recessed into a 2.5 μm-deep cavity led to the results shown in Fig. 3.14. The energy curve had a definite minimum at the smallest lubricant volume (40 nL) that achieved full-site coverage, as expected. The simulation dynamics clearly confirmed the role played by the wetting boundary for this type of sites. The hydrocarbon lens preferentially spread along the sidewalls, and eventually achieved complete coverage of the site reaching into the corners. Only by wetting the hydrophobic sidewalls did the HD lens gain enough energy to balance the energetic costs of the local increase of surface curvature required to fill up the square corners.

Notably, the numerically-predicted minimal total energy shape of HD lenses faithfully-reproduced experimental observations of dip-coated ones (Fig. 3.15).

3.5 Control over dip-coated lens volumes[6]

The dynamics of capillary self-assembly depends on lubricant lens parameters, not least its volume (Sec. 2.5.1). In the perspective of extending capillary SA of parts at large (*e.g.* wafer-level) scales, control of lens volume is critical to a reliable and repeatable process.

[5]For sufficiently-small scales the *line tension* of the lubricant lens may play a role.

[6]Work done at MemsLab, Electrical Eng. Dept., Univ. of Washington (Seattle, WA, USA), in collaboration with K. F. Böhringer and R. Baskaran.

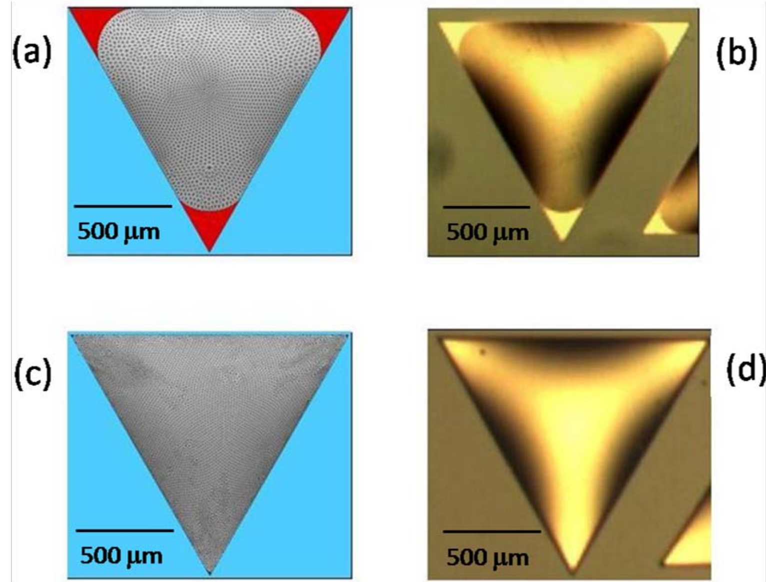

Figure 3.15: Simulated minimal energy configuration of a HD lens on a superficial **(a)** and recessed **(c)** triangular site; HD lens dip-coated over a superficial **(b)** and recessed **(d)** site (substrate submerged in water; color and depth enhanced by DIC optical microscopy). All sites are of the CH_3/SiO_2 class.

To investigate the lens-to-lens volume reproducibility, dip-coating experiments on 2.5 x 2 cm^2 silicon dies containing 10 x 10 square arrays of rectangular binding sites of the CH_3/SiO_2 class were performed. The sites had dimensions of $0.7\,mm \times 1.4\,mm$ (area of 1 mm^2), spaced apart by 500 μm (the filling ratio was 0.433; the site pitch was smaller than the capillary length). The sites were placed 3 mm away from the edges of the dies to minimize edge effects [253]. For both the superficial and recessed sites, we smoothed the site corners (Fig. 3.16). With this design we tried to:

1. enforce complete site coverage also for superficial sites, by smoothing out the very site regions left unwet by the lubricant (Sec. 3.4.3);
2. minimize the dispersion of the position of the triple-contact line, and of the values of lens volume.

The fraction of the side length of the sites that was rounded was 20%, in order to preserve directionality (see Fig. 2.22).

Triethylene-glycol dimethacrylate (TEGDMA) ($\gamma_{TEGDMA/H_2O} = 15.6\,mJ/m^2$, $\mu = 9.37 \cdot 10^{-3}\,Pa \cdot s$, $\rho = 1.133\,g/cm^3$, $L_c^{TEGDMA/H_2O} = 3.46\,mm$) was used as lubricant monomer, mixed with 3% wt. of a UV-sensitive cross-linker (Irgacure 819, Ciba). Dip-coating was performed in a beaker filled with TEGDMA and DI water (Fig. 3.17). The chips were first completely immersed in the

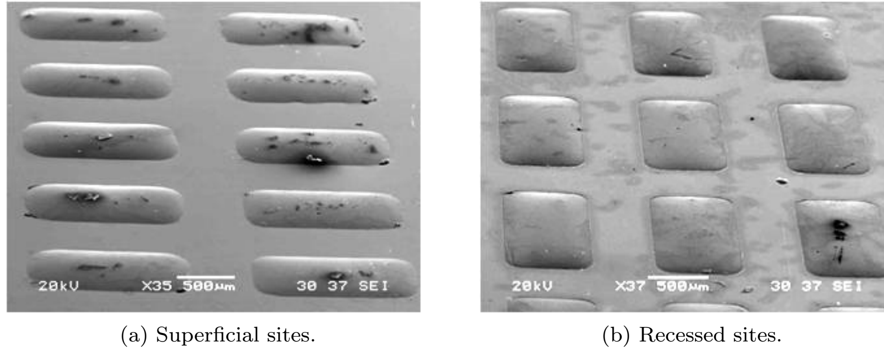

(a) Superficial sites. (b) Recessed sites.

Figure 3.16: SEM pictures of dip-coated TEGDMA lenses over smoothed rectangular sites (area = 1 mm^2) .

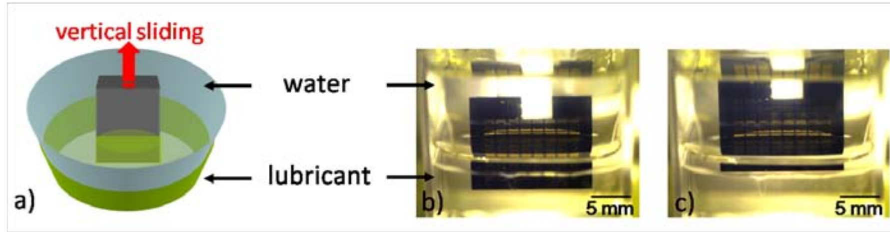

Figure 3.17: TEGDMA dip-coating on rectangular binding sites.

monomer and then withdrawn through water. The dip-coating speed varied within 10 ÷ 100 mm/min ($Ca = 10^{-4} \div 10^{-3}$), as controlled by means of a software-programmable dip-coater (KSV Ltd.) and visually-tracked by a high-speed camera. The chips were slid vertically (*i.e.* perpendicular to the fluid interfaces, with the site rows parallel to them). After dip-coating, the coated lenses were polymerized under UV light while still under water.

To compare individual lens volumes, the height of the lenses at their center was measured by contact profilometry[7]. Since the measured lens profile proved to be perfectly-circular in most cases, this quick measurement gave a reliable though not very-accurate reference for the lens volume.

Upon vertical withdrawal of the chips, monomer film dewetting, break-up and formation of individual lenses started from the sites situated at the edges of the chips, and from there it progressed toward the center. The in-plane profile of the monomer/water contact line was consequently curved, being higher at the center than at the edges. By optical inspection it was noted that:

1. the order in which the lenses were formed by the monomer was highly-sensitive to the *placement* of the chip: any slight positional tilt of the chip

[7] We measured the entire profile of the lenses across their width with a stylus profilometer, and extracted the height of the central point.

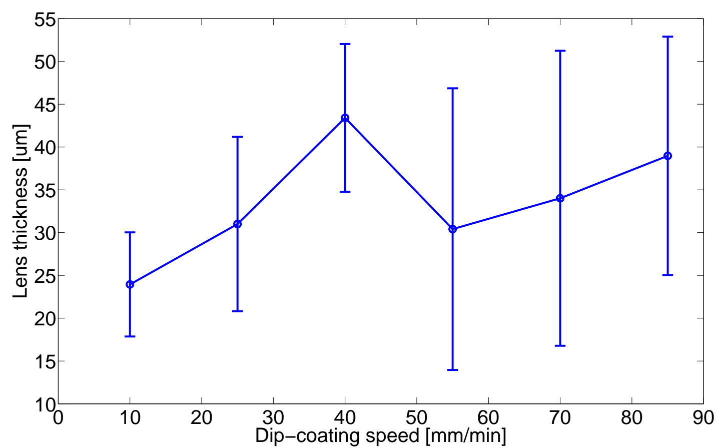

(a) Lens thickness for superficial sites.

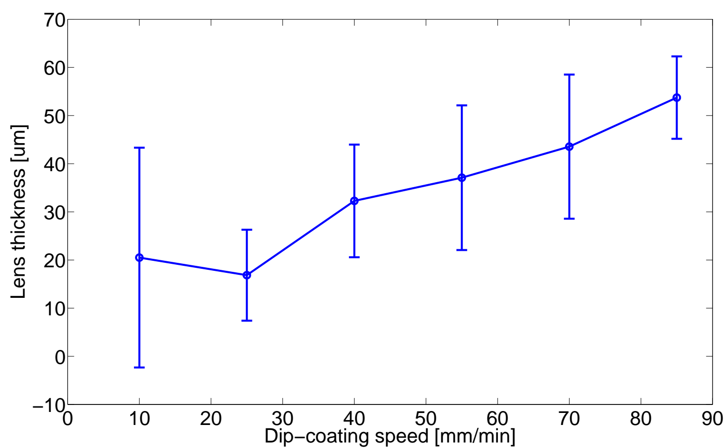

(b) Lens thickness for recessed sites.

Figure 3.18: Measured height of TEGDMA lenses as function of dip-coating speed (averages and $2-\sigma$ dispersion values computed from around 100 measurements for each speed value).

from its perfectly-horizontal position caused the dewetting to start from the higher edge, ending at the lower one;

2. the in-plane curvature of the monomer/water contact line diminished with increasing chip withdrawal velocity: the line became almost horizontal for velocities in excess of 60 mm/s. In this condition, all the lenses of a single row singulated almost simultaneously.

Recessed sites showed perfect coating conformality. Interestingly, full-site coverage was also evident in most of the superficial smoothed sites.

Measurement results were similar for both superficial and recessed sites (compare Fig. 3.18a and 3.18b). The average lens thickness (volume) resulted roughly proportional to the dipping velocity. Anyway, significant dispersion in lens height values was also observed in all cases. Lens-to-lens variation was spatially random and did not show any identifiable trend across the chip surface; still, *results for recessed sites showed better uniformity* compared to the superficial ones (Fig. 3.19). We did not observe any relevant dependence on the distance of the coating sites from the edges of the dies.

Our observations are consistent with Hartmann's on the dip-coating of hemispherical polymeric microlenses [253]. They may imply that constant withdrawal speed, forced lens pinning at site edges and controlled substrate orientation are still *not* sufficient to achieve a very-low dispersion in deposited lens volumes. We thus hypothesize that the volume of lenses deposited by dip-coating over patterned substrates is, *ceteribus paribus*, fundamentally dependent on: 1) local fluid flow conditions, 2) local dynamics of lens pinch-off, and 3) thin fluid film capillary break-up. We did not investigate how these parameters could be influenced, since we lacked appropriate optics.

3.6 Conclusions

We experimentally and numerically demonstrated that adding an even relatively-thin wetting sidewall to binding sites patterned on planar surfaces enforces their *conformal* fluid dip-coating. This achieved, arbitrary site patterns, also featuring very-acute angles and concavities, can be *effectively* exploited for capillary part-to-substrate SA. Moreover, this site modification: 1) enhances the repeatability of the dip-coating process and its insensitivity to local surface defects, 2) is easy to integrate with standard process flows, and 3) may significantly ease the adoption of fluid dip-coating over large (*e.g.* 8'' wafers) patterned substrates.

Moreover, our experiments supported the *unsuitability* of dip-coating to dispense fluid lenses of tightly-uniform volumes over microfabricated sites. Nonetheless, our results may not be definitive: we may have missed the proper region in parameter space where volume control of dip-coated lenses may be possible.

Overall, dip-coating remains in our opinion the technique of choice for the fast coating of extensive arrays of patterned sites.

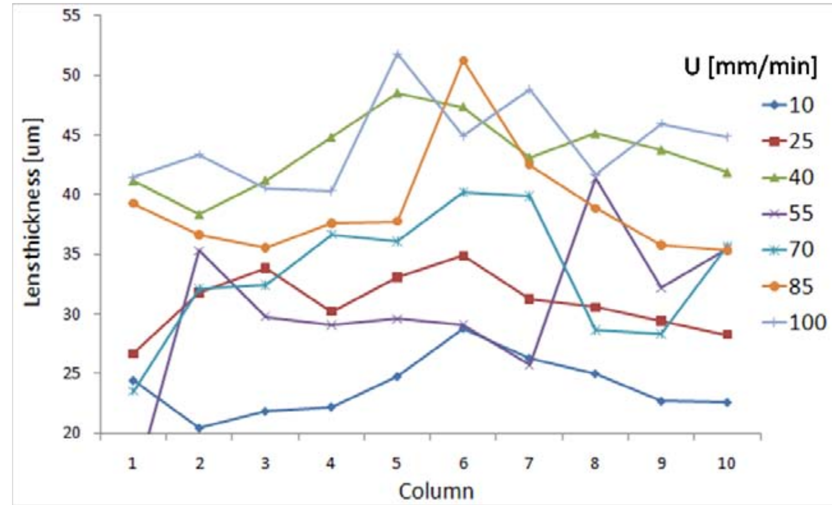

(a) Superficial sites.

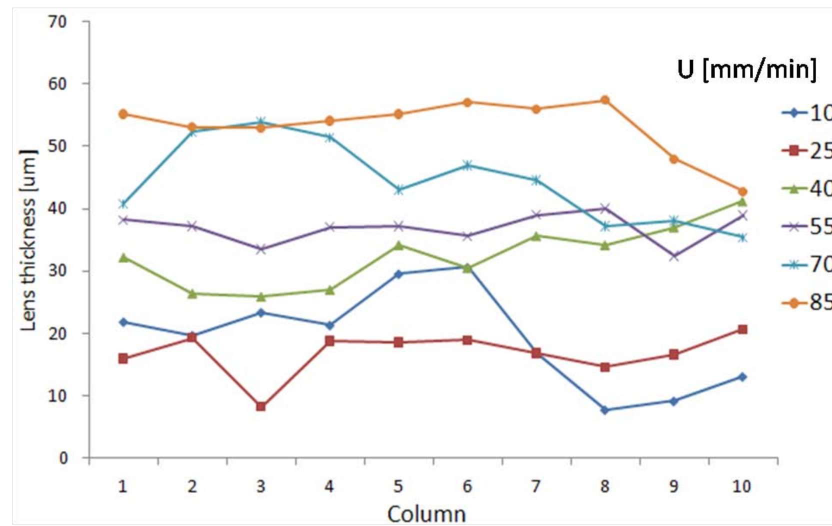

(b) Recessed sites.

Figure 3.19: Across-die distribution of TEGDMA lenses's height as function of dip-coating speed (average of ten measurements shown for each site column).

Chapter 4

Solder-based Interconnects in Capillary Part-to-Substrate Self-Assembly

In this Chapter we demonstrate a simple procedure - partly mutuated from flip-chip soldering, and generalizing previous results - that allows to seamlessly establish solder-based electro-mechanical interconnects in a capillary part-to-substrate (self-)assembly process. While we used In/Au as metal couple for our proof-of-concept, we outline how to extend such methodology to other materials. We discuss in details the disruptive phenomena that might hinder the yield of this post-assembly step, with special attention to thermal treatment. Our results open interesting perspectives for adopting capillary SA for die integration over exotic (*e.g.* non-planar, flexible) substrates.

4.1 Functional interconnections

Establishing reliable electro-mechanical interconnects between parts and substrates is critical for the full development of capillary part-to-substrate SA.

Xiong's attempt was sequential: capillary alignment and mechanical binding of LEDs to the pre-conditioned substrate was mediated by a curable polymer, then post-assembly electroplating of solder columns realized the electrical interconnects [135]. By separating the two functionalities, they could be optimized without mutual interference; but the method required extensive post-processing and relatively-large dedicated substrate structures (for electroplating) that were probably used only at the time of assembly. Fukushima's enhancement of robotic pick-and-place with capillary self-alignment featured wafer-level alignment and transfer of dies to the target substrates, and thereby substantial post-processing

(*i.e.* vias drilling and filling with copper) to realize electrical connections [148].

In molten-solder-driven SA [118], upon solder cooling electro-mechanical interconnects are established at once. The entire assembly process develops in hosting fluids kept at temperatures higher than the solder melting point, though. This induces continuous degradation of metals (*i.e.* growth of both solder oxides and intermetallic compounds (IMCs)) which, for long assembly times, may be problematic for microbumps [261].

Scott *embedded* solder bumps inside the binding sites to be coated by the lubricant [133]. After capillary assembly, thermal reflow enforced solder bonding. The method utilized the lubricant only for temporary mechanical binding, which was decoupled from bonding.

We thought Scott's method offered important advantages:

1. it performed the assembly at room temperature, avoiding the aforementioned solder consumption issues;

2. it realized electrical and mechanical interconnections at once;

3. it looked compatible with existing packaging flows.

Anyway, the original proposal was demonstrated using a composite lead-based solder - whose melting point was lower than the boiling point of all involved fluids - that was deposited on the binding sites by dip-coating. These represent severe processing limitations, because: a) lead can no longer be used in electronic manufacturing; in fact, alternatives to lead-based solders are being intensively investigated [118, 262, 263]; and b) solder dip-coating does not allow the tight control over solder bump dimensions that is required especially for advanced interconnect pitches. Moreover, we wanted to understand the full details of the process and to assess its main failure modes - both aspects being unsatisfactorily described in literature.

We hereby present a generalization and detailed analysis of Scott's method beyond its original setting. We opted for Indium and Tin as lead-free Au-wetting solders with good electro-mechanical properties [264, 265] and relatively-low melting point (156 and 232 ^oC for pure In and Sn phases, respectively).

4.2 The experimental procedure

4.2.1 Materials and methods

For the fabrication of both dummy parts and substrates (Fig. 4.1), we started with clean 8", 725 μm-thick silicon wafers with a 200 nm-thick top layer of silica. Ti/Au layers (50/100 nm-thick) were evaporated onto silica.

As for substrate chips, this Ti/Au layer was used as seed for subsequent masked electroplating of the metallic bumps. We electroplated an under-bump metallurgy (UBM) composed by: 1) Ni (1 μm), used as barrier against the diffusion and dissolution of Au - which in the case of In starts even at room temperature, the rate being not as high as with Sn, though [264]; and 2) an

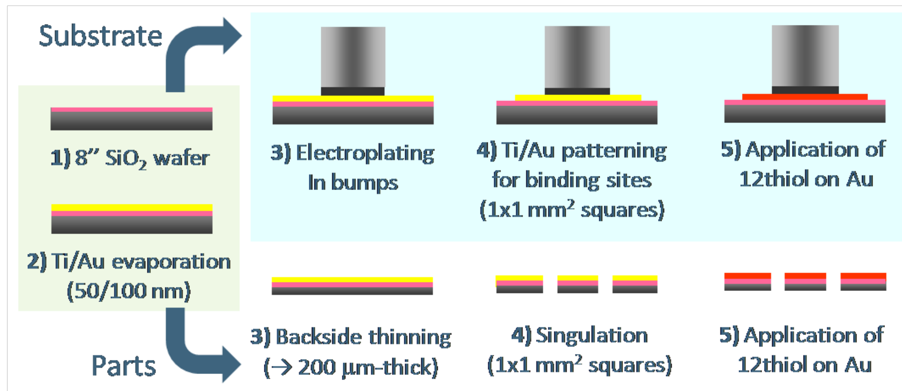

Figure 4.1: Processing steps for the fabrication of dummy parts and substrate for preliminary tests. Relative dimensions out of scale for representation purposes.

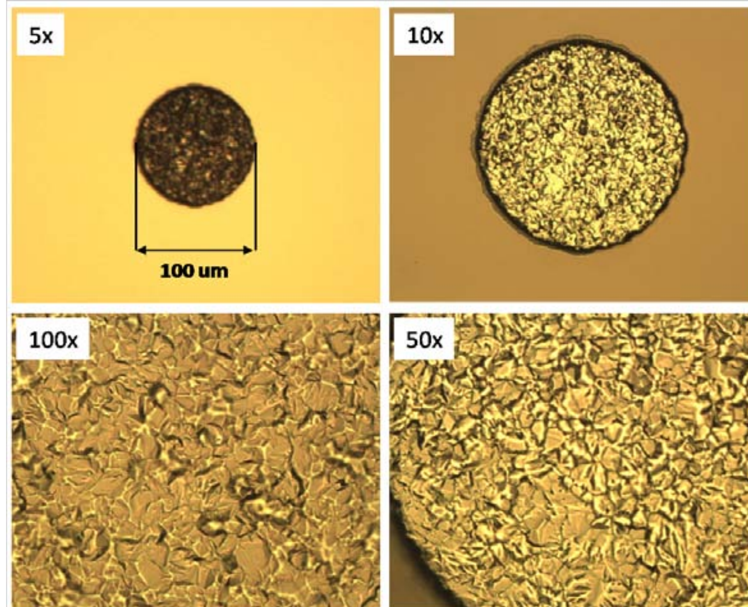

Figure 4.2: Optical pictures of an electroplated In/Au/Ni(/Au/Ti) bump.

Au layer (300 nm) to promote the adhesion of In onto the underlying surface; adhesion would be otherwise easily hindered by the fast oxidation of the Ni surface, leading to dewetting and poor interfacial properties [222]. An In layer (Fig. 4.2) or Sn layer, 7 μm-thick on average, was then electrodeposited on top of the stack. The as-plated surface roughness of both bump types was as high as 4 μm (Ra), as measured by laser interferometry (Fig. 4.21). Bumps diameters ranged from 50 to 400 μm. By mechanical profilometry, we could measure an average tolerance in bumps thickness of about 2 μm across full 8" wafers. Bumps closer to the wafer edge tended to be thicker, probably because of edge effects[1]. Several centro-symmetric bump arrays were designed. The seed layer was later lithographically patterned and etched to define a $1 \times 1\ mm^2$ square superficial binding site around each bump array. The binding sites were spaced 1 mm-apart by silicon dioxide (*i.e.* hydrophilic) spacer areas. The wafers were then diced into small chips containing arrays of sites. After standard cleaning procedures, the chips were immersed overnight in a 1 mM ethanolic solution of DDT SAMs to make them hydrophobic[2] (see Sec. 3.4.2).

As for the parts, as-evaporated wafers were backside-thinned down to 200 μm, diced into $1 \times 1\ mm^2$ square dies and treated as above to selectively make their Au (*i.e.* functional) side hydrophobic. Native silicon oxide rendered the other sides of the parts hydrophilic. Because: 1) we were mainly interested in solder/metal wetting, and 2) we wanted to use a variety of solder bump arrays on the same substrate chips, in this exploratory study we did not pattern bonding pads on the Au-coated part sides. Also, by adopting mechanical dicing (for convenience) and relying on *edge*-alignment for registration of square parts, we had to disregard the assessment of ultimate capillary alignment accuracy: dicing had an intrinsic tolerance of about 10 μm - by itself much higher than the best claimed capillary self-alignment performances [131, 200].

After full treatment, both substrates and parts were stored in ethanol to preserve the chemical pre-conditioning and minimize surface contamination.

4.2.2 Solder oxide removal

All our experiments were performed in typical laboratory atmosphere at room temperature. Under such conditions, solder surfaces are covered by a few nm-thick self-passivating layers of native oxides[267]. Oxides, besides being electrical semiconductors or insulators, are mechanically stiff: they prevent proper solder/metal wetting. This issue is well-known in soldering [222]. Solder oxides are commonly removed using fluxes or forming agents (*e.g.* hydrogen- or formic acid-rich gaseous mixtures) [268] - the specific chemistries being dependent on the types of oxide [267].

[1] Electric fields, stronger at the edge than at the center of the wafers, induce different rates of metal deposition.

[2] [266] reports anhydrophobic character of the Au surface under laboratory conditions. In our experiments, though, the water CA measured on untreated Au surfaces showed large variations ($30^o \div 70^o$), making it unreliable (as expected from uncontrolled laboratory conditions). The use of thiolates allows a superior control of surface chemistry.

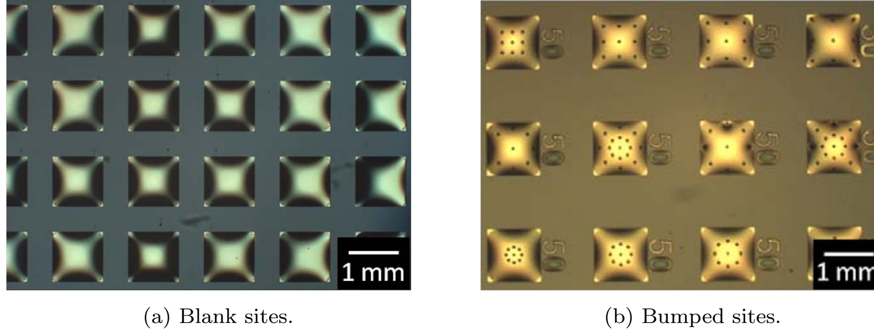

(a) Blank sites. (b) Bumped sites.

Figure 4.3: HD dip-coating over bumped superficial sites. Numbers indicate bumps diameter (μm). Colors and depth enhanced by differential interference contrast (DIC) optical microscopy.

Anyway, our constraints made standard procedures not straightforward to apply. First, fluxes are reducing agents: for long assembly procedures, they might deteriorate solders, as discussed above. Second, even wanting to use fluxes as lubricants, we were not able to selectively dip-coat fluxes onto our binding sites, due to both their relatively-high viscosity (recall Sec. 3.4.2) and partial solubility in water. Therefore, we proposed and tested an alternative solution[3].

Our approach then consisted in: 1) chemically-removing the oxides from the solder surface just before 2) selectively dip-coating the binding sites with lenses of an inert fluid. The inert lubricant would protect the solder from oxide regrowth - or at least significantly slow down the oxidation rate if the oxygen concentration was kept low - throughout the ensuing capillary assembly step and right up to the subsequent thermal treatment (described later) - unless the lubricant lens was accidentally distorted or even removed during the process. Hexadecane (HD) appeared to suit this purpose, as well, due to the relatively-low solubility of oxygen in it and its high boiling point (287 ^{o}C).

We thus dipped the substrates in 10% wt. HCl (pH $<$ 2) for up to 5 minutes to etch away the solder oxides, then thoroughly rinsed the substrates with DI water and ethanol, dried them with a nitrogen flow and immediately slid them through an air/HD/DI water interface, thus forming stable lenses of HD (Aldrich, purity $>$ 99%) - as described in Sec. 3.4.2. The substrates were then left in water to undergo the assembly process.

Comparison between Fig. 4.3a and Fig.4.3b and c shows that the presence of arbitrary arrays of solder bumps did not influence the dip-coating of binding sites. This held true as long as: 1) the lenses were thicker than the bumps, and 2) the bumps were placed far enough from the edges of the sites, to avoid local pinning of the lenses (compare *e.g.* Fig. 4.4a with 4.4b). Notably, SAMs

[3]We preferred to pursue this approach rather than a systematic search for proper fluxes - which nonetheless may be worth pursuing in the future.

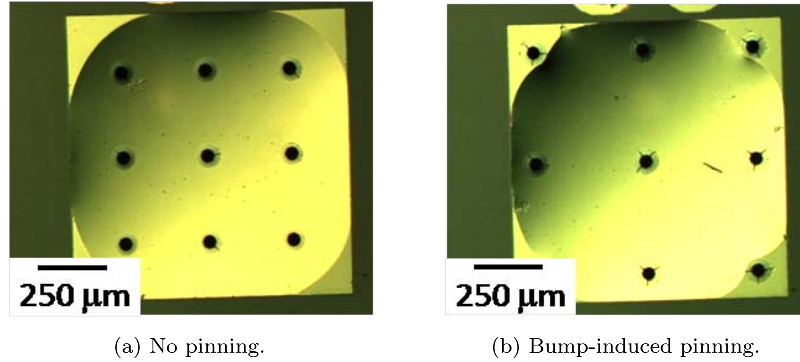

(a) No pinning. (b) Bump-induced pinning.

Figure 4.4: Pinning of HD/water triple contact line induced by bumps close to site edges. Bump diameter: 50 μm. Substrates submerged in water. Colors and depth enhanced by DIC optical microscopy.

layers resulted essentially unaltered after the short exposure to diluted HCl, which indeed only caused a minor reduction of the average measured water CAs - from the original 110° down to 108°.

4.2.3 The capillary assembly step

The parts were extracted from the ethanol-filled reservoirs and directed in water by pipetting toward the substrates. Thereby the parts wandered across the substrates, aided by fluidic stirring, in search for unfilled binding sites. Upon capillary assembly (Sec. 2.1), parts floated on top of the HD lenses and did not touch the bumps. This was deduced: 1) by optical inspection, and 2) by noting that the parts still oscillated laterally in response to impulsive agitation imparted to the beaker hosting the fluidic assembly: a similar motion could not take place in presence of contact (*i.e.* friction) between bumps and parts.

The assembly dynamics was essentially stochastic, and filling of the full array of sites was asymptotic. The time a part takes to achieve its final alignment starting from partial overlap with the site depends on the properties of the lubricant (interfacial energy, volume, density and viscosity): it may range from fractions of second (as in our case) to tens of seconds using very viscous lubricants [31]. We were rarely able to fill all binding sites by part pipetting only and within a reasonable amount of time (*e.g.* 4 minutes for 100 parts): most commonly we had to fill few residual sites manually with the aid of tweezers. Unbound, interstitial or misplaced parts could be carefully removed from the substrates by laminar fluid flow and eventually recycled for other assembly runs - though this was not straighforward. High filling rates required an excess amount of parts as compared to the number of sites (*i.e.* high *redundancy*).

More details on all the aforementioned issues are presented in Chapter 7.

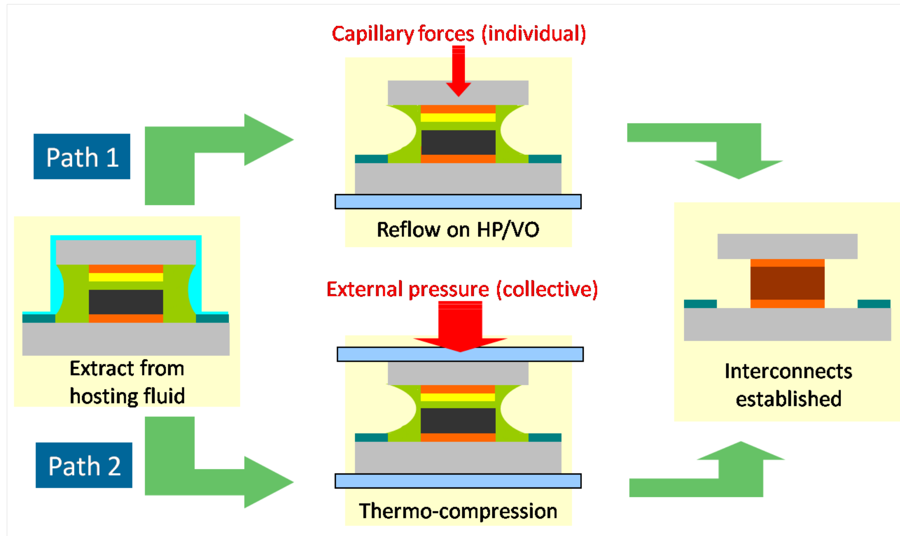

Figure 4.5: Paths to post-assembly solder bonding.

4.2.4 Post-assembly solder bonding

Consistently with the materials described above, after capillary assembly the substrates looked essentially hydrophilic: the assembled parts exposed their hydrophilic sides to the surface and were separated by hydrophilic spacer areas on the substrate surface. Thus, upon extraction from the assembly space through a clean water/air interface, the substrates were covered by a residual, relatively-thin water film. This was beneficial, as it preserved part alignment during subsequent translations of the substrate in air - *i.e.* the hydrocarbon lenses and the thin water cover provided together sufficient force to keep the parts in place - as long as evaporation did not sensibly affect the water film. The thickness of the residual water film on the substrate upon extraction depended on the velocity and angle of extraction of the substrates with respect to the surface of the hosting fluid, as expected from our dip-coating experiments (Ch. 3). In our experiments, under these conditions no particular care seemed necessary to transfer the substrate from the assembly space to the bonding stage. Note that, up to this point, the parts were still floating on the HD lenses, above the bumps.

We did not reflow the bumps before performing bonding, as is instead commonly done in flip-chip assembly. This way we wanted to avoid excessive formation of solder/Au intermetallics, which form readily even at room temperatures [269]; particularly, being the bumps rather thin and IMCs melting point higher than that of pure solder, their diffusion toward the bump surface could have prevented the solder from wetting the Au surface.

Two bonding methods were tested: *without* and *with* external pressure applied at the time of metal joining (Fig. 4.5).

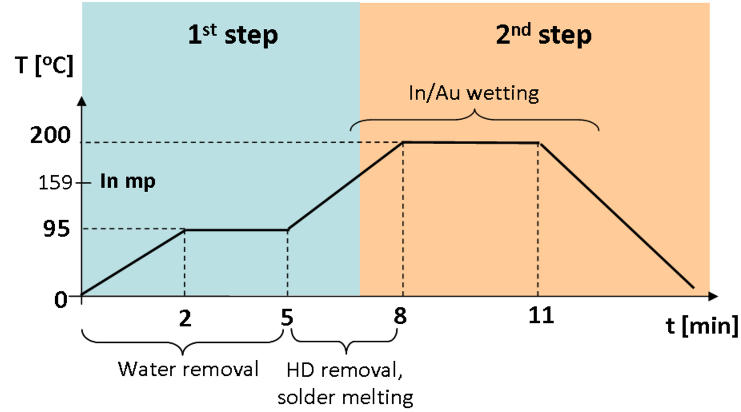

Figure 4.6: The thermal profile for the In reflow step.

By the first method, the substrates were set on a hot plate (HP) or vacuum oven (VO) and reflowed. The thermal profile of the reflow step showed in Fig. 4.6 was optimized for the particular In/Au metal and DI water/HD fluid couples hereby utilized. Specifically, after a slow temperature ramp-up we kept the temperature of the hot plate at 95 ^{o}C for 3 minutes to let all residual DI water evaporate from parts and substrate. Upon subsequent increase of temperature, we saw by real-time optical inspection that HD was completely removed at temperatures between 150 ^{o}C and 160 ^{o}C, *i.e.* far below its boiling point (287 ^{o}C) but at the very point of solder melting. Thus we assumed that In/Au wetting could start in presence of HD, *i.e.* still in absence of In oxide and under vertical compressive pressure produced by the fluid menisci on each *individual* part (Sec. 2.2). Finally, the temperature was kept at 200 ^{o}C (*i.e.* reasonably higher than the melting point of pure In (156 ^{o}C) [265]) for up to 3 minutes to enforce full In/Au wetting and bonding. Simple modifications were required to adapt this procedure to the use of Sn. Note that this proposed procedure includes the original proposal of Scott (where bonding could take place inside the hosting fluid) as a particular case. Detailed analysis of the phenomena associated with this 2-steps thermal treatment are described in Sec. 4.3.1.

As an alternative, we performed the collective metal-solder bonding step with the help of a thermo-compression (TC) bonding machine, *e.g.* between the arm and the chuck of a flip-chip assembly tool (Fig. 4.7). Once extracted from the assembly space, the substrate carrying the assembled parts was placed on the chuck of the tool. Shortly after, the arm of the tool was brought into bare contact with the whole array of assembled parts, so that they were ideally *locked* in place[4]. Plane parallelism between arm and chuck was critical at this

[4]Locking alone avoids pop-up, collapse, free fall and displacement of parts during HP thermal processing (described in Sec. 4.3.1). Anyway, TC also inhibits molten-solder driven self-alignment between solder bumps and bonding pads - *i.e.* a *refinement* of the eventually-

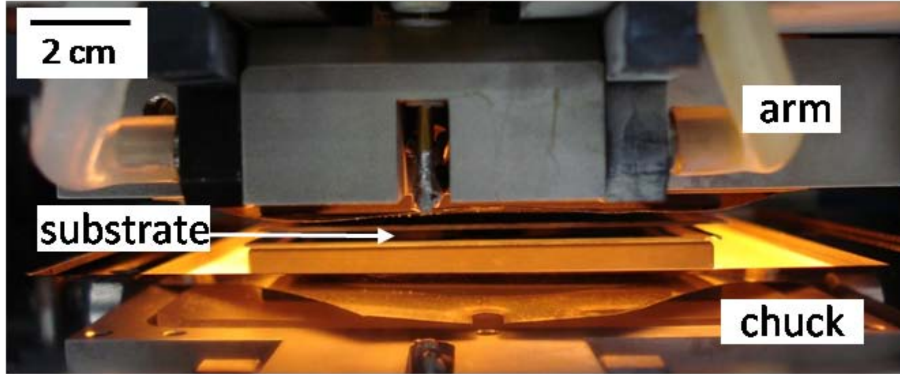

Figure 4.7: Collective thermo-compression bonding of parts onto a substrate.

stage to preserve the alignment of the parts on their binding sites. A thermo-compressive step was then performed. A pressure of 2.5 MPa was applied on each bump. The thermal profile was carefully adapted to avoid violent release of pressure build up by the lubricant lenses confined below the parts, which might still induce defects in the definitive assembly.

Finally, for both bonding methods, all treated samples were inspected and tested after slow cooling down to room temperature. Characterization of the metal joints obtained by both methods is presented in Sec. 4.3.2.

4.3 Results and characterizations

4.3.1 Phenomena associated with reflow

Here we discuss failure modes during thermal treatments *without* external pressure. See Fig. 4.8 for reference.

The 2-steps no-pressure thermal treatment

As already mentioned, in the first step, the substrate temperature was set slightly below the water evaporation point (100 ^{o}C, in turn lower than the HD evaporation point). If the temperature was brought to this level too-rapidly, or was directly brought to the second setpoint, the large induced temperature gradient could originate violent convective and Marangoni flows (Sec. 2.2) in the residual water film. Once incepted, the flows violently displaced the parts from the sites, and the parts could even end up being tilted upside-down to expose their hydrophobic side to air. The fluid flows gathered the parts at the

rough pre-alignment achieved at the end of the whole site-wide capillary alignment step (see Sec. 2.5.1). Moreover, upon contact between arm and parts, the residual thin water film forms a fluid meniscus (Ch. 2) and can eventually displace the parts from in-plane registration.

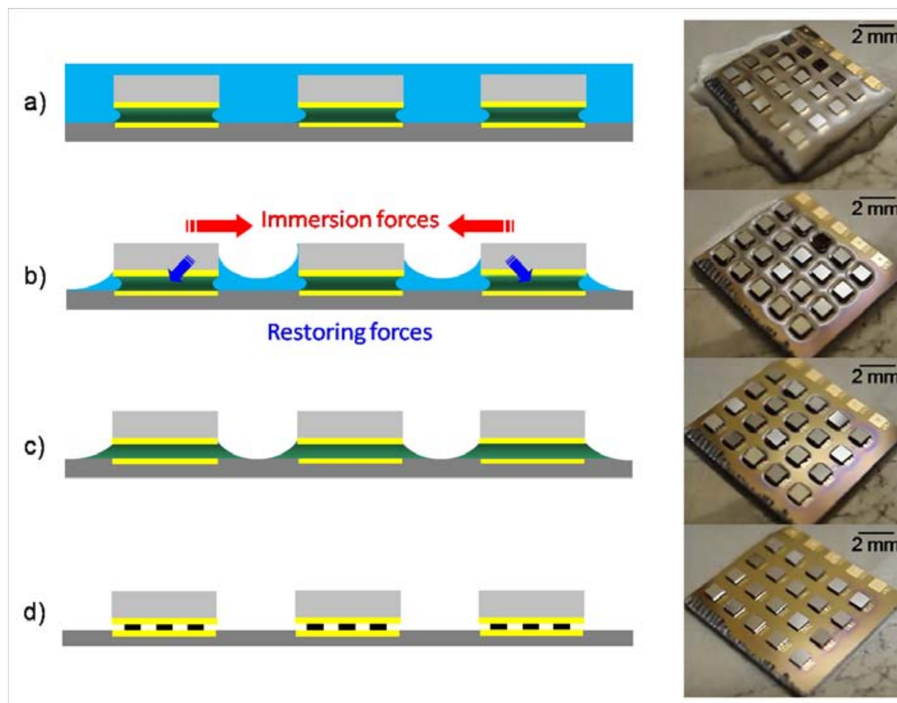

Figure 4.8: Main events during the progress of the 2-steps thermal treatment *without* external pressure. Left: schematic diagram of the process (relative dimensions are out of scale); right, video frames of the corresponding stages of the actual process (all parts measured $1 \times 1 \times 0.2\ mm^3$; diameters of underlying In bumps ranging from 260 to 300 μm).

edges of the fluid film until this was completely evaporated or removed from the substrate, which happened quickly (Fig. 4.9).

In the second step, after removal of the residual water film from the substrate, the substrate temperature was set above the melting point of the solder to achieve solder bonding (second setpoint). In our case, the solder melting point was lower than the evaporation point of the lubricant, so the lubricant could still protect the solder against (re)oxidation at the time of solder/metal wetting. In absence of HD at the time of solder melting – as it happened with Sn bumps – forming or reducing gases during the bonding stage were needed to avoid solder oxide regrowth.

At temperatures above 120 ^{o}C SAMs of thiolates like DDT are completely desorbed from the metal surfaces [84, 270]. Such low desorption temperature is mainly due to the weak, mostly electrostatic bond between the -SH head groups of the SAMs and the gold surface. As a comparison, desorption of trichlorosilane SAMs covalently-bound onto oxide surfaces takes place at much higher temperatures (about 400 ^{o}C). Because of this, we expected the solder/metal wetting

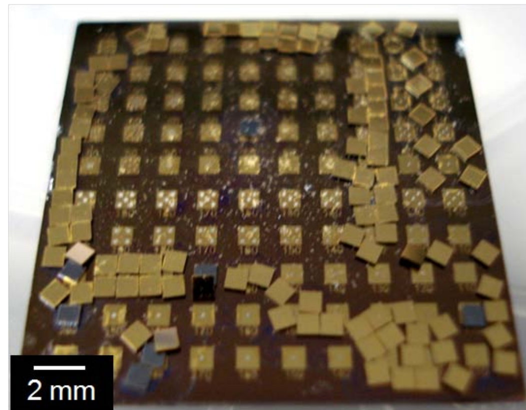

Figure 4.9: Disruption of capillary assembly after fast thermal treatment.

and the formation of interfacial IMCs not to be hampered by the organic monolayer (nor from solder oxide and HD layers, for what described above). This is in contrast with the TC bonding method, where the contact between solder and Au surfaces is enforced already at room temperature: it is thus mediated by the alkanethiol monolayer.

If the heating rate from the first to the second thermal setpoint was too fast, some parts could *pop-up* from the sites to land even very far from the original positions. We attributed this spectacularly disruptive phenomenon to 1) an impulsive discharge of excess pressure build up in the lubricant lenses, and/or to 2) very-fast evaporation of water residues.

Lubricant spreading

When the water evaporated, the hydrocarbon lenses spread over the substrate, *i.e.* the hydrocarbon/air/solid triple contact line lost the geometrical constraint imposed by the chemical wetting contrast between site and spacer surface (Fig. 4.8c). This happens because hydrocarbons well wet the hydroxyl end groups of the oxidized spacer surface in absence of water [84]. Once lubricant spreading happens, the part is subjected to smaller restoring forces toward its aligned equilibrium position than in the previous condition, because the surface tension of alkanes (*e.g.* 27.47 mJ/m^2 for hexadecane) is far lower than that of water ($72\,mJ/m^2$). In this condition, in a sort of spatial symmetry breaking, small fluctuations may induce displacements from alignment, which may be practically irreversible since the friction between the surfaces of the part and the substrate may be far larger than the capillary restoring force.

Importantly, as a consequence of lubricant spreading and/or of asymmetric rupture of the residual lubricant film - previously confined between the parts and the underlying binding sites - parts may violently stick to their underlying bumps at the end of a vertical free fall. In so doing, they may deviate from their original in-plane alignment (Fig. 4.10).

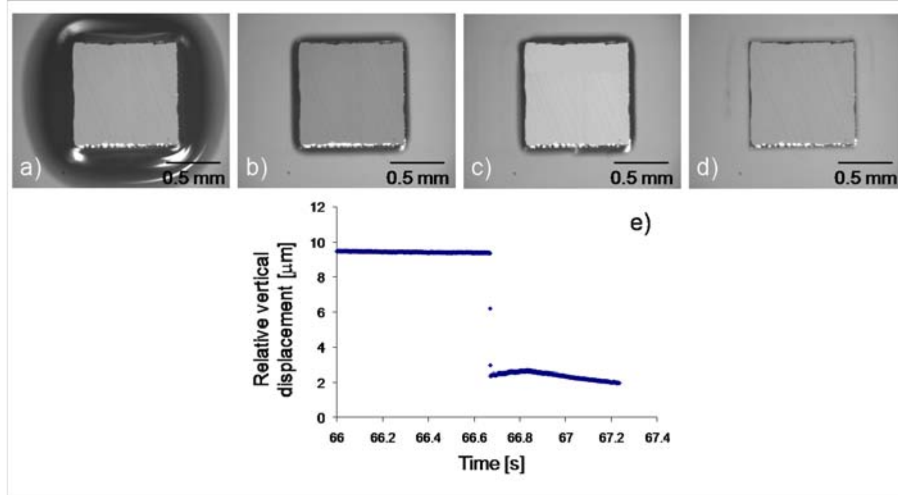

Figure 4.10: Vertical part displacement during thermal treatment. **a)** A part ($1\times1\times0.5\ mm^3$ silicon die) assembled on a matching binding site after complete water evaporation while the underlying iso-octane lens is spreading (as in Fig. 4.8c). A sudden vertical movement of the part takes place between frames **(b)** and **(c)** due to an asymmetric rupture of the residual iso-octane film. Final part position shown in **(d)**. **e)** A free fall of 7 μm happened within 3 ms (data from real-time laser interferometry (Polytec) at 1 KHz sampling rate).

Part aggregation by immersion forces

During evaporation, the thickness of the residual layer of water gradually thins down. Rupture of the film starts at the unfilled (hydrophobic) sites eventually present on the surface of the substrate (see *e.g.* Fig. 4.8a), making the film no more uniform. Below a film thickness roughly equal to the parts' thickness, the parts protrude from the surface of the film. Furthermore, if (as in our case): 1) the lateral sides of the parts are wet by water, 2) the interpart distance is smaller than water capillary length, and 3) there remains enough water to bridge adjacent parts, then the parts experience immersion forces. As described in Sec. 2.2, the intensity of such capillary forces is roughly inversely proportional to the lateral distance between the parts[5], and it is also influenced by the parts thickness and wetting behavior, as this affects the bridge curvature. As a result, in the presence of liquid bridges the parts are no longer isolated and experience *collective* forces. These forces are attractive because the curvature of the bridges - as defined by the contact angle of water on silicon oxide - is the same along the edge of all parts, which were all equal[6]. These forces are balanced only with respect to those parts which are surrounded by a centro-symmetric array of other

[5]In all performed experiments, the intersite distance was always inferior to the capillary length of water, consistently with the approximations leading to Eq. 2.19.

[6]The sign of the force depends on $\sin\psi_1 \cdot \sin\psi_2$ (Sec. 2.2), which was positive in all cases.

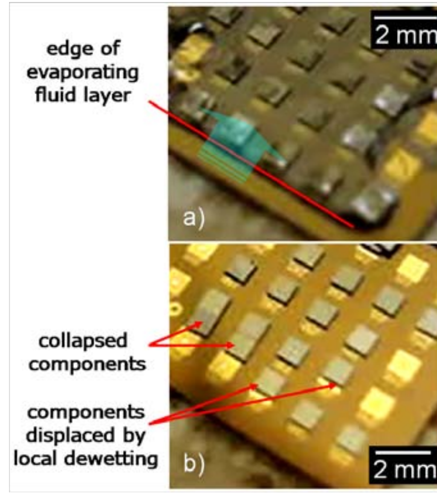

Figure 4.11: Collapse and aggregation of parts during thermal reflow. **a)** Beginning, **b)** end of the reflow process.

parts (Fig. 4.8b and 4.11a). Consequently, the parts situated along the perimeter of the fluid layer experience a net force pointing toward the center of the fluid layer. If this net force overcomes (*e.g.* because of the increasing curvature of the bridges with fluid evaporation) the competing, restoring capillary force due to the lubricant menisci, the parts violently collapse toward adjacent parts (Fig. 4.11b). This collapse is more probable if, because of asymmetries in the surrounding water film, the hydrocarbon lens underneath the part has already spread. A single collapse may involve more than one part, and it is enhanced and/or cascaded by parts which are interstitial or not properly aligned.

Solutions to overcome this problem may be: 1) reduce the surface tension of the hosting fluid prior to reflow *e.g.* by adding surfactants or liquids of lower surface tension (Sec. 2.2) prior to the reflow step; 2) increase the spacing between the arrayed sites; 3) reduce part thickness, as far as part functionalities and mechanical rigidity are not compromised; 4) apply pressure on the parts to lock them in place during the thermal treatment, *i.e.* perform thermo-compressive bonding. In our experiments *e.g.* with square parts of $1 \times 1 \times 0.2\ mm^3$ size, in absence of external part locking and applied pressure, we could not avoid collapse among adjacent parts during thermal treatment if the spacing between them was smaller than 250 μm.

Asymmetric de-wetting and capillary centering

If hydrophobic spots *(e.g.* test patterns, residues from earlier process steps) are present on the spacer surrounding the sites, they can induce displacement of parts during water evaporation. When the thickness of the hosting fluid becomes sufficiently small, the fluid starts to sense the chemical character of

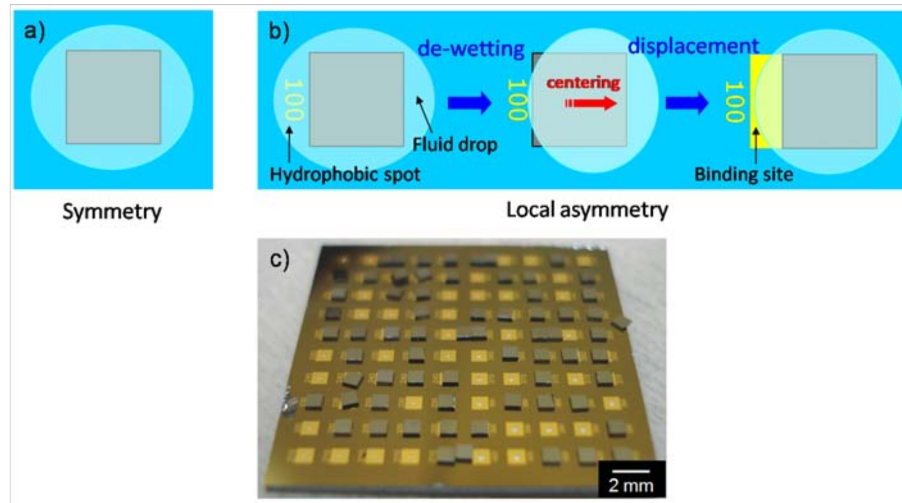

Figure 4.12: Effects on final part placement of local wetting (a)symmetries in the neighborhood of a binding site: fully-symmetric case **(a)**, asymmetric case **(b)**, and actual examples on a 10×10 array of 1 mm^2 square binding sites after thermal treatment **(c)**.

the substrate. As opposed to the fully-symmetric case shown in Fig. 4.12a, the hydrophobic spots behave as nucleation points for the distortion of the thin water film, due to water de-wetting (Fig. 4.12b). Since the water/air interface has higher energy than that between hydrocarbon and water, the capillary force associated with the former fluid couple prevails on the competing latter (due to the undelying lubricant meniscus), hence the part moves to the centre of the distorted water lens (this is called capillary *centering* effect [221]), leaving the starting, aligned position. Fig. 4.12c shows experimental evidence of such phenomena.

4.3.2 Characteristics of interconnects

In/Au interconnects were established by means of both methods described in previous Sections. Nearly all assembled parts subjected to both bonding methods were stably attached to the substrates, independent of array configurations. Bonding yield was apparently lower for sparse arrays of bumps of small diameters (< 100 μm), due to the fragility and rather easy disruption of the solder joints upon manual substrate handling. This observation suggests that, for such bonding conditions, the use of proper polymer *underfill* to avoid premature bond failures may be mandatory. Integrating the underfill in a capillary part-to-substrate SA process flow is an important open issue.

All bonded samples were inspected, as hereby described.

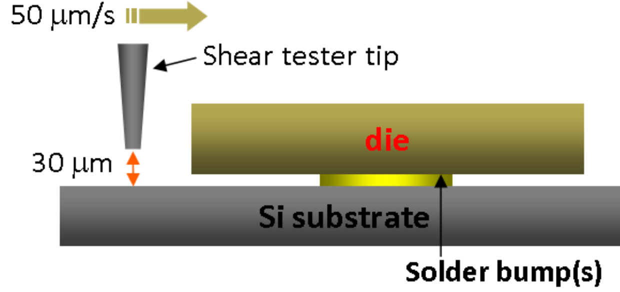

Figure 4.13: Mechanical shear test on bonded parts.

Bump diameter [μm]	$220 \div 400$	
Bump height [μm]	9 ± 1	
bonding method	HP	TC
# of measured samples	67	60
average shear strength [MPa]	5.58	4.73
Standard deviation [MPa]	1.12	0.98

Table 4.1: Summary of shear test results.

Mechanical properties

Bonded samples were subjected to automated mechanical shear tests. As shown in Fig. 4.13, the tip of the shear tester (XYZ Inc.) pushed on the side of the part and was positioned 30 μm above the substrate surface, so that the shear movement of part would be as parallel to the substrate plane as possible. The tool imposed a constant shear rate (50 $\mu m/s$) to the tip and simultaneously sensed the force opposing its motion. The tests were performed at room temperature on parts bonded over sites containing a single central bump. Both brittle (Fig. 4.14a) and plastic (Fig. 4.14b) failures by shear stress were recorded.

We wanted to ascertain preliminarily whether the adhesion of the parts to the substrate was due to fluid-mediated stiction. Complete fluid removal by thermal treatment appeared *a priori* not trivial, due to the wicking action of the small space (imposed by the thickness of the bumps) between parts and sites. Shear test results are shown in Fig. 4.15 for both HP and TC bonding. Both graphs evidence a quadratic relation between maximal shear force exerted by the bumps and bumps diameter, suggesting the absence of fluid-mediated stiction. Furthermore, no traces of residual water nor HD were detected on both parts and substrates after shearing (see *e.g.* Fig. 4.17). Both kinds of evidence show that completely removing all fluids from the samples after complete thermal treatment is feasible, as compared to the case of common fluxing agents. Shear data measured for bumps with diameters smaller than 200 μm were very noisy and difficult to interpret. Because of this, they were discarded from statistics.

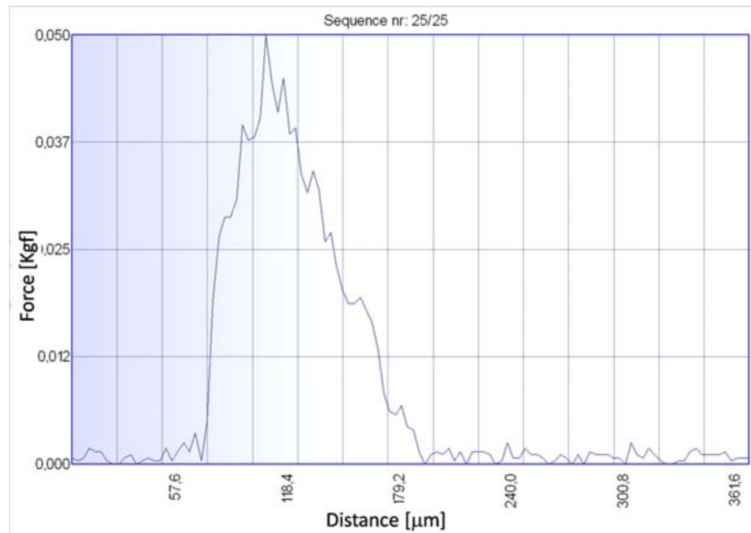

(a) Brittle mechanical failure.

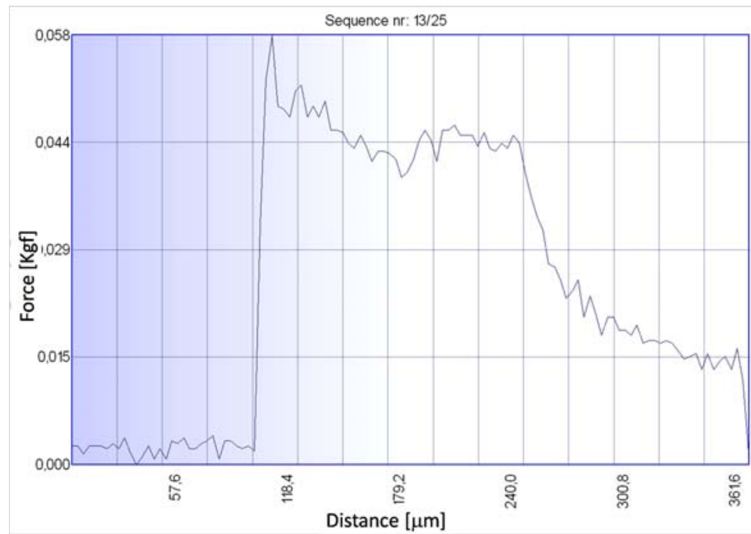

(b) Plastic yield before failure.

Figure 4.14: Traces from mechanical shear tests on bonded parts.

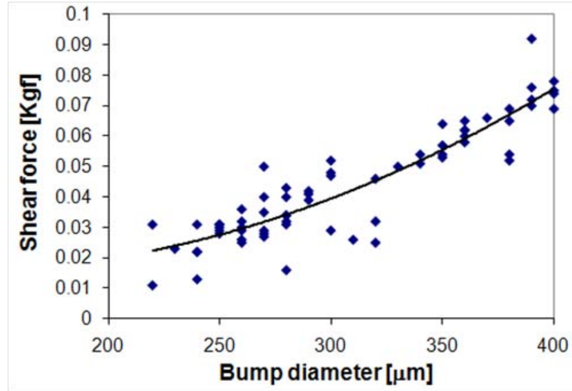

(a) HP-bonded parts.

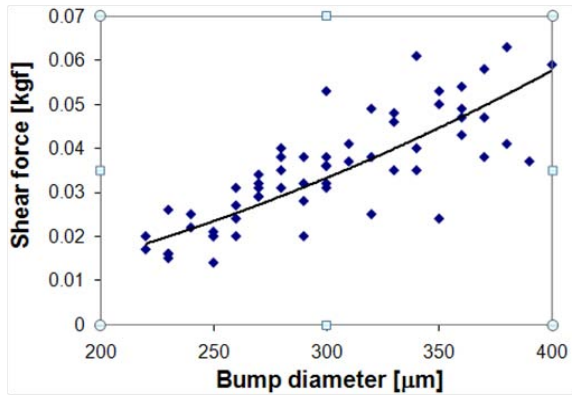

(b) TC-bonded parts.

Figure 4.15: Shear force vs. bump diameter after mechanical shear tests.

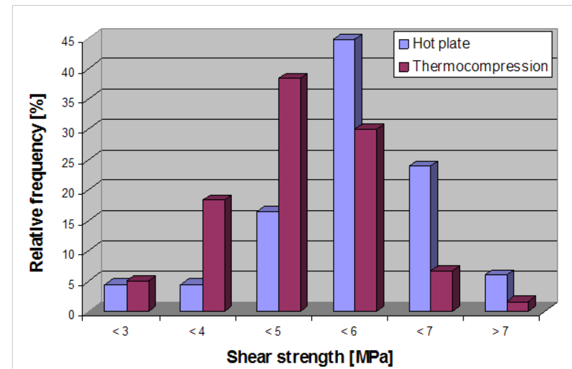

Figure 4.16: Shear strength distributions for HP- and TC-bonded samples.

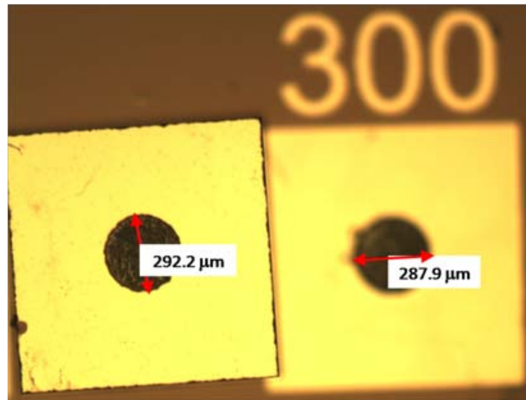

Figure 4.17: Optical picture of a $1 \times 1\,mm^2$ square part (in focus) and its corresponding binding site after HP bonding and shear test.

Measured shear strength values (Fig. 4.16) were in line with earlier literature on In/Au bumps [265]. A summary of data is presented in Table 4.1. No substantial difference in mechanical performance was detected between the HP and TC bonding.

Structural properties

To investigate the structure of the In bumps after bonding, we analyzed cross-sections of the solder joints by SEM and EDX. Figs. 4.18c and 4.18c show examples of 9 μm-thick bumps (sketched in Fig. 4.18a) bonded by HP and TC, respectively. In our experiments, it was difficult to avoid embedding hard particles (mainly silicon carbide, deriving from grinding sheets) into the soft solder layer during sample preparation (*i.e.* grinding and polishing of the cross-sectioned samples embedded in hardened epoxy). Also, milling the surface of the cross-sections by focused ion beam (to clean it prior to EDX inspections) partly removed the exposed In, leaving voids in its place.

The overall appearance of the bumps was rather similar in the two cases. The thin Au adhesion layer deposited on top of the Ni barrier layer was consumed by reacting with In and forming large grains of InAu IMCs. These grains diffused across most of the bump height, probably as consequence of ripening. EDX analysis showed that these IMCs were In-rich (Fig. 4.18d); this is coherent with the equilibrium phase diagram of the In/Au system [269] and the initial composition of our bumps, which had a relative excess of In content compared to Au. The IMCs grains were enclosed in a matrix of pure In. No evident trace of In/Ni IMCs was detected at the Ni interface, probably due to limited reflow time as compared to the slow reaction time of Ni with In [271]. On the top bump side, the Au layer (coming from the Au-coated part side) was also consumed. Interestingly, a layer of unreacted In was still present in such upper part of the bump. We concluded that, under the adopted reflow conditions, Au/In IMCs

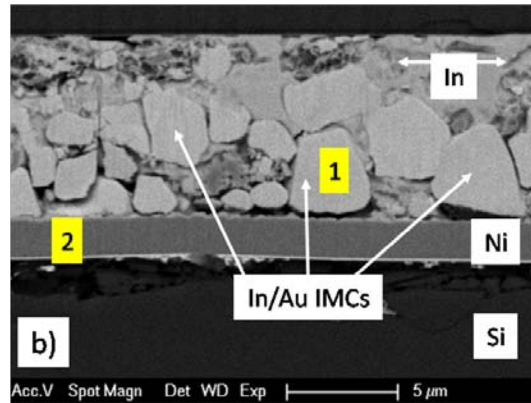

(a) A HP-treated In/Au bump.

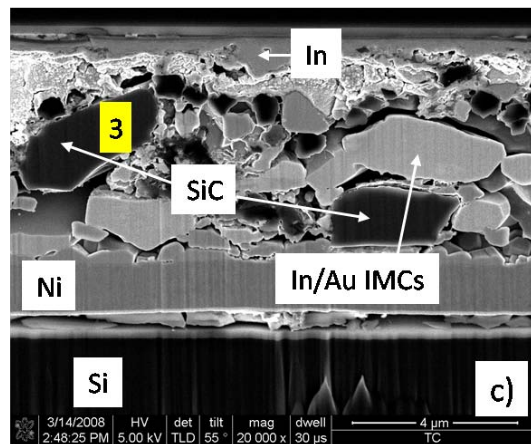

(b) A TC-treated In/Au bump.

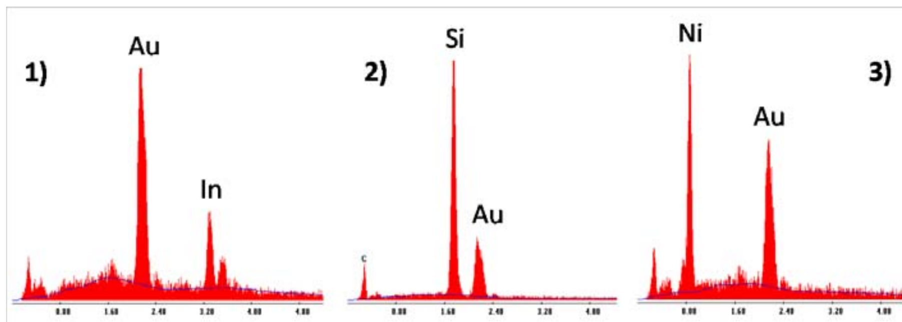

(c) EDX spectra corresponding to the spots 1, 2 and 3 in the above pictures.

Figure 4.18: SEM/EDX analysis of bonded samples.

spread through the bumps, except for the top part where a thin layer of pure In was available for wetting and bonding. The large amount of IMCs, tougher than pure In, may explain the shear strength values measured for the bumps, higher than for pure In [265].

Figure 4.19 show several SEM imagings of the Au part surface as resulting after shear tests. The solder bump profile was typically replicated on the Au surface of the part with fidelity; again, the behaviour under shear for both HP- and TC-bonded samples was rather similar. A wetting precursor layer [272] was seen (Fig. 4.19a) spreading along the edge of the solder imprint, testifying the good quality of the In/Au wetting achieved (with both bonding procedures). This is evidence at once of 1) the effectiveness of our procedure in removing the native solder oxide from the bumps and in preventing its regrowth, and of 2) the lack of interference from the SAM layer on proper In/Au wetting. Upon shearing, bulk In, from 1 to 4 μm in thickness as measured by mechanical profilometry, was transferred to the part surface (as evidenced in the inset of Fig. 4.19a). Moreover, the stripes on the surface of transferred In are evidence of the ductile behaviour of In under shear. In most of examined cases, the plane of failure under shear was entirely inside bulk In. In fewer cases, as in Fig. 4.19b, the failure plane also intersected the bump/part interface, exposing a region of interfacial In/Au IMCs formed at the time of wetting.

Finally, nondestructive scanning acoustic microscopy evaluations were conducted on few bonded samples[7] using a SONIX Fusion system (resolution: 5 μm by 5 μm). For TC samples, occasional incomplete contact and/or partial delamination between bumps and parts was evidenced (Fig. 4.20a and b). For delamination, we assumed that it appeared *after* the bonding as result of manual handling and transportation of the substrates; in fact, delaminations did not appear on bumps with large diameters (> 250 μm; Fig. 4.20c), supporting that delamination may cause failure especially of small, fragile solder joints in absence of proper underfill. Anyway, incomplete solder/part contact at the time of bonding (*e.g.* because of partial tilt induced on the part by the arm of the bonder), or locally-incomplete removal of native oxide from the bump surface cannot be excluded. For HP samples, inspections revealed the occasional presence of small voids in the solder joints, right at the part/solder interface (Fig. 4.20). Besides the aforementioned incomplete oxide removal, causes of voids may be: 1) the use of as-plated rough bumps and/or of incomplete solder reflow: the rough topology of the top solder surface may eventually cause or ease liquid entrapment in small cavities formed at the solder/part interface; 2) the overall profile of the top solder surface, mainly determined by the local bump electroplating conditions. By mechanical and optical profilometry we could derive that solder bumps located near the center of the wafer tended to have a convex profile (*i.e.* they tended to host a cavity in their center), while bumps located near the wafer edge tended to have a mushroom-like concave profile.

Voids were apparently absent in TC samples, possibly due to the higher applied load during TC bonding which helped squeezing out liquids eventually

[7] Courtesy of James Hou, SONIX Applications Group.

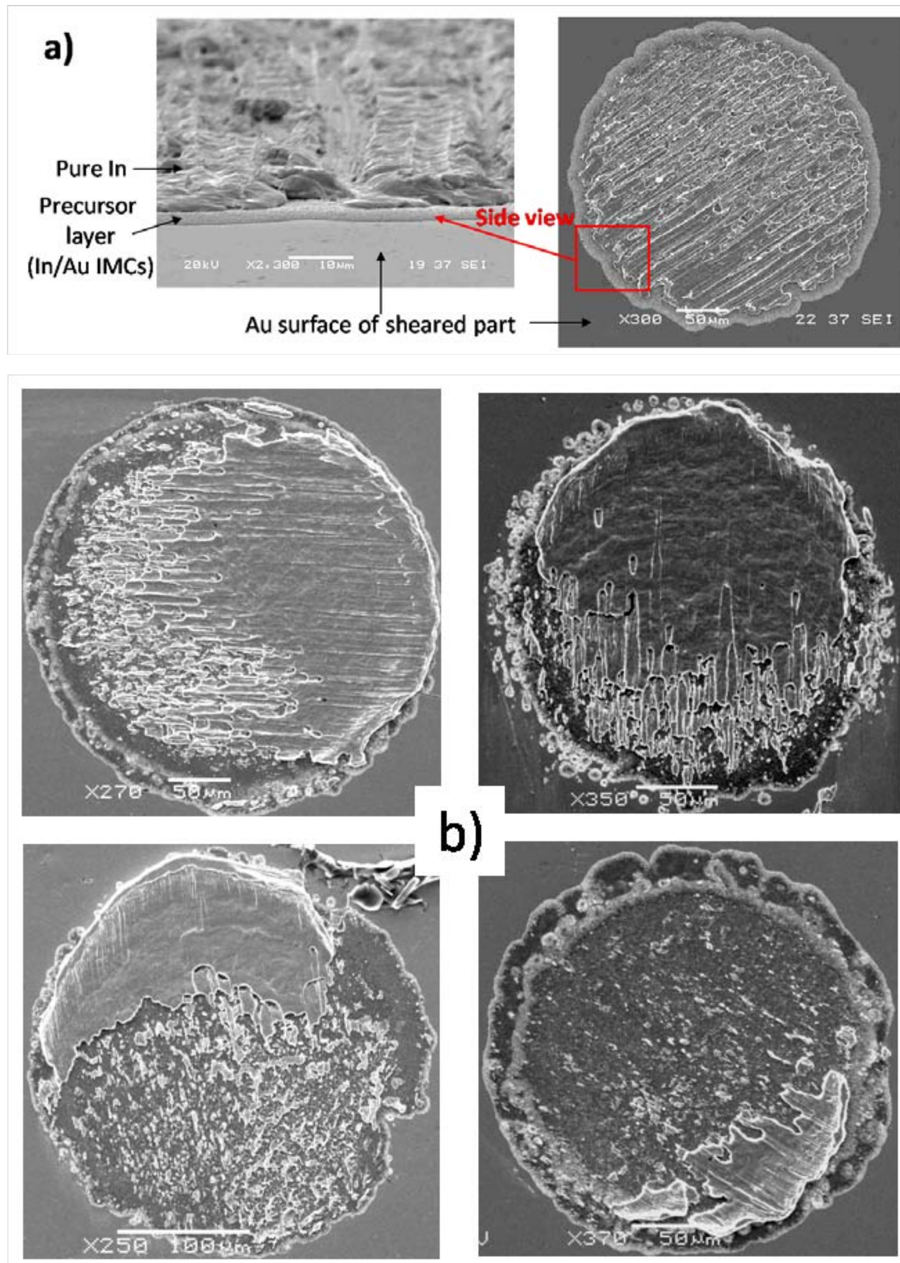

Figure 4.19: **a)** In transfer from bumps to the Au surface of parts, after shear failure. **b)** Planes of shear failure at the In/Au interface.

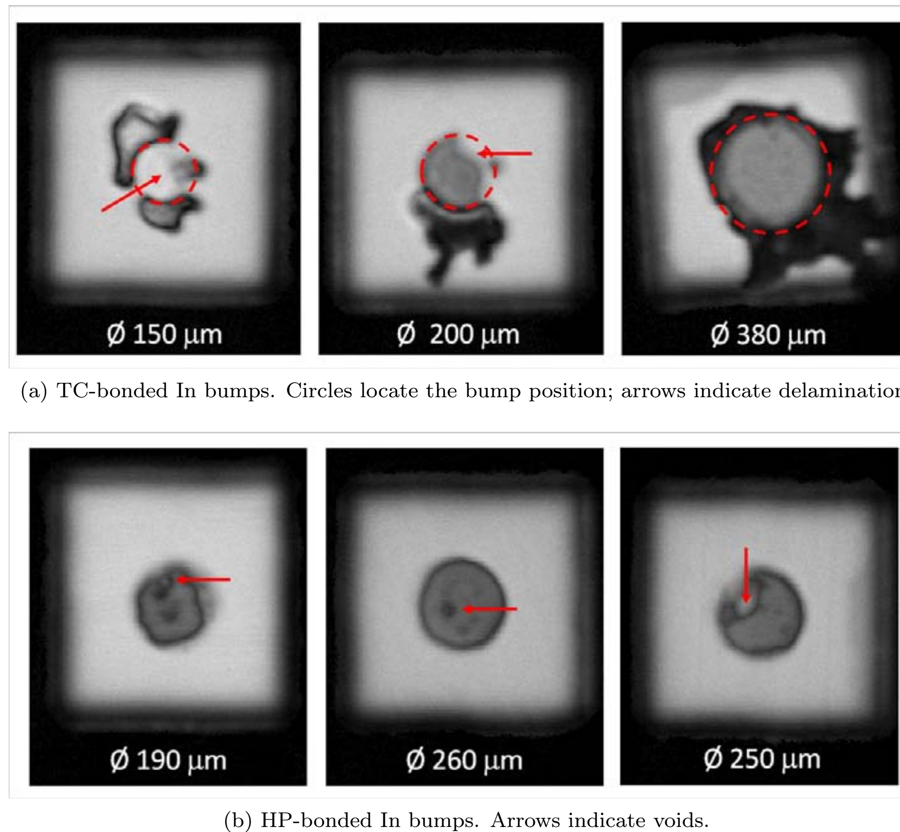

(a) TC-bonded In bumps. Circles locate the bump position; arrows indicate delamination.

(b) HP-bonded In bumps. Arrows indicate voids.

Figure 4.20: Scanning acoustic micrographs of bumps after bonding.

entrapped at the inferface and creating a more uniform contact between bumps and parts. Additional post-bonding reflow may be required to reduce voiding. Voids influence on shear performance could not be characterized, though it may be significant.

A viable alternative process that may avoid pre-bonding solder reflow and yet obtain very-smooth solder bumps, in spite of as-plated solder roughness and local electroplating conditions, entails the *fly-cutting* of the bumps, *e.g.* "shaving" the bumps by means of a rotating tip, operating at wafer level, before performing bonding. The tool allows controlling the final height of the bumps, and deliver bumps of much improved smoothness (see Fig. 4.21 for the case of Sn bumps). This should help obtaining better bonding yield and performance for both bonding methods. Preliminary bonding experiments using fly-cut Sn solder bumps and Au pads showed promising results, to be further investigated.

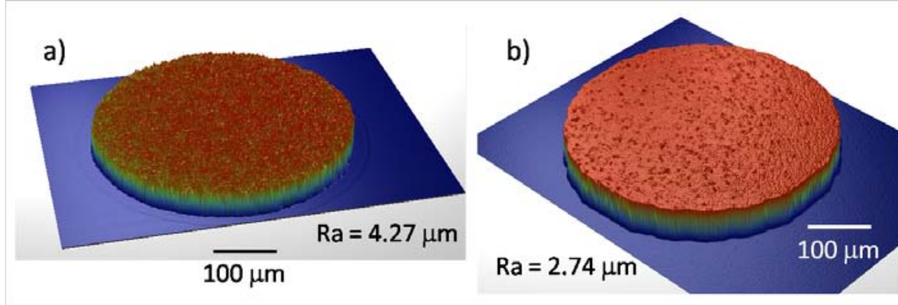

Figure 4.21: Surface roughness of a Sn bump (diameter: 400 μm) before **(a)** and after **(b)** fly-cut, as measured by laser profilometry. The reduction of roughness (Ra) is evident after the treatment.

Electrical properties

We tested the electrical functionality of our In-based interconnects through a test structure featuring a daisy chain.

The matching square patterns of the 1×1 mm^2 binding sites and parts are shown in Fig. 4.22a and 4.22b, respectively. They were lithographycally patterned and etched on a Ti/Ni/Au layer (50/500/50 nm-thick; measured sheet resistance: 0.67 $\Omega/\square$) evaporated over 8" silicon oxide-covered Si wafers. The binding sites included 4 electroplated In bumps (diameter: 120 μm), whose relative position within the site matched that of equal-sized bonding pads patterned on the metal-coated side of the parts. The bumps were externally addressable by independent gold pads, to enable post-assembly eletrical measurements. The cross-linking between the bonding pads formed multiple equivalent electrical paths between the external pads. Substrates and parts were chemically preconditioned as described in Sec. 4.2.1. An HD-coated binding site and the final, self-assembled and bonded structure are shown in Fig. 4.22a and 4.22c, respectively. Though this binding site design was not optimal for conformal dip-coating purposes, we opted for it because of overall ease of processing.

In/Au bonding was performed with both procedures described above. After correct assembly and alignment of parts on the binding site in one of the 4 degenerate possible configurations, the electrical paths linking each pair of external pads was ideally identical. After assembly, 2-point resistance measurements were performed between pairs of external pads. The measured resistance value of 28$\pm$2.8 Ω. According to a simplified model of the structure (sketched in Fig. 4.23), where the entire electrical resistance is attributed to the paths of thin metal layers between the external pads, we expected a resistance value $R_{AB} \simeq 27$ Ω. We attributed the discrepancy partly to the contact resistance of the probes of the measurement tool, and particularly to the eventual tolerances in the dimensions of the evaporated metal layer; interlayer diffusion might also have altered their resistivities.

Moreover, we saw no significant difference in measured resistance values be-

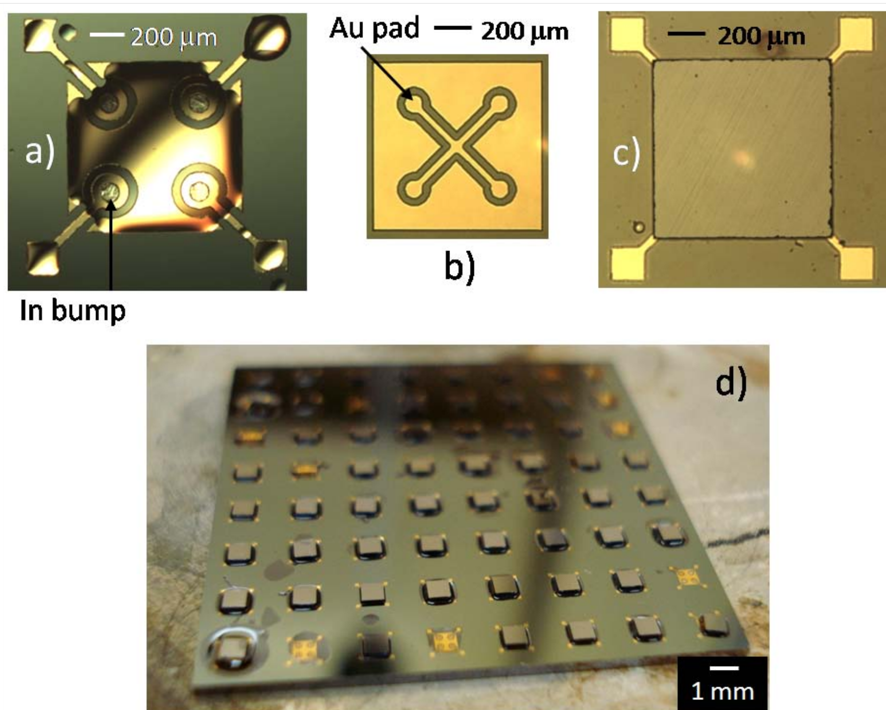

Figure 4.22: Electrical test structure. **a)** As-coated binding site with 4 externally-addressable In bumps. **b)** Functionalized Au side of the parts. **c)** Self-assembled and bonded part on binding site. **d)** Substrate-level bonding on HP of the test structures.

tween HP and TC samples - HP samples showed a higher dispersion of resistance values, though. This is evidence that the eventual presence of SAMs does not prevent the electrical functionality of the interconnects. We did not investigate the actual fate of the organic interlayer.

Overall, though we were not able to determine the contact resistance of single In bumps, our experiments proved the electrical functionality of interconnects.

4.3.3 Further insights

As mentioned, though the boiling point of HD is 287 ^{o}C, depending on their size the HD lenses completely evaporated at much lower temperatures - around 160 ^{o}C in our experiments. We do not expect significant differences employing longer-chain hydrocarbons. Thus, performing HP bonding in a reducing or very-low oxygen concentration atmosphere is mandatory for solders with higher melting points. This would also allow for more flexible reflow profiles. In our experiments, Sn/Au bonding between bumps and parts could be achieved only

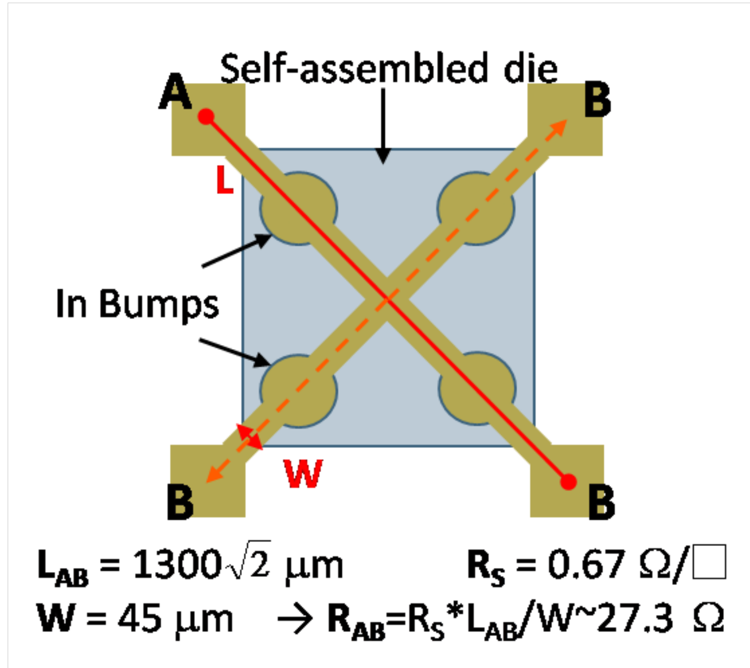

Figure 4.23: Model of the electrical resistance of the test structure.

for parts bonded under forming gas atmosphere.

We qualitatively observed that the adopted bonding method influenced the alignment of the parts on the binding sites. In TC bonding, the applied external load should ideally freeze the position of the parts by putting them in contact with the underlying bumps. In practice, imperfect parallelism between chuck and arm of the bonder may cause lateral displacement of parts, especially if the parts stand in a vertically-tilted position - which may not be a rare evenience [243]. Also, the distribution of the bumps inside the binding site and the uniformity of their thickness may influence the final position of the parts under the applied pressure: the bumps should provide a symmetric co-planar support to the parts. In HP bonding, the final position of the parts is sensitive to the dynamics of removal of fluids, thus to the profile adopted for the thermal treatment, which also controls the solder re-oxidation rate.

As mentioned, part-to-substrate alignment was directly affected by dicing and lithographical tolerances during fabrication, which alone amounted to ± 5 μm. This prevented us, in the first place, from estimating the alignment accuracy achievable with our methods.

4.4 Conclusions

We experimentally demonstrated a procedure to seamlessly-establish lead-free solder-based interconnects within a capillary part-to-substrate SA process. We analyzed the mechanical and electrical properties of the resulting interconnects.

According to our experimental evidence, we conclude that:

1. *the issue of the oxide passivating the solder bumps is effectively overcome* by chemically-removing the oxide right before coating the bumps with a non-reducing fluid - which needs to be preserved throughout subsequent assembly and bonding operations;

2. alkanethiol SAMs seem *not* to prevent metallic bonding between oxide-free solder and Au surfaces;

3. *no substantial difference* in mechanical and electrical performance exists between interconnects established with and without application of external load during bonding, though the former case yields better process reliability and repeatability.

Observation 1) is of paramount relevance. 3) is also greatly interesting: it promotes the technique to the assembly of parts over *e.g.* curved, stretchable or fragile substrates, which cannot tolerate substantial load for bonding purposes.

Future work will need to address the mandatory integration of underfill in the process flow, the further optimization of bonding parameters, the use of alternative fluids to enhance assembly and reflow steps, and the estimation of the accuracy achievable in part-to-site alignment after solder bonding.

Chapter 5

Avoiding Mutual Adhesion between Parts

Mutual adhesion between parts can be thought of as a 3D self-assembly process interfering with a 2D, *i.e.* part-to-substrate, assembly process. It can significantly lower the yield of the intended process, therefore it must be avoided. This Chapter briefly discusses possible ways to face this issue. Key role is played by the proper conditioning of mating surfaces.

5.1 The interfering 3D self-assembly process

In the standard embodiment of capillary SA (Sec. 2.1), the functional side of the parts is conditioned to be hydrophobic - more generally, to repel the hosting liquid while being selectively wet by the lubricant. During the assembly process, the parts are immersed in the hosting fluid - normally, water. Part dispensing and mixing, part movement across the substrate and part recycling make the possibility that the parts get into direct physical contact not negligible. If the parts get in contact through their hydrophobic sides[1], they will attract each other because of the *hydrophobic interaction* in water (Sec. 2.2). As a consequence, they will eventually stick together - normally, in an irreversible way. This basic phaenomenon is exploited *e.g.* recent works on 3D SA of microparts [273, 274, 275]. But for our purpose, it is a troublesome *interference*: it makes the involved parts no longer useful for the assembly, since their functional sides, henceforth hidden, can no longer sense the available binding sites.

It is partly to avoid these events, besides reducing long-term effects of water on device reliability and avoiding surface contaminations, that the parts are stored in low surface-tension inert liquids (*e.g.* ethanol, methanol) when unused.

[1] Considering two-dimensional parts with one hydrophobic side out of two, the probability of mating with both hydrophobic sides is ideally 1/4.

Besides, during the above mentioned operations air bubbles may be created or introduced in water. Air bubbles are highly-hydrophobic and mobile. Driven upward by buoyancy, they will adsorb (and eventually dissolve) at the interface between water and the external fluid (*e.g.* at the water/air interface); otherwise, during part stirring they will float all around the assembly space. In all cases, they may easily stick to both the hydrophobic lubricant lenses of the substrate sites and/or on the functional side of the parts. In the first event, the bubbles will compromise if not prevent the correct alignment and/or pose of the parts on the sites. In the latter, they may catalyze multi-part aggregations, where the number of parts eventually involved would depend on the relative size of the bubble and parts.

Diluting water with miscible, inert and low-surface-tension liquids may be an option to overcome the issue. Anyway, this would also proportionally decrease the interfacial tension of the original fluid couple, thus affecting capillary alignment and restoring forces (Sec. 2.2).

Moreover, if a temporarily assembled part is accidentally removed from its binding site (*e.g.* by collision with an impending part), it will most probably bear a fraction of the lubricant lens on its hydrophobic side (see Ch. 7). This lens largely-extends the spatial range of the hydrophobic interaction (Sec. 3.1), so that the chance of mutual adhesion between parts becomes even higher. In fact, such spatial amplification of the hydrophobic interaction was the very basis of the first microscopically-engineered capillary 3D self-assembly method [119, 128] – in our case, interfering with the desired 2D assembly process.

By the same token, in molten-solder-driven SA, it is also to avoid mutual adhesion between parts that molten solder bumps are normally not incorporated on the floating parts themselves, but only on the substrate sites. When the bumps are on the parts, they need anyway not be exposed to the surface, so to minimize and eventually avoid altogether the chance of aggregation with other parts [29].

In spite of being a potentially-serious yield killer, the issue of mutual part adhesion was rarely mentioned in the capillary part-to-substrate SA literature.

We propose to face this issue applying *smart* surface chemistry on the functional side of every part.

5.2 The unnecessary assumption[2]

We thought that the issue of mutual part adhesion arises from an implicit and undisputed assumption: once in place, the chemical pre-conditioning of the functional side of the parts is *fixed*, *i.e.* the parts' surface chemistry cannot adapt to the changes in local chemical environment.

This needs not to be so. In principle, by endowing each part with passive chemical sensing properties and the ability to adapt their surface state[3], we

[2]Full details can be found in [276].

[3]This amounts to endow the parts with a chemical and passive conformational switching mechanism.

thought the issue could be solved effectively.

With specific reference to the standard embodiment of capillary SA, we envision the utilization of *switching surface chemistries*, *i.e.* that are hydrophilic when in contact with water - in general, chemistries that like to be wet by the hosting fluid, thus repelling other parts - and turn hydrophobic when in contact with the hydrophobic lubricant[4].

Surface chemistries able to react in response to external stimuli of various physical nature and correspondingly change their properties or perform specific tasks (*e.g.* motion, transport or other forms of mechanical work) are presently object of intense study and show promise for interesting and far-reaching applications [277].

We envision to employ switching macromolecules or some families of polymers on the functional side of the parts to perform selective switching of surface wetting character according to the chemical properties of the local environment.

5.2.1 Molecular switches

One option consists in attaching to the functional side of the parts macromolecules endowed with (at least) two moieties with substantially different chemical character, *i.e.* one lyophilic and the other lyophobic. The molecules need to expose to the environment the moieties determining the surface wetting character with mutual exclusivity; and, as already said, the transition has to take place only when required, namely when the solvent in contact with their functionalized side happens to change according to their movements in the assembly space. A vast class of macromolecules, collectively named *molecular switches* and which are important in virtually every significant biological process, appears to suit this purpose.

According to Kay [277], molecular switches are nanometric structures that influence the system as a function of their state, as opposed to motors which influence the system as a function of the trajectories of their components. That is, returning the switch to its original state cancels its effect, while it does not in the case of a motor. Both switches and motors work efficiently only when out of thermodynamic equilibrium: they need an external input (*i.e.* energy, and eventually information) to operate [5]. Particularly, switches exist in at least two stable configurations, and the transitions between states are triggered by external stimuli (*e.g.* chemical, electro-magnetic, mechanical).

In the molecular switches of our interest, the groups of opposing functionalities are only *mechanically* interlocked and not covalently-bound to each other. They are still molecules nonetheless (and not supramolecular complexes), as covalent bonds must be broken to separate the constituent parts. Typical ex-

[4] The set of parts would then behave as if supervised by an omniscient *demon*. The demon would know the exact position, orientation and movement of each part and tempestively switch its surface chemistry according to the modification of its local chemical environment.

[5] Both molecular switches and motors are examples of nanometric ratchets that achieve biased motion on periodic asymmetric energy potentials in presence of Brownian perturbations [277, 278].

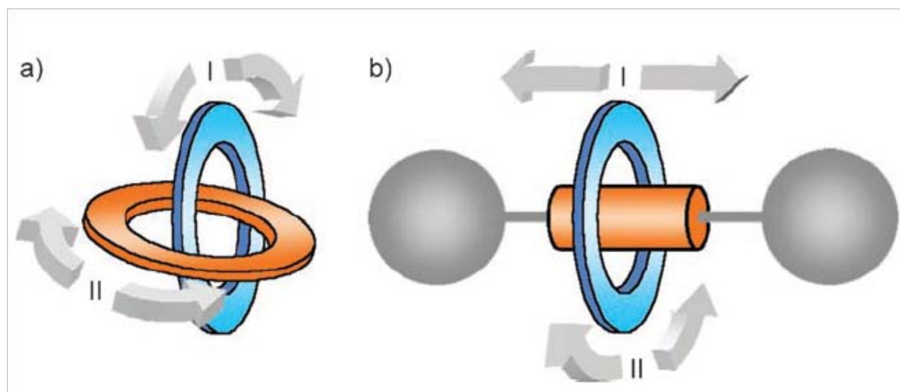

Figure 5.1: Large-amplitude movement modes for a [2]catenane **(a)** and a [2]rotaxane **(b)**, after [277].

amples are rotaxanes and catenanes (Fig. 5.1). The mechanical bond severely restricts the relative degrees of freedom of the components in several directions, but it still allows large amplitude motion along specific directions. For our purposes, this means that, when one of the macrocycles is attached to the substrate surface, the other still has some available degrees of freedom to change its relative position and orientation.

Rotaxanes are molecular shuttles composed of one or more macrocyclic structures locked onto a linear central thread and thereby confined (*i.e.* prevented from dethreading) by bulky stoppers, placed at both thread ends (Fig. 5.1b). Catenanes are instead chemical structures in which two or more macrocycles are interlocked (Fig. 5.1a). In both cases. the large-amplitude motions are: pirouetting of the macrocycle around the thread (in rotaxanes) or the other ring (in catenanes), and translation of the macrocycle along the thread (in rotaxanes, also called shuttling) or around the other ring (in catenanes). Because of synthesis, rotaxanes and catenanes without sites of attractive interaction between the macrocycles and thread are relatively rare. It is more common that the thread and or macrocycles consist of one or more *stations*. Motions therefore become the movements on, off, and between such stations, with rates dependent on the strength of the intercomponent interactions (Fig. 5.2). Importantly, both have the ability to change the relative positions of their interlocked components (*i.e.* to hop between stations) by means of external triggers such as *e.g.* light, temperature, pH, reversible covalent bond formation.

If the macrocycles embody different chemical functionalities, when the switches are attached (*e.g.* by covalent bond) to a surface their state transitions are expected to induce corresponding surface wetting changes. The trigger we propose to use, given our boundary conditions, is the *difference in pH* between the hosting fluid (*e.g.* water, whose pH can be easily tailored) and the lubricant (*e.g.* HD). As an example, the (1+1+1+1) catenane described in [279] (Fig. 5.3) suits the desired chameleontic performance. When in a polar solvent, the am-

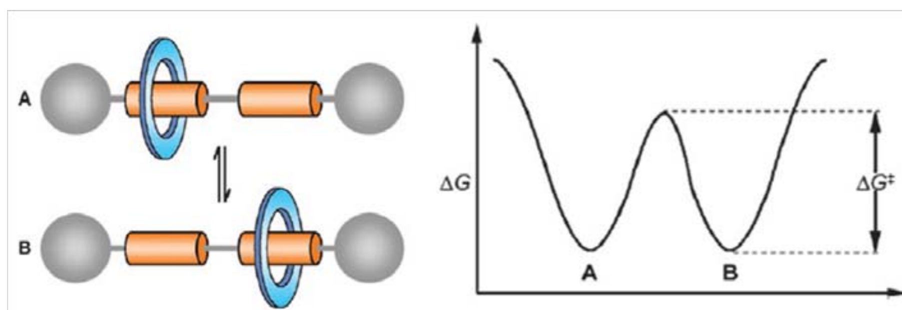

Figure 5.2: Idealized free-energy profile for movement between two identical stations in a [2]rotaxane, after [277].

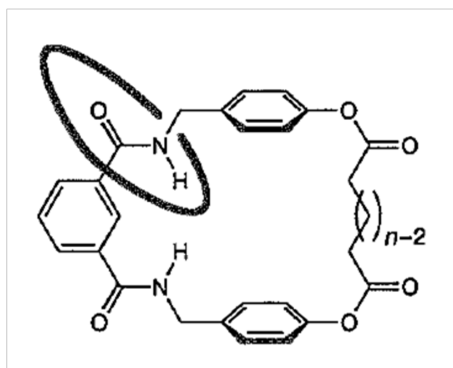

Figure 5.3: An example of catenane with amphiphilic units sensitive to the pH of the local chemical environment, after [279].

phiphilic units of the catenane arrange themselves so that the polar groups are at the surface of the supramolecular structure, where they can form hydrogen bonds with the solvent molecules, while the lipophilic groups are hidden so to minimize their interactions with the solvent; in nonpolar solvents the situation is reversed.

From a processing point of view, the present solution involving macromolecules seems rather attractive because such macromolecules can reportedly be grafted onto surfaces where alkyl or silane-based SAMs are pre-deposited [279]. Alkyl SAMs were already employed in our process, as described in earlier Chapters. Thus the additional process load required by this additional functionalization amounts to a single process step.

5.2.2 Switching polymers

A class of microgels, whose main representative is poly-N-isopropylacrylamide (pNIPAAM), may also suit our purpose. pNIPAAM is a thermo-sensitive poly-

mer, *i.e.* it undergoes physical changes when subjected to external thermal stimuli. The changes affect, among others, the polymer's volume [280] and wettability. Such properties can be enhanced by proper modifications and preparations of the polymer. When pure, pNIPAAM is hydrophilic at temperatures below 32°, hydrophobic at higher temperatures. When co-polymerized with acrylic acid, its wetting character becomes sensitive to the pH of the local chemical environment. The switch in wetting character can also be made reversible [281].

We envision the possibility of depositing *(e.g.* by spinning) a thin layer of acrylic acid-modified pNIPAAM on the functional side of the parts - eventually pre-conditioned with an hydrophilic SAM coating to improve the adhesion of the polymer - as alternative embodiment of the general idea.

Chapter 6

Modeling of Self-Assembly Dynamics

In this Chapter we model the *collective dynamics* of ensembles of passive parts self-assembling by fluidic means.

We present two approaches. The first is *analytical*. We borrow from literature two models inspired by chemical kinetics, generalize them to include both assembly and *dis-assembly* events - and *criticize* them. The second approach rides our criticism and is built around programmable software agents, therefore called *agent-based* modeling. This latter approach is supported by simulations which, besides reproducing well-known experimental results, are furthermore used to investigate issues that were so far outside the reach for earlier modeling attempts.

6.1 Dynamics of self-assembling systems

Fundamental to Nature, and pervasive in biology, chemistry and technology [82, 83, 76], self-assembly has such a wide range of expressions and applications that it is not possible to capture them all within the limited margins of these pages. All life forms are probably examples of dynamic, coded, active and hierarchical self-assembly, while even many passive and static examples, such as *e.g.* crystals and proteins, show some kind of self-correcting properties.

Vast literature is dedicated to the modeling of self-assembly dynamics.

Models based on master equations, inspired by analogy with chemical kinetics, were first introduced by Hosokawa to describe the time evolution of the discrete aggregates emerging in passive self-assembling systems [282, 283], and formalized and further developed by Klavins for active, programmable robotic assemblies [284]. The idea is to write, for each of the temporary configurations of parts that can be reached by the process, the rate equations combining all

the events causing their creation and destruction. A matricial master equation is thus obtained; rate constants can be derived by fitting the experimental data.

As for other applications, Adleman developed a model for the SA of linear polymers out of molecular units [285]. The model is based on difference and differential equations with initial conditions, and allows the characterization of the resulting equilibria of the systems. Dehon described a stochastic model of a self-assembled nanowire-based address decoder [286]. White proposed a model for self-reconfigurable cellular robots based on passive stochastic self-organization [287]. Klavins introduced a graph grammar-based approach to model active, reconfigurable assembly of programmable units [96, 288]. Finally, Mermoud considered the modeling of self-assembly processes at multiple levels of abstractions and scales [289].

6.2 Analytic models for static passive SA

We focus on the dynamics of static[1] passive SA processes only. Probabilistic approaches are common for the theoretical modeling of the dynamics of stochastic[2] SA. Models that mathematically relate control and environmental parameters (*e.g.* shape and number of parts and binding sites, volumes, parts mobility, duration of experiments) to process requirements (*e.g.* expected time to achieve a predefined yield, throughput) are of foremost interest. SA proceeds by *discrete asynchronous deterministic*[3] *interactional* (mainly collisional) *events*, each taking place with non-null probabilities and error rates. Discrete mathematics and difference equations would constitute the natural setting for its description. However, discrete-time models quickly become exceedingly complex. Besides being easier and more intelligible, continuous-time models based on differential equations can be thought as the limit of discrete models for large numbers of interacting parts and for high frequency of binding events[4]. It is no less impressive that such simplifications lead to meaningful results.

In Secs 6.2.1 and 6.2.2, we present our generalization of two analytical models - originally proposed by Verma [151] and by Zheng [99] - describing the dynamics of part-to-substrate and part-to-part passive self-assembling systems, respectively. The generalization is derived by introducing dis-assembly events in both models, *i.e.* by considering the assembly as eventually *reversible.*

For ease of modeling, we hereby assume that:

1. part mobility and mixing is so that the parts can efficiently explore the entire physical assembly space and have the same chance of interaction *(i.e. well-stirred* solutions);

[1] There is no contradiction here: we model the dynamics of self-assembling parts along their history of energy minimization.

[2] "Stochastic" is hereby used in the acception defined in Note 21 of Ch. 1.

[3] We hereby refer to supramolecular assembly excluding quantum uncertainties.

[4] Chemical *reaction-rate equations* are ordinary differential equations (ODEs) that apply in the *thermodynamic limit*, *i.e.* for boundless assembly space Ω, infinite cardinality N of ensemble, and finite element density N/Ω [290].

2. all binding sites have the same probability[5] of being filled;
3. assembly at one site does not affect the availability of any other site for assembly, nor its probability of being filled;
4. the binding (*i.e.* assembly) and breaking (*i.e.* dis-assembly) probabilities are time-invariant and independent on the number of parts and binding sites present;
5. only two-body events are possible, both for assembly (*i.e.* the result of each assembly event is a *dimer*) and dis-assembly.

These simplifying assumptions, as well as other limitations intrinsic to the analytic approach, will be critically assessed in Sec. 6.3, which will set the background to the introduction of a novel numerical framework for the study of the dynamics of fluidic self-assembly processes - namely, the agent-based modeling framework - which can positively tackle many of the downsides of common chemistry-inspired approaches.

We first define the parameters used in the analytical models described below:
$N_P \equiv$ number of parts;
$N_S \equiv$ number of binding sites (for 2D assembly) or target carriers (for 3D assembly);
$x(t) \equiv$ number of assembled parts = number of filled binding sites[6];
The above three parameters satisfy the inequality $0 \leq x \leq N_S \leq N_P$.
$R_A \equiv$ rate of assembly;
$R_D \equiv$ rate of dis-assembly.

6.2.1 The steady-state model[7]

This model does not consider the actual time evolution (*i.e.* history) of the system: according to the steady-state hypothesis, the asymptotic result of self-assembly process is set by the *equilibrium of the concurrent assembly and dis-assembly forces* acting in the system[8]. Applied to part-to-substrate SA, the result of the model resembles that of a superficial adsorption process[9] [201].

We first assume phaenomenologically that the rate[10] of assembly R_A is proportional to the number of unassembled parts $(N_P - x)$ and to the number of unfilled sites $(N_S - x)$, *i.e.* $R_A = k_A(N_P - x)(N_S - x)$ where k_A is the assembly rate constant. The rate of dis-assembly R_D is assumed to be proportional to

[5]Similarly to Sec. 2.5, this may be defined by the capture cross-section (CCS) of the site. The CCS may depend on physical (*e.g.* surface energy) and geometrical parameters.

[6]The time dependence of $x(t)$ will be assumed throughout, but it will not be explicited in the following equations for formal conciseness.

[7]This is a generalization of the model originally presented by Verma in [151].

[8]These forces represent the origin of the processes (whose name depends on the context, *e.g.* generation/recombination, birth/death) included in the ensuing *master equation*.

[9]This should not come as a surprise, since assumptions conceptually-similar to 1)-3) of the previous Section were also used *e.g.* by Langmuir to derive his adsorption isotherm [291].

[10]The explicit form of R_X is called *propensity function* in probabilistic contexts: $R_X \cdot dt$ expresses the probability for the event X to happen in the next infinitesimal time dt [290].

the number of filled sites by a dis-assembly rate constant k_{D_1}, *i.e.* $R_D = k_{D_1}x$. This is a form of self-disassembly which may take place in noisy environments, *e.g.* when excessive vibration is induced on the substrate and transferred to the assembled parts to the point that they escape their energy minimum state.

To achieve the steady state, we require that:

$$\frac{dx}{dt} = R_A - R_D = 0 \Rightarrow R_A|_{x_{eq}} = R_D|_{x_{eq}} \tag{6.1}$$

Solving this quadratic equation for x_{eq} and defining $C_1 \equiv k_{D_1}/k_A$, the filling ratio (or yield) $\chi \equiv x_{eq}/N_S$ is obtained from the only possible equilibrium solution:

$$\chi = \frac{1}{2} + \frac{N_P + C_1}{2N_S} - \sqrt{\left(\frac{1}{2} + \frac{N_P + C_1}{N_S}\right)^2 - \frac{N_P}{N_S}} \tag{6.2}$$

The model suggests that a high assembly yield can be achieved by using redundant parts (*i.e.* a large part-to-binding site ratio; this is indeed commonly done in the experimental literature [150, 142, 29, 164]); by increasing the constant k_A representing the probability of assembly (e.g. by enhancing shape matching and selectivity between the parts and the sites; by improving part mobility and avoiding *frustration* *i.e.* the obstruction of binding sites); and by decreasing the probability of dis-assembly represented by k_{D_1} (*e.g.* by designing the system so that the desired assembly configuration is robust against vibrational noise, turbulent flow and other physical interferences).

Alternatively, dis-assembly of assembled parts may be caused by the number of residual parts present in the assembly space. The corresponding dis-assembly rate is $R_D = k_{D_2}x(N_P - x)$. Since assembly proceeds by collisions, this dis-assembly process may be present in systems where the parts need to have enough kinetic energy to wander in assembly space, and by hitting already assembled parts they may disassemble them or knock them out of place (see *e.g.* [164]). For $C_2 \equiv k_{D_2}/k_A$, the filling ratio derived from Eq. 6.1 in this case becomes:

$$\chi = \frac{1}{1 + C_2} \tag{6.3}$$

Finally, both self-disassembly of assembled parts and concurrent dis-assembly induced by residual parts can be described in a single model. By putting $R_D = k_{D_1}x + k_{D_2}x(N_P - x)$ in Eq. 6.1, the general result for the filling ratio is:

$$\chi = \frac{N_S + (1 + C_2)N_P + C_1}{2(1 + C_2)N_S} - \sqrt{\left(\frac{N_S + (1 + C_2)N_P + C_1}{2(1 + C_2)N_S}\right)^2 - \frac{N_P}{(1 + C_2)N_S}} \tag{6.4}$$

which includes Eq. 6.2 and 6.3 as special cases for $C_2 = 0$ and $C_1 = 0$, respectively.

6.2.2 Nonlinear time-continuous model[11]

The time evolution of self-assembling systems is in general a nonlinear process, due to the collective and interactive behavior of the ensemble of parts. This is best described by a time-continuous model based on ODEs.

For clarity, in this setting it is more convenient to express the assembly and dis-assembly probability constants, introduced in the previous section, as inverse of time constants. We therefore define the average *time-to-assembly* $T_A \equiv 1/k_A$ and the average *time-to-disassembly* $T_D \equiv 1/k_D$, which represent the expected time for an effective (*i.e.* leading to assembly) or destructive (*i.e.* leading to dis-assembly) single part/single site collision, respectively[12]. These are, in principle, phenomenological parameters characteristic of the assembly system which could be experimentally estimated during multiple assembly runs (*e.g.* Zheng and Jacobs give an estimate of T_A - what they call "single-component-single-carrier" capture time - in their paper). We define a self-assembly system *efficient* if $0 < T_A < T_D$, *i.e.* parts have time to assemble before some type of dis-assembly takes place.

As in the steady-state model, we assume that the assembly rate is proportional to the number of residual parts and to the number of unfilled sites, *i.e.* $R_A = [(N_P{-}x)(N_S{-}x)]/T_A$. We also introduce a general dis-assembly term D, which is a function of the number of filled sites x. Hence, we can derive a general, first-order differential equation for the time evolution of the number of filled sites:

$$\frac{dx}{dt} = \frac{(N_P - x)(N_S - x)}{T_A} - \frac{D(x)}{T_D} \tag{6.5}$$

The hypothesis of considering only two-body events (assumption 3 of Section 6.2) has the mathematical consequence of making $D(x)$ of order 2 in x at maximum. This in turns allows a closed-form analytical solution of Eq. 6.5, whose details depend on the specific form of $D(x)$.

Using the initial condition $x(t = 0) = 0$, the solution to Eq. 6.5 can be put in the form:

$$x(t) = x_2 \frac{e^{(x_1 - x_2)\frac{t}{T_A}} - 1}{e^{(x_1 - x_2)\frac{t}{T_A}} - \frac{x_2}{x_1}} \tag{6.6}$$

where $x1 > x2 > 0$ are the roots of the second-order polynomial in x which appears during the solution of Eq. 6.5; they depend on N_P, N_S, T_A, T_D and on the coefficients of $D(x)$. According to Eq. 6.6, $x(t)$ shows an exponentially increasing trend with assembly time. In the limit of long assembly times, we get:

[11] This is a generalization of the model originally proposed by Zheng and Jacobs in [99].

[12] If the system is so that such time constants are proportional to the volume of the assembly space V, than the time (rate) constants may also express a dependence on (the inverse of) V. This is done *e.g.* in chemical kinetics [290].

$$\lim_{t \to \infty} x(t) = x_2 \tag{6.7}$$

Furthermore, by inverting Eq. 6.6 the time required to achieve a desired assembly yield can be predicted.

According to the model, the number of parts assembled at a certain time is thus dependent on the duration of the assembly process, on the number of parts, on the number of sites and on the time constants of the system. We now look at particular cases.

1. *Irreversible assembly.* This is the case for $T_D \to \infty$, for which we get $x_1 = N_P$ and $x_2 = N_S$. Hence, in *absence* of dis-assembly events, according to Eq. 6.7 the model predicts the asymptotic filling of *all* binding sites in time (see Fig. 6.1a and 6.1b), consistently with Eq. 6.4 for $C_1 = C_2 = 0$. This means that, in principle (*i.e.* excluding defects and damage to parts), stochastic SA can achieve 100% assembly yield. In practice, the assembly may need to terminate within a prefixed time: the maximal assembly yield may be out of reach in a real process.

   Case (1) is the particular case originally considered by Zheng and Jacobs [99]. In their experimental work, they reported the exponentially-increasing yield of the assembly for a linear increase of assembly time. They also estimated the time-to-assembly constant T_A by measuring the mean capture time for a single part and a single target carrier in the assembly space. Exponential increase of assembly yield as a function of time was also demonstrated by Stauth and Parviz [143].

2. *Dis-assembly proportional to residual parts and filled sites.* In this case, typical of part-to-substrate assembly with no substrate vibration, the dis-assembly term of Eq. 6.5 has the form $D(x) = x[N_P - x]/T_D$, which leads to $x_1 = N_P$ and $x_2 = N_S/(1 + T_A/T_D)$. Thus, according to the model a finite time-to-disassembly constant implies an asymptotical yield always lower than 100%. In analogy to Zheng and Jacobs' work, T_D could be estimated as the mean time-to-disassembly of single assembled parts.

3. *Dis-assembly in part-to-part assembly.* For a general treatment of dis-assembly events in this setting, all possible collision events between assemblies (*i.e.* dimers) on one side, and assemblies, unassembled parts and residual target carriers on the other need to be considered - each of these events can in principle induce dis-assembly. The dis-assembly term of Eq. 6.5 then assumes the form:

$$D(x) = \frac{x[(N_S - x) + (N_P - x) + \frac{x-1}{2}]}{T_D}$$

The closed-form solution of Eq. 6.5 for this case, though not handy, can nonetheless be interpreted along similar lines as those discussed in the previous scenarios.

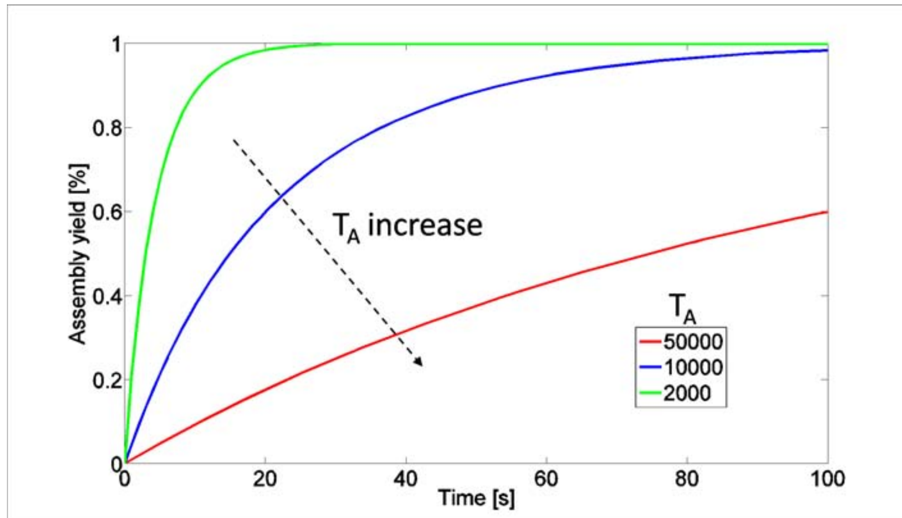

(a) Effect of T_A on assembly yield χ, for $N_P = 500$, $N_S = 100$ and $T_D \to \infty$.

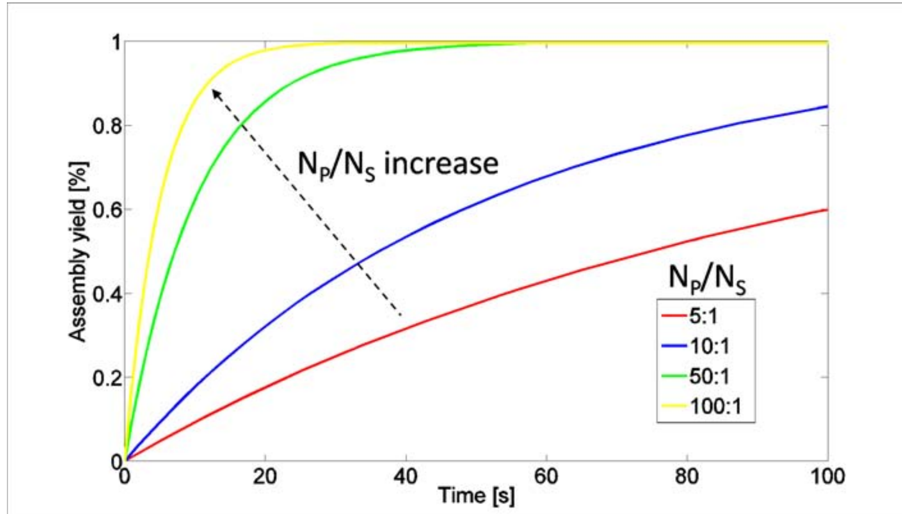

(b) Effect of redundancy N_P/N_S on assembly yield χ, for $T_A = 50000\,s$ and $T_D \to \infty$.

Figure 6.1: Assembly histories predicted by Eq. 6.6

6.3 Critics to analytical modeling

Though possibly capturing the average behavior of the stochastic processes [292], the aforementioned analytic, master equation-based descriptions of the dynamics of SA has some remarkable limitations.

The constants introduced in the models developed in the previous sections lump many interacting factors. Some of them may be experimentally determined (*e.g.* mean time-to-(dis)assembly). Nonetheless, a complete theoretical model should be able to derive such parameters from first principles, *e.g.* from the equations describing the physics of the interactions driving the assembly. Besides, such lumping is a simplification/generalization that avoid the models to be application-specific.

Multi-body collision events were not considered. These are less and less probable the larger the number of parts involved[13]. Still, they may take place and influence the history of the assembly. For example, in capillary part-to-substrate SA more than one part can impinge on the same binding site, and the removal of one of them may alter the integrity of the site fluid coating.

Assembly history may affect the sites' probability of being filled. For instance, in part-to-substrate SA filling of sites may constitute a barrier to the filling of neighboring sites. In 3D SA, the dimers that result from assembly events (and that are not removed from the assembly space, *i.e.* that do not *annihilate*) keep on interacting with unassembled parts: they may act as *promoters* or *barriers* for assembly. This fact, not deeply studied in the literature, is simply neglected in the previous models.

As seen above, enhanced assembly speed and yield may be achieved using large parts-to-sites ratios, *i.e.* high redundancy. This can be done without significant consequences on the processing costs when the excess parts can be retrieved after a concluded assembly run and recycled in further runs. Anyway, there could be a limit on the maximum number of parts present in the environment during assembly runs. A high part density may increase the chance of collision and damage, thus irreversibly decreasing the yield. It may also impair the transport and mixing of the parts themselves: this would alter the assembly rates, making them density-dependent. Thus the assumptions of the models presented above are valid for ensembles containing not-too-many parts, or parts whose occupied (*e.g.* excluded) volume is reasonably smaller than the total volume. This may mine the validity of the mean-field approach,though, which does not capture deviations from average behaviors.

More fundamentally, the concepts of part density and excluded volume entail the actual volume (*i.e.* the spatial extent) of the parts and of the physical assembly space. The spatial dimension of the processes is eluded in an analytical approach, which conveniently assumes that the parts are point-like (*i.e.* of neglibible volume) and the assembly space is unbounded (*i.e.* of infinite volume or/and with periodic boundary conditions) - *i.e.* the thermodynamic limit (see

[13]Reactions requiring the simultaneous intervention of more than 2 elements are rare in nature: most of them are actually only pair-wise sequential.

Note 4). Abstract though fully-stochastic numerical (*e.g.* Monte Carlo) simulations also face a similar difficulty in handling detailed spatial constraints for inter-part interactions [290]. Furthermore, the requirement of sufficiently-low part density and excluded volume is in analogy with models of ideal solutions and very-diluted gases. In this setting, though, the discrete nature of assembly events may not be neglected. For example, assembly events may be interpreted as transitions between the reachable, discrete states of the system. The system could then be described by an oriented graph governed by probabilistic transition rules. The theories of Markov chains [284] and graph grammars [288] could constitute solid foundations for similar approaches, which nonetheless remain at a rather high abstraction level.

Finally, the assembly processes are considered as *reaction-limited*, *i.e.* it is assumed that all parts are sufficiently mobile to reach all available binding sites. This requires ideal stirring and transport mechanisms. The more common - and possibly more realistic - *diffusion-limited* assembly processes [293], where parts can practically have access only to a small fraction of the assembly space and thus of binding sites, require different mathematical models to be described, possibly involving spatially-dependent diffusion and transport terms.

6.4 ABM of 3D fluidic self-assembly[14]

To overcome the aforementioned limitations of analytic and stochastic modeling, we thought agent-based modeling (ABM) could help.

ABM represents a well-understood and known tool to simulate networks of links and nodes and, more generally, sets of interacting agents [294]. It may be likened to an evolution of object-oriented languages. It is widely used *e.g.* in programming videogames, and to simulate complex adaptive system dynamics [295, 296]. ABM is built around sets of agents - representing the entity to be simulated - which are defined by and which move and interact with each other according to user-programmable rules. The agents have finite spatial dimensions, and can be enclosed in a bounded assembly space. We thought that such features, when applied to geometrical self-assembly, could be well-suited to reproduce its dynamics realistically. In fact, one can easily see that, under similar conditions, finite component dimensions, bounded assembly spaces, diffusion-limited and geometrical (deterministic or probabilistic) collision dynamics among multiple components can straightforwardly be encoded.

The NetLogo model

We developed our agent-based model of 3D FSA using NetLogo (NL)[15]. Our customized interface is shown in Fig. 6.2. NL concurrently simulates the behavior of many interacting agents as specified by programmable boundary conditions

[14]Work started at the Santa Fe Institute (Complex System Summer School 2009, Santa Fe, NM, USA).
[15]NetLogo is available at: http://ccl.northwestern.edu/netlogo/.

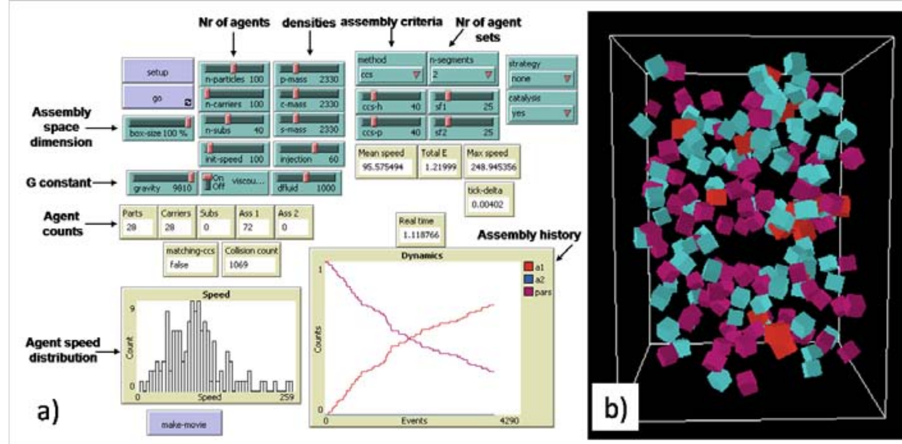

Figure 6.2: The customized NetLogo graphical interface of our 3D FSA agent-based model. **a)** Control parameters and real-time statistics, **b)** snapshot from a simulation of Zheng and Jacobs' 3D FSA process between two sets of agents (magenta = LEDs, cyan = glass carriers) self-assembling into packaged (red) units by the MCCS criterion.

and interaction rules. Such rules may be applied to agents (so-called *turtles*) and/or to pre-defined spatial locations of the simulated space (so-called *patches*). Interestingly for our purposes, NL allows controlling all roto-translational degrees of freedom and the instantaneous direction of movement of each agent. We could therefore define interaction rules that qualitatively reproduced the geometry and Newtonian dynamics of actual (F)SA processes. In our code the agents (*i.e.* the devices to be assembled) were defined in terms of number of sets and of agents within each set; and by the shape, volume, density and initial speed magnitude of each agent. Each agent's initial position and direction of motion was chosen randomly from uniform distributions; the initial speed magnitude was set equal for all agents. We defined the dimensions of the assembly space; and we implemented gravity (to model part sedimentation), the fluidic drag (using the Stokes approximation for low Reynolds numbers [297]) induced by the hosting fluid on the floating agents, and external energy injections to simulate agent stirring (*e.g.* the source of esternal energy to induce part movement and counteract fluidic drag and gravitational sedimentation). We encoded elastic, hard-sphere 2-bodies collisions, both between agents (*i.e.* we excluded multi-bodies collision) and between agents and the boundaries of the assembly space; and we defined 2 alternative criteria - either based on probability or on matching geometric conditions (*i.e.* the *matching capture cross-section* (MCCS) criterion, described in Fig. 6.4) - for sterically-effective (*i.e.* leading to assembly) inter-agent collision. All spatial and dynamic parameters were consistently scaled with reference to the intrinsic NL volumetric unit (the patch). We online monitored relevant parameters and statistics, such as *e.g.* detailed assembly his-

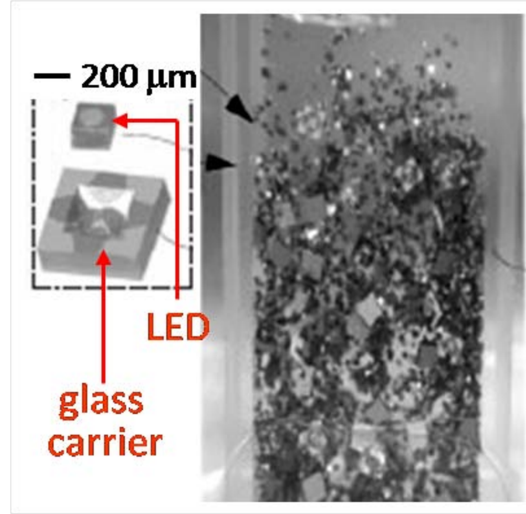

Figure 6.3: The 3D FSA process developed by Zheng and Jacobs. LEDs stochastically assembled into shape-matching glass carriers, and were thereby retained by the capillary forces of molten solder (illustration elaborated from [99]).

tory and agent velocity distribution. In absence of gravity and fluidic drag, the agent velocity distribution assumed (at least qualitatively) a Maxwellian profile after sufficiently-long simulation times (independently of the initial speed magnitude), as expected from the Newtonian, *perfect gas*-like collision mechanics encoded[16].

The main purpose of building such model was to prove that it could indeed be used to simulate stochastic SA processes at low level (*i.e.* encoding physico-geometrical details). To pursue this, we adopted the data from the 3D FSA process experimentally demonstrated by Zheng and Jacobs ([99], see Fig. 6.3) to test and tune our model. We remark that, since we devised our model to be able to encode all physical, macroscopical boundary conditions relevant for the actual process to be simulated, if all these conditions are known from the experiments and accordingly thereby set, our model can fit actual experimental data using in principle a *single* parameter, *i.e.* either the probability of effective collision or each agent's CCS. This single parameter may moreover be related to the "single-component-single-carrier" capture time defined by Zheng and Jacobs in their model (presented in the same paper, *i.e.* [99]).

Once this was achieved (Sec. 6.4), we used our model to *start* investigating the influence of several design parameters (Sec. 6.4.1) - some of which so far out of reach for other modeling approaches - and of assembly strategies (Sec. 6.4.1) on FSA yield; moreover, we predicted possible histories of a yet-unperformed FSA process involving 3 co-existing sets of parts (Sec. 6.4.1).

[16]Further thoughts on this matter in Sec. 6.4.2.

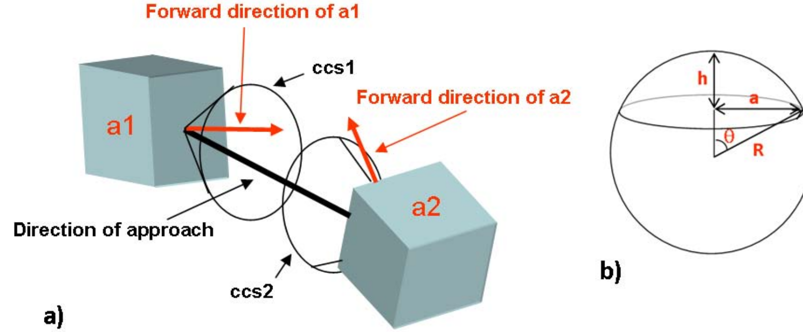

Figure 6.4: Matching capture cross-section (MCCS) criterion for effective (*i.e.* leading to self-assembly) inter-agent collisions. **a)** Each of the two colliding agents (a1 and a2) has a predefined CCS with respect to the direction of mutual approach. If, at the time of collision, the instantaneous movement direction of either agent is outside its own CCS (as for a2, in this case), the collision does not lead to assembly. The CCS was set equal for each agent for simplicity, and it is defined by the geometrical parameter θ_{CS} which describes the solid angle of the CCS as follows (refer to **(b)**): for a sphere of radius R, the area of a spherical cap of aperture θ_{CS} is $A = \pi(a^2 + h^2)$; given that $a = R\sin\theta_{CS}$ and $h = R(1 - \cos\theta_{CS})$, the corresponding solid angle is $A/R^2 = 2\pi(1 - \cos\theta_{CS})$.

Reproducing Zheng and Jacobs' 3D FSA process

Fig. 6.5a and 6.5b compare simulative and experimental data, respectively, for the actual 3D FSA process of Zheng and Jacobs for the case with equal numbers of LEDs and carriers ($= 100$). All agent and assembly space parameters reflected as much as possible the known experimental conditions. The approximation closest to the actual setup - which had a liquid volume of $12 \times 12 \times 27\,mm^3$ - we could simulate for the assembly space's volume and aspect ratio was $13 \times 13 \times 26\,mm^3$, due to the discreteness of the set of definable patches. We also assumed an initial agent velocity (as it was not measured by the experimenters) of 100 mm/s. Fig. 6.5a shows average assembly histories for 3 values of the parameter θ_{CS}. As expected, larger CCSs lead to faster assembly; $\theta = 80^o$ closely fits experimental data.

6.4.1 ABM Investigations

Redundancy and agent density

In a 10× consistently-downscaled version of the full-scale system (to reduce computation time), we simulated the effects of redundancy (*i.e.* of LEDs-to-carriers ratio; Fig. 6.6a) and of assembly space-to-component volume ratio (*i.e.* agent density in assembly space; Fig. 6.6b) on assembly rates. Results

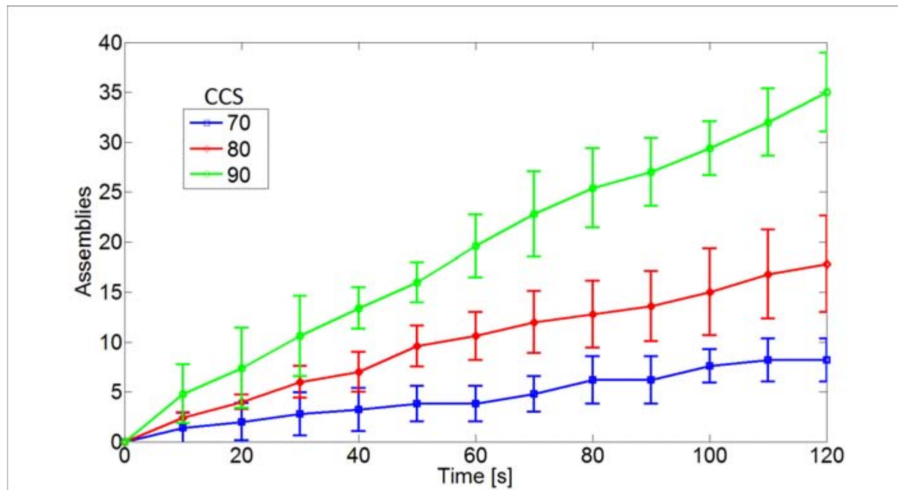

(a) Full-scale simulations (assembly space volume: 4394 mm^3; agents: 100 LEDs + 100 carriers; assumed initial agent speed: 100 mm/s) using θ_{CS} as the only fitting parameter (averages and standard deviations of 5 histories shown for each θ_{CS} value).

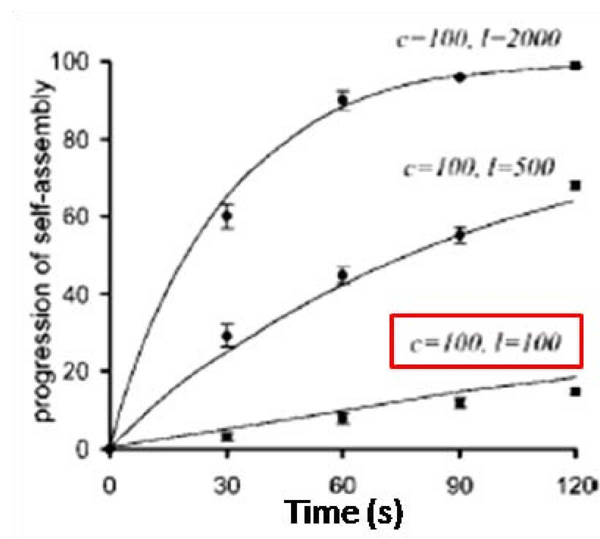

(b) Experimental results of the 3D fluidic SA process of Zheng and Jacobs, after [99].

Figure 6.5: ABM of Zheng and Jacobs' 3D FSA process. Full-scale simulations with $\theta_{CS} = 80^o$ fairly match the experimental data (case: LEDs (l) = carriers (c) = 100; from [99]).

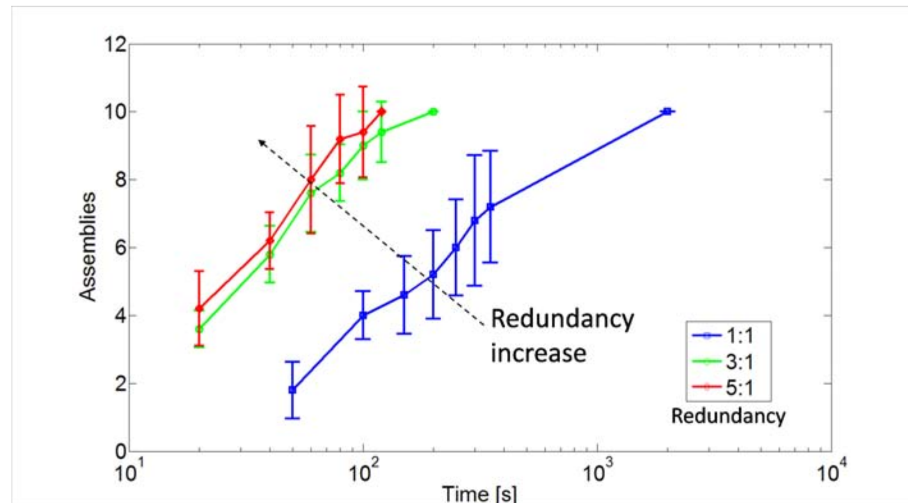

(a) Effect of carriers-to-LED ratio on assembly.

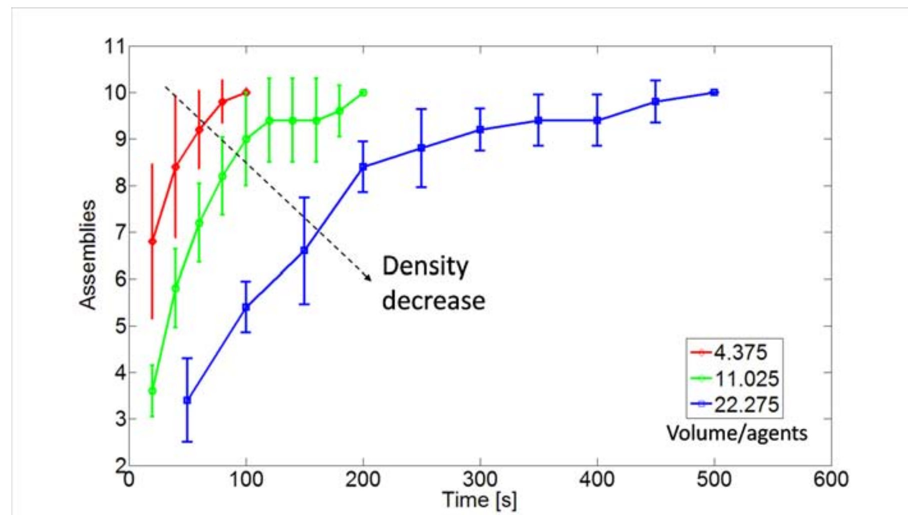

(b) Effect of space-to-agent volume ratio (*i.e.* agent density in assembly space) on assembly.

Figure 6.6: ABM investigations on a 3D FSA downscaled system (reference model: 10 + 10 agents; 10× smaller assembly space; 100 mm/s initial agent speed; assembly criterion: MCCS with $\theta_{CS} = 80^o$). Averages and standard deviations of 5 histories shown for each case.

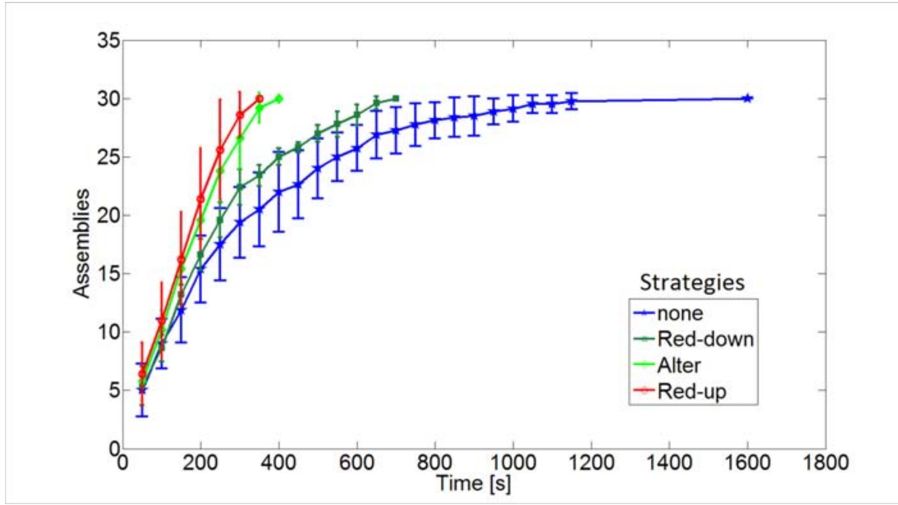

Figure 6.7: ABM investigations: role of assembly strategies (initial and boundary conditions: assembly space: $5 \times 5 \times 5\ mm^3$; 60 LEDs + 30 carriers; agent velocity: $100\,mm/s$; assembly criterion: MCCS with $\theta_{CS} = 80^o$). Averages and standard deviations of 5 histories shown for each sampling time.

show that higher redundancy increase the assembly rate, as it was expected and well known. Moreover, the assembly rate also increases when the same total number of agents is embedded in a smaller assembly space, which may nonetheless represent *a posteriori* an intuitive consideration. Investigations on agent density in assembly space were so far out of reach in numerical models.

Assembly strategies and role of assemblies

In all FSA processes (performed and) simulated so far, given the initial conditions, populations of agents evolved according to actual assembly events only. However, this needs not to be necessarily so: agent populations may be *externally*-supplied with more of their own agents during the assembly process, as well, according to pre-defined strategies.

We investigated the effects on assembly rates of *feeding strategies* on our downscaled FSA system. We devised 3 basic strategies subjected to the constraint of constant total number of agents in the (fixed) assembly space. Specifically, at the very time of every assembly event, a new component was added which was: for the *red*(undancy)-*up* strategy, an LED; for *alter*(nate), alternatively a carrier and a LED; for *red*(undancy)-*down*, a carrier.

Fig. 6.7 shows the synopsis of the results for simulated strategies. All feeding strategies increased the assembly rate as compared to the standard (*i.e. none*) case. Moreover, feeding LEDs (*i.e.* increasing redundancy at run time and as compared to initial agent populations) has larger positive effects on the assembly

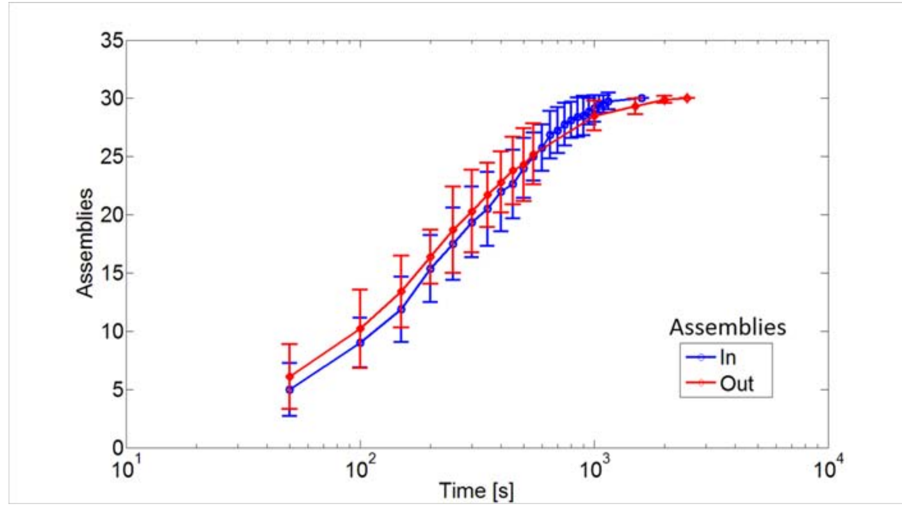

Figure 6.8: ABM investigations: role of assemblies (*i.e.* inert dimers)(initial and boundary conditions: assembly space: $5 \times 5 \times 5$ mm^3; 60 LEDs + 30 carriers; agent velocity: $100\, mm/s$; assembly criterion: MCCS with $\theta_{CS} = 80^o$). Averages and standard deviations of 10 histories shown for each sampling time.

rates, as compared to feeding carriers.

Furthermore, we investigated the role of inert assemblies (*i.e.* of dimers in our case, having excluded multi-body assemblies): do they work as promoters or barriers for unassembled agents? To tackle this, we devised a strategy (*Out*) where assemblies were removed from the assembly space as soon as they formed (*i.e.* assembly led to annihilation of involved agents).

Our preliminary results (Fig. 6.8) hint at a barrier (promoter) role for assemblies during the initial (final) stages of the processes, respectively. This is derived from the simulative evidence that, in presence of assemblies in the assembly space (*i.e.* with the ordinary *In* strategy), the rate of assembly is lower at the beginning of the process and higher at the end as compared to the As-out strategy. We interpret this as follows: when the number of reactants is highest (*i.e.* at beginning) the presence of inert assemblies block the assembly reaction; instead, when the reactants are almost extinct and their search for mating agents in assembly space harder (*i.e.* close to the end) the the presence of the assemblies, by now pretty numerous, act instead to *compartimentalize* the assembly space, so that the agents are essentially confined within smaller subspaces, and consequently their search is substantially more efficient (akin to Fig. 6.6b). Nonetheless, further analysis is needed to support this evidence.

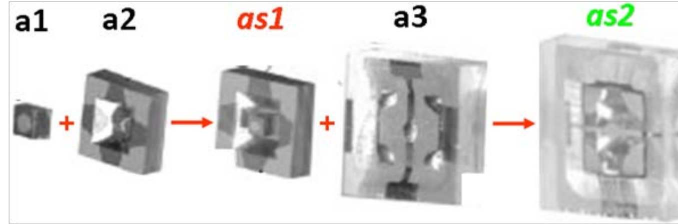

(a) Constrained assembly sequence (illustration elaborated from [99]).

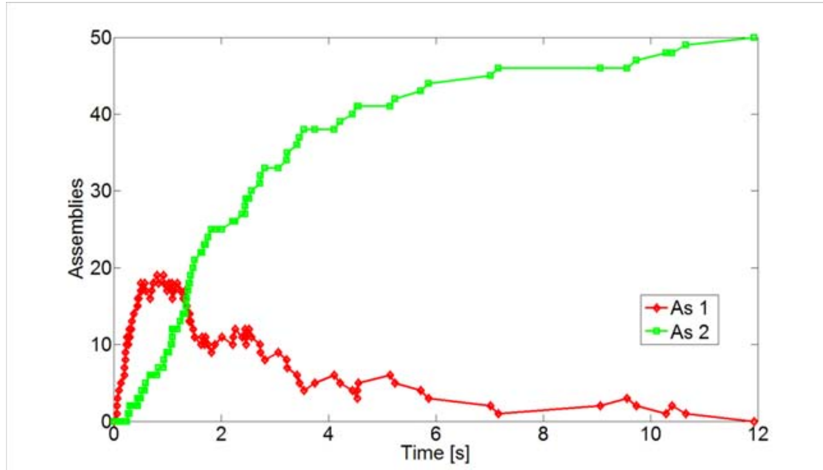

(b) An ABM realization of the process.

Figure 6.9: Hypothetical sequential 3D FSA process, with 3 sets of agents ($a1$ to $a3$) present in the assembly space at starting time (initial and boundary conditions: 50 $a1$, 100 $a2$, 100 $a3$; agent velocity: $100\,mm/s$; assembly space: $15 \times 15 \times 15\,mm^3$; assembly criterion: probabilistic with 25 % probability of effective collision).

A sequential 3D FSA process

Finally, we used our model to predict the behavior of a hypothetical, sequential 3D FSA process involving 3 sets of agents co-existing in the assembly space since the beginning of the process. The corresponding, constrained assembly sequence is: $(a1 + a2) + a3 \rightarrow as1 + a3 \rightarrow as2$, as sketched in Fig. 6.9a. This is different from the 3-agents FSA process originally demonstrated by Zheng and Jacobs, as they performed the 2 steps of the directed assembly in 2 separate assembly runs, each with only 2 initial sets of agents (a1 and a2, and as1 and a3, respectively) [99].

ABM simulations of the proposed process (Fig. 6.9b presents one realization) indicated that, for the chosen parameters, as2's should increase exponentially, as expected from a single-step reaction-limited assembly process, while as1's

should progress in a non-monotonic way due to the agents' relative abundance and probability of effective collisions (in the general case, different for each set of agents) affecting their rate of birth and death. Parameter tuning may optimize yield and explicit the interplay between reaction- and diffusion-limited processes.

6.4.2 Analogy with molecular dynamics

Our ABM represent a sort of *macroscopic* molecular dynamics (MD).

Hereby parts of finite volume and detailed geometry are enclosed in a bounded space, interacting deterministically according to elastic Newtonian dynamics. There is no energy nor material exchange with the outside environment, and the temperature of the isolated and adiabatic space is fixed by the initial velocity of the parts - the total kinetic energy being conserved throughout. As the model runs and the parts diffuse in space, one would then expect them, consistently with our hypothesis and boundary conditions, to assume a Maxwell-Boltzmann equilibrium velocity distribution. Such distribution is in fact seen in our real-time statistics (see *e.g.* Fig.6.2a). Therefore, except for the physical assembly details, our model is conceptually similar to baseline MD.

6.5 Conclusions

This Chapter was dedicated to the modeling of the collective dynamics of passive self-assembly processes.

We generalized two analytical, chemical kinetics-inspired models, proposed earlier in literature, to capture *reversible* assembly processes (*i.e.* including both assembly and dis-assembly events); but, in spite of their handiness, we altogether *criticized* the mean-field, master equation-based analytical approach for lack of specificity and realism. To constructively overcome this criticism, we introduced ABM as a natural realistic framework to explore MEMS FSA's vast parameter space (including design parameters that were so far out of reach for modeling) and to elucidate some standing issues, including *e.g.* scaling, collective phenomena and assembly strategies - critically-important for a deeper understanding and wider appreciation of FSA processes.

Our implementation of ABM was computationally expensive: for each simulation run, NL stores each agent's degrees of freedom, velocity components and neighboring agents. Also, it constitutes only a geometrical approximation of actual (F)SA processes. We envision implementing the assembly physics and dynamics with physical engines embedded in object-oriented codes. This might radically increase realism and match with experimental details, while possibly reducing the simulation time.

Chapter 7

Conclusions and Further Challenges

Almost all literature dedicated to capillary SA deals with proofs of concepts and demonstrators. Such positive yet preliminary evidence rarely suffice to capture the interest of industrial parties. Bridging the gap between academic concepts and industrial development is no small effort: it requires substantial re-thinking of ideas and their twisting into novel forms to fit the set of constraints imposed by the exploiters.

This speculative Chapter concludes our investigations on capillary part-to-susbtrate SA by reviewing the main causes of failure and the open (residual, if you will) issues challenging capillary SA on its way to industrial establishment. By *failure* we hereby mean any event which can negatively affect the overall yield of the process and/or avoid meeting the specifications (for *e.g.* alignment accuracy, device reliability) required for the desired application. For each evoked issue we contextually propose solutions and/or perspectives, either suggested by our experiments or elaborated from literature survey.

Conclusions

The physical chemistry-rooted concept of self-assembly - *i.e.* the enabling of a system components to accomplish unsupervised assembly and organizing tasks - is presently permeating many different scientifical and technological disciplines: from material science to robotics and artificial intelligence [298], from medicine to social science [299] and evolution theory [300, 94]. SA is inducing the adoption of novel bottom-up approaches in many other fields - including manufacturing.

In this regard, a broad class of SA techniques is rapidly gaining recognition for its benefits for the construction of heterogeneous micro- and nanosystems

(see Sec. 1.3). SA can perform tasks that would otherwise be very hard to accomplish (*e.g.* at nanoscale), as well as leverage assembly tasks that are presently performed by established yet possibly sub-optimal techniques (*e.g.* pick&place). Capillary SA constitutes the broad context where the present thesis offered original contributions.

Our work aimed at a deeper understanding of the potentialities and limitations of capillary SA towards its utilization in microsystems packaging. Several of its multiple aspects and open issues were tackled. Hopefully some of them were cleared - and some others unleashed:

- We experimentally-measured and numerically-modeled ***lateral capillary forces*** arising from small perturbations of fluid menisci. In so doing we deepened their understanding and provided a sound foundation for their wide-ranging applications. Our experimental setup can constitute a reference testbench for further investigations into the magnitudes, directionality and scaling properties of lateral capillary forces.

- We described a potential ***novel method to measure the advancing contact angle*** of liquids. Our experimental setup enabled the explotation of the Gibbs' inequality for the purpose. The method may be particularly suited for the measurements of *very-small* angles - though not limited to them - useful for the assessment of the state of high-energy surfaces.

- We demonstrated ***perfectly-conformal fluid dip-coating*** of binding sites patterned on planar surfaces. This was achieved for sites of even *arbitrary* geometry by introducing of a relatively-thin wetting sidewall around the entire site perimeter. Coating conformality enables the *effective* encoding of geometrical information into binding sites. This is critical to drive the desired registration and alignment of parts onto the sites. Our topological enhancement of binding sites also improved dip-coating robustness against unideal surface conditions, which is needed to extend the process to large substrate scales (*e.g.* wafer-scale processing). Even so, we were not able to obtain precise control on the volume of fluid lenses deposited onto patterned sites. Whether dip-coating allows very-uniform delivery of lens volume remains an open question.

- We demonstrated a general procedure to establish ***solder-mediated interconnections*** between parts and substrates within a capillary SA process. The ordered sequence of steps - inducing the controlled removal of involved fluids and solder/metal wetting - was optimized for In/Au metal joints in order to avoid disruptive phaenomena associated with thermal treatment and to preserve the part-to-site alignment achieved during the capillary SA step. We demonstrated the substantial equivalence of electrical and mechanical properties of the interconnections established either by exploting only the axial capillary pressure acting on *individual* parts or by means of *collective* thermocompression bonding. This evidence enables capillary assembly of parts onto exotic substrates which cannot tolerate

the imposition of large loads (*e.g.* flexible and/or curved substrates, substrates embedding fragile and/or porous materials). We were anyway *not* able to assess the ultimate alignment accuracy of the complete process, because of relatively-large tolerances in sample fabrication.

- We proposed a solution to the neglected problem of ***mutual adhesion between parts*** during capillary SA caused by their hydrophobic interaction. We thought of switching surface chemistries able to sense the local chemical environment and accordingly change their wetting character from hydrophilic to hydrophobic. Proposed embodiments of the idea involve surface functionalizations by molecular switches or by pNIPAM-based polymers, both sensitive to external stimuli such as *e.g.* light, temperature and solution pH.

- We proposed two chemical kinetics-based ***analytic models of SA dynamics*** that generalize earlier models by including dis-assembly events. While capturing the essence of SA's average and asymptotic dynamics, such handy models are nonetheless based on rather simplifying if not unrealistic assumptions. To overcome these limitations, we introduced the novel ***agent-based model*** of fluidic SA. The proposed model simulates realistic SA realizations based on Newtonian dynamics and criteria of geometric matching, and accounts for many parameters that were previously out of reach, such as *e.g.* bounded assembly space and finite part dimensions, diffusion-limited processes and time-dependent part injections. The model - tested by reproducing, using essentially a *single* fitting parameter, experimental data published in 2005 - was used to get novel insights into SA processes.

As a precipitate of our investigations, we claim that *SA methods and techniques will have profound impacts on assembly and packaging technologies*, complementing and enhancing them in the near-to-mid-term, and eventually replacing them in the long-term. The hybrid assembly way, pioneered by the convergence of robotic and capillary assembly, can seriously boost near-term industrial applications by overcoming the long-standing throughput/placement accuracy trade-off afflicting pick&place-like techniques. We hope to have positively contributed to this rising trend.

In the long term, we envision a further convergence between several SA methods - eventually arranged in a hierarchical modality. For instance, at nanoscopic circuit level (di)electrophoretic SA can precisely place circuital elements such as *e.g.* nanoparticles and NEMS components; the parts hosting the circuits could then be assembled by fluidic SA, wherein the capture section of capillary binding sites may be spatially-extended in combination with electric or magnetic fields.

Speculations on open issues

We top off this concluding Chapter with a ***critical outline*** of what, after our contributions, are the main issues still challenging the full industrial establishment of capillary SA. We think of: 1) fluids, 2) coating, 3) part stirring and transport, 4) selectivity and error correction, 5) interconnections. For each evoked issue we will contextually propose solutions or perspectives - either suggested by our direct experiments or elaborated after literary noodlings.

Fluids

Though water is, so far, the hosting fluid of choice in standard capillary SA, it may not be compatible with the fabrication and packaging of many common electronic devices. Device passivation layers, especially oxides, are inherently hygroscopic: after being soaked in water the devices may retain large quantities of water, which is a challenge for their electro-mechanical reliability. Moisture and water leakages are well-known degraders of device performance in the long term [301]. Hence a substitute for water - at least as hosting fluid – still compatible with the discussed set of requirements may be preferable in some cases.

Inverting the role of hydrocarbons and water is an option, though an expensive and less environmentally-friendly one altogether, given the much larger amount of hydrocarbons required as compared to the standard scenario. Alternatively, the highly-stable, chemically- and biologically-inert perfluorodecalin might be used as hosting fluid, combined with water as lubricant; the interfacial energy of such couple is similar to that of water/hexadecane [110].

In general, unless eventually relaxed according to specific assembly tasks, the need of high interfacial energy between the fluid couple to efficiently drive the SA process may limit the choice of the fluid couple to a combination of a polar and an apolar liquid (Sec. 2.2). Excluding hydrofluoric acid (whose polar character is even stronger than that of water) for evident safety and material compatibility reasons, some organic ionic solutions might be used as polar liquids, while hydro- or fluorocarbons may still be preferable as their apolar companions.

Lubricant coating

Since the position of the lubricant lenses on the substrate signals to the approaching parts the presence of an available binding site, the lubricant must wet the substrate only in correspondence with the binding sites.

Superficial binding sites (defined in Sec. 3.4.1) are fabricated by patterning thin (metallic or polymeric) films deposited on the surface of the substrates, and then eventually functionalizing them to tune their wetting properties (Fig. 7.1a). We demonstrated that their performance is not optimal.

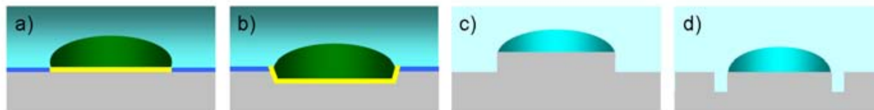

Figure 7.1: Chemical and topological definition of binding sites: a) superficial, b) recessed, c) mesa, and d) trenched site. Relative dimensions are out of scale.

Selectivity

When using superficial binding sites, if the wetting contrast between binding sites and spacer is low, coating selectivity is compromised. The comparison of water CAs measured on site and spacer surfaces provides a rough estimate of their wetting contrast. In our experience, a difference above 60° between the respective advancing CAs is sufficient to allow selective fluid coating. Sparse drops of lubricant on the spacer may introduce false positive assemblies, as parts meet the drops and stick in place as if on an effective binding site. Such drops may form during fluid coating if the spacer is not properly clean (*e.g.* adsorbed contaminants or residual particles from earlier processing steps reduce the energy of oxidized surfaces, decreasing their hydrophilic character), or as result of capillary break-up of lubricant films or neighboring lenses (*e.g.* satellite lenses [249]). The issue of false positive assemblies is the more important the smaller the dimensions of the parts to be assembled.

High surface wetting contrast is fundamental when using liquids as hosting fluids. Conversely, in dry SA the topology of the sites can additionally help selectively confining the lubricant lenses. Particularly, *mesa* sites (*i.e.* sites placed *above* the level of the spacer, Fig. 7.1c) are surrounded by a ring of air, which repels water [149]. The same confinement may be achieved by realizing trenches around the sites (*trenched* sites, Fig. 7.1d). Note that, thanks to the Gibbs' inequality (Eq. 2.10), the lens confining power of mesa/trenched sites can be significantly superior to that of superficial sites [302]. Anyway, unless chemical conditioning is also employed, dip-coating is not effective on surfaces having *only* topologically-defined binding sites. Moreover, superficial, mesa and trenched sites alone do not provide by themselves coating conformality - unless large lens volumes or perfectly-wetting lubricants are used (see Sec. 3.4.4).

Conformality

In Chapter 3 we discussed the importance of coating conformality on the performance of capillary part-to-substrate SA. We thereby demonstrated that by engraving the binding sites into even very-shallow cavities (*i.e.* by surrounding the perimeter of the superficial sites with a thin wetting sidewall, as shown in Fig. 7.1b), complete conformal coating of arbitrary planar site geometries can be easily and systematically achieved.

Here we remark that the thickness of the sidewall of such recessed sites (of the order of few micrometers) may well be comparable with the thickness of standard substrate passivation layers, so that its integration into production lines process flows may be simple – it could require only a single additional etch step. Moreover, this simple topological enhancement makes the coating process more robust against non-ideal conditioning of the binding sites, and the lubricant lenses less prone to distortions or disruptions during assembly.

Control of lubricant lens volume

The volume of the deposited lubricant lenses has direct influence on the assembly performance. As shown in Chapter 2, the smaller the volume the smaller the height of the confined fluid meniscus, thus the larger the restoring forces, both lateral and vertical. However, upper and lower bounds to lens volumes need to apply. Too small a volume may further amplify de-wetting from sharp corners and produce sparse coverage of the site patterns, negatively affecting capillary self-alignment; conversely, for too-high lens volumes, the parts may easily end up being tilted with respect to the underlying site. A tilted pose makes the alignment of the part with respect to the underlying binding site very loose, and it may compromise the final bonding. Part tilt was predicted numerically [227] and observed experimentally [244] in the presence of large lubricant lenses[1].

According to our experiments , lens-to-lens volume uniformity, required to enhance process reproducibility and predictability, is hard to be obtained by dip-coating (see Sec. 3.5). Further investigations on the dynamics of capillary pinch-off of fluid lenses are needed to control and optimize this operation. Alternatively, jetting [246, 247], especially if used in a parallel deposition modality, may allow a better control on lens volumes.

Fragility of coated binding sites

Static self-assembly assumes the availability and physical integrity of unfilled binding sites at *all* times. On the contrary, several of the phaenomena discussed in these Sections may compete to distort or even disrupt the lubricant coating of the binsding sites, thus severely compromising their functionality.

As a partial solution, we had qualitative evidence that recessed binding sites enhance the resiliance of lubricant lenses onto the sites. Additionally, choosing lubricants with optimal chemical affinity for the surfaces of the binding sites (*e.g.* with very small CAs) may further increase the robustness of the lubricant against perturbations.

[1] Another cause of such improper part settlement is the modality of approach of the part toward the site: if, instead of approaching it vertically from above, the part touches the lubricant lens by a lateral sliding movement, the capillarity-driven motion of the part may be opposed by the friction acting between the part and the spacer, resulting in an incomplete part-to-site overlap and most likely a tilted final pose. Externally-induced post-assembly substrate vibration was proposed as a way to restore a parallel part pose [243].

Binding sites on pre-processed substrates

How to condition BEOL-processed substrates, containing *e.g.* electronics, interconnections, MEMS or other structures, for capillary SA? Such conditioning should be compatible with all previous processing steps, and should not impose many and/or costly additional steps to the process flow.

The definition of binding sites requires, at the design level, an accurate floorplanning of the target substrate (see Sec. 2.5.1). The related additional substrate processing steps would include, in the general case, the deposition, patterning, etching and functionalization of thin films. On the part side, matching patterns would need to be defined with similar operations. In this respect, we suggest that, unless a very-accurate and reliable part singulation technique is available (*e.g.* stealth dicing?), a highly-precise part-to-site alignment should not rely on part edges, but on patterns defined *inside* the edges by *e.g.* lithography and etching.

While the full impact of such overload on process integration was not investigated, it is our opinion that these finalizing steps would be compatible with existing production flows and new approaches, such as *e.g.* 3D stacked ICs. Particularly, the added benefits of recessed binding sites, discussed above, may well repay the additional processing load in the perspective of assembling very-large amounts of small components onto large pre-processed substrates.

Stirring and transport of parts

Once the parts are immersed in the hosting fluid, a source of kinetic energy - external and/or internal - needs to be provided to the system to make the parts efficiently explore the assembly space and find their optimal configuration in the assembling structure (Sec. 1.2.3). This fundamental aspect of self-assembling processes is critical in terms of time-to-assembly and assembly throughput.

Since the parts are normally much denser than the hosting fluid, they start to fall to the bottom of the assembly space as soon as they are immersed in the fluid. If the substrate is placed on the bottom and care is not used, the parts may randomly distribute over its surface. Only a fraction of them will correctly assemble, while the lubricant coating of many sites may be seriously disrupted by local agglomerations of the parts. According to our experience, this is a scenario to be avoided.

Pipetting was commonly used to dispense parts in the assembly space and to locally-induce the flow of the hosting fluid to mix, move and transport the parts across the substrate[2]. It is a sort of manipulation by contactless tweezers: pipetting can eventually address the position and placement of individual parts. Anyway, and in spite of its simplicity, pipetting is an essentially-supervised, serial and hardly-reproducible method to impart movement to parts. Moreover, it mainly produces laminar fluid flow when directly applied above planar substrates. This further decreases its efficiency, because:

[2]Pipetting was used in the experiments described in Chapter 4.

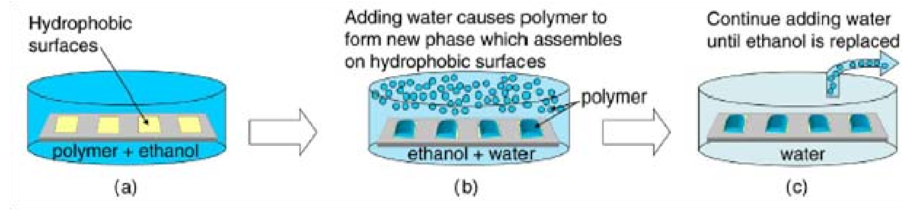

Figure 7.2: Insoluble liquid energy minimization, after Morris [303].

1. laminar fluid flow induces a two-dimensional (*i.e.* superficial) sliding movement of the parts on the substrate, which is inefficient in the presence of fragile binding sites, already-filled binding sites and other dislocated parts - the latters representing barriers to assembly;

2. the lateral force F_D (*i.e.* parallel to the substrate surface) induced by the fluidic drag of the laminar pipetted flow on the parts lying flat on the substrate is given by [233]:

$$F_D \approx \frac{1}{2} C_D A_D \rho_F V_A^2 \tag{7.1}$$

   where C_D is the drag coefficient, A_D is the cross-sectional area of a single part, ρ_F is the density of the fluid, Q is the injected volume flow rate and V_A the average fluid flow velocity. If the part is very thin, F_D is accordingly very small, while being possibly opposed by the frictional force between part and substrate surfaces. A strong fluid flow is therefore needed to move the parts, but it may also disrupt other assembled parts;

3. it is difficult to draw back on the substrate the parts which fell out of its edges by pipetting.

   Increasing the buoyancy of the parts by reducing their density relative to the hosting fluid may partially leverage these issues.

An interesting method called *insoluble liquid energy minimization* (Fig. 7.2), which provides at the same time lubricant deposition on chemically-conditioned parts and sites and a local, inter-part fluidic actuation mechanism, was introduced by the Whitesides' Group ([119, 128, 121, 125] and investigated by Morris [303]. The method involves diluting the lubricant (*e.g.* a polymer) in a solvent (*e.g.* ethanol) and subsequently adding to the solution the actual hosting fluid (*e.g.* water) – which has to be miscible with the solvent but not with the lubricant - till the solvent is completely removed. By doing this, the lubricant precipitates from the solutions and selectively deposits on the available (*e.g.* hydrophobic) binding sites, both on substrates and on free-standing structures and parts. At the same time, concentration gradients around the aggregating lubricant lenses induce pretty strong local Marangoni flows, which were demonstrated to boost the movement and assembly of parts [100].

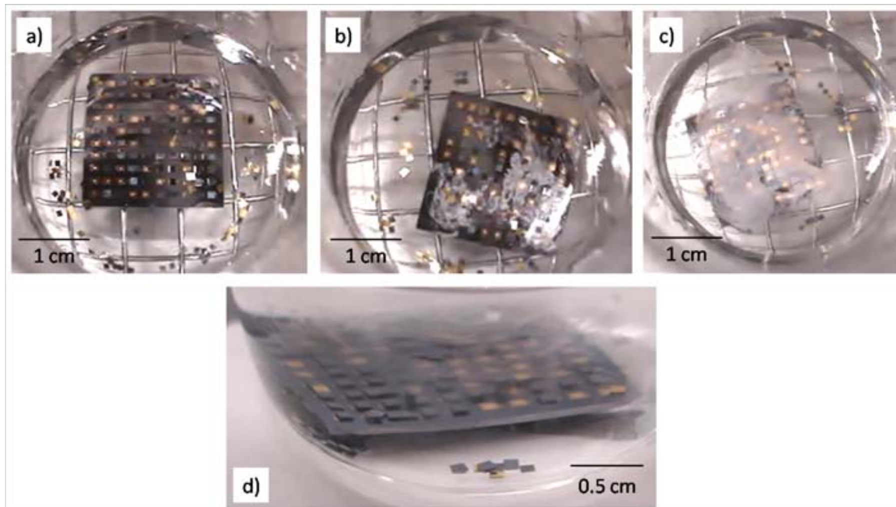

Figure 7.3: Agitation of $1 \times 1 \times 0.2\,mm^3$ parts on a patterned substrate by ultrasonic acoustic waves in water **(a-c)**, evidencing the dispersion of HD lenses. Disruption of binding sites and part displacement is seen in **d)**.

At the other extreme, *pulsating turbulent flow* of the hosting fluid was introduced by Zheng and co-workers as stirring method for 3D SA applications [29]. This technique exploits the drag induced on the parts by the fluid flow itself, which can be created *e.g.* by a programmable piston. The fluidic drag force scales with the square of the linear size of parts: in a downscaling perspective, it may be efficient as it prevails over body forces. The pulsating flow may be potentially applied also to 2D capillary assembly. In this case, our experience suggests careful tuning of the turbulent flow velocity to avoid lubricant lens disruption, removal of assembled parts and formation of air bubbles which may cause unintended consequences (*e.g.* mutual adhesion of parts).

By the same token, parts agitation by ultrasonic acoustic waves is not recommended in capillary SA - even when the acoustic forces are comparable to or larger than the weight of the parts, thus effective in displacing them - because ultrasounds easily induce solubilization of the originally-immiscible fluid couple, *i.e.* they disperse the lubricant lenses into the hosting fluid by creating microemulsions (Fig. 7.3).

Substrate tumbling is an efficient method to externally drive part-to-substrate capillary SA [140]. Its basic idea entails fixing the substrate to one of the walls of a beaker, and making the beaker rotate along one of its axis, possibly parallel to the substrate surface (Fig. 7.4). The rotation may be controlled by programmable linear motor. The intended result is to alternatively tilt the substrate up and down, *e.g.* to have the substrate lying on the bottom of the beaker during half the period, and on the top during the other half. This way, while in the down phases the parts can wander on the surface of the substrate,

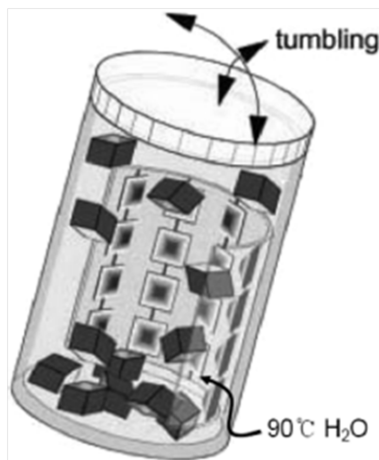

Figure 7.4: Substrate tumbling, after Chung [140].

in the up phases they are removed by gravity from the substrate unless they are correctly assembled on the sites. The selectivity of this mechanical part removal and assembly-check operation is greatly-enhanced by the wetting contrast between functional and non-functional sides of the parts. Moreover, the tumbling method can address the movement and assembly correction of all parts simultaneously (see next subsection); it can run unsupervised, as well.

In all cases - unless purposely intended [110] - when performing 2D and 3D SA in the bulk of the hosting fluid and exploiting the hydrophobic interaction, the parts need to avoid being adsorbed at the fluid/air interface. Adsorption at this interface is energetically-favourable for chemically-conditioned parts: they will expose their hydrophobic side(s) to air to minimize their solvation energy. Once adsorbed, the parts will stick at this interface and be unavailable for bulk assembly. On the other hand, interfacial adsorption induces a better organization of assemblies, as compared to bulk processes [275]; Knuesel and Jacobs demonstrated a Langmuir-Blodgett-like part-to-substrate assembly of microscopic solar cells exploting this effect in conjunction with energy cascades [141]. A simple way to avoid the possibility of interfacial adsorption of part is completely-filling sealed containers hosting the assembly process.

Finally, for dry SA - as opposite to the standard embodiment - vibration and in-plane movement of the substrate is the method of choice to induce essentially-random movement of the parts. This modality was pioneered by Böhringer [304] and further developed by his research team in several variants, particularly in combination with additional, orienting and aligning features, complementarily-micromachined on the parts and substrate [191, 189]. In a recent embodiment, they claimed an extremely-high assembly yield by exploiting three different movement modalities for the parts, as selected by the magnitude and frequency of the vertical *and* lateral vibrations of the substrate; the parts were in turn designed to fit by gravity into substrate traps [98].

Selective binding and error correction

The parts to be assembled are normally thin enough (*i.e.* their thickness-to-length/width aspect ratio is low enough) so to be considered approximately two-dimensional, *i.e.* to have only two sides of largest and equal area, only one of which is chemically-functional for assembly purposes. Given this simple boundary condition - in which there is complete geometrical symmetry between the two major part sides - and the stochastic dynamics of the assembly, the chances for the parts to land on the binding sites with the functional side or with the opposite are equal. The wetting contrast between the two sides leverages the problem: ideally, the hydrophobic side is strongly wet by the lubricant, while the hydrophilic is not (*e.g.* the CA of alkanes on oxides in water is 180°). In the latter case, the part is unbound and can be removed *e.g.* by a gentle directional fluid flow or by tilting the substrate upside down (as in tumbling). Fig. 7.5 supports this observation by presenting SE simulations on the effect of the fluid contact angle θ_t on the top pad on the restoring capillary force arising from the vertical movement of the pad.

Also, when the substrate is immersed in liquid (and in contrast to dry SA), selective removal of unbound parts may hardly be achieved by vibrating the substrate, because: 1) fluidic drag largely attenuates the displacement of the parts (*i.e.* the induced part oscillations are overdamped); 2) the external vibration of the substrate is transferred uniformly to *all* the parts, which thus cannot be individually addressed or moved *relatively* to others.

If the fluid flow used to remove the unbound parts is too strong or the collisions between parts are too energetic, correctly assembled parts may also be removed [233]. This causes the disruption of the liquid meniscus bridging part and site. Consequently, not only is the shape and coverage of the residual lubricant lens on the site deformed: it can also be largely reduced since part of the lubricant may be picked up by the part. The ratio of such partition depends on the details of the rupture dynamics [305]. For slow rupture (*i.e.* quasi-static limit), the transfer ratio depends entirely on the degree of wetting of the liquid on the separated surfaces, namely on the respective receding contact angles (Fig. 7.6) [306]. The bridge is broken into two equal pieces if the receding CAs are equal (as *e.g.* in the case of functional part sides and binding sites featuring the same surface chemistries); otherwise, the larger fraction is kept on the surface with lower fluid CA. The transfer ratio is moreover very-sensitive to small variations in CA. If on the other hand the rupture is fast (as *e.g.* for the dis-assembly of correctly assembled parts), the bridge is partitioned in equal halves independently of the details of wetting [307].

Furthermore, more than one part may impinge on the same available binding site. While this event is evidently not functional to the assembly purpose, the selective removal of all these parts except for one may not be trivial, and is anyway one cause for the presence of lubricant on the functional side of parts. A solution of this problem resides in endowing the binding sites with chaperons and pedestals, which physically impede the agglomeration of more than one part on the same binding site, and moreover can help inducing unique in-plane

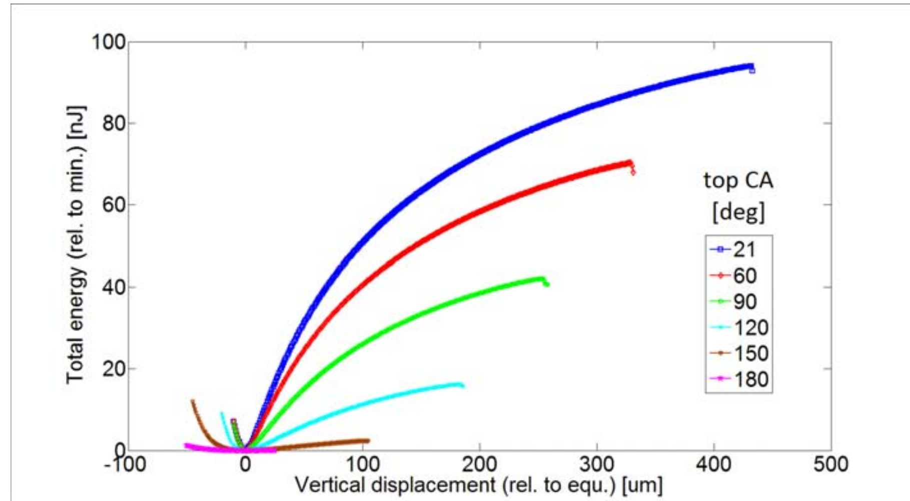

(a) Total energy (relative to the minimum)-versus-vertical displacement (relative to the equilibrium height).

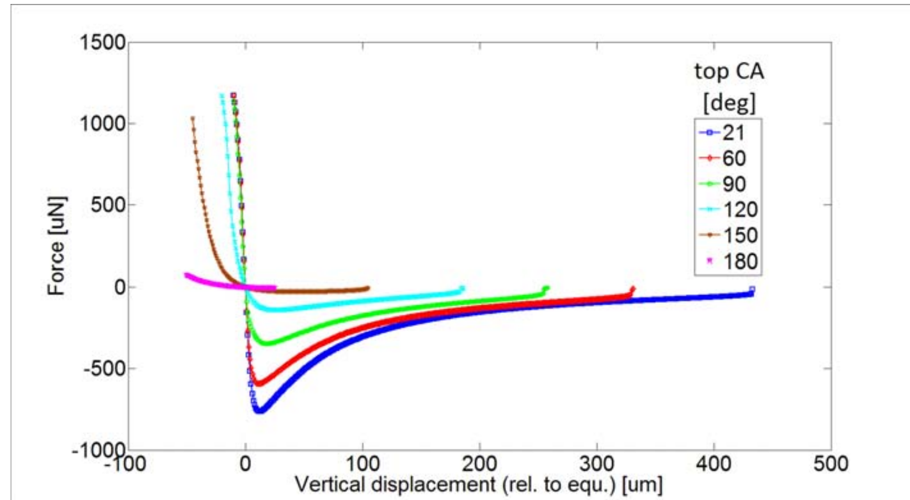

(b) Restoring force-versus-vertical displacement (relative to the equilibrium height).

Figure 7.5: Finite-element simulations of the effect of wetting - as measured by the contact angle θ_t of the lubricant (HD, volume: $100\,nL$) on the top pad - on the vertical capillary restoring force between $1 \times 1\,mm^2$ square pads in water. The position of and the fluid contact angle θ_b on the bottom pad was kept fixed. The energy landscape in **(a)** resembles the Morse potential used to model intermolecular forces [230].

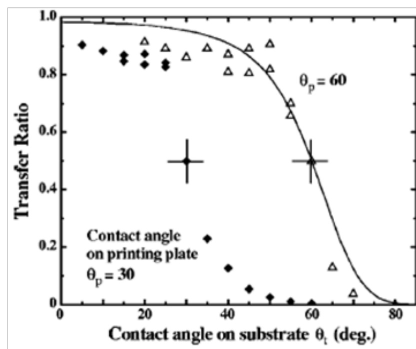

(a) Lubricant transfer ratio as a function of the lubricant CA on the bottom pad (θ_b) for two values of the CA on the top pad (θ_t, diamonds: 30°, triangles: 60°), after [305]. The solid curve represents the function $K_{T,1}$ for $\theta_t = 60^o$ of [306].

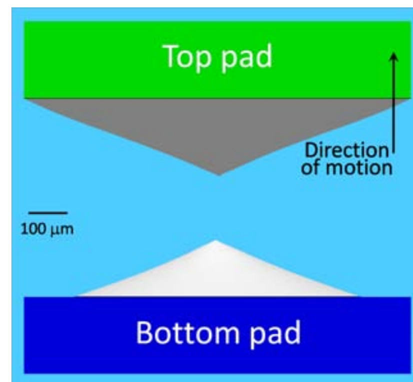

(b) Lubricant transfer for $\theta_b = 21^o$ and $\theta_t = 0^o$ after bridge break-up.

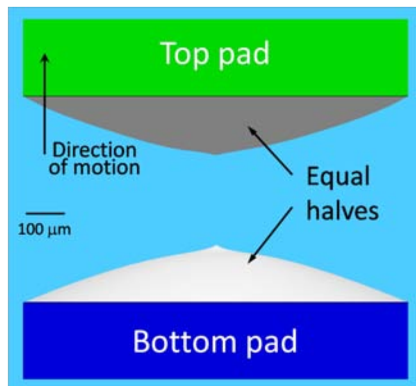

(c) Lubricant transfer for $\theta_b = \theta_t = 21^o$ (as of HD on DDT-coated Au binding sites) after bridge break-up.

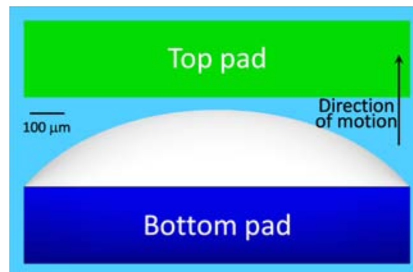

(d) Lubricant transfer for $\theta_b = 21^o$ and $\theta_t = 180^o$ (*i.e.* top pad exposing its *hydrophilic* side to the lubricant).

Figure 7.6: Finite-element simulations of lubricant transfer from binding site to part with equal footprint ($1 \times 1\, mm^2$) after quasi-static vertical part detachment.

orientation of the assembled parts [146].

We remark that when a fraction of the lubricant lens is removed, the residual lens does not conformally cover the site - unless recessed site patterns are adopted, as mentioned - while the fraction kept on the part enhances the mutual adhesion between parts (discussed in Chapter 5).

A solution to the issue of vertical part orientation was proposed by Soga [308]. It involves the realization of dummy, removable structures on the non-functional side of the parts to alter the part symmetry and consequently alter the fluid flow around the part. As a result, the parts tend to land on the binding sites with the correct (*i.e.* functional) side exposed. Experimental results and fluid dynamic simulations fairly support this claim.

Electrical interconnections

Solder metals are so far the materials of choice to establish electrical interconnections in capillary SA. In this respect, metal deposition by masked electroplating method provides good control over solder bump dimensions. It is also more reproducible and it can produce bumps of essentially any thickness – which may not be trivial to achieve with by dip-coating. Removal of the oxide from the solder surface is necessary to achieve wetting and metallic bonding.

The profile of the solder surface is also important: with a convex profile, wetting is easier; while with a concave profile some liquid can be trapped between the metallic surfaces at the time of bonding, preventing their full contact and eventually inducing voids at the solder/metal interface (see Sec. 4.3.2).

We stress that the proper application of an underfill layer between part and substrate is mandatory for capillary SA reliability and industrial adoption (see Sec. 4.3.2). Its integration within a capillary SA process flow needs to be a priority for any further work in the field.

An interesting alternative to solders might be constituted by conductive adhesives and polymers [309]. In principle, they could serve both as lubricants (in the liquid phase) and as electromechanical binders (after polymerization). However, while their suitability as lubricant can be indirectly inferred from closely-related experiments involving flux [310], the electrical properties and performance of these classes of polymers are so far inferior to those of solders, which might hinder the large benefit of short electrical interconnects associated with flip-chip-like assembly.

Possible methods to establish solder interconnect in capillary part-to-substrate SA were presented in Chapter 4, together with a detailed discussion of disruptive phenomena eventually associated.

Bibliography

[1] Marc J. Madou. *Fundamentals of Microfabrication and Nanotechnology*. CRC Press, 2010.

[2] International Technology Roadmap for Semiconductors (ITRS). available at: http://www.itrs.net. Technical report.

[3] J. Fang and K. F. Bohringer. *Comprehensive Microsystems*, chapter Self-assembly, pages 403–430. Elsevier, 2008.

[4] G. T. A. Kovacsa, N. I. Maluf, and K. E. Petersen. Bulk micromachining of silicon. *Proceedings of the IEEE*, 86:1536–1551, 1998.

[5] J. M. Bustillo, R. T. Howe, and R. S. Muller. Surface micromachining for microelectromechanical systems. *Proceedings of the IEEE*, 86:1552–1574, 1998.

[6] H. Guckel. High-aspect-ratio micromachining via deep x-ray lithography. *Proceedings of the IEEE*, 86:1586–1593, 1998.

[7] K. E. Petersen. Silicon as mechanical material. *Proceedings of the IEEE*, 70:420–457, 1982.

[8] W. S. N. Trimmer. Microrobots and microelectromechanical systems. *Sensors and Actuators*, 19:267–287, 1989.

[9] M. Gad el Hak, editor. *The MEMS Handbook*. CRC Press, 1998.

[10] A. A. Berlin and K. J. Gabriel. Distributed mems: new challenges for computation. *IEEE Computer Science and Engineering*, 4:17–29, 1997.

[11] I. F. Akyildiz, W. Su, Y. Sankarasubramaniam, and E. Cayirci. Wireless sensor networks: a survey. *Computer Networks*, 38:393–422, 2002.

[12] C.-Y. Chong and S. P. Kumar. Sensor networks: evolution, opportunities and challenges. *Proceedings of the IEEE*, 91:1247–1256, 2003.

[13] E. Aarts and R. Roovers. Ic design challenges for ambient intelligence. In *IEEE Design, Automation and test in Europe Conference and Exhibition*, pages 2–7, 2003.

[14] J. Bohn, V. Coroama, M. Langheinrich, F. Mattern, and M. Rohs. *Ambient Intelligence*, chapter Social, economic and ethical implications of ambient intelligence and ubiquitous computing, pages 5–29. Springer-Verlag, 2005.

[15] G. K. Fedder, R. T. howe, T.-J. K. Liu, and E. P. Quevy. Technologies for cofabricating mems and electronics. *Proceedings of the IEEE*, 96:306–321, 2008.

[16] O. Brand. Microsensors integration into systems-on-chip. *Proceedings of the IEEE*, 94:1160–1176, 2006.

[17] S. F. Fang, K. Adomi, S. Iyer, H. Morco, and H. Zabel. Gallium arsenide and other compound semiconductors on silicon. *J. Appl. Phys.*, 68:R31–58, 1990.

[18] P. F. Van Kessel, L. J. Hornbeck, R. E. Meier, and M. R. Douglass. A mems-based projection display. *Proceedings of the IEEE*, 86:1687–1704, 1998.

[19] Analog Devices. available at http://analog.com/imems/. Technical report.

[20] C. Van Hoof, K. Baert, and A. Witvrouw. The best material for tiny, clever sensors. *Science*, 306:986–7, 2004.

[21] A. Witvrouw, A. Mehta, A. Verbist, B. Du Bois, S. Van Aerde, J. Ramos-Martos, J. Ceballos, A. Ragel, J. M. Mora, M. A. Lagos, A. Arias, J. M. Hinoiosa, J. Spengler, C. Leinenbach, T. Fuchs, and S. Kronmuller. Processing of mems gyroscopes on top of cmos ics. In *IEEE International Solid-State Circuits Conference (ISSCC'05)*, 2005.

[22] A. E. Franke, J. M. Heck, T.-J. King, and R. T. Howe. Polycrystalline silicon-germanium films for integrated microsystems. *IEEE J.of Microelectromechanical Systems*, 12:160–171, 2003.

[23] J. F. Carpentier, A. Cathelin, C. Tilhac, P. Garcia, P. Persechini, P. Conti, P. Ancey, G. Bouche, G. Caruyer, D. Belot, C. Arnaud, C. Billard, G. Parat, J. B. David, P. Vincent, M. A. Dubois, and C. Enz. A sige:c bicmos wcdma zero-if rf front-end using an above-ic baw filter. In *IEEE International Solid-State Circuits (ISSCC'05)*, 2005.

[24] W. Kuo and T. Kim. An overview of manufacturing yield and reliability modeling for semiconductor products. *Proceedings of the IEEE*, 87:1329–1344, 1999.

[25] R. R. A. Syms, E. M. Yeatman, V. M. Bright, and G. M. Whitesides. Surface-tension powered self-assembly of microstructures the state of the art. *IEEE J. Microelectromechanical Systems*, 12:387–417, 2003.

[26] E. W.Â H. Jager, E. Smela, and O. Inganas. Microfabricating coniugated polymer actuators. *Science*, 290:1540–5, 2000.

[27] W. R. Davis, J. Wilson, S. Mick, J. Xu, H. Hua, C. Mineo, A. M. Sule, M. Steer, and P. D. Franzon. Demistifying 3d ics: the pros and cons of going vertical. *IEEE Design and Test of Computers*, 22:498–510, 2005.

[28] K. F. Bohringer, R. S. Fearing, and K. Y. Goldberg. *The Handbook of Industrial Robotics*, chapter Microassembly, pages 1045–1066. John Wiley & SOns, 1999.

[29] W. Zheng, J. Chung, and H. O. Jacobs. Fluidic heterogeneous microsystem assembly and packaging. *IEEE J. Microelectromechanical Systems*, 15:864–870, 2006.

[30] M. B. Cohn, K. F. Bohringer, J. M. Novorolski, A. Singh, C. G. Keller, K. Y. Goldberg, and R. T. Howe. Microassembly technologies for mems. In *Proceedings of SPIE Micromachining and Microfabrication Process Technology IV*, 1998.

[31] V. Sariola, Q. Zhou, R. Laass, and H. N. Koivo. Experimental study on droplet based hybrid microhandling using high speed camera. In *IEEE/RSJ International Conference on Intelligent Robots and Systems*, 2008.

[32] L. S. Goodman. Geometrical optimization of controlled collapse interconnections. *IBM Journal of Research and Development*, 13:251–265, 1969.

[33] Y. Zhang, R. Zhao, D. K. Harris, and R. W. Johnson. A computational study on solder bump geometry, normal, restoring and fillet forces during solder reflow in the presence of liquefied underfill. *IEEE Transactions on Electronic Packaging Manufacturing*, 25:308–317, 2002.

[34] C. Kallmayer, H. Oppermann, G. Engelmann, E. Zakel, and H. Reichl. Self-aligning flip-chip assembly using eutectic gold/tin solder in different atmospheres. In *IEEE International Electronics Manufacturing technology Symposium*, 1996.

[35] G. Humpston. Flip chip solder bonding for microsystems. *IEE Colloquium on assembly and connections in microsystem*, 1997.

[36] Q. Tan and Y. C. Lee. Soldering technology for optoelectronic packaging. In *IEEE Electronic Components and Technology Conference*, 1996.

[37] L. S. Goodman. Geometrical optimization of controlled collapse interconnections. *IBM Journal of Research and Development*, 13:251–265, 1969.

[38] C. Kallmayer, H. Oppermann, G. Engelmann, E. Zakel, and H. Reichl. Self-aligning flip-chip assembly using eutectic gold/tin solder in different atmospheres. In *IEEE International Electronics Manufacturing technology Symposium*, 1996.

[39] G. Humpston. Flip chip solder bonding for microsystems. *IEE Colloquium on assembly and connections in microsystem*, 1997.

[40] K. F. Harsh, W. Zhang, V. M. Bright, and Y. C. Lee. Flip-chip assembly of si-based rf-mems. In *IEEE Conference on Microelectromechanical Systems*, 1999.

[41] H. Van Brussel, J. Peirs, D. Reynaerts, A. Delchambre, G. Reinhart, N. Roth, M. Weck, and E. Zussman. Assembly of microsystems. *Annals of the CIRP*, 49:451–472, 2000.

[42] J. Israelachvili. *Intermolecular and surface forces.* Academic Press, 1994.

[43] Y.-P. Zhao, L. S. Wang, and T. X. Yu. Mechanics of adhesion in mems-a review. *Journal Adhesion Sci. Technol.*, 17:519–546, 2003.

[44] R. S. Fearing. Survey of sticking effects for micro parts handling. In *IEEE/RSJ Int. Workshop on Intelligent Robots and Systems (IROS),*, 1995.

[45] F. Arai, D. Ando, and T. Fukuda. Adhesion forces reduction for micro manipulation based on micro physics. In *Proc. IEEE Conference on Micro Electro Mechanical Systems*, pages 354–359, 1996.

[46] F. Arai and T. Fukuda. A new pick up and release method by heating for micromanipulation. In *Proc. IEEE Workshop on MEMS*, pages 383–388, 1997.

[47] C.-J. Kim, R. S. Muller, A. Pisano, and M. G. Lim. Polysilicon microtweezers. *Sensors and Actuators A (Physical)*, 33:221–227, 1992.

[48] C. G. Keller and R. T. Howe. Hexsil tweezers for teleoperated microassembly. In *Proc. IEEE Workshop on MEMS*, pages 72–77, 1997.

[49] C.-J. Kim, A. Pisano, and R. S. Muller. Si-processed overhanging microgripper. *IEEE J. Microelectromechanical Systems*, 1:31–36, 1992.

[50] C. Bark, T. Binnenbose, G. Vogele, T. Weisener, and M. Widmann. Gripping with low viscosity fluids. In *Proc. IEEE Workshop on MEMS*, pages 301–5, 1998.

[51] K. MÃžlhave, T. M. Hansen, D. N. Madsen, and P. BÃžggild. Toward pick-and-place assembly of nanostructures. *Journal of Nanoscience and Nanotechnology*, 4:279–282, 2004.

[52] B. Nelson, Y. Zhou, and B. Vikramaditya. Sensor-based microassembly of hybrid mems devices. *IEEE Control Systems Magazine*, 18:35–45, 1998.

[53] B. Nelson and B. Vikramaditya. Visually guided microassembly using optical microscopes and active vision techniques. In *Proc. IEEE Int. Conf. on Robotics and Automation (ICRA)*, pages 3172–7, 1997.

[54] J. Wei, M. Porta, M. Tichem, and P.M. Sarro. A contact position detection and interaction force monitoring sensor for micro-assembly applications. In *Transducers*, 2009.

[55] J. T. Feddema and R. W. Simon. Cad-driven microassembly and visual servoing. In *Proc. IEEE Int. Conf. on Robotics and Automation (ICRA)*, 1998.

[56] C. G. Keller and R. T. Howe. Nickel-filled hexsil thermally-actuated tweezers. In *Proceedings of 8th International Conference on Solid-state Sensors and Actuators (Transducers'95)*, pages 376–9, 1995.

[57] R. Guerre, U. Drechsler, D. Jubin, and M. Despont. Selective transfer technology for microdevice distribution. *J. Microelectromechanical Systems*, 17:157–165, 2008.

[58] A. S. Holmes and S. B. Saidam. Sacrificial layer process with laser-driven release for batch assembly operations. *IEEE J. Microelectromechanical Systems*, 7:416–422, 1998.

[59] C. H. Wang, A. S. Holmes, and S. Gao. Laser-assisted bump transfer for flip-chip assembly. In *IEEE Int. Symp. On Electronic Materials and Packaging*, pages 86–90, 2000.

[60] A. Singh, A. Horsley, M. B. Cohn, A. P. Pisano, and R. T. Howe. Batch transfer of microstructures using flip-chip solder bonding. *IEEE J. Microelectromechanical Systems*, 8:27–33, 1999.

[61] M. M. Maharbiz, M. B. Cohn, R. T. Howe, R. Horowitz, and A. P. Pisano. Batch micropackaging by compression-bonded wafer-wafer transfer. In *IEEE Conference on Micro Electro Mechanical Systems*, pages 482–9, 1999.

[62] M. B. Cohn. *Assembly techniques for microelectromechanical systems.* PhD thesis, University of California at Berkley, 1992.

[63] E. P. K. Tsang. *Foundations of constraint satisfaction.* Academic Press, 1993.

[64] S. Russel and P. Norvig. *Artificial intelligence: a modern approach*, chapter Constraint satisfaction problems. Prentice Hall, 2003.

[65] I. Miguel. *Dynamic flexible constraint satisfaction and its applicatio to AI planning.* PhD thesis, University of Edinburgh, 2001.

[66] A. Oddi, F. Fages, and F. Rossi, editors. *Recent Advances in Constraints.* Springer, 2009.

[67] S. Kirkpatrick, C. D. Gelatt Jr., and M. P. Vecchi. Optimization by simulated annealing. *Science*, 220:671–680, 1983.

[68] A. Das and B. K. Chakrabarti. Quantum annealing and analog quantum computation. *Rev. Mod. Phys.*, 80:1061–1081, 2008.

[69] N. Metropolis, A. W. Rosenbluth, M. N. Rosenbluth, A. H. Teller, and E. Teller. Equations of state calculations by fast computing machines. *Journal of Chemical Physics*, 21:1087–1091, 1953.

[70] B. Hajek. Cooling schedules for optimal annealing. *Mathematics of Operation Research*, 13:311–329, 1988.

[71] S. Wolf and R. N. Tauber. *Silicon processing for the VLSI Era. Volume 1: Process Technology.* Lattice Press, 1999.

[72] C. Kittel and H. Kroemer. *Thermal physics.* W. H. Freeman and Company, 1980.

[73] T. Hogg. Robust self-assembly using highly designable structures. *Nanotechnology*, 10:300–7, 1999.

[74] P. Ball. *The self-made tapestry.* Oxford University Press, 1999.

[75] J.-M. Lehn. *Supramolecular chemistry: concepts and perspectives.* Wiley, 1995.

[76] J.-M. Lehn. Toward complex matter: Supramolecular chemistry and self-organization. *Proc. Nat. Ac. Sc.*, 99:4763–8, 2002.

[77] E. Klavins. Programmable self-assembly. *IEEE Control System Magazine*, 24:43–56, 2007.

[78] M. Fialkowski, K. J. M. Bishop, R. Klajn, S. K. Smoukov, C. J. Campbell, and B. A. Grzybowski. Principles and implementations of dissipative (dynamic) self-assembly. *J. Phys. Chem. B*, 110:2482–2496, 2006.

[79] Y. Yin, Y. Lu, B. Gates, and Y. Xia. Template-assisted self-assembly: a practical route to complex aggregates of monodispersed colloids with well-defined sizes, shapes, and structures. *Journal of the American Chemical Society*, 123:8718–8729, 2001.

[80] H. Wu, V. R. Thalladi, S. Whitesides, and G. M. Whitesides. Using hierarchical self-assembly to form three-dimensional lattices of spheres. *Journal of the American Chemical Society*, 124:1449–514502, 2002.

[81] C. J. Morris, H. Ho, and B. A. Parviz. Bridging between nano- and micro-scales for system integration: controlled capillary force-driven self-assembly. In *Proc. IEEE Conf. on Nanotechnology*, 2005.

[82] G. M. Whitesides and B. Grzybowski. Self-assembly at all scales. *Science*, 295:2418–2421, 2002.

[83] G. M. Whitesides and M. Boncheva. Beyond molecules: Self-assembly of mesoscopic and macroscopic components. *Proceedings of the National Academy of Sciences*, 99:4769–4774, 2002.

[84] F. Schreiber. Structure and growth of self-assembling monolayers. *Progress in Surface Science*, 65:151–256, 2000.

[85] S. G. Rao, L. Huang, W. Setyawan, and S. Hong. Large-scale assembly of carbon nanotubes. *Science*, 425:36–37, 2003.

[86] Y. Xia, B. Gates, and Z.-Y. Li. Self-assembly approaches to three-dimensional photonic crystals. *Advanced Materials*, 13:409–413, 2001.

[87] D. J. Norris, E. G. Arlinghaus, L. Meng, R. Heiny, and L. E. Scriven. Opaline photonic crystals: how does self-assembly work? *Advanced Materials*, 16:1393–9, 2004.

[88] O. Ikkala and G. ten Brinke. Functional materials based on self-assembly of polymeric supramolecules. *Science*, 295:2407–9, 2002.

[89] P. W. K. Rothemund, N. Papadakism, and E. Winfree. Algorithmic self-assembly of dna sierpinski triangles. *PLOS Biology*, 2:e424, 2004.

[90] M. Boncheva and G. M. Whitesides. Making things by self-assembly. *MRS Bullettin*, 30:736–742, 2005.

[91] C. J. Morris, S. A. Stauth, and B. A. Parviz. Self-assembly for microscale and nanoscale packaging: steps toward self-packaging. *IEEE Transactions on Advanced Packaging*, 28:600–611, 2005.

[92] M. Boncheva, D. A. Bruzewicz, and G. M. Whitesides. Millimeter-scale self-assembly and its applications. *Pure Appl. Chem.*, 75:621–630, 2003.

[93] H. Leff and A. F. Rex. *Maxwell's demon 2: Entropy, Classical and Quantum Information, Computing.* Taylor and Francis, 2002.

[94] E. D. Schneider and D. Sagan. *Into the cool Energy flow, thermodynamics and life.* University of Chicago Press, 2005.

[95] J. A. Pelesko. *Self-Assembly. The Science of Things that Put Themselves Together.* Chapman & Hall/CRC, 2007.

[96] E. Klavins, R. Ghrist, and D. Lipsky. Graph grammars for self assembling robotic systems. In *Proc. Int. Conf. Robotics and Automation*, pages 5349–5355, 2004.

[97] R. Landauer. Inadequacy of entropy and entropy derivatives in characterizing the steady state. *Physical Review A*, 12:636–8, 1975.

[98] J. Hoo, R. Baskaran, and K. F. Bohringer. Programmable batch assembly of microparts with 100 In *Proc. 15th International Conference on Solid-State Sensors, Actuators & Microsystems*, 2009.

[99] W. Zheng and H. O. Jacobs. Fabrication of multicomponent microsystems by directed three-dimensional self-assembly. *Advanced Functional Materials*, 15:732–8, 2005.

[100] C. J. Morris and B. A. Parviz. Self-assembly and characterization of marangoni microfluidic actuators. *J. Micromech. Microeng.*, 16:972–980, 2006.

[101] K. F. Bohringer. *Programmable Force Fields for Distributed Manipulation, and Their Implementation Using Microfabricated Actuator Arrays.* PhD thesis, Cornell University (Ithaca, USA), Department of Computer Science, 1997.

[102] K. Saitou. Conformational switching in self-assembling mechanical systems. *IEEE Transactions on Robotics and Automation*, 15:510–520, 1999.

[103] R. D. Barish, R. Schulman, P. W. K. Rothemund, and E. WInfree. An information-bearing seed for nucleating algorithmic self-assembly. *Proc. Nat. Ac. Sc.*, 106:6054–9, 2009.

[104] S. E. Chung, W. Park, S. Shin, S. A. Lee, and S. Kwon. Guided and fluidic self-assembly of microstructures using railed microfluidic channels. *Nature Materials*, 7:581–7, 2008.

[105] M. Mastrangeli, S. Abbasi, C. Varel, C. van Hoof, J.-P. Celis, and K. F. Bohringer. Self-assembly from milli- to nanoscale: methods and applications. *J. Micromech. Microeng.*, 19:083001, 2009.

[106] B. R. Martin, D. C. Furnage, T. N. Jackson, T. E. Mallouk, and T. S. Mayer. Self-alignment of patterned wafers using capillary forces at a water-air interface. *Advanced Functional Materials*, 11:381–386, 2001.

[107] M. R. Tupek and K. T. Turner. Submicron aligned wafer bonding via capillary forces. *J. Vac. Sci. Technol.*, 25:1976–1981, 2007.

[108] C. Py, P. Reverdy, L. Doppler, J. Bico, B. Roman, and C. N. Baroud. Capillary origami: Spontaneous wrapping of a droplet with an elastic sheet. *Physical Review Letters*, 98:156103, 2007.

[109] X. Guo, H. Li, B. Y. Ahn, E. B. Duoss, K. J. Hsia, J. A. Lewis, and R. G. Nuzzo. Two- and three-dimensional folding of thin film single-crystalline silicon for photovoltaic power applications. *Proc. Nat. Ac. Sc.*, 106:20149–20154, 2009.

[110] N. Bowden, I. S. Choi, B. A. Grzybowski, and G. M. Whitesides. Mesoscale self-assembly of hexagonal plates using lateral capillary forces: synthesis using the 'capillary bond'. *J. Am. Chem. Soc.*, 121:5373–5391, 1999.

[111] N. Bowden, S. R. J. Oliver, and G. M. Whitesides. Mesoscale self-assembly: capillary bonds and negative menisci. *J. Phys. Chem. B*, 104:2714–2724, 2000.

[112] D. B. Wolfe, A. Snead, C. Mao, N. B. Bowden, and G. M. Whitesides. Mesoscale self-assembly: capillary interactions when positive and negative menisci have similar amplitudes. *Langmuir*, 19:2206–2214, 2003.

[113] N. Bowden, F. Arias, T. Deng, and G. M. Whitesides. Self-assembly of microscale objects at a liquid/liquid interface through lateral capillary forces. *Langmuir*, 17:1757–1765, 2001.

[114] B. A. Grzybowski, N. Bowden, F. Arias, H. Yang, and G. M. Whitesides. Modeling of menisci and capillary forces from the millimeter to the micrometer size range. *J. Phys. Chem.*, 105:404–412, 2001.

[115] I. S. Choi, M. Weck, B. Xu, N. L. Jeon, and G. M. Whitesides. Mesoscopic, templated self-assembly at the fluid-fluid interface. *Langmuir*, 16:2997–9, 2000.

[116] E. Klavins. *Control Problems in Robotics*, chapter Toward the Control of Self-Assembling Systems, pages 153–168. Springer, 2003.

[117] P. W. K. Rothemund. Using lateral capillary forces to compute by self-assembly. *Proceedings of the National Academy of Science*, 97:984–9, 2000.

[118] E. Saeedi, S. Abbasi, K. F. Bohringer, and B. A. Parviz. Molten-alloy driven self-assembly for nano and micro scale system integration. *Fluid Dynamics & Materials Processing*, 2:221–246, 2007.

[119] A. Terfort, N. Bowden, and G. M. Whitesides. Three-dimensional self-assembly of millimetre-scale components. *Nature*, 386:162–4, 1997.

[120] W. T. S. Huck, J. Tien, and G. M. Whitesides. Three-dimensional mesoscale self-assembly. *J. Am. Chem. Soc.*, 120:8267–8, 1998.

[121] J. Tien, T. L. Breen, and G. M. Whitesides. Crystallization of millimeter-scale objects with use of capillary forces. *J. Am. Chem. Soc.*, 120:12670–1, 1998.

[122] T. L. Breen, J. Tien, S. R. J. Oliver, T. Hadzic, and G. M. Whitesides. Design and self-assembly of open, regular, 3d mesosctructures. *Science*, 284:948–951, 1999.

[123] T. D. Clark, J. Tien, D. C. Duffy, K. E. Paul, and G. M. Whitesides. Self-assembly of 10-um-sized objects into ordered three-dimensional arrays. *J. Am. Chem. Soc.*, 123:7677–7682, 2001.

[124] D. H. Gracias, M. Boncheva, O. Omoregie, and G. M. Whitesides. Biomimetic self-assembly of helical electrical circuits using orthogonal capillary interactions. *Applied Physics Letters*, 80:2802–4, 2002.

[125] T. D. Clark, R. Ferrigno, J. Tien, K. E. Paul, and G. M. Whitesides. Template-directed self-assembly of 10-um-sized hexagonal plates. *J. Am. Chem. Soc.*, 124:5419–5426, 2002.

[126] H. O. Jacobs, A. R. Tao, A. Schwartz, D. H. Gracias, and G. M. Whitesides. Fabrication of a cylindrical display by patterned assembly. *Science*, 296:323–5, 2002.

[127] D. H. Gracias, J. Tien, T. L. Breen, C. Hsu, and G. M. Whitesides. Forming electrical networks in three-dimensions by self-assembly. *Science*, 289:1170–2, 2000.

[128] A. Terfort and G. M. Whitesides. Self-assembly of an operating electrical circuit based on shape complementarity and the hydrophobic effect. *Advanced Materials*, 10:470–3, 1998.

[129] M. Boncheva, D. H. Gracias, H. O. Jacobs, and G. M. Whitesides. Biomimetic self-assembly of a functional asymmetrical electronic device. *Proc. Nat. Ac. Sc.*, 99:4937–4940, 2002.

[130] U. Srinivasan. *Fluidic self-assembly of microfabricated parts to substrates using capillary forces*. PhD thesis, University of California at Berkeley, 2001.

[131] U. Srinivasan, D. Liepmann, and R. T. Howe. Microstructure to substrate self-assembly using capillary forces. *IEEE J. Microelectromechanical Systems*, 10:17–24, 2001.

[132] U. Srinivasan, M. A. Helmbrecht, C. Rembe, R. S. Muller, and R. T. Howe. Fluidic self-assembly of micromirrors onto microactuators using capillary forces. *IEEE Journal on Selected Topic in Quantum Electronics*, 8:4–11, 2002.

[133] K. L. Scott, T. Hirano, H. Yang, H. Singh, R. T. Howe, and A. N. Niknejadk. High-performance inductors using capillary based fluidic self-assembly. *IEEE J. Microelectromechanical Systems*, 13:300–9, 2004.

[134] K. F. Bohringer. Surface modification and modulation in microstructures: controlling protein adsorption, monolayer desorption and micro-self-assembly. *J. Micromech. Microeng.*, 13:S1–S10, 2003.

[135] X. Xiong, Y. Hanein, J. Fang, Y. Wang, W. Wang, D. T Schwartz, and K. F. Bohringer. Controlled multibatch self-assembly of microdevices. *IEEE J. Microelectromechanical Systems*, 12:117–127, 2003.

[136] M. Liu, W. M. Lau, and J. Yang. On-demand multi-batch self-assembly of hybrid mems by patterning solders of different melting points. *J. Micromech. Microeng.*, 17:2163–8, 2007.

[137] R. Sharma. Thermally controlled fluidic self-assembly. *Langmuir*, 23:6843–9, 2007.

[138] C. R. Barry, C. J. Hoon, and H. O. Jacobs. Approaching programmable self-assembly from nanoparticle-based devices to integrated circuits. In *Proceedings of Foundations of Nanoscience*, 2004.

[139] J. Chung, W. Zheng, and H. O. Jacobs. Programmable reconfigurable self-assembly: approaching the parallel heterogeneous integration on flexible substrates. In *Proc. IEEE International Conference on MEMS*, 2005.

[140] J. Chung, W. Zheng, T. J. Hatch, and H. O. Jacobs. Programmable reconfigurable self-assembly: parallel heterogeneous integration of chip-scale components on planar and nonplanar surfaces. *IEEE J. Microelectromechanical Systems*, 15:457–464, 2006.

[141] R. J. Knuesel and H. O. Jacobs. Self-assembly of microscopic chiplets at a liquid-liquid-solid interface forming a flexible segmented monocrystalline solar cell. *Proc. Nat. Ac. Sc.*, 107:993–8, 2010.

[142] S. A. Stauth and B. A. Parviz. Self-assembled single-crystal silicon circuits on plastic. *Proc. Nat. Ac. Sc.*, 103:13922–7, 2006.

[143] S. A. Stauth and B. A. Parviz. Integration of silicon components onto plastic substrates using fluidic self-assembly. In *Proc. International Conference on MEMS, NANO and Smart Systems*, 2005.

[144] E. Saeedi, S. Kim, and B. A. Parviz. Self-assembled crystalline semiconductor electronics on glass and plastic. *J. Micromech. Microeng.*, 18:075019 (7pp), 2008.

[145] S. S. Kim, E. Saeedi, D. R. Meldrum, and B. A. Parviz. Self-assembled heterogeneous integrated fluorescence detection system. In *Proc. 2nd IEEE Int. Conf. Nano/Micro Engineered and Molecular Systems*, pages 927–931, 2007.

[146] W. Zheng and H. O. Jacobs. Self-assembly process to integrate and interconnect semiconductor dies on surfaces with single-angular orientation and contact-pad registration. *Advanced Materials*, 18:1387–1392, 2006.

[147] A. H. Cannon, Y. Hua, C. L. Henderson, and W. P. King. Self-assembly for three-dimensional integrations of functional electrical components. *J. Micromech. Microeng.*, 15:2172–8, 2005.

[148] T. Fukushima, Y. Yamada, H. Kikuchi, T. Tanaka, and M. Koyanagi. Self-assembly process for chip-to-wafer three-dimensional integration. In *IEEE Electronic Components and Technology Conference*, pages 836–841., 2007.

[149] T. Fukushima, H. Kikuchi, Y. Yamada, T. Konno, J. Liang, K. Sasaki, K. Inamura, T. Tanaka, and M. Koyanagi. New three-dimensional integration technology based on reconfigured wafer-on-wafer bonding technique. In *IEEE International Electronic Device Meeting*, pages 985–8., 2007.

[150] H.-J. J. Yeh and J. S. Smith. Fluidic assembly for the integration of gaas light-emitting diodes on si substrates. *IEEE Photon. Technol. Lett*, 46:706–709, 1994.

[151] A. K. Verma, M. A. Hadley, H.-S. J. Yeh, and J. S. Smith. Fluidic self-assembly of silicon microstructures. In *Proc. 45th IEEE Electronic Components and Technology Conference*, pages 1263–1268, 1263-1268.

[152] J. S. Smith. High density, low parasitic direct integration by fluidic self assembly (fsa). In *Tech. Digest of International Electron Devices Meeting*, pages 201–204, 2000.

[153] E. J. Snyder, J. Chideme, and G. S. W. Craig. Fluidic self-assembly of semiconductor devices: a promising new method of mass-producing flexible circuitry. *Jpn. J. Appl. Phys.*, 41:4366–4369, 2002.

[154] H.-J. J. Yeh and J. S. Smith. Fluidic self-assembly of microstructures and its application to the integration of gaas on si. In *Proc. IEEE Workshop on Micro Electro Mechanical Systems*, pages 279–284, 1994.

[155] J. J. Talghader, J. K. Tu, and J. S. Smith. Integration of fluidically self-assembled optoelectronic devices using a silicon-based process. *IEEE Photon. Technol. Lett.*, 7:1321–3, 1995.

[156] J. K. Tu, J. J. Talghader, M. A. Hadley, and J. S. Smith. Fluidic self-assembly of ingaas vertical cavity surface emitting lasers onto silicon. *IEEE Electron. Lett.*, 31:1448–9, 1995.

[157] I. Soga, Y. Ohno, S. Kishimoto, K. Maezawa, and T. Mizutani. Fluidic assembly of thin gaas blocks on si substrates. *Jpn. J. Appl. Phys.*, 424:2226–2229, 2003.

[158] I. Soga, S. Hayashi, Y. Ohno, S. Kishimoto, K. Maezawa, and T. Mizutani. Direct integration of gaas hemts on aln ceramic substrates using fluidic self-assembly. *IEEE Electron. Lett.*, 41, 2005.

[159] S. Yando. Method and apparatus for fabricating an array of discrete elements, 1969.

[160] C. J. Fonstad. Magnetically-assisted statistical assembly a new heterogeneous integration technique. *MIT Technical Report*, 2002.

[161] D. I. Cheng, J. J. Rumpler II, J. M. Perkins, M. Zahn, C. G. Fonstad, E. S. Cramer, R. W. Zuneska, and F. J. Cadieu. Use of patterned magnetic films to retain and orient micro-components during fluidic assembly. *Journal of Applied Physics*, 105:07C123, 2009.

[162] S. Shet, V. R. Mehta, A. T. Fiory, M. P. Lepselter, and N. M. Ravindra. The magnetic field-assisted assembly of nanoscale semiconductor devices: A new technique. *Journal of the Minerals, Metals and Materials Society*, 56:32–4, 2004.

[163] Q. Ramadan, Y. S. Uk, and K. Vaidyanathan. Large scale microcomponents assembly using an external magnetic array. *Applied Physics Letters*, 90:172502–1, 2007.

[164] S. B. Shetye, I. Eskinazi, and D. P. Arnold. Self-assembly of millimeter-scale components using integrated micromagnets. *IEEE Trans. Magn.*, 44:4293–6, 2008.

[165] S. B. Shetye, I. Eskinazy, and D. P. Arnold. Part-to-part and part-to-substrate magnetic self-assembly of millimeter scale components with angular orientation. In *Proc. IEEE Int. Conf. on MEMS*, 2009.

[166] B. A. Grzybowski, H. A. Stone, and G. M. Whitesides. Dynamic self-assembly of magnetized, millimetre-sized objects rotating at a liquid-air interface. *Nature*, 405:1033–6, 2000.

[167] B. A. Grzybowski and C. J. Campbell. Complexity and dynamic self-assembly. *Chemical Engineering Science*, 59:1667–1676, 2004.

[168] B. A. Grzybowski and G. M. Whitesides. Macroscopic synthesis of self-assembled dissipative structures. *Journal of Physical Chemistry B*, 105:8770–5, 2001.

[169] B. A. Grzybowski and G. M. Whitesides. Directed dynamic self-assembly of objects rotating on two parallel fluid interfaces. *Journal of Chemical Physics*, 116:8571–7, 2002.

[170] J. M. K. Ng, M. J. Fuerstman, B. A. Grzybowski, H. A. Stone, and G. M. Whitesides. Self-assembly of gears at a fluid-air interface. *Journal of American Chemical Society*, 125:7948–7958, 2003.

[171] B. A. Grzybowski, M. Radkowski, C. J. Campbell, J. Lee, and G. M. Whitesides. Self-assembling fluidic machines. *Applied Physics Letters*, 84:1798–1800, 2004.

[172] M. Tanase, D. M. Silevitch, A. Hultgren, L. A. Bauer, P. C. Searson, G. J. Meyer, and D. H. Reich. Magnetic trapping and self-assembly of multicomponent nanowires. *J. Appl. Phys.*, 91:8549–8551, 2002.

[173] H. Ye, Z. Gu, T. Yu, and D. H. Gracias. Integrating nanowires with substrates using directed assembly and nanoscale soldering. *IEEE Trans. Nanotech.*, 5:62–6, 2006.

[174] T. B. Jones and J. P. Kraybill. Active feedback-controlled dielectrophoretic levitation. *J. Appl. Phys.*, 60:1247–1252, 1986.

[175] K. V. I. S. Kaler and A. K. C. Tai. Dynamic (active feedback controlled) dielectrophoretic levitation of canola protoplasts. In *IEEE Proc. Annual International Conference Engineering in Medicine and Biology Society*, pages 267–8, 1998.

[176] C. F. Edman, R. B. Swint, C. Gurtner, R. E. Formosa, S. D. Roh, K. E. Lee, P. D. Swanson, D. E. Ackley, J. J. Coleman, and M. J. Heller. Electrid field directed assembly of ingaas led onto silicon circuitry. *IEEE Photonic Technology Letters*, 12:1198–1200, 2000.

[177] A. O Riordan, P. Delaney, and G. Redmond. Field configured assembly: programmed manipulation and self-assembly at the mesoscale. *Nano Letters*, 4:761–5, 2004.

[178] S. C. Esener, D. Hartmann, M. J. Heller, and J. M. Cable. *Critical Review of Optical Science and Technology*, chapter DNA assisted micro-assembly: a heterogeneous integration technology for optoelectronics. Photonics West, 1998.

[179] S. W. Lee, H. A. McNally, D. Guo, M. Pingle, D. E. Bergstrom, and R. Bashir. Electric-field-mediated assembly of silicon islands coated with charged molecules. *Langmuir*, 18:3383–6, 2002.

[180] S. W. Lee and R. Bashir. Dielectrophoresis and electrohydrodynamics-mediated fluidic assembly of silicon resistors. *Applied Physics Letters*, 83:3833–5, 2003.

[181] S. W. Lee and R. Bashir. Dielectrophoresis and chemically mediated directed self-assembly of micrometer-scale three-terminal metal oxide semiconductor field-effect transistors. *Advanced Materials*, 17:2671–7, 2005.

[182] P. A. Smith, C . D. Nordquist, T. N. Jackson, T. S. Mayer, B. R. Martin, J. Mbindyo, and T. E. Mallouk. Electric-field-assisted assembly and alignment of metallic nanowires. *Applied Physics Letters*, 77:1399–1401, 2000.

[183] L. A. Nagahara, I. Amlani, J. Levenstein, and R. K. Tsui. Directed placement of sospended carbon nanotubes for nanometer-scale assembly. *Applied Physics Letters*, 80:3826–8, 2002.

[184] J. J. Boote and S. D. Evans. Dielectrophoretic manipulation and electrical characterization of gold nanowires. *Nanotechnology*, 16:1500–5, 2005.

[185] Y. Liu, J. H. Chung, W. K. Liu, and R. S. Ruoff. Dielectrophoretic assembly of nanowires. *J. Phys. Chem. B*, 110:14098–106, 2006.

[186] S. J. Papadakis, Z. Gu, and D. H. Gracias. Dielectrophoretic assembly of reversible and irreversible metal nanowire networks and vertically aligned arrays. *Applied Physics Letters*, 88:233118–20, 2006.

[187] S. Evoy, N. DiLello, V. Deshpande, A. Narayanan, H. Liu, M. Riegelman, B. R. Martin, B. Hailer, J.-C. Bradley, W. Weiss, T. S. Mayer, Y. Gogotsi, H. H. Bau, T. E. Mallouk, and S. Raman. Dielectrophoretic assembly and integration of nanowire devices with functional cmos operating circuitry. *Microelectronic Engineering*, 75:31–42, 2004.

[188] R. H. M. Chan, C. K. M. Fung, and W. J. Li. Rapid assembly of carbon nanotubes for nanosensing by dielectrophoretic force. *Nanotechnology*, 15:S672–7, 2004.

[189] J. Fang and K. F. Bohringer. Parallel micro components-to-substrate assembly with controlled poses and high surface coverage. *J. Micromech. Microeng.*, 16:721–730, 2006.

[190] R. Baskaran, J. H. Hoo, B. Cheng, and K. F. Bohringer. Catalyst enhanced micro scale batch assembly. In *Proc. IEEE International Conference on MEMS*, 2008.

[191] J. Fang and K. F. Bohringer. Wafer-level packaging based on uniquely orienting self-assembly (the duo-spass processes). *IEEE J. MIcroelectromechanical Systems*, 15:531–540, 2006.

[192] J. Fang and K. F. Bohringer. High yield batch packaging of micro devices with uniquely orienting self-assembly. In *Proc. IEEE International Conference on MEMS*, pages 12–5, 2005.

[193] J. Fang and K. F. Bohringer. Uniquely orienting dry micro assembly by two-stage shape recognition. In *Digest of Technical Papers, Transducers 05*, 2005.

[194] Y. Y. Ong, Y. L. Lim, L. L. Yan, E. B. Liao, and V. Kripesh. Dry self-assembly & gang bonding of micro-components from silicon carrier to substrate wafer. In *International Electronic Manufacturing Technology*, pages 486–491, 2006.

[195] Y. Y. Ong, Y. L. Lim, L. L. Yan, S. Vempati, E. B. Liao, V. Kripesh, and S. U. Yoon. Self-assembly of components using shape-matching. In *Electronics Packaging Technology Conference*, pages 826–9, 2007.

[196] V. Sariola, Q. Zhou, and H. N. Koivo. Hybrid microhandling: a unified view of robotic handling and self-assembly. *J. Micro-Nano Mech.*, 4:5–16, 2008.

[197] P. Lambert, M. Mastrangeli, J.-B. Valsamis, and G. Degrez. Spectral analysis and experimental study of lateral capillary dynamics for flip-chip applications. *Microfluidics and Nanofluidics*, pages DOI: 10.1007/s10404–010–0595–2, 2010.

[198] A. Takei, K. Matsumoto, and I. Shimoyama. Capillary torque caused by a liquid droplet sandwiched between two plates. *Langmuir*, 26:2497–2504, 2010.

[199] X. Xiong, S.-H. Liang, and K. F. Bohringer. Geometric binding site design for surface-tension driven self-assembly. In *Proc. IEEE International Conference on Robotics and Automation*, pages 1141–1148, 2004.

[200] K. Sato, K. Lee, M. Nishimura, and K. Okutsu. Self-alignment and bonding of microparts using adhesive droplets. *Int. Journal. Precision Engineering and Manufacturing*, 8:75–79, 2007.

[201] A. W. Adamson. *Physical chemistry of surfaces*. Wiley, 1990.

[202] P.-G. de Gennes, F. Brochard-Wyart, and D. Quere. *Capillarity and Wetting Phenomena: Drops, Bubbles, Pearls, Waves*. Springer, 2004.

[203] L. A. Girifalco and R. J. Good. A theory for the estimation of surface and interfacial energies. i. derivation and application to interfacial tension. *J. Phys. Chem.*, 61:904–909, 1957.

[204] E. M. Kosower. *An introduction to Physical Organic Chemistry*. Wiley, 1969.

[205] V. Gutmann. Solvent effects on the reactivities of organometallic compounds. *Coord. Chem. Rev.*, 18:225, 1976.

[206] A. A. Darhuber and S. M. Troian. Principles of microfluidic actuation by modulation of surface stresses. *Annu. Rev. Fluid Mech.*, 37:425–455, 2005.

[207] J. N. Israelachvili and M. L. Gee. Contact angles on chemically heterogeneous surfaces. *Langmuir*, 5:288–9, 1989.

[208] P. G. de Gennes. Wetting: statics and dynamics. *Reviews of Modern Physics*, 57:827–863, 1985.

[209] R. N. Wenzel. Resistance of solid surfaces to wetting by water. *Industrial and Engineering Chemistry*, 28:988–994, 1936.

[210] A. B. D. Cassie and S. Baxter. Wettability of porous surfaces. *Trans. Faraday Soc*, 40:546–551, 1944.

[211] L Gao and T. J. McCarthy. How wenzel and cassie were wrong. *Langmuir*, 23:3762–5, 2007.

[212] H. Gau, S. Herminghaus, P. Lenz, and R. Lipowsky. Liquid morphologies on structured surfaces: from microchannels to microchips. *Science*, 283:46–9, 1999.

[213] J. F. Oliver, C. Huh, and S. G. Mason. Resistance to spreading of liquids by sharp edges. *Journal of Colloid and Interface Science*, 59:568–581, 1977.

[214] A. C. Mitropoulos. The kelvin equation. *Journal of Colloid and Interface Science*, 317:643–8, 2008.

[215] R. B. Bird, R. C. Armstrong, and O. Nassager. *Dynamics of polymeric liquids - Vol. 1.* John Wiley, 1977.

[216] P. A. Kralchevsky and K. Nagayama. Capillary interactions between particles bound to interfaces, liquid films and biomembranes. *Advances in Colloid and Interface Science*, 85:145–192, 2000.

[217] D. Chandler. Interfaces and the driving force of hydrophobic assembly. *Nature*, 437:640–7, 2005.

[218] E. E. Meyer, K. J. Rosenberg, and J. Israelachvili. Recent progress in understanding hydrophobic interactions. *Proc. Nat. Ac. Sc.*, 103:15739–15746, 2006.

[219] B. Berge and J. Peseux. Variable focal lens controlled by an external voltage: An application of electrowetting. *European Physical Journal E*, 3:159–163, 2000.

[220] M. De Volder, J. Peirs, D. Reynaerts, J. Coosemans, R. Puers, O. Smal, and B. Raucent. A novel hydraulic microactuator sealed by surface tension. *Sensors and Actuators A: Physical*, 123-4:547–554, 2005.

[221] P. Lambert. *Capillary forces in microassembly.* Springer, 2007.

[222] R. J. K. Wassink. *Soldering in electronics.* Electrochemical Publications, 2005.

[223] S. K. Patra and Y. C. Lee. Quasi-static modeling of the self-alignment mechanism in flip-chip soldering - part 1: single solder joint. *Journal of Electronic Packaging*, 113:337–342, 1991.

[224] S. K. Patra and Y. C. Lee. Modeling of self-alignment mechanism in flip-chip soldering - part ii: multichip solder joints. In *Proc. Electronic Components and Technology Conference*, 1991.

[225] B. Yost, J. McGroarty, P. Borgesen, and C.-Y. Li. Shape of a nonaxisymmetric liquid solder drop constrained by parallel plates. *IEEE Transactions on Components, Hybrids and Manufacturing Technology*, 16:523–6, 1993.

[226] W. Lin, S. K. Patra, and Y. C. Lee. Design of solder joints for self-aligned optoelectronics assembly. *IEEE Transactions on Components, Packaging and Manufacturing Technology - Part B*, 18:543–551, 1995.

[227] J. Lienemann, A. Greiner, J. G. Korvink, X. Xiong, Y. Hanein, and K. F. Bohringer. Modelling, simulation and experiment of a promising new packaging technology parallel fluidic self-assembly of microdevices. *Sensors Update*, 13:3–43, 2003.

[228] K. F. Bohringer, U. Srinivasan, and R. T. Howe. Modelling of capillary forces and binding sites for fluidic self-assembly. In *EEE International Conference on MEMS*, pages 369–374, 2001.

[229] S.-H. Liang, X. Xiong, and K. F. Bohringer. Toward optimal designs for self-alignment in surface tension driven micro-assembly. In *IEEE International Conference on MEMS*, pages 9–12, 2004.

[230] N. Van Veen. Analytical derivation of the self-alignment motion of flip-chip soldered components. *Transactions of the ASME*, 121:116–121, 1999.

[231] K. Sato, K. Ito, S. Hata, and A. Shimokohbe. Self-alignment of microparts using liquid surface tension: behaviour of micropart and alignment characteristics. *Precision Engineering*, 27:42–50, 2003.

[232] R. W. Bernstein, X Zhang, S. Zappe, M. Fish, M. Scott, and O. Solgaard. Characterization of fluidic microassembly for immobilization and positioning of drosophila embryos in 2-d arrays. *Sensors and Actuators A*, 114:191–6, 2004.

[233] C. Lin, F. Tseng, and C.-C. Chieng. Studies on size and lubricant effects for fluidic self-assembly of microparts on patterned substrates using capillary effect. *Journal of Electronic Packaging*, 130:021005–1, 2008.

[234] C. D. Cooper and F. C. Alley. *Air pollution control: a design approach.* Waveland, 1994.

[235] X. Zhang, C.-C. Chen, R. W. Bernstein, S. Zappe, M. P. Scott, and O. Solgaard. Microoptical characterization and modeling of positioning forces on drosophila embryos self-assembled in two-dimensional arrays. *IEEE J. Microelectromechanical Systems*, 14:1187–1197, 2005.

[236] C. Clasen, B. P. Gearing, and G. H. McKinley. The flexure-based microgap rheometer (fmr). *J. Rheol.*, 50:883–905, 2006.

[237] W. T. Thomson and M. D. Dahleh. *Theory of vibration with applications.* Prentice Hall, 1998.

[238] S. Henein. *Conception des structures articulees a guidages flexibles de haute precision.* PhD thesis, Ecole Polytechnique Federale de Lousanne, 2000.

[239] K. A. Brakke. The surface evolver. *Experimental Mathematics*, 1:141–165, 1992.

[240] A. Greiner, J. Lienemann, J.G. Korvink, X. Xiong, Y. Hanein, and K. F. Bohringer. Capillary forces in micro-fluidic self-assembly. In *Proc. 5th International Conference on Modeling and Simulation of Microsystems*, pages 198–201, 2002.

[241] A. A.O. Tay, H. Li, X. Gao, J. Chen, and V. Kripesh. Simulation of forces acting on tiny chips during fluidic self-assembly. In *Proc. Electronics Packaging Technology Conference*, 2006.

[242] J. Lienemann. Modeling and simulation of the fluidic controlled self-assembly of micro parts. Master's thesis, Albert Ludwig University Frieburg, 2002.

[243] S. Abbasi, A. X. Zhou, and R. Baskaran K.l F. Bohringer. Part tilting in capillary-based self-assembly: modeling and correction methods. In *Proc. IEEE MEMS*, 2008.

[244] K. L. Scott, R. T. Howe, and C. J. Radke. Model for micropart planarization in capillary-based microassembly. In *Proc. 12th International Conference on Solid-State Sensors, Actuators and Microsystems (Transducers '03)*, pages 1319–1322, 2003.

[245] C. Lin, F. Tseng, and C.-C. Chieng. Orientation-specific fluidic self-assembly process based on a capillary effect. *J. Micromech. Microeng.*, 19:115020 (12pp), 2009.

[246] J. Leopoldes, A. Dupuis, D. G. Bucknall, and J. M. Yeomans. Jetting micron-scale droplets onto chemically heterogeneous surfaces. *Langmuir*, 19:9818–9822, 2003.

[247] J. Y. Kim, C. Ingrosso, V. Fakhfouri, M. Striccoli, A. Agostiano, M. L. Curri, and J. Brugger. Inkjet-printed multicolor arrays of highly luminescent nanocrystal-based nanocomposites. *Small*, 5:1051–7, 2009.

[248] P. R. Schunk, A. J. Hurd, and C. J. Brinker. *Liquid film coating*, chapter Free-meniscus coating processes. Chapman and Hall, 1997.

[249] W. Moench and H. Zappe. Fabrication and testing of micro-lens arrays by all-liquid techniques. *Journal of Optics A*, 6:330–7, 2004.

[250] L. Landau and B. Levich. Dragging of a liquid by a moving plate. *Acta Physicochimica*, 17:42, 1942.

[251] B. M. Deryagin and S. M. Levi. *Film coating theory.* Focal Press Ltd., 1964.

[252] A. A. Darhuber, S. M. Troian, J. M. Davis, and S. M. Miller. Selective dip-coating of chemically micropatterned surfaces. *Journal of Applied Physics*, 88:5119–5126, 2000.

[253] D. M. Hartmann, O. Kibar, and S. C. Esener. Optimization and theoretical modeling of polymer microlens arrays fabricated with the hydrophobic effect. *Applied Optics*, 40:2736–2746, 2001.

[254] R. J. Jackmann, D. C. Duffy, E. Ostuni, N. D. Willmore, and G. M. Whitesides. Fabricating large arrays of microwells with arbitrary dimensions and filling them using discontinuous dewetting. *Anal. Chem.*, 70:2280–7, 1998.

[255] H. A. Biebuyck and G. M. Whitesides. Self-organization of organic liquids on patterned self-assembled monolayers of alkanethiolates on gold. *Langmuir*, 10:2790–3, 1994.

[256] N. L. Abbott, G. M. Whitesides, M. L. Racz, and J. Szekely. Using finite element analysis to calculate the shapes of geometrically confined drops of liquid on patterned, self-assembled monolayers: a new method to estimate excess interfacial free energies. *J. Am. Chem. Soc.*, 116:290–4, 1994.

[257] J. C. Love, L. A. Estroff, J. K. Kriebel, R. G. Nuzzo, and G. M. Whitesides. Self-assembled monolayers of thiolates on metals as a form of nanotechnology. *Chem. Rev.*, 105:1103–1169, 2005.

[258] K. L. Scott. PhD thesis, University of California at Berkeley, 2004.

[259] M. R. Houston and R. Maboudian. Stability of ammonium fluoride-treated si(100). *J. Appl. Phys.*, 78:3801–8, 1995.

[260] H. Y. Erbil, G. McHale, and M. I. Newton. Drop evaporation on solid surfaces: constant contact angle mode. *Langmuir*, 18:2636–2641, 2002.

[261] C. J. Morris and B. A. Parviz. Micro-scale metal contacts for capillary force-driven self-assembly. *J. Micromech. Microeng.*, 18:015022 (10pp), 2008.

[262] M. Abtew and G. Selvaduray. Lead-free solders in microelectronics. *Materials Science and Engineering*, 27:95–141, 2000.

[263] K. N. Tu, A. M. Gusak, and M. Li. Physics and materials challenges for lead-free solders. *Journal of Applied Physics*, 93:1335–1353, 2003.

[264] J. Glazer. Metallurgy of low temperature pb-free solders for electronic assembly. *International Materials Reviews*, 40:65–93, 1995.

[265] C.-C. Liu, Y.-K. Lin, M.-P. Houng, and Y.-H. Wang. The microstructure investigation of flip-chip laser diode bonding on silicon substrate by using indium-gold solder. In *IEEE Trans. Components and Packaging Technologies*, volume 26, pages 635–641, 2003.

[266] F. E. Bartell and M. A. Miller. Alteration of the free surface energy of solids. ii. effect of heat treatment of metals in air. *J. Phys. Chem.*, 40:889–894, 1936.

[267] J. F. Kuhmann, A. Preuss, B. Adolphi, K. Maly, T. Wirth, W. Oesterle, W. Pittroff, G. Weyer, and M. Fanciulli. Oxidation and reduction kinetics of eutectic snpb, insn, and ausn: A knowledge base for fluxless solder bonding applications. *IEEE Trans. Components, Packaging and Manufacturing Technology - Part C*, 21:134–141, 1998.

[268] W. Lin and Y. C. Lee. Study of fluxless soldering using formic acid vapor. *IEEE Trans. on Adv. Pack.*, 22:592–601, 1999.

[269] H. Okamoto and T. B. Massalski. Phase diagrams and binary gold alloys. *ASM International*, pages 142–153, 1987.

[270] E. Delamarche, B. Michel, H. Kang, and C. Gerber. Thermal stability of self-assembled monolayers. *Langmuir*, 10:4103–8, 1994.

[271] S. Wakiyama, H. Ozaki, Y. Nabe, T. Kume, T. Ezaki, and T. Ogawa. Novel low-temperature coc interconnection technology for multichip lsi (mcl). In *Proc. 57th Electronic Components and Technology Conf.*, pages 610–5, 2007.

[272] Y. M. Liu and T. H. Chuang. Interfacial reactions between liquid indium and au-deposited substrates. *J. Electr. Mat.*, 29:405–410, 2000.

[273] S. Park, J.-H. Lim, S.-W. Chung, and C. A. Mirkin. Self-assembly of mesoscopic metal-polymer amphiphiles. *Science*, 303:348–351, 2004.

[274] H. Onoe, K. Matsumoto, and I. Shimoyama. Three-dimensional sequential self-assembly of microscale objects. *Small*, 3:1383–9, 2007.

[275] M. Rycenga, J. M. McLellan, and Y. Xia. Controlling the assembly of silver nanocubes through selective functionalization of their faces. *Adv. Mat.*, 20:2416–2420, 2008.

[276] M. Mastrangeli, W. Ruythooren, and C. Whelan. Method for performing parallel stochastic assembly, 2010.

[277] D. A. Leigh E. R. Kay and F. Zerbetto. Synthetic molecular motors and mechanical machines. *Angew. Chem. Int. Ed.*, 46:72–191, 2007.

[278] P. Reimann. Brownian motors: noisy transport far from equilibrium. *Physics Reports*, 361:57–265, 2002.

[279] D. A. Leigh, K. Moody, J. P. Smart, K. J. Watson, and A. M. Z. Slawin. Catenane chameleons: Environment-sensitive translational isomerism in amphiphilic benzylic amide [2]catenanes. *Angew. Chem. Int. Ed. Engl.*, 35:306–310, 1996.

[280] S. Hofl, L. Zitzler, T. Hellweg, S. Herminghaus, and F. Mugele. Volume phase transition of "smart" microgels in bulk solution and adsorbed at an interface: a combined afm, dynamic light, and small angle neutron scattering study. *Polymer*, 48:245–254, 2007.

[281] T. Sun, G. Wang, L. Feng, B. Liu, Y. Ma, L. Jiang, and D. Zhu. Reversible switching between superhydrophilicity and superhydrophobicity. *Angew. Chem. Int. Ed.*, 43:357–360, 2004.

[282] K. Hosokawa, I. Shimoyama, and H. Miura. Two-dimensional micro-self-assembly using the surface tension of water. *Sensors and Actuators A*, 57:117–125, 1996.

[283] K. Hosokawa, I. Shimoyama, and H. Miura. Dynamics of self-assembling systems analogy with chemical kinetics. *Artificial Life*, 1:413–427, 1995.

[284] E. Klavins, S. Burden, and N. Napp. *Robotics: Science and Systems*, chapter Optimal Rules for Programmed Stochastic Self-Assembly, pages 9–16. MIT Press, 2006.

[285] L. Adleman, Q. Cheng, A. Goel, M.-D. Huang, and H. Wasserman. Linear self-assemblies: equilibria, entropy and convergence rates. In *6th Int. Conf. on Difference Equations*, 2004.

[286] A. DeHon, P. Lincoln, and J. E. Savage. Stochastic assembly of sublithographic nanoscale interfaces. *IEEE Trans. Nanotechnol.*, 2:10, 2003.

[287] P. J. White, K. Kopanski, and H. Lipson. Stochastic self-reconfigurable cellular robotics. In *IEEE Int. Conf. Robotics and Automation*, 2004.

[288] E. Klavins, R. Ghrist, and D. Lipsky. A grammatical approach to self-organizing robotic systems. *IEEE Trans. Autom. Control*, 51:949–962, 2006.

[289] G. Mermoud, J. Brugger, and A. Martinoli. Toward multi-level modeling of self-assembling intelligent micro-systems. In *Proc. Int. Conf. on Autonomous Agents and Multiagent Systems*, pages 89–96, 2009.

[290] D. Gillespie. Stochastic simulation of chemical kinetics. *Annual Review of Physical Chemistry*, 58:35–55, 2007.

[291] I. Langmuir. The constitution and fundamental properties of solids and liquids. part i. solids. *J. Am. Chem. Soc.*, 38:2221–2295, 1916.

[292] N. G. Van Kampen. *Stochastic processes in physics and chemistry.* North Holland, 2007.

[293] L. M. Sander. Diffusion-limited aggregation: a kinetic critical phenomenon? *Contemp. Phys.*, 41:203–218, 2000.

[294] M. Luck, R. Ashri, and M. DInverno. *Agent-based software development.* Artech House, 2004.

[295] J. H. Miller and Scott E. Page. *Complex Adaptive Systems An Introduction to Computational Models of Social Life.* Princeton University Press, 2007.

[296] F. Schweitzer. *Brownian agents and active particles.* Springer, 2003.

[297] R. B. Bird, W. Stewart, and E. N. Lightfood. *Transport phenomena.* John Wiley and Sons, 2002.

[298] R. Kurzweil. *The singularity is near*. Viking Adult, 2005.

[299] P. Ball. *Critical mass*. William Heinemann, 2004.

[300] S. Kauffman. *At home in the universe*. Oxford University Press, 1995.

[301] M. Ohring. *Reliability and Failure of Electronic Materials and Devices:*. Academic Press, 1998.

[302] C. G. Tsai, C. M. Hsieh, and J. A. Yeh. Self-alignment of microchips using surface tension and solid edge. *Sensors and Actuators A*, 139:343–9, 2007.

[303] C. J. Morris, H. Ho, and B. A. Parviz. Liquid polymer deposition on free-standing microfabricated parts for self-assembly. *J. Microelectromechanical Systems*, 15:1795–1804, 2006.

[304] K.-F. Bohringer, K. Goldberg, M. Cohn, R. Howe, and A. Pisano. Parallel microassembly with electrostatic force fields. In *Proc. IEEE International Conference on Robotics & Automation*, 1998.

[305] A. A. Darhuber, S. M. Troian, and S. Wagner. Physical mechanisms governing pattern fidelity in microscale offset printing. *Journal of Applied Physics*, 90:3602–9, 2001.

[306] A. V. Chadov and E. D. Yakhnin. Investigation of the transfer of liquid from one solid surface to another 1. slow transfer. method of approximate calculation. *Kollodny Zhurnal*, 41:817–820, 1979.

[307] A. V. Chadov and E. D. Yakhnin. Investigation of the transfer of a liquid from one solid surface to another 2. dynamic transfer. *Kollodny Zhurnal*, 45:1183–8, 1983.

[308] I. Soga, Y. Ohno, S. Kishimoto, K. Maezava, and T. Mizutani. Fluid dynamic assembly of semiconductor blocks for heterogeneous integration. *Jpn. J. Appl. Phys.*, 43:5951–5954, 2004.

[309] Y. Li, , and C. P. Wong. Recent advances of conductive adhesives as a lead-free alternative in electronic packaging: Materials, processing, reliability and applications. *Materials Science and Engineering*, 51:1–35, 2006.

[310] J.-M. Kim, K. Yasuda, and K. Fujimoto. Resin self-alignment processes for self-assembly systems. *Transactions of the American Society of Mechanical Engineers*, 127:18–24, 2005.